INFLUENCE OF ISOSPIN DEPENDENT NUCLEAR CHARGE RADIUS IN HEAVY ION COLLISIONS AT INTERMEDIATE ENERGIES

A THESIS

Submitted to the

FACULTY OF SCIENCE

THAPAR INSTITUTE OF ENGINEERING
AND TECHNOLOGY (TIET), PATIALA
for the degree of

DOCTOR OF PHILOSOPHY

By

Sangeeta

Regn. No. 901312005

THAPAR INSTITUTE
OF ENGINEERING & TECHNOLOGY
(Deemed to be University)

SCHOOL OF PHYSICS AND MATERIALS SCIENCE

TIET, PATIALA-147004, PUNJAB
INDIA

.

I dedicate this work to my beloved Mom and Dad I'm blessed with
For their endless love, support and encouragement
The most overwhelming key to my success
The ones, who believed me and had faith.
And to
Nirankari Baba Hardev Singh Ji Maharaj
&
Satguru Mata Savinder Hardev Ji Maharaj
Whose teaching of tolerance, patience and love to humanity becomes
support to deal with every situation of life.
A part of this dedication goes to my brother
For his irreplaceable joy and laughter in my life.

THAPAR INSTITUTE
OF ENGINEERING & TECHNOLOGY
(Deemed to be University)

CANDIDATE'S DECLARATION

I hereby certify that the thesis entitled "**INFLUENCE OF ISOSPIN DEPENDENT NUCLEAR CHARGE RADIUS IN HEAVY ION COLLISIONS AT INTERMEDIATE ENERGIES**" is partial fulfillment of the requirements for the award of degree of Doctor of Philosophy in the School of Physics and Materials Science (SPMS), Thapar Institute of Engineering and Technology (TIET), Patiala, is a record of my own work carried under the supervision of **Prof. O. P. Pandey**, Head SPMS, TIET, Patiala and **Dr. Varinderjit Kaur**, Assistant Professor, Khalsa College, Patiala. The matter presented in this thesis has not been submitted by me in part or full for the award of any other degree in any other university or institute.

Sangeeta

(Sangeeta)

This is to certify that the above statement made by the candidate is correct to the best of our knowledge.

Supervisor & Head SPMS

(Prof. O. P. Pandey)

Supervisor

(Dr. Varinderjit Kaur)

Dean R & SP

(Prof. Rafat Siddique)

External examiner

(Dr. Chandana Bhattacharya)

Date: 2nd November, 2018

Acknowledgements

At the outset, I submit my thesis at the feet of ***God*** and express my gratitude and indebtedness to Him for countless blessings. I bow to Him with limitless gratitude and humility. Without His will, this Ph. D. would not have been initiated - not to mention completion. It is a pleasant aspect that I now have the opportunity to acknowledge with respect, all those persons who are in one way or another have contributed in making this thesis possible.

First and Foremost, I would like to express profoundest gratitude to my Ph. D. supervisors ***Prof. O. P. Pandey***, Head, School of Physics and Materials Science, Thapar Institute of Engineering and Technology (TIET), Patiala . His guiding spirit and integral views on research has not only given this work its present shape but also helped me to become a better person in every way of life. I have known him as a disciplined and principle-centered person. Despite of his busy schedule, he was readily available for me to conquer every problem. Thank you for believing in me and encouraging my research.

I extend my heartfelt gratitude to my second supervisor ***Dr. Varinderjit Kaur***, Assistant Professor, Department of Physics, Khalsa College, Patiala. Her dynamic guidance and continuous motivation inspired me to discover my own dormant potentials. Her inspiring suggestions have been precious for the development of the content of this thesis. Without her kind and patient instruction, it was not possible for me to finish my Ph. D. work. I learned a lot from her. I also thank to *Dr. Mandeep Singh*, Assistant Professor, Department of Electrical & Instrumentation Engineering (TIET) for his helpful views and encouragement.

I am happy to acknowledge the members of my doctoral committee *Prof. Manoj K. Sharma*, *Dr. Mahesh K. Sharma* and *Dr. S. Jana* for their useful suggestions, during the six-month progress report. I wish to express my thanks to all the faculty and staff of the SPMS. I extend my sincere thanks to *Prof. Kulvir Singh.* I express my thanks to *Prof. Rafat Siddique*, Dean Research and Sponsored Projects for providing the possible research facilities here at TIET. I am very much thankful to *Prof. Manju Arora* (Mohindra College, Patiala), who motivated me to learn physics during my graduation.

I acknowledge with thanks the co-operation and encouragement extended by *Prof. R. K. Puri*, Panjab University for their fruitful discussions and novel views. I will always

be deeply indebted to *Prof. Prakash Gopalan*, Director, TIET and *Dr. Gurbinder Singh*, Registrar, TIET for their invaluable support during the hard phase of my Ph. D. I also acknowledge the support of *Dr. Suneel Kumar* and *Dr. Anupriya jain* during initial period of research.

I sincerely thank to *Dr. A. Saxena* and *Dr. B. K. Nayak*, NPD, BARC, Mumbai, for their encouragement, constant support and giving me opportunities to participate in various experiments at BARC-TIFR Pelletron, Mumbai during my research internship at BARC. This internship helped me to understand various technical details of experimental nuclear physics.

I would like to thank my lab mates *Dr. Mandeep Kaur*, *Dr. Manpreet Kaur* (SGGSW University), *Ms. Kamaldeep Kaur* and *Dr. Rubina Bansal* for their invaluable discussions and pleasant company. I am also thankful to members of other lab groups specially *Dr. Deepika Jain*, *Dr. Gudveen Sahney*, *Dr. Rajni*, *Ms. Gurjit*, *Ms. Amandeep Kaur* and *Ms. Pallavi Gupta* for making this experience an enjoyable event.

The journey of Ph. D. will not be easy without the support of my friends. I owe a deep sense of gratitude to my friends *Neha*, *Kanishka* and *Shivani* for all the fantastic moments we spent together. I would love to mention my cheerful bestie *Amanu* (Amandeep Kaur). I am fortunate enough to have you. Because of you, I laugh a little harder, cry a little less and smile a lot more. You all made my stay at Thapar (Since my M.Sc.) joyful and memorable. A specials thanks goes to my friends *Sneha* and *Pankaj* from Central University of Jharkhand; *Mohd. Shuaib*, *Tabbasum*, *Mariyah*, *Muntazir* and *Suhel* from Aligarh Mulslim University; *Nabendu* from Gauhati University, *Aman Gandhi* from Banaras Hindu University and *Nishchal Dwivedi* from BARC. We all met in conferences held for few days but made life long friendship.

Words are not sufficient to express my inner sentiments towards my family. I am forever grateful to my grandparents *Amma* (I always miss you!) and *Papa ji*, whose values paved the way for regular attending congregations and self-less service to humanity. Of course, goal could not have been achieved without the blessings and immense moral support of my parents ***Mr. Suresh Kumar*** and ***Mrs. Asha Rani***. Mumma-You are my greatest teacher, a teacher of compassion, love and fearlessness. My daddy- who taught me to be wise, how to pick myself up after a failure and rise above. I thanks to

them for their unconditional love, patience and belief in me, which gave me the necessary motivation and strength to endure research and complete my thesis. I feel very lucky to have the best person in this world, my brother ***CMA Naresh***. He guided me a lot and never makes me feel down even when I was not confident. Thanks a lot for being there for me.

I really enjoyed and cherished the moments spent with my li'l champs, my cousins ***Nitesh*** and ***Sonalika***, whose smiling faces and company refreshed my mind during the frustrating hours of my doctorate degree.

The financial assistance from Department of Science and Technology (DST), Government of India, New Delhi, in terms of Innovation in Science Pursuit for Inspired Research (INSPIRE)-Fellowship under AORC Programme (grant no. DST/INSPIRE/03/2014/000234) is gratefully acknowledged.

A word of thanks to those people who never doubted my intentions.

Patiala

2^{nd} November, 2018.

(Sangeeta)

List of Publications :

A. Journals :

1. Influence of isospin dependent nuclear charge radii on fragmentation in heavy ion collisions.
   Sangeeta, Anupriya jain and Suneel Kumar,
   Nucl. Phys. A **927** 220-231 (2014).

2. Initialization effects via nuclear charge radii parameterizations on the nuclear stopping and its relation to distribution and production of light mass fragments.
   Sangeeta,
   Acta Phys. Pol. B **47**, 991-996 (2016).

3. Structural effects through nuclear charge radius in mass asymmetric collisions.
   Sangeeta and Varinderjit Kaur,
   Acta Phys. Pol. B **48**, 623-627 (2017).

4. Structural and isospin effects on balance energy and transition energy via different nuclear charge radii parameterizations.
   Sangeeta and Varinderjit Kaur,
   Nucl. Phys. A **966**, 20-33 (2017).

5. Influence of nuclear charge radius parameterization on the excitation function of nuclear stopping.
   Sangeeta and Varinderjit Kaur,
   Ind. J. Sci. and Tech. **10**, 31 (2017).

6. Effect of clusterization technique as per different radii parameterizations on collective flow.
   Sangeeta and Varinderjit Kaur,(to be submitted)

7. Quest for the balancing geometry of reduced flow and transition geometry of elliptical flow at intermediate energy heavy ion collisions.
   Sangeeta and Varinderjit Kaur, (to be submitted)

B. International/ National Symposia/ Workshops/ Conferences:

8. Isospin effect on elliptical flow for mass asymmetric nuclear collisions. (Poster Presentation)
   Sangeeta and Suneel Kumar,
   Proc. of the Int. DAE Symp. on Nucl. Phys. **58**, 410 (2013).
   58^{th} Symposium on Nuclear Physics (as international event), Bhabha Atomic Research Center, Mumbai, Dec 2-6, 2013.

9. Sensitivity of the transition energy towards mass asymmetry of the colliding nuclei.
   Anupriya Jain, **Sangeeta Arora** and Suneel Kumar,
   EPJ web of conferences **66**, 03039 (2014).
   International Nuclear Physics Conference (INPC), Firenze, Italy, 2-7 June 2013.

10. Light mass fragments production due to isospin dependent radius of colliding nuclei. (Oral Presentation)
    Sangeeta, Anupriya Jain and Suneel Kumar,
    Raman Memorial Conference, 07-08 Feb. 2013, University of Pune, Pune, INDIA.

11. Transverse momentum dependence of elliptical flow for different radius parameterizations. (Poster Presentation)
    Sangeeta and Suneel Kumar,
    Proc. Of DAE Symp. On Nucl. Phys. **59**, 454 (2014).
    59^{th} DAE-BRNS Symposium On Nuclear Physics, Banaras Hindu University, Varanasi, Dec. 08-12, 2014.

12. Influence of isospin dependence of radius on fragmentation.
    Anupriya Jain, **Sangeeta** and Suneel Kumar,
    Proc Indian Natn Sci Acad **81** No. 1 February 2015 Special Issue, pp. 70-74.
    International Conference on Matter at Extreme Conditions : Then and Now, Variable Energy Cyclotron Centre-Kolkata, India, January 15-17, 2014

13. Effect of nuclear charge radii parameterizations and Fermi momentum on the fragmentation. (Oral Presentation)

Sangeeta,

Workshop on High Performance Computing 2015, Inter-University Accelerator Centre, New Delhi March 11-13, 2015.

14. Effect of nuclear charge radii parameterizations and Fermi momentum on the transverse momentum and multiplicity of light fragments. (Poster Presentation)
    Sangeeta and Navjot Kaur Virk,
    Proc. Of DAE Symp. On Nucl. Phys. **60**, 430 (2015).
    60^{th} DAE-BRNS Symposium On Nuclear Physics, Sri Sathya Sai Institute of Higher Learning, Prasanthi Nilayam, A.P. India, Dec. 7-11, 2015.

15. Transition energy of neutron-rich colliding pairs in intermediate energy heavy ion collisions. (Poster Presentation)
    Navjot Kaur Virk and **Sangeeta**,
    Proc. Of DAE Symp. On Nucl. Phys. **60**, 528 (2015).
    60^{th} DAE-BRNS Symposium On Nuclear Physics, Sri Sathya Sai Institute of Higher Learning, Prasanthi Nilayam, A.P. India, Dec. 7-11, 2015.

16. Role of different nuclear charge radii parameterizations on the thermal equilibrium in nuclear reactions. (Oral Presentation)
    Sangeeta and Varinderjit Kaur,
    EPJ web of conferences **146**, 12017 (2017).
    at International Conference on Nuclear Data for Science and Technology ND(2016) 11-16 Sep. 2016 Bruges (**Belgium**)

17. Effect of different nuclear radii parameterizations on the equilibrium using collision dynamics. (Poster Presentation)
    Sangeeta and Varinderjit Kaur,
    Proc. Of DAE Symp. On Nucl. Phys. **62**, 596 (2017).
    62^{th} DAE-BRNS Symposium On Nuclear Physics, Thapar Institute of Engineering and Technology, Patiala, Dec 20-24, 2017.

18. Influence of isospin dependent level density parameter on neutron induced reaction cross section (Oral Presentation)

Sangeeta, B. K. Nayak, A. Saxena, S. V. Suryanarayan, G. Mohanto and B. Pandey,

Proc. Of DAE Symp. On Nucl. Phys. **62**, 390 (2017).

DAE-BRNS Symposium on nuclear physics, Thapar Institute of Engineering and Technology, Patiala, Dec 20-24, 2017.

19. Determination of hexadecapole deformation for 160Gd nucleus using quasi-elastic scattering

    Sukanya De, G. Mohanto, A. Parihari, E.T. Mirgule, B. Srinivasan, P.C. Rout, M. Kushwaha, **S. Arora**, C. Joshi, A. Sharma, B.K. Nayak and A. Saxena,

    Proc. Of DAE Symp. On Nucl. Phys. **62**, 398 (2017).

    DAE-BRNS Symposium on nuclear physics, Thapar Institute of Engineering and Technology, Patiala, Dec 20-24, 2017.

20. Effect of clusterization algorithm with isospin-dependent nuclear charge radii parameterization on azimuthal angle distribution of elliptical flow. (Poster Presentation)

    Sangeeta,

    International Conference on Nuclear, Particle and Accelerator Physics (ICNPAP-2018), Central University of Jharkhand, Brambe, Ranchi, Oct. 23-26, 2018.

21. Isospin effect on elliptical flow for mass asymmetric nuclear collisions (Thesis Poster)

    G. Mohanto, A. Parihari, P.C. Rout, E. T. Mirgule, S. De, K. Mahata, M. Kushwaha, S. P. Behera, A. Gandhi, **Sangeeta**, N. Deb, D. Sarkar, B. Srinivasan, B. K. Nayak, and A. Saxena (Accepted)

    63^{th} Symposium on Nuclear Physics (as international event), Bhabha Atomic Research Center, Mumbai, Dec 10-14, 2018.

22. Collective enhancement of nuclear level density

    Sangeeta (Accepted)

    63^{th} Symposium on Nuclear Physics (as international event), Bhabha Atomic Research Center, Mumbai, Dec 10-14, 2018.

Contents

Abstract **1**

1 Introduction **5**

1.1 Heavy-ion collisions: an introduction 5

1.2 Phase diagram of nuclear matter 9

1.3 Isospin dependence of nuclear equation of state: 11

1.4 Isospin dependence of nuclear radius 16

1.5 Initialization effects through nuclear radius 20

1.6 Description of various Phenomena occurring at intermediate energies . . . 22

1.6.1 Multi-fragmentation 23

1.6.2 Collective Flow 26

1.6.3 Nuclear Stopping 32

1.7 Organisation of thesis 36

2 Methodology **38**

2.1 Introduction 38

2.2 Review of various theoretical approaches in HICs at intermediate energies . 38

2.2.1 Many body molecular dynamics approach and its recent updates . . 41

2.3 Isospin dependent Quantum Molecular Dynamics (IQMD) model 44

2.3.1 Initialization 44

2.3.2 Propagation 49

2.3.3 Nucleon-nucleon collisions 57

2.3.4 Pauli blocking 60

2.4 Secondary algorithms 62

3 Influence of isospin dependent nuclear charge radii on fragmentation 63

3.1 Introduction . . . 63

3.2 Results and discussion . . . 66

3.2.1 Collision rate of nuclear reaction . . . 66

3.2.2 System size effects on final state fragment multiplicities . . . 67

3.2.3 Isospin effects on multiplicity of fragments . . . 70

3.3 Comparison with ALADIN experimental data on IMF's multiplicity . . . 72

3.4 Summary . . . 73

4 Structural and isospin effects on collective flow 74

4.1 Introduction . . . 74

4.2 Neutron and proton density profile . . . 78

4.3 Results and discussion . . . 80

4.3.1 Incident energy dependence of reduced flow and elliptical flow . . . 80

4.3.2 Radius dependence of balance energy and transition energy . . . 84

4.3.3 Impact parameter dependence of balance energy and transition energy 89

4.4 Balance geometry and transition geometry . . . 91

4.4.1 Collision geometry dependence of reduced flow and elliptical flow . 91

4.4.2 Incident energy dependence of $\hat{b}_{bal}$ and $\hat{b}_{trans}$ . . . 95

4.5 Clusterization technique as per isospin dependent nuclear charge radius . . 97

4.6 Summary . . . 102

5 Structural effects via different nuclear charge radii parameterizations on nuclear stopping with momentum dependent interactions 104

5.1 Introduction . . . 104

5.2 Parameters for describing nuclear stopping . . . 106

5.3 Results and discussion . . . 108

5.3.1 System size dependence on nuclear stopping . . . 108

5.3.2 Initial $< N/Z >$ dependence of global nuclear stopping observables 110

5.3.3 Effect of nuclear radii parameterizations on the equilibrium using collision dynamics . . . 113

5.4 Effect of nuclear radius along with momentum dependent interactions (MDI) 114

5.4.1 Rapidity dependence of nucleons in final state 116
5.4.2 Excitation function of nuclear stopping 118
5.5 Summary 118

6 Initialization effects on thermalization with mass-asymmetry 120
6.1 Introduction 120
6.2 Theoretical interpretation of density and temperature 121
6.3 Result and discussion 123
6.3.1 Time evolution of average density and temperature 124
6.3.2 Correlation between maximal value of average temperature and nuclear stopping 126
6.3.3 Correlation between fragment multiplicity and nuclear stopping . . 128
6.3.4 Nuclear stopping due to projectile and target nuclei 130
6.4 Summary 131

7 Summary and outlook 132
7.1 Summary 132
7.2 Outlook 135

Bibliography 136

List of Figures

1.1 A Schematic view of various reaction channels in the low energy heavy-ion collisions. The figure is reproduced from Ref. [9]. 6
1.2 A schematic view of the heavy ion collisions in the intermediate energy regime. 7
1.3 Phase diagram of the nuclear matter. The y-axis presents the temperature (in MeV) and the x-axis presents the baryons density normalized to the density of the ground state (ρ/ρ_o) of the nuclear matter. Figure is reproduced from the Ref. [21] 9
1.4 Concept of symmetry energy: A typical predictions for the NEOS of asymmetric nuclear matter using Skyrme-Hartree-Fock (SHF) model (with SIII type). The top most line represents energy density relation for pure neutron matter and the isospin-asymmetry is indicated for each curve by ratio ρ_n/ρ_p. The difference of top and bottom lines represents the symmetry energy [40]. 14
1.5 Brief outline of different types of experimental methods developed to measure nuclear radius [51]. 17
1.6 A schematic diagram of heavy ion collisions at (i) central colliding geometry (b = 0 fm) and (ii) non-central colliding geometry (b > 0 fm). In case (ii) nucleons are geometrically separated into participant and spectator matter for impact parameter 'b'. 27
1.7 Schematic behaviour of the magnitudes of directed flow (left side) and elliptical flow (right side) as a function of the bombarding kinetic energy per nucleon in the laboratory frame. The Full lines represents flow of nucleons: proton and neutron flow while, dashed lines represents pion flow. Figure is taken from Ref. [147]. 28

1.8 Pictorial view of the various possibilities in nuclear stopping. 32

2.1 Single nucleonic trajectory from time 0.1 fm/c to 200 fm/c moving under mean field inside the nucleus of $^{50}_{20}$Ca (upper panels) and $^{197}_{79}$Au (lower panels) initialized with four different nuclear charge radii parameterizations: R_{LDM}, R_{NGO}, R_{PP} and R_{RR} (left to right panels respectively). 48

2.2 The elastic and inelastic cross sections for proton-proton (pp) and proton-neutron (pn) collisions in the IQMD model. The neutron-neutron cross section is assumed to be equal to proton-proton cross section. The total cross section is equal to the sum of the elastic and inelastic cross sections. The figure is taken from Ref. [94, 256, 257]. 59

3.1 Time evolution of average nucleonic density for the reactions of $^{50}_{20}Ca+^{50}_{20}Ca$ (left panels) and $^{197}_{79}Au+^{197}_{79}Au$ (right panels) for central collisions at E = 50 MeV/nucleon (upper panels) and E = 400 MeV/nucleon (lower panels). 64

3.2 Upper panels displays the rate of nucleon-nucleon binary collisions for the reactions of $^{50}_{20}$Ca+$^{50}_{20}$Ca (upper left panel) and $^{197}_{79}$Au+$^{197}_{79}$Au (upper right panel) at $\hat{b} = 0$. Lower panels displays the average mass of the largest fragment (A^{max}) as a function of composite mass (A_{tot}) at 200 fm/c for central (lower left panel) and semi-central (lower right panel) collisions. . . 66

3.3 The mean multiplicity of FN's, LMF's, MMF's and IMF's as a function of total mass of the system (A_{tot}) at 200 fm/c for central collisions (left panels) and semi-central collision (right panels). 68

3.4 N/Z dependence of multiplicity of FN's (upper panels) and LMF's (lower panels) at incident energy of 50 MeV/nucleon for semi-central collisions for two isobaric series with mass 80 (left panels) and 120 (right panels) units. 70

3.5 The average multiplicity of IMF (M_{IMF}) as a function of Z_{bound} for the reactions of $^{124}_{50}Sn+^{124}_{50}Sn$ at 600 MeV/nucleon (top panels) and $^{197}_{79}Au+^{197}_{79}Au$ at 400 MeV/nucleon (bottom panels) at 200 fm/c Comparison has been made with experimental data of ALADIN Collaboration [128, 282]. 72

4.1 Pictorial view of reduced flow below, at and above balance energy. Figure is modified from Ref. [147] 75

4.2 Pictorial view of elliptical flow below, at and above transition energy. Figure is reproduced from Ref. [147]. 77
4.3 The neutron density profile $\rho_n(r)$ (left panels) and proton density profile $\rho_p(r)$ (right panels) for $^{80}_{40}$Zr (upper panels) and $^{80}_{29}$Cu (lower panels) nucleus initialized in the IQMD with four different radii parameterizations at time t = 0 fm/c. 79
4.4 Energy dependence of reduced flow (left panels) and elliptical flow (right panels) of particles having Z=1 for the reaction of $^{50}_{20}$Ca+$^{50}_{20}$Ca (upper panels) and $^{197}_{79}$Au+$^{197}_{79}$Au (lower panels) representing the structural effects at $\hat{b} = 0.3$. The different lines corresponds to results obtained by using different radii parameterizations as explained in the text. 81
4.5 Energy dependence of reduced flow (left panles) and elliptical flow (right panels) of particles having Z=1 for the reaction of $^{80}_{40}$Zr+$^{80}_{40}$Zr (upper panels) and $^{80}_{29}$Cu+$^{80}_{29}$Cu (lower panels) representing isospin effects at $\hat{b} = 0.3$. Lines have the same meaning as in Fig.4.4. 82
4.6 Radius dependence of E_{bal} (upper panel) and E_{trans} (lower panel) for all the reactions of structural series. The different symbols corresponds to results obtained by using different radii parameterizations as explained in the text. The dotted lines represents the power law fit. 85
4.7 Radius dependence of E_{bal} (upper panel) and E_{trans} (lower panel) for all the reactions of isospin series. Symbols and lines have same meaning as in Fig.4.6. 87
4.8 Scaled impact parameter dependence of E_{bal} (upper panel) and E_{trans} (lower panel) for the reaction of $^{197}_{79}$Au+$^{197}_{79}$Au. 90
4.9 Scaled impact parameter dependence of reduced flow for the reactions of $^{50}_{20}$Ca+$^{50}_{20}$Ca (upper panel) and $^{197}_{79}$Au+$^{197}_{79}$Au (lower panel) at different incident energies for two nuclear charge radii parameterizations: R_{LDM} (left panels) and R_{RR} (right panels). Different lines in figure represents different incident energies in upper and lower panels. 92

4.10 Scaled impact parameter dependence of elliptical flow for the reactions of $^{50}_{20}$Ca+$^{50}_{20}$Ca (upper panel) and $^{197}_{79}$Au+$^{197}_{79}$Au (lower panel) at different incident energies for two nuclear charge radii parameterizations: R_{LDM} (left panels) and R_{RR} (right panels). Different lines in figure represents different incident energies in upper and lower panels. 94

4.11 Incident energy dependence of $\hat{b}_{bal}$ (upper panel) and $\hat{b}_{trans}$ (lower panel) for the reactions of $^{50}_{20}$Ca+$^{50}_{20}$Ca and $^{197}_{79}$Au+$^{197}_{79}$Au. 96

4.12 The azimuthal angle dependence of $dN/d(Cos2\phi)$ of FNs for the reactions of $^{50}_{20}$Ca+$^{50}_{20}$Ca at incident energy of 50 MeV/nucleon (upper panel) and 400 MeV/nucleon (lower panel) for two nuclear charge radii parameterizations: R_{LDM} (left panels) and R_{RR} (right panels). Different lines in figure represents different clusterization techniques mentioned in Table. 4.2. . . . 98

4.13 The azimuthal angle dependence of $dN/d(Cos2\phi)$ of FNs for the reactions of $^{197}_{79}$Au+$^{197}_{79}$Au at incident energy of 50 MeV/nucleon (upper panel) and 400 MeV/nucleon (lower panel) for two nuclear charge radii parameterizations: R_{LDM} (left panels) and R_{RR} (right panels). Different lines in figure represents different clusterization techniques mentioned in Table. 4.2. . . . 100

5.1 Panels (a) and (d) displays the rapidity distribution of LMF's for central $^{50}_{20}$Ca+$^{50}_{20}$Ca and $^{197}_{79}$Au+$^{197}_{79}$Au collisions respectively at E = 50 MeV/nucleon. Panels (b) and (c) represents $< R_P >$ whereas (e) and (f) represents $< 1/(Q_{ZZ}/nucleon) >$ as a function of system mass in central (upper panels) and semi-central (lower panels) collisions at E = 50 MeV/nucleon. 109

5.2 Nuclear stopping observable $< R >$ (left panels) and $< 1/(Q_{ZZ}/nucleon) >$ (right panels) as a function of neutron-to-proton ratio in semi-central collisions of two isobaric series with mass 80 (lower panels) and 120 (upper panels) units at E = 50 MeV/nucleon. Symbols have the same meaning as in Fig. 5.1. 111

5.3 The collision number dependence of $< varxz >$ for the reactions of $^{50}_{20}$Ca+$^{50}_{20}$Ca (upper panel), $^{58}_{28}$Ni+$^{58}_{28}$Ni (middle panels) and $^{197}_{79}$Au+$^{197}_{79}$Au (lower panel) at E = 400 MeV/nucleon for different radii parameterizations. 112

5.4 The rapidity distribution dN/dY for the reaction of $^{58}_{28}$Ni+$^{58}_{28}$Ni (left panels) and $^{124}_{50}$Sn+$^{124}_{50}$Sn (right panels) at incident energy of 400 MeV/nucleon. The top, middle and bottom panels are for protons, neutron and all nucleons respectively. 115

5.5 Incident energy dependence of R_P (upper panels) and R_E (lower panels) for the reactions of $^{58}_{28}$Ni+$^{58}_{28}$Ni (left panels) and $^{124}_{50}$Sn+$^{124}_{50}$Sn (right panels). The different lines have same meaning as in Fig. 5.4. 117

6.1 The time evolution of average scaled density (upper panels) and average temperature (lower panels) for central mass-symmetric (left panels) and mass-asymmetric (right panels) collisions with A_{tot} = 100 a.m.u. at E = 100 MeV/nucleon for four different nuclear charge radii parameterizations (described by various lines). 125

6.2 Correlation between maximal value of average temperature and nuclear stopping for mass-symmetric (left panels) and mass-asymmetric (right panels) nuclear reactions with A_{tot} = 100 a.m.u. (upper panels) and 248 a.m.u. (lower panels) at E = 100 MeV/nucleon for six different collisions geometries (described by various symbols) and lines have same meaning as in Fig. 6.1. 127

6.3 Multiplicity of FNs (left panels) and LMFs (right panels) as a function of nuclear stopping for mass-symmetric (upper panels) and mass-asymmetric (lower panels) nuclear reactions with A_{tot} = 100 a.m.u. at E = 100 MeV/nucleon. 129

6.4 Collision geometry dependence of nuclear stopping due to projectile (upper panel) and target (lower panel) nuclei for the reaction of $^{14}_{7}$N+$^{86}_{36}$Kr (η=0.7) at E = 100 MeV/nucleon. Lines have the same meaning as in Fig. 6.3. . . 130

List of Tables

2.1 The values of $\alpha(MeV)$, $\beta(MeV)$ and γ for different NEOS [18]. 54

2.2 The values of $\alpha(MeV)$, $\beta(MeV)$ and γ for different momentum dependent NEOS [18]. 55

2.3 Values of a(s) and b(s) for different intervals of $\sqrt{s}$. 59

3.1 The value of exponent τ for different fragments and for different radii parameterizations at $\hat{b} = 0.0$ and $\hat{b} = 0.5$ 69

4.1 The values of exponent τ obtained from power law fit with radius in Fig. 4.6 and Fig. 4.7 for all the reactions of structural and isospin series. 88

4.2 List of different clusterization techniques. 99

4.3 The values of Radius of Curvature (ROC) obtained from Fig. 4.12 and 4.13 for all the reactions of $^{50}_{20}$Ca+$^{50}_{20}$Ca and $^{197}_{79}$Au+$^{197}_{79}$Au. 101

ABSTRACT

The study of isospin degree of freedom in the heavy-ion collisions (HICs) at intermediate energies signifies the abstraction of nuclear equation of state of isospin-asymmetric nuclear matter under the high pressure and density. This has been done in the literature via Coulomb interactions, symmetry energy, isospin momentum dependent interactions as well as isospin dependent nucleon-nucleon cross-section. The objective of present work is to emphasize the isospin effects through isospin dependent nuclear charge radius. A detailed theoretical investigation has been performed by using the dynamic microscopic theory- Isospin dependent Quantum Molecular Dynamics (IQMD) model on the multi-fragmentation, nuclear stopping, thermalization, directed flow and elliptical flow. The results thus obtained are compared with the experimental data.

In **chapter 1** the comprehensive description of nuclear reactions and development of various heavy-ion accelerators from beam energy of KeV/nucleon to GeV/nucleon has been presented. The heavy-ion collisions at intermediate energies and its importance with the help of phase diagram of the nuclear matter has been described. The isospin dependence of nuclear equation of state has been discussed through isospin dependent hydrodynamical model ingredients: Coulomb interactions, symmetry energy and nucleon-nucleon cross section. In addition to that the isospin degree of freedom through an essential model ingredient i.e. isospin dependent nuclear charge radii parameterizations and its possibility to affect the reaction dynamics at intermediate energies has been discussed. The chapter also outlines a brief experimental as well as theoretical literature review of the various phenomena occurring at intermediate energies.

Various theoretical tools to define the evolution of nuclear reaction dynamics at intermediate energies has been discussed in **chapter 2**. A detailed description about the IQMD model has been presented. The secondary algorithms viz. Minimum Spanning Tree (MST) method, its updated versions MSTM (with momentum constraint) method has also been discussed which are further used to identify fragments from the final stage phase-space of the reaction generated by IQMD.

In **chapter 3**, study on the initialization effects via nuclear charge radii on fragmentation for the whole mass range of periodic table by taking isospin-asymmetric nuclear reactions using IQMD model is presented. Calculations are performed for three different isospin dependent nuclear charge radii parameterizations as well as for liquid drop model (LDM) radius. Our study reveals that there is a significant role of nuclear charge radii on fragmentation at incident energy E = 50 MeV/nucleon. In addition to that the study done on the isospin degree of freedom through nuclear charge radii on the the initial N/Z dependence of various fragments: free nucleons (FNs) [A= 1], light mass fragments (LMFs) [$2 \geq$ A ≥ 4], medium mass fragments (MMF's) [$5 \geq$ A ≥ 9] and intermediate mass fragments (IMFs) [$5 \geq$ A $\geq$ $A_{tot}/6$] has been described. Moreover, the isospin dependent radius is more suitable to reproduce experimental findings of INDRA Collaboration for the multiplicity of IMF's as a function of Z_{bound}.

Chapter 4 describes the structural and isospin effects through isospin dependent and independent nuclear charge radii parameterizations on the nuclear flow: (i) reduced flow and (ii) elliptical flow within the framework of IQMD model. The calculations have been carried out by using two different approaches: (i) for the reaction series having fixed N/Z ratio and (ii) for the isobaric reaction series with different N/Z ratio. Our results indicate that there is a considerable effect of radii parameterizations on the excitation function of reduced flow ($\frac{\partial v_1}{\partial Y^{red}}$) and elliptical flow ($v_2$). Both balance energy ($E_{bal}$) and transition energy (E_{trans}) are enhanced with increase in the radii of reacting nuclei and found to follow a power law. The exponent τ values show that the elliptical flow is more sensitive towards different nuclear charge radii as compared to reduced flow. Moreover, our theoretical calculation of impact parameter dependence of E_{bal} and E_{trans} are in the agreement with the experimental data provided by FOPI, INDRA and ALADIN collaborations. The study of influence of nuclear charge radius has been extended to obtain the balancing and transition geometries from the scaled impact parameter dependence of reduced flow and elliptical flow. The role of clusterization technique by keeping the momentum constraint as per the isospin dependent nuclear charge radii parametrization has been optimized on the azimuthal angle dependence of $dN/d(Cos2\phi)$.

Chapter 5 represents the significance of initialization effects on the nuclear stopping for entire regime of intermediate energy. The initialization effects on the global nuclear stopping parameters via different nuclear charge radii parameterizations using IQMD model at E = 50 MeV/nucleon is presented. From the study, it has been concluded that, as the production of fragments increases, the values of global stopping parameters, anisotropy ratio and quadrupole moment decreases with increase in the nuclear charge radii. The influence of nuclear charge radii on nuclear stopping is almost same for central and semi-central collisions. In addition, the role of isospin dependent nuclear charge radii parameterizations on the N/Z dependence of global stopping parameters is also studied. The excitation function of nuclear stopping has been depicted at incident energies between 30 to 1500 MeV/nucleon by including and also by excluding the momentum dependent interactions (MDI). Our study reveals that role of change in the radius parametrization on the nuclear stopping is more emphasized around 400 MeV/nucleon. MDI affects the nuclear stopping at relatively low energy and its role diminishes with increase in the incident energy. Moreover, the isospin dependent radius parametrization along with MDI is able to reduce the gap between theoretical calculations and experimental findings of INDRA and ALADIN collaborations.

In **chapter 6**, the structural effects through nuclear charge radius on the multifragmentation as well as thermal equilibrium achieved in the HICs have been studied for mass-symmetric and mass-asymmetric collisions using IQMD model. The role of nuclear charge radii parameterizations on the thermal equilibrium by studying the correlation of maximal value of average temperature achieved in the highly interacting nuclear matter and multiplicity of FNs and LMFs with momentum-based anisotropy ratio over the entire collision geometry has been emphasized. The influence of radius on the contribution of projectile and target nuclei in the nuclear stopping has been studied in detail. Our study reveals that the increase in the available phase space at initial stage through different nuclear charge radii parameterizations, enhance the temperature of nuclear system and reduces the nuclear stopping for both types of reactions. The influence of nuclear charge radii on the thermalization is more pronounced for mass-symmetric reactions compared to

mass-asymmetric reactions. Moreover, the lighter colliding pair are good probe to study the role of nuclear radius in the thermalization.

Finally, in **chapter 7**, the results obtained in this study are summarized. Based on this study conclusion drawn is presented. Also, the extension of this work has been presented as future work.

Chapter 1

Introduction

1.1 Heavy-ion collisions: an introduction

Nuclear physics has come a long way to provide a clear picture of bulk properties of nucleus like nuclear size, shape, distribution of neutrons and protons, density, binding energy (B.E.) and the various processes involved during nuclear reactions [1, 2]. The foundation of nuclear physics has been established with the historical experiment in the world of science i.e. α-scattering experiment by E. Rutherford using Geiger's gas counter in 1906 [3]. Later on, in 1912, the term 'nucleus' was introduced to the world, as a positively charged massive central part of the atom. A century has been passed, various modern techniques are advanced to elaborate the nuclear physics from nucleus-nucleus collisions to nucleon-nucleon collisions and has reached to the study of quark gluon plasma. The ions, as they have electric charge, can be controlled and accelerated via electric as well as magnetic fields. Such energetic (or accelerated) light-ions or nuclear beams with energy of few kilo electron volt (keV) to mega electron volt (MeV), are able to strike nuclei with any mass number as target. In the early phase of development, these experiments helped to study the fusion-fission phenomena, fission mass distribution and quasi-elastic scattering. But nowadays, one is able to accelerate nuclear beams from proton to $^{208}_{82}$Pb and heavier nuclei up to giga electron volt (GeV) at particle accelerator centre like Isolde (CERN) and TRIUMF (Vancouver) [4,5]. Through high-energy accelerators, it is possible to produce radioactive ion beam facility. These facilities open up many new avenues to explore exotic nuclei.

The nuclear force is the field which is created by neutrons and protons themselves and keep them intact in the nucleus. In the heavy ion collisions (HICs), when two heavy

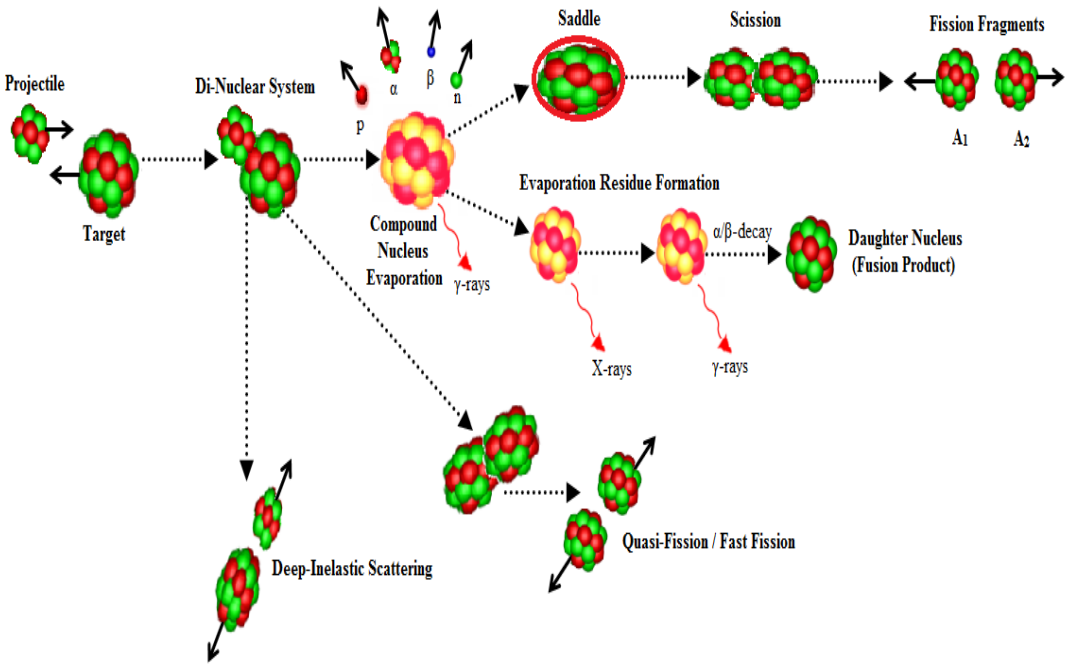

Figure 1.1: A Schematic view of various reaction channels in the low energy heavy-ion collisions. The figure is reproduced from Ref. [9].

ions or nuclei (having mass number, A $\geq$ 4) are brought nearer to each other, in every respect, one nucleus enters into the field of new nuclear forces of other nucleus. Such collisions at some incident energies give rise to many other phenomena which are exploited for different applications like nuclear medicines, nuclei weaponry production and also to unfold the science behind the various phenomena occurring in nature like supernova explosions, cooling of neutron stars, dark matter and fundamental research of nuclear structure.

Based on the incident energies, the HICs have been widely divided into three categories. The first category is termed as low energy HICs or heavy ion reactions (HIRs), with incident energy, E $\leq$ 15 MeV/nucleon. Here considerable progress has been made to understand the important processes of fusion-fission reaction mechanism and formation of new elements in the heavier side of periodic table termed as super-heavy nuclei [6]. In the reaction dynamics of low energy there is complex co-relation between Coulomb forces (long range) and nuclear forces (short range) which is also referred as attractive mean field. This category of nuclear reactions is restricted to nucleus-nucleus collisions

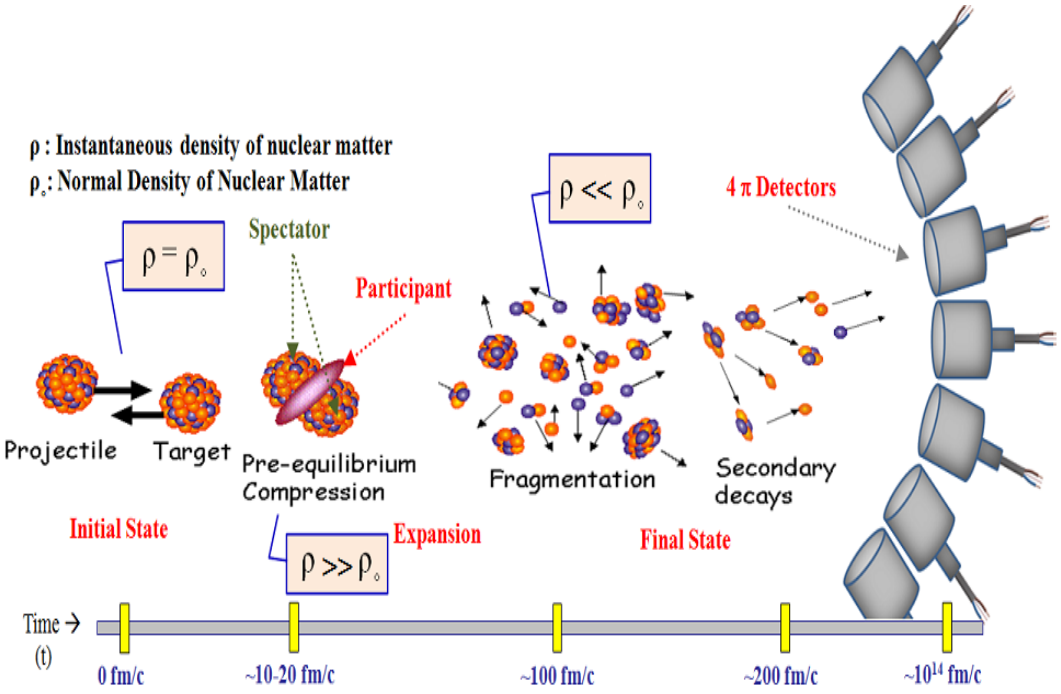

Figure 1.2: A schematic view of the heavy ion collisions in the intermediate energy regime.

only where nucleon-nucleon (NN) repulsive collisions are negligible. The different nuclear processes involved in this energy regime can be elaborated either as compound nucleus (CN) or non-compound nucleus (NCN) reactions [7]. Fig. 1.1 presents the schematic view of different reaction mechanisms at low incident energy regime. In this figure, the solid lines demonstrate the motion of nuclei/particles or γ and X rays; whereas, the dotted lines refers the reaction mechanism to the next step. The CN reactions are further classified into fusion-fission phenomena through saddle and scission points for the formation of daughter nuclei after the emission of X / γ rays [8]. The NCN reaction mechanism further results in deep-inelastic, quasi-fission as well as fast-fission based on the entrance channel properties like mass number of colliding nuclei, deformation in orientation and barrier height in comparison to the nuclear temperature and angular momentum [9–11]. The study of these reactions are helpful to give plausible description of low density phenomena like cluster-radioactivity, structure of halo-nuclei, nucleus deformations, fission fragment mass distribution, nuclear level density parameter, formation of super-heavy nuclei and incomplete fusion [12–14].

The second category termed as high energy HICs (E > 2.0 GeV/nucleon), deals with the study of quark gluon plasma. The mass of neutron and proton are approximately around 1 GeV. Therefore, one needs incident energy probably more than 2 GeV/nucleon for a successful nucleon-nucleon collision to break the confined state of hadrons. At such high energy, the temperature of the confinement is so high that pure nuclear matter does not exist and the dynamics involves purely nucleon-nucleon collision with negligible role of Pauli's blocking. With further increase in the incident energy, it is possible to study internal structure of hadrons like distribution of quarks and its density, interaction among the fundamental particles like leptons, k-mesons, π-mesons and bosons [15, 16].

The third category is the intermediate energy HICs with incident energies ranging between 25 MeV/nucleon and 2.0 GeV/nucleon are supportive to create a highly dense, thermally excited and compressed nuclear matter state which depends on various entrance channel conditions such as composite system mass, mass asymmetry, charge asymmetry, incident energy and impact parameter [17, 18]. In the higher part of this energy regime, the reaction dynamics is dominated by nucleon-nucleon collisions over the mean field. Thus, nucleons are still interacting with each other due to mean field but its effect on the dynamics of reaction gets weaker with increase in the incident energy. Fig. 1.2 shows a schematic view of the HICs at intermediate energies. Firstly, projectile and target nuclei are boosted towards each other with some incident energy. In this initial state (at time, t = 0 fm/c), the density of the nuclear matter in the interior of the colliding nuclei is equal to normal nuclear density in the ground state ($\rho = \rho_o$). Here $\rho_o = 0.16$ fm^{-3} is normal nuclear matter density at ground state and ρ is the instantaneous density of the participating nuclear matter. When both the nuclei collide with each other, the pre-equilibrium or compression state occurs (at t $\approx$ 10-20 fm/c) and the density of condensed matter becomes two to three times more than the normal nuclear matter density i.e. $\rho \gg \rho_o$. After the compression, the nuclear matter tends to expand due to pressure gradient and results in the formation of different types of small nuclei (at t $\approx$ 100 fm/c) [19]. This process is called fragmentation process. Here, the average density of system becomes less than the normal nuclear matter density i.e. $\rho \ll \rho_o$. At this stage, the fragments are very excited which cools down in the final state up to t $\approx$ 200 fm/c. Some of the highly excited fragments further undergo secondary decay. These fragments are detected by using 4 π

array of neutrons and various charge detectors. The in-depth knowledge on studying the highly dense nuclear matter can be understood with the help of phase diagram of the nuclear matter which is comprehensively defined in the following section.

1.2 Phase diagram of nuclear matter

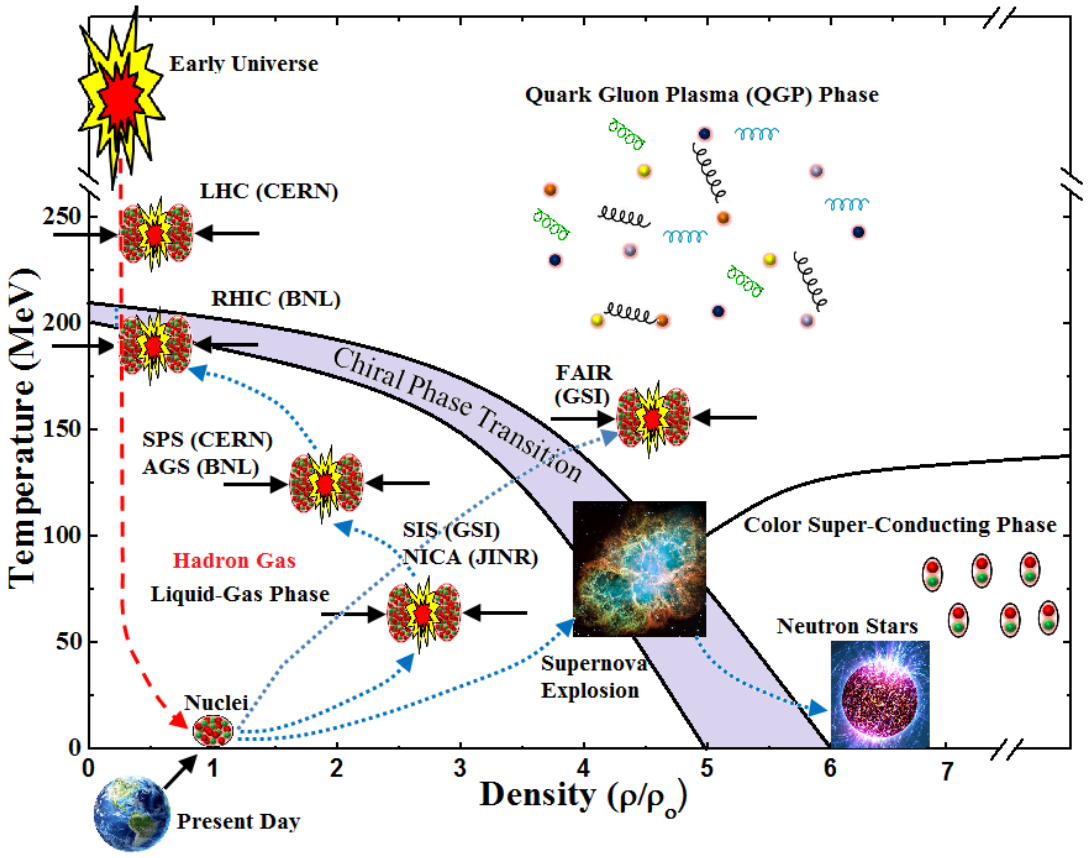

Figure 1.3: Phase diagram of the nuclear matter. The y-axis presents the temperature (in MeV) and the x-axis presents the baryons density normalized to the density of the ground state (ρ/ρ_o) of the nuclear matter. Figure is reproduced from the Ref. [21]

It is well established fact that, matter exists in three states: solid, liquid and gaseous which depends upon the temperature and pressure. Likewise, the different state of nuclear matter also depends upon temperature and density of nucleons, as shown in Fig. 1.3. The y-axis presents the temperature (in MeV) and the x-axis presents the baryons density normalized to the density of the nuclear matter in the ground state (ρ/ρ_o). In

the normal conditions or at ground state, the density of the nuclear matter is 0.15-0.17 nucleons/fm^3 or 2.7×10^{17} kg/m^3 which expresses the **liquid phase** of the nuclear matter. Up to the temperature of few MeV, there exists **mixed-phase** or liquid-gas phase where nucleon freely moves inside the volume of nucleus alike Van der Waals gas [20]. Here quarks and gluons are confined in hadrons (shown below chiral phase transition line). With an increase in the temperature and density, the bound state of quark and gluon breaks down to form quark gluon plasma (QGP) which is second phase transition of the nuclear matter, called **gaseous phase** of the nuclear matter [22]. On the other hand, at very high densities and low temperature, the nuclear matter exists in **solid state**: color super-conducting phase and neutron stars.

The red dashed line in the figure represents the path traced by the universe from its beginning to the present day. After big bang, the extremely hot universe starts expanding. The cooling of the nuclear matter results in the formation of heavy particles like hadrons and matter begins to dominate the energy which is continuing till date. The fundamental understanding on the origin of Universe, constitutes of the nuclear matter and existence of present world can be obtained through the research on nuclear matter at high baryon densities [23].

Accelerator facilities for HICs

As discussed in Sec. 1.1, many accelerator facilities have been established world wide to study different phases of the nuclear matter. These facilities are: the heavy-ion Synchrotron SIS at Gesellschaft f*ü*r Schwerionenforschung mbH (GSI) Darmstadt (Germany), Alternating Gradient Synchrotron (AGS) at Brookhaven National Laboratory (BNL), Super Proton Synchrotron (SPS) at Conseil Europen pour la Recherche Nuclaire (European Council for Nuclear Research, CERN), the GANIL Cyclotron at East Laosing, Relativistic Heavy Ion Collider (RHIC) at BNL and Large Hadron Collider (LHC) at CERN [24, 25]. In future, the Compressed Baryonic Matter (CBM) experiment [26] at the Facility for Antiproton and Ion Research (FAIR) at GSI and the Nuclotron-based Ion Collider fAcility (NICA) [27] at JINR, Dubna will also study nuclear matter at large baryon density. The heavy ion collisions and QGP at high temperature-density can be investigated in the laboratory frame. The SIS covers the beam energy of the range 0.1-2.0 GeV/nucleon, AGS up to 33 GeV/nucleon and SPS operates up to $\sqrt{s_{NN}} = 450$

GeV. These experimental facilities are marked in the phase diagram at their respective temperature-density points.

Importance of HICs

The nuclear matter at high temperature and density can be produced by colliding two nuclei. At the collision point, the two nuclei fuses into each other to form thermally excited nuclear matter. The rise in temperature and density of the nuclear matter depends upon the incident energy of colliding nuclei. The temperatures achieved in the nuclear collisions ranges around 1000 MeV and above. An average energy of 1 MeV corresponds to a temperature of 1.2×10^{10} K. The relation between the macroscopic quantities (thermodynamical variables): temperature, pressure and density of the nuclear matter describes the nuclear equations of state (NEOS). There are two possible ways to define the NEOS of highly dense, thermally excited and compressed nuclear matter. The first one is from astrophysical observation and another is through heavy ion collisions. In the astrophysical observations, the heavenly objects are remote in space and time. On the other hand, the heavy ion collisions offers a unique possibility to explore the NEOS which is essential to visualize the phases of the nuclear matter.

The NEOS further signalizes the physics corresponding to formation of early universe, supernova explosions, formation and cooling rate of neutron stars. Moreover, in the intermediate energy regime, the reaction dynamics experience the transition from mean field towards the leading role of nucleon-nucleon collisions. This provides an opportunity to study the behavior of various phenomena and observables as they are affected by the transition. In the study of such phenomenon, the isospin degree of freedom has important role. The main advantage of studying HICs at intermediate energies is that by choosing different collision systems, incident energies and impact parameters, one can access different densities and asymmetries of the nuclear matter. Therefore, in the next section, the isospin dependent NEOS is discussed.

1.3 Isospin dependence of nuclear equation of state:

The nuclear equation of state (NEOS) tells, how much the nuclear matter can be compressed at different thermodynamical conditions taken under consideration [28]. These

thermodynamical conditions varies with incident energy. The higher is the applied energy, the more compressibility in the nuclear matter (or density) can be achieved. The internal energy of infinite nuclear matter (consisting of nucleons only), can be decomposed into three parts: thermal energy (E_{th}), compressional energy (E_c) at zero temperature and ground state energy (E_o) at ρ=ρ_o=0.166±0.027 fm^3 of the nuclear matter. This can be written as:

$$E_V(\rho, T) = E_{th}(\rho, T) + E_c(\rho, T = 0) + E_o(\rho = \rho_o, T = 0) \tag{1.1}$$

The estimation of the (in)compressibility can be obtained by considering the energy content in the piece of volume 'V' of the infinite nuclear matter, as follows [29]:

$$E_V(\rho, T) = \int_V \rho(r).W[\rho(r), T(r)]dV \tag{1.2}$$

Here $\rho(r)$ and T(r) are the instantaneous density and temperature of the nuclear matter at 'r' (distance from the center in fm) respectively. The energy density functional $W[\rho(r), T(r)]$ defines the equation of state (EOS) of considered volume of the nuclear matter. The ground state energy density functional $W[\rho(r) = \rho_o, T(r) = 0]$ is 16±0.5 MeV/nucleon. The compressional part is distinguished by the curvature of $W[\rho(r), T(r) = 0]$ at $\rho(r)$ nearly equals to ρ_o. Larger is the curvature, more energy will be needed to compress the nuclear matter. The nuclear (in)compressibility constant 'K' is defined by the change in the energy of a nucleus with respect to the change in the radius. Theoretically, the NEOS are widely categorised as soft NEOS and hard NEOS corresponding to (in)compressibility constant K = 200 MeV/nucleon and 380 MeV/nucleon respectively.

The isospin degree of freedom mainly concerned to how many protons and neutrons contributes in a particular phenomenon of the nuclear reaction. Study of neutron-rich/deficient nuclei (termed as isospin asymmetric nuclear matter) have latterly attained much interest and attention due to the development of radioactive beam facilities at the Radioactive Ion Beam Facility (RIBF) at RIKEN in Japan [30], the Cooling Storage Ring (CSR) facility at HIRFL in China [31], Facility for Rare Isotope Beam (FRIB) in USA [32], SPIRAL2/GANIL in France [33], the FAIR at GSI in Germany [34] and ANURIB (Advanced National facility for Unstable & Rare-Isotope Beams) at Variable Energy Cyclotron Center (VECC), Kolkata (India) [35]. This has keyed up new interest on the subfield emerging from the nuclear physics research, called isospin degree of

freedom. The key point to elucidate the isospin-asymmetric nuclear matter is to obtain the isospin dependence of NEOS. This research contains the enchanting possibilities to study how differently the NEOS of isospin asymmetric nuclear matter differs from the NEOS of isospin symmetric nuclear matter. The isospin dependence of the NEOS is predominantly manifested through symmetry energy, Coulomb potential, isospin dependence of nucleon-nucleon cross-section and of momentum dependent interactions, which are discussed under the following sub-headings:

Symmetry energy:

The symmetry energy principally defines the difference between the B.E. of isospin-symmetric nuclear matter and pure neutron matter. In other words, the variation of B.E. as the neutron-to-proton ratio varies from isospin-symmetric nuclei (N=Z) to isospin-asymmetric nuclei (N≠Z) with fixed number of nucleons defines the symmetry energy. The Bethe-Weizsäcker (BW) [36, 37] epitomize the energy 'E' of a nucleus in terms of atomic mass (A), proton number (Z) and neutron number (N = A - Z) as:

$$E = E(A, N, Z) = -a_V A + a_s A^{2/3} + a_c \frac{Z(Z-1)}{A^{1/3}} + a_A \frac{(N-Z)^2}{A} + \delta. \tag{1.3}$$

Here, the fourth term $\left(a_A \frac{(N-Z)^2}{A}\right)$ manifest symmetry energy with symmetry energy term: $a_A \approx 21$ MeV. Further, symmetry energy has been explained in the form of symmetry potential as a function of density in three different mathematical expression as follow [38, 39]:

$$V^1_{sym} = cF_1(u)\delta_a\tau_z, \tag{1.4}$$

$$V^2_{sym} = cF_2(u)\delta_a\tau_z \; + \; \frac{1}{2}cF_2(u)\delta_a^2, \tag{1.5}$$

$$V^3_{sym} \; = \; cF_3(u)\left[\delta_a\tau_z \; - \; \frac{1}{4}\delta_a^2\right], \tag{1.6}$$

where $\tau_z = 1$ for neutron and -1 for proton. Here, $F_1(u) =$ u, $F_2(u) \; = \; u^2$, $F_3(u) \; = \; u^{1/2}$ and $u = \frac{\rho}{\rho_0}$. The δ_a is relative neutron excess i.e. $\delta_a \; = \; \frac{\rho_n - \rho_p}{\rho_n + \rho_p}$. Here, ρ, ρ_o, ρ_n *and* ρ_p are the total, normal, neutron and proton densities respectively. The strength 'c' is of the order of 32 MeV to reproduce the fourth term of the Bethe-Weizsäcker mass formula.

A fundamental elucidation of symmetry energy is represented in Fig. 1.4, through the predictions of the NEOS of the nuclear matter using Skyrme-Hartree-Fock (SHF) model (with SIII type) [40]. The top to bottom energy density curves are for different

isospin-asymmetries in terms of neutron-to-proton density ratio: ρ_n/ρ_p = 0, 0.2, 0.4, 0.6 and 0.8-1.0 (top to bottom solid lines in Fig. 1.4). At normal nuclear matter density, $\rho \approx 0.16 fm^{-3}$, the difference between the energy density relation of pure neutron matter and symmetric matter is approximately around 32 MeV.

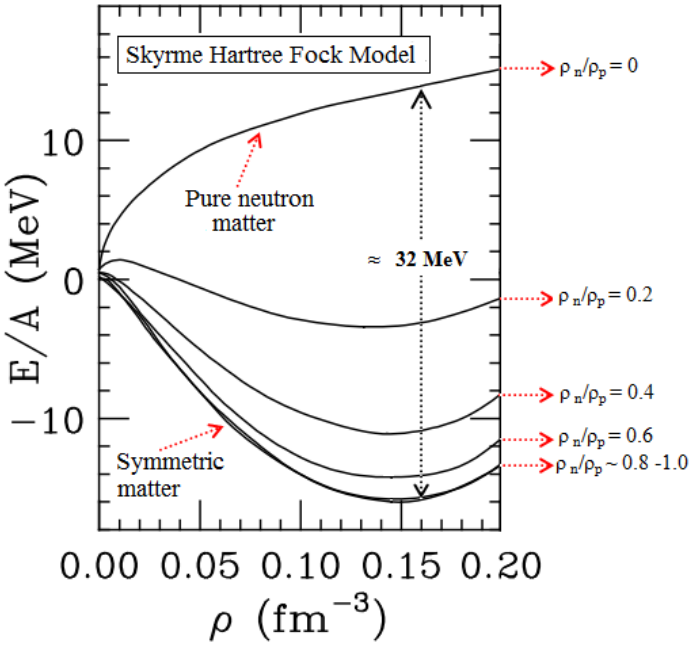

Figure 1.4: Concept of symmetry energy: A typical predictions for the NEOS of asymmetric nuclear matter using Skyrme-Hartree-Fock (SHF) model (with SIII type). The top most line represents energy density relation for pure neutron matter and the isospin-asymmetry is indicated for each curve by ratio ρ_n/ρ_p. The difference of top and bottom lines represents the symmetry energy [40].

Coulomb Interactions:

The term isospin refers to particles which are almost identical to each other but having different isospin states, for example: neutrons and protons. The neutrons and protons differ with electric charge along with minor difference in size and mass. The neutrons are neutral particles, however, due to positive electric charge of protons, the interaction between neutron-neutron, proton-proton and neutron-proton is different. In presence of Coulomb field, the trajectory of projectile deviate from its straight path. The third term in Eqn. 1.3 refers to Coulomb interactions in a nucleus. The consideration of Coulomb interactions into the calculations of total interaction potential is superior to study the in-medium nucleon-nucleon interactions and its effect on the fundamental

properties of the nuclear medium. At intermediate energies, the initial correlation between the hadrons is broken without the production of fundamental particles. Thus repulsive Coulomb interaction is an isospin-asymmetry term which offers a major contribution to account for isospin degree of freedom among nucleonic interaction.

Isospin dependent nucleon-nucleon cross-section:

In the condensed zone, the nucleon-nucleon cross-section plays a significant role. In a study made by Cassing *et al.* [41], the in-medium nucleon-nucleon cross-section have been introduced by G-matrix theory. The isospin effects via nucleon-nucleon cross-section is introduced in the calculations intrinsically via parameterized forms taken from imaginary part of G-matrix [42, 43]. The cross-section becomes isospin dependent because of difference between the effective interactions of neutron-proton (np) and neutron-neutron (nn)/proton-proton (pp). Moreover, the np cross-section in free space (σ_{np}^{free}) is higher than the nn or pp cross-section ($\sigma_{nn}^{free} or \sigma_{pp}^{free}$) with a factor of approximately three. This is because, the np interactions involves isospin-singlet as well as isospin-triplet state whereas, only isospin-singlet state is involved in nn and pp interactions.

The isospin degree of freedom has been widely examined through the Coulomb potential, symmetry energy and nucleon-nucleon cross-section on the observables such as multi-fragmentation, collective flow and nuclear stopping. The repulsive momentum dependent interations (MDI) also play an important role in the nuclear reaction dynamics specifically at peripheral collisions. In a study, Liu *et al.* [44] considered an isospin degree of freedom in MDI and proposed isospin momentum dependent interactions (Iso-MDI). The isospin degree of freedom has also been studied through the clusterization technique: isospin dependent minimum spanning tree method (Iso-MST) [45]. Present thesis is focused on the theoretical investigation of isospin degree of freedom in the nuclear reaction dynamics via isospin dependent nuclear charge radii parameterizations at intermediate energies. The evolution in the interpretation of the nuclear charge radii parameterizations from isospin independent forms to isospin dependent forms has been discussed in the next section.

1.4 Isospin dependence of nuclear radius

For a long time, the abstraction of the nuclear charge radii has become a key center in the nuclear structure research. The root mean square (rms) nuclear charge radii of stable nuclei can be derived from various experimental techniques. The rms radii is defined as:

$$< r_{rms}^2 >^{1/2} = \sqrt{\frac{3}{5}} R_{oo}. \tag{1.7}$$

Here, $R_{oo} = r_o A^{1/3}$ and $r_o = 1.12 - 1.4\ fm$. The α-scattering experiment was able to give the very first estimation on nuclear size as distance of closest approach $\approx 5 \times 10^{-15}$ fm in 1919. Afterward, in 1928, α-decay was further interpreted as tunneling effect in a pioneering work applying quantum mechanics to nuclear physics [46, 47]. Variety of experiments have been performed to determine the nuclear radius with particle scattering, which is still a favoured technique. Tanihata *et al.* in 1985 [48, 49], used the projectile-fragmentation technique to measure the rms radius of light nuclei in the p-shell region. In these calculations, the total interaction cross-section σ_I has been taken directly related to the interaction nuclear radius of projectile $R_I(p)$ and target $R_I(t)$ as follows:

$$\sigma_I = \pi[R_I(p) + R_I(t)]^2 \tag{1.8}$$

Similar kind of study has been performed by Ozawa *et al.* [50] for the measurement of radii of light nuclei through interaction cross-section and deduced the isotopic as well as isospin dependence of nuclear radii. In addition to this, the comparison of experimental Coulomb-energy difference for the set of two (having same mass) mirror nuclei pairs have been used to calculate the rms charge radii. For nuclei in the region between Z = 54 and Z = 70 (rare-earth nuclei), the nuclear charge radii has been deduced from electron and muon scattering as well as through isotopic-shift data. These studies represent the isotonic and isobaric dependency of nuclear charge radii [52]. In the tremendous work done by Fricke *et al.* [53], the rms radii of various isotopes, isotones and isobars having charge between Z = 6 and Z = 126 have been calculated by probing the nuclei with four well understood methods (electromagnetic interactions) namely K X-ray spectroscopy, optical spectroscopy, elastic electron scattering measurement and muonic spectroscopy. The scattering cross-section, half-lives of α particles, cluster and proton emission methods

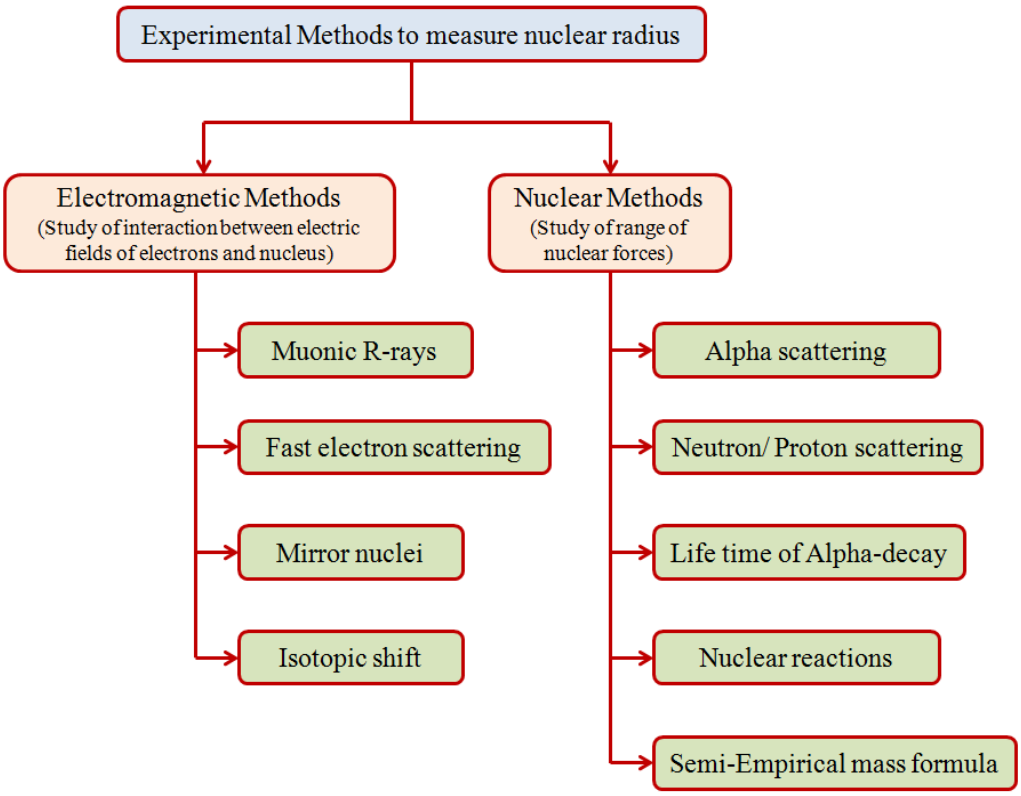

Figure 1.5: Brief outline of different types of experimental methods developed to measure nuclear radius [51].

are also being used significantly to investigate the size as well as distribution of nucleons in the corresponding nucleus [54–58]. In the recent communications, Angeli and co-workers have provided an updated experimental data for rms radii of nuclei from $_{1}$H to $_{96}$Cm (including approximately 909 isotopes) [59,60] . The information also reveals the isotopic as well as the isotonic behavior of nuclear radius [61]. Fig. 1.5 shows a brief outline of the various types of experimental techniques used to estimate nuclear radius.

The radii determined via fast electron scattering provides information about the distribution of charge whereas, the neutron scattering experiments provide information about the distribution of neutron matter inside the nucleus. The radius estimation via these two techniques is not identical which implies that neutron matter and nuclear charge are not equally distributed through out a nucleus. Though, the available literature is confined to charge radii only and the information about the neutron distribution is inadequate

in the literature [58, 60]. Therefore, for the present work the focus is on the nuclear charge radius only. With the advancement in the experimental techniques and accuracy in the estimation of rms radii, the theoretical models have also given a good description on the nuclear charge radii and its isospin dependence. The various nuclear charge radii parameterizations have been discussed in next section.

Nuclear charge radii parameterizations

Knowledge about the nuclear parameters including nuclear charge radii is of great interest for low density and low energy exotic phenomena like neutron skin thickness (difference between the rms radius of neutron and proton) [62, 63] and halo nuclei [64] which has become hot topics of present day research. The nuclear charge radii is useful key to extract the information about the de-coupling of proton and neutron, proton distribution inside the nucleus and provide valuable information to understand the complete picture of nucleon-nucleon interactions inside the nucleus. Some of the nuclear charge radii parameterizations proposed in the literature are briefly discussed under the following sub-headings:

(a) R_{LDM}**:**

Based on the experimental findings and the saturation property of nucleus, the liquid drop model (LDM) [65, 66] proposed the following expression for the nuclear radii calculations:

$$R_{LDM} = r_0 A^{1/3}. \tag{1.9}$$

The above equation represents a form of R_{oo} from Eqn. 1.7. Here r_0 is a constant, but the experimental findings indicate that the value of r_o is not same for all the nuclei. The results obtained by $A^{1/3}$ law deviates from the experimentally measured rms radii of nuclei. Moreover, this law reveals that the radius of isobaric nuclei is same which is in disagreement with experimental observations of isotonic, isobaric and isotopic dependence of rms radii. Later on, various other parameterizations have also been proposed in the literature which are again isospin independent [67–70]. These nuclear charge radii parameterizations are able to reproduce experimental rms radii up to some extent. Although, none of the these formulae explained the isotopic shift and optical isotopic shift. Thus,

the isospin independent nuclear charge radii parameterizations seems not to be valid for nuclei far from the line of stability.

(b) R_{NGO}**:**

First isospin dependent nuclear charge radii formula was proposed by Ngô and Ngô [71]. A phenomenological formula which is dependent on the mass number (A), neutron number (N) and proton number (Z) of nucleus, reads as:

$$R_{NGO} = \frac{(1.1375 + 1.875 \times 10^{-4} A) N A^{1/3} + 1.128 Z A^{1/3}}{A}. \tag{1.10}$$

This radii parametrization is extracted from the model of energy-density formalisation in which calculation of ion-ion potential have been done. The model was improved by using Fermi-density distribution. This formula took isotopic dependence into account and is labelled as R_{NGO} in this thesis.

Many theoretical calculations exist for nuclear radii; some examples of these calculations are energy-density formalism calculation [72], Hartee-Fock-Bogoliubov (HFB) calculations [73], Hartree-Fock (HF) calculations [74], relativistic Hartee-Fock (RHF) calculations [75] and Relativistic Mean Field (RMF) theory [76]. Based on these calculations, many parameterized forms have been proposed in order to modify $A^{1/3}$ law and to obtain a single expression which could be able to reproduce the experimental findings of nuclear charge radii.

(c) R_{PP}**:**

Several semi-empirical formulae for rms radii are suggested in the literature, one of them, which improves the expression in Eqn. 1.7 by adding isospin dependent terms is:

$$< r^2_{rms} >^{1/2} = \sqrt{\frac{3}{5}} \left[r_0 A^{1/3} \left(1 + \kappa_1 \frac{1}{A} + \alpha_1 \frac{N-Z}{A} + \kappa_2 \frac{1}{A^2} + \alpha_2 \frac{N-Z}{A^2} \right) \right]. \tag{1.11}$$

The expression in the square bracket is the nuclear charge radii parametrization R_{oo} and the values of parameters: r_o, κ_i and α_i (where, i=1,2) can be obtained by least squares fit to the available experimental rms radii of stable nuclei. Various parameterizations have been proposed in order to modify the nuclear charge radii obtained from the LDM with additional $I = (N - Z)/A$ (isospin parameter) term in $A^{1/3}$ dependence of nuclear charge

radii, to account for its isospin dependence. The Pomorska and Pomorski [77,78] proposed a parametrization which is labelled by R_{PP} and reads as:

$$R_{PP} = 1.256A^{1/3}(1 - 0.202I). \tag{1.12}$$

This formula was based on the charge distribution within the deformed nucleus and it describes the experimentally known charge mean square radii of even-even nuclei much better than $A^{1/3}$ law.

(d) R_{RR}**:**

A recently parameterized form of the nuclear charge radius proposed by Royer and Rousseau [79–81] which is labelled by R_{RR} has been proposed as:

$$R_{RR} = 1.2332A^{1/3} + \frac{2.8961}{A^{2/3}} - 0.18688A^{1/3}I. \tag{1.13}$$

It is more precise and able to reproduce experimental charge radius of nuclei more accurately. In addition to isospin parameter, the $Z^{1/3}$-dependent nuclear charge radii are also available in the literature. However, with this formula, the isobaric behaviour of nuclear charge radii still remain a question. Hence R_{NGO}, R_{PP} and R_{RR} parameterizations of nuclear charge radii have been used in this thesis to study the isospin degree of freedom in various phenomena occurring at intermediate energies.

1.5 Initialization effects through nuclear radius

It has been known since quite some times that different forms of nuclear charge radii parameterizations do affect the low density and low energy phenomena significantly [82, 83]. It has been concluded that different strengths and terms of nuclear charge radii can affect fusion barrier as well as cluster radioactivity [84–86]. Similar effects have also been observed for the binding energies [87, 88]. Moreover, nuclear radius is related to the distribution of the nuclear density. The neutron skin thickness is a very sensitive probe to measure the pressure difference that exist between the neutrons and protons [89]. This neutron skin thickness is sensitive to the symmetry energy and to the equation of state of isospin-asymmetric nuclear matter [90–92]. An extensive study made by Brown [93] proclaims that it is possible to extract the information about neutron equation of state (neutron EOS) by knowing the rms radii of neutron from a stable nucleus such as $^{208}_{82}$Pb.

The nuclear charge radii parametrization is also a topic of interest for the intermediate energy HICs in virtue of sensitivity of theoretical models of this field. In these models, the nuclear charge radii parametrization, which is the first and an essential model ingredient used to construct the nuclear matter, is generally considered to be an isospin independent quantity. The extensively used parametrization of the nuclear charge radii is the one proposed by the liquid drop model (LDM) i.e. R_{LDM} [65] represented in Eqn. 1.9. The value of r_o is 1.12 fm in Isospin-dependent Quantum Molecular Dynamics (IQMD) model [94] (used in present thesis), 1.142 fm in Quantum Molecular Dynamics (QMD) [18] and 1.18 fm in Inter Nuclear Cascade (INC) model [95]. In the literature, there are other models also like Monte Carlo (MC) method [96], Fermionic Molecular Dynamics (FMD) model [97], Anti-symmetrized Molecular Dynamics (AMD) model [98] and nucleus-nucleus optical potential [99]. But none of these took isospin into consideration through nuclear charge radius. However, in the present day, various isospin-dependent forms of nuclear charge radii are available in the literature.

It is evidenced from the literature that the small variation in the interaction range between the nucleons through different parameterizations of the Skyrme forces [100], scaled Gaussian width of the wave packets [101] and neutron skin thickness [102, 103] can lead to notable effects in the neutron-to-proton ratio of fragments, multi-fragmentation and collective flow in HICs at intermediate energies. This signifies the sensitivity of reaction dynamics towards interaction range. Now it is crucial to know that, how the nuclear reaction dynamics of the intermediate energy regime will be affected by the change in interaction range among the nucleon as one considers the isospin dependent nuclear charge radii parametrization to initialize the nucleus.

Few studies are also available in the literature on the structural effects via nuclear charge radii on the reaction dynamics at intermediate energies. Puri and collaborators [104, 105] investigated the role of structural effect on the transverse in-plane flow and its disappearance for the reactions of $^{12}_{6}$C+$^{12}_{6}$C and $^{197}_{79}$Au+ $^{197}_{79}$Au. The study reveals a strong dependence of flow on the radius of the colliding nuclei. Moreover, Gautam [106] studied the role of the nuclear structural effects (via nuclear charge radius) on reaction dynamics for isobaric colliding pairs through transverse in-plane flow as well as multi-fragmentation. However, these studies are not adequate to describe structural effects as well as isospin

effects via nuclear charge radius on fragmentation, nuclear stopping, thermalization and collective flow for the whole mass range of the periodic table, entire collision geometry as well as for the isobaric series of the nuclear reaction. The present thesis intend to address the same for a wide composite mass number and initial neutron-to-proton ratio range.

With regards to various parameterizations of nuclear charge radii proposed in the literature, four of these are used to fulfil the current aim. Also, because of growing interest in the study of isospin degree of freedom, one of the chosen parameterizations is the liquid drop model (LDM) [65] i.e. R_{LDM}, which is isospin independent and the other three are isospin dependent [71, 77, 81] i.e. R_{NGO}, R_{PP} and R_{RR} to account for **isospin effects**. The isospin dependent radii parameterizations are the improved versions of $A^{1/3}$ law with additional isospin parameter (I). It is worth mentioning that these radii parameterizations have been considered such that the radius of a particular nucleus follows the pattern: $R_{LDM} < R_{NGO} < R_{PP} < R_{RR}$. This kind of pattern has been considered to study the influence of increase in radius on the various phenomena occurring at intermediate energies in a systematic way i.e. to optimize the **structural effects**. As the radius increases, the density of the nuclear matter will decrease which further affects the interaction range and thus the reaction dynamics. Moreover, the density in the core of nucleus will decrease but consequently the surface diffusion of the nucleolus will increase which further affects the surface interactions. The present study is fully theoretical and the calculations are also compared with available experimental data of fragmentation, directed flow, elliptical flow as well as nuclear stopping to investigate whether the isospin dependence through nuclear charge radii alters the isospin degree of freedom or not. These phenomena and the literature are reviewed in next section.

1.6 Description of various Phenomena occurring at intermediate energies

The estimation of compression achieved during the violent phase of collision in the heavy-ion collisions can be made by observing different phenomena like multi-fragmentation, collective flow and nuclear stopping. The observable parameters of such phenomena are helpful to pin down the reaction mechanism through out the time span. The physical significance and the literature review of these phenomena are briefly dis-

cussed one by one in the following sections:

1.6.1 Multi-fragmentation

In the phenomena like fission and evaporation residue, only one neutron/proton or other small nuclei is emitted at one time. When projectile nuclei hits the target nuclei at the incident energy much larger than the binding energies of both nuclei, the colliding nuclei gets shattered into many pieces called multi-fragmentation. The term 'multi-fragmentation' was principally proposed by Bondorf *et al.* in 1976 [107, 108]. The multi-fragmentation is a process where more then two fragments or nucleons are emitted in a short period of time from the highly compressed zone of the nuclear matter. This can be linked to the boiling of water. When the temperature of water is larger than its boiling point, it starts evaporating water molecules in the form of vapours in the bulk. Similarly, multi-fragmentation signalizes onset of evaporation of small particles (or fragments) from the highly excited and hot nuclear matter. Therefore, the multi-fragmentation is an important phenomenon to account for phase transition of the nuclear matter from liquid to gaseous phase [109]. To rationalize the multi-fragmentation in an organized way, the fragments are categorized on the basis of mass number and described as FN's (free nucleons) [$A = 1$], LMF's (light mass fragments) [$2 \leq A \leq 4$], MMF's (medium mass fragments) [$5 \leq A \leq 9$], IMF's (intermediate mass fragments) [$5 \leq A \leq A_{tot}/6$] and HMF's (heavy mass fragments). A schematic view of multi-fragmentation process is shown in Fig. 1.2. The multiplicity and the size of out-products of the reactions robustly depends upon the various physical observables and model ingredients which are discussed in the following sections:

Theoretical attempts

The production of particles is associated with entrance channel conditions like incident energy [110], colliding geometry [111], composite mass [112] and mass-asymmetry [113] of colliding nuclei. The density of compressed nuclear matter increases with increase in incident energy and decreases with increase in impact parameter. Hence, the central collisions at high energy gives onset of the NEOS and the peripheral collisions give insight to the pattern of very cold fragment emission from spectator zone. The multiplicity of various fragments are found to follow a power law fit with the composite system mass in

numerous studies. The slope factor of this power law behaviour gives unique estimation of the liquid-gas phase transition in the nuclear matter for a wide range of nuclei in the periodic table for different isospin dependent or independent model ingredients. Zhang *et al.* [114] abstracted the dependence of multiplicity of IMFs on the number of neutrons, charge particles and light charge particles to study the pre-equilibrium emission for the isospin-asymmetric reactions of $^{112}_{50}$Sn+ $^{112}_{50}$Sn (N/Z = 1.24) and $^{124}_{50}$Sn+ $^{124}_{50}$Sn (N/Z = 1.5) using IQMD model. The reaction with higher N/Z yields more neutrons and lesser charge particles compared to reaction with lower N/Z. Therefore, the neutron-deficient reactions are more prone to emit heavier fragments [115]. The inclusion of Coulomb interaction reduces the isospin ratio of gas to liquid phase (isospin fractionation ratio). Whereas, the symmetry energy intensify the same. The isospin fractionation ratio increases as the initial N/Z ratio increases and decreases with increase in total mass of colliding nuclei [116]. In a recent article, Wu *et al.* [117] studied the isospin effects by measuring the comparative contribution of Coulomb interaction and symmetry energy for the semi-central collisions of mass-asymmetric nuclear reaction of $^{40}_{18}$Ar+$^{197}_{79}$Au using Improved Quantum Molecular Dynamics (ImQMD) at incident energies of 35, 50 and 100 MeV/nucleon. The production of fragments and kaons are found to be reduced drastically under MDI [118]. In a study by Imal *et al.* [119], the Statistical Multi-fragmentation Model (SMM) has been used for the reactions of $^{112,124}_{50}$Sn+$^{112,124}_{50}$Sn to account for the production cross-section as well as the isotopic yield distribution of projectile-like fragments. The work of Jain *et al.* [120] using IQMD model, reveals that the effect of isospin dependent nucleon-nucleon cross-section on initial N/Z dependence of FN's, LMF's and IMF's using IQMD model is very feeble.

Experimental attempts

The experimental study on the multi-fragmentation is going on since late 30's. In such experiments, the particles with mass number greater than α-particles but smaller than the mass number of fission fragments emitted and dubbed as intermediate mass fragments (IMF's) ($3 \leq Z \leq 20$) [121]. Till mid 50's,, the production cross-section of these fragments was complicated to determine and the phenomenon was considered subtle and unusual [122]. The experimental study of multi-fragmentation on the entrance channel conditions was firstly observed by the Berkeley group through mass-asymmetry and incident energy ranging between 50 and 110 MeV/nucleon [123]. The ISOSPIN Col-

laboration established at INFN (Italy) starts studying the isospin effects for neutron-rich as well as neutron-deficient nuclear reactions for peripheral colliding geometry at incident energy of 35 MeV/nucleon [124]. The FOPI and ALADIN groups at GSI have published systematic experimental data for a wide range of system mass (for various isotopes between nuclei $^{12}_{6}C$ to $^{208}_{82}Pb$) covering incident energy between 100 MeV/nucleon and 1 GeV/nucleon [125–127]. The rise and fall behavior in the production of IMFs as a function of Z_{bound} is vitally shown and explained by FOPI Collaboration for the reaction of $^{197}_{79}$Au+$^{197}_{79}$Au [128] i.e. mass-symmetric reactions. The mass-asymmetric nuclear reaction using $^{197}_{79}$Au as a fixed target with C, Al and Cu beams have been studied by extensively by Trautmann and collaborators [129]. The further development of secondary beams have extended scope of study towards isospin plane [130–132].

The NIMROD multi detector build at Texas Agricultural and Mechanical University (TAMU), consist of 4π array of neutron and charged particle detection system to study the mechanism involved in the heavy ion reactions which covers the angle between 3 and 170 degrees [133,134]. This collaboration observed the isospin dependence of the NEOS by observing isobaric & isotropic yield ratio, neutron-to-proton ratio of various fragments and role of symmetry energy for the symmetric nuclear reactions of $^{124}_{50}$Sn+$^{124}_{50}$Sn, $^{124}_{54}$Xe+$^{124}_{50}$Sn and $^{112}_{50}$Sn+$^{112}_{50}$Sn at E = 28 MeV/nucleon [135]. The another leading group that is analyzing the different aspects of multi-fragmentation is INDRA group at GANIL (France). This group mainly studied the nearly asymmetric nuclear reactions of $^{36}_{18}$Ar+$^{58}_{28}$Ni, $^{155}_{64}$Gd+$^{238}_{92}$U and $^{129}_{54}$Xe+$^{nat}_{50}$Sn (at incident energy between 30 and 95 MeV/nucleon), $^{58}_{28}$Ni+$^{58}_{28}$Ni (at incident energy between 32 and 90 MeV/nucleon), $^{208}_{82}$Pb+$^{197}_{79}$Au (at incident energy of 29 MeV/nucleon) and $^{36}_{18}$Ar+KCl to optimize the entrance channel effects through system mass and incident energy, the role of Coulomb instabilities, correlation of fragment velocity and kinetic energy spectra [136]. The collaborative work done by INDRA and ALADIN groups examined the projectile fragmentation and observed the bimodal behaviour in the heaviest fragment distribution [137]. The study of isospin effects through isotopic shift and symmetry energy in the disassembly of hot nuclear systems has pin down the cause of multi-fragmentation and formation of various fragments [138, 139]. These extended studied reveals that reaction dynamics at low incident energies is caused by a dynamical hindrance of the IMFs emission at low angular momentum [140].

1.6.2 Collective Flow

The collective flow is a phenomena which is related to the amount of momentum attained by the emitted particle and its direction of emission from the fire ball. Therefore, the collective flow or nuclear flow provide clear vision to the thermodynamical state of overlapping region of colliding nuclei. This information is further essential for the knowledge of the NEOS. The pressure gradient developed in the compressed nuclear matter give rise to the flow of fragments in a particular direction during expansion stage. The direction of flow of particles is away from the central fire ball region also called participant zone i.e. from high pressure to low pressure region. The collective flow describes the azimuthul momentum distribution of ejected particles. The Fig. 1.6 shows a schematic view of heavy-ion collisions at (i) central colliding geometry (b = 0 fm) and (ii) non-central colliding geometry (b > 0 fm). In figure, the projectile and target nuclei moves towards each other in +Z and -Z axis respectively. The impact parameter (b) is defined as the vector connecting the center of two nuclei or the perpendicular distance between the centres of both nuclei towards +X axis. The X-Z plane called as the reaction plane or longitudinal plane.

The collective flow is of two types: isotropic flow and anisotropic flow. In central collisions, the shape of the compressed zone is spherical therefore the distribution of fragments is isotropic in the transverse plane called the ***radial flow***, also called isotropic flow [141]. The participant matter formed in non-central collision is of lenticular shape. In this shape, the transverse plane (X-Y plane) has short axis and the longitudinal plane has long axis. The nucleons along the short axis are under more pressure compared to nucleons along long axis. The pressure dependent position as well as momentum of nucleons result in the anisotropic distribution of particles called anisotropic flow. The spatial anisotropy of the compressed zone (occur for short period of time) and multiple inter nucleonic collisions give rise to momentum anisotropy in the final stage. The anisotropic flow is further categorised into directed flow, elliptical flow, triangular flow, quadrupole flow and higher order anisotropic flows. In this thesis, only directed flow and elliptical flow are studied.

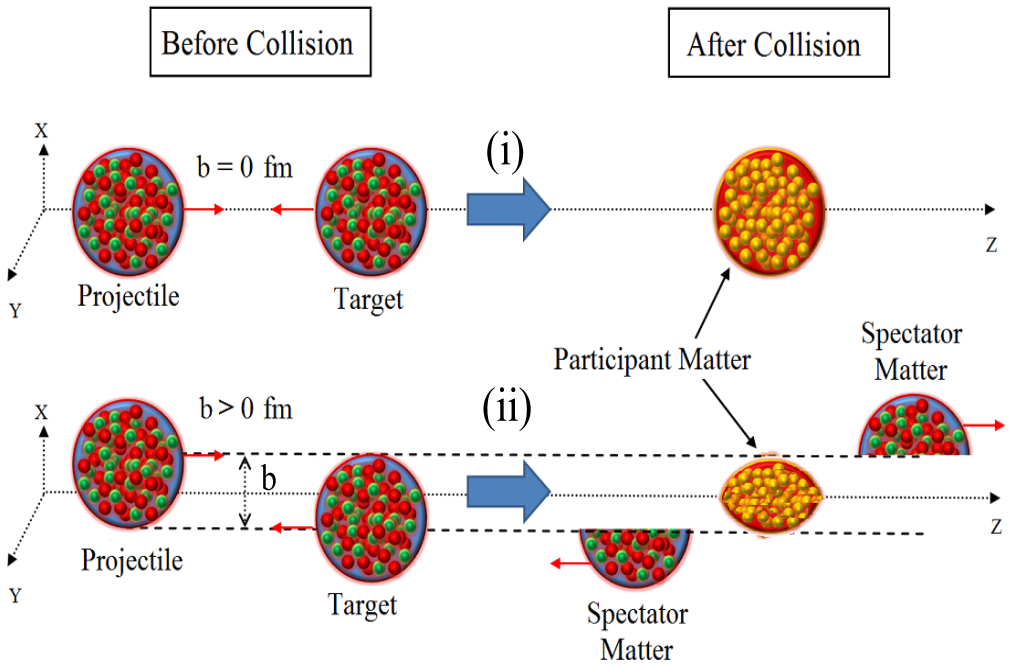

Figure 1.6: A schematic diagram of heavy ion collisions at (i) central colliding geometry (b = 0 fm) and (ii) non-central colliding geometry (b > 0 fm). In case (ii) nucleons are geometrically separated into participant and spectator matter for impact parameter 'b'.

Directed flow

The directed flow referred to the preferential emission of particles in the reaction plane but in the sideward direction i.e. towards forward and backward direction. In forward directed flow, the emitted particles are inclined near 0° in the forward hemisphere and backward directed flow represents the motion of emitted particles towards backward hemisphere near 180°. The magnitude of directed flow changes its sign from negative to positive with increase in beam energy and follows Cos(ϕ) behaviour with incident energy. This behaviour of directed flow is shown in case (i) (for nucleons) of Fig. 1.7. At low incident energies, the particles are deflected towards backward direction i.e. negative angles and gives negative magnitude representing the attractive part of the nuclear mean field [142]. However, as the beam energy increases up to few hundreds of MeV/nucleon, the particles start emitting towards positive angles in forward direction giving positive magnitude of directed flow signalizing the repulsive nucleon-nucleon collisions [143]. While

going from negative to positive value, the zero value of directed flow come across where attractive mean field compensates with strength of repulsive nucleon-nucleon collisions. The energy at which zero flow occurs is dubbed as energy of vanishing flow (EVF) or balance energy (E_{bal}) [144]. On further increasing the beam energy the transition time between projectile and target nuclei decreases [145]. Hence the value of directed flow become very small and does not changes its sign again which consequently does not signalize any other phenomena. Therefore, at relatively higher energies i.e. at AGS & SPS energies and at very peripheral colliding geometry, it is significant to study elliptical flow [146].

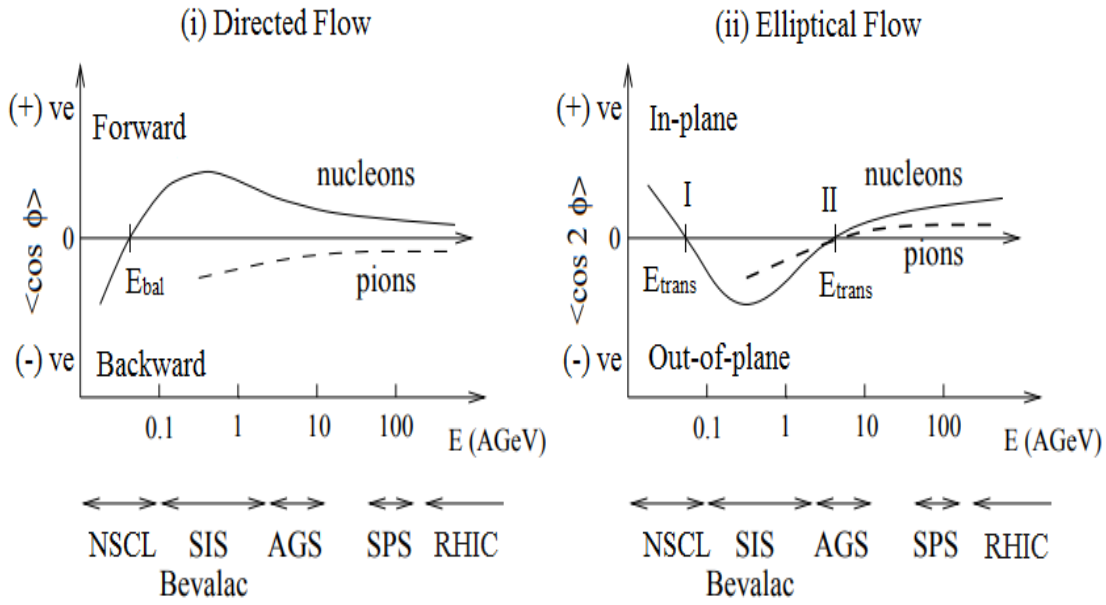

Figure 1.7: Schematic behaviour of the magnitudes of directed flow (left side) and elliptical flow (right side) as a function of the bombarding kinetic energy per nucleon in the laboratory frame. The Full lines represents flow of nucleons: proton and neutron flow while, dashed lines represents pion flow. Figure is taken from Ref. [147].

Elliptical flow

The elliptical flow describes the in-plane and out-of-plane particle distribution in elliptical or almond type shape at mid-rapidity region. In case of in-plane emission, the elliptical distribution peaks at 0° and 180° i.e. in the reaction plane and yield positive

value of elliptical flow. However, the out-of-plane emission also called squeeze-out emission corresponds to peaks at +90° and -90° i.e. perpendicular to the reaction plane and yields negative value of elliptical flow. The elliptical flow at mid-rapidity signifies the ellipsoidal distribution of emitted particles. Due to the variable size of participant zone and shadowing of spectator matter, the strength of nucleon-nucleon collision differs with different reaction conditions. Elliptical flow is a phenomenon which depends upon the complex correlation between the strength of nucleon-nucleon collisions, rotation of participant matter and shadowing of spectator matter. The transition of elliptical flow from positive value to negative value with increase in beam energy gives description about the dominance of nucleon-nucleon collision over the shadowing of the spectator matter. The excitation function of elliptical flow follows the behaviour of Cos (2ϕ) as shown in case (ii) (for nucleons) of Fig. 1.7. The energy at which this transition occurs is called first phase of transition energy (E_{trans}) marked by **I** in the figure. With further increase in incident energy, the elliptical flow also undergoes the second phase of transition energy, marked by **II** in the figure. This transition explains that at high beam energies, the passing time of spectator matter over the participant matter decreases and the expansion time becomes two times faster [148, 149].

Both the directed and elliptical flows have been extensively studied theoretically and experimentally. These studies are briefly discussed in the following two sections:

Theoretical attempts

The strength of directed and elliptical flow has provided a comprehensive description of the NEOS and its isospin dependence. These isospin effects can be conveniently observed at peripheral colliding geometry. The study based on isospin in terms of neutron-to-proton ratio using Isospin dependent Boltzmann Uehling Uhlenbeck (IBUU) model for the reactions of $^{48}_{20}$Ca+$^{58}_{26}$Fe and $^{48}_{24}$Cr+$^{58}_{28}$Ni having same composite mass concludes that the collisions with higher N/Z tends to have more attractive interaction as compared to the collision with lower N/Z. Therefore, the balance energy is higher for neutron-rich system [39]. The change of sign and magnitude of collective flow robustly depends upon isospin-asymmetry of colliding nuclei [150]. The directed flow shows sensitivity to the choice of the NEOS but strength of elliptical flow is same for soft and stiff NEOS [151]. The study made for the reaction of $^{197}_{79}$Au+$^{197}_{79}$Au using Ultra-relativistic Quantum Molec-

ular Dynamics (UrQMD) model above incident energy of 100 MeV/nucleon reveals that collective flow of light particles (protons, neutrons, deuterons, tritons, ^{3}He, and ^{4}He) describes the importance of medium-modified nucleon-nucleon elastic cross-sections [152]. The beam energy dependence of mid-rapidity slope of directed flow called ***reduced flow*** and its disappearance has been enormously studied for the in-medium nucleon-nucleon cross-section using Boltzmann Uehling Uhlenbeck (BUU) model for the reaction of $^{40}_{18}$Ar+ $^{51}_{23}$V [153]. Westfall *et al.* [154] provided the very first examination of system size effects on the balance energy for the mass range between 24 and 190 a.m.u. This mass dependence is further scaled to $A^{-1/3}$ fit. This reveals the competition between both the attractive and repulsive interactions. The attractive mean field associated to the surface of the interacting projectile and target nuclei should be scaled to $A^{2/3}$, while the repulsive nucleon-nucleon collision should be scaled to the mass number (A). The increase in the balance energy with increase in initial N/Z ratio of colliding nuclei (keeping composite mass same) reflects the role density dependence of symmetry energy [155]. The study of mass dependence of balance energy has further upgraded to pin down the isospin effects [156]. This study shows that how the isospin degree of freedom affects the dominance of attractive mean field and repulsive nucleon-nucleon collisions [157]. Moreover, the examination of directed flow signalize the phase transition of the nuclear matter in relativistic HICs [158].

The mid-rapidity emission perpendicular to beam axis was firstly shown by Stöcker [17, 159] in early 80's. It gave the idea of calculating the angular distributions of emitted protons from nearly central collisions using Fluid Dynamical model. The isospin dependent NEOS can be extracted through studying neutron-rich colliding nuclei [160]. Apart from initial N/Z ratio, the isospin effects in elliptical flow has also been explained through Coulomb energy, symmetry energy and isospin dependence of nucleon-nucleon cross-section for mass and isospin-symmetric as well as asymmetric nuclear reactions. [161–165].

Experimental attempts

The very first observation of sideward flow was observed in 1984 by Gustafsson *et al.* [166] in an experiment performed at Bevalac in Berkeley. The out-of-plane emission (also called squeeze-out elliptical flow) was experimentally observed by two competing collaborations: Plastic-Wall/Ball group at Bavalac (Berkeley) and Diogene Collaboration

at Saturne Synchrotron in Saclay (France) at nearly same time. The Plastic-Wall/Ball group observed a pronounced component in momentum as well as co-ordinate space perpendicular to the reaction plane at mid-rapidity as a signature of out-of-plane emission of fragments for the reaction of $^{197}_{79}$Au+$^{197}_{79}$Au at 400 MeV/nucleon [167]. The Diogene Collaboration provided the experimental data for the transverse momentum, rapidity and impact parameter dependence of elliptical flow for the Ne-induced reactions: Ne+NaF, Ne+Nb and Ne+Pb at beam energy of 800 MeV/nucleon. The azimuthal distribution of particles show peaks at mid-rapidity [168]. The transition energy E_{trans} of elliptical flow has been firstly observed by NAUTILUS Collaboration at GANIL (France) for the reaction of $^{64}_{30}$Zn +$^{58}_{28}$Ni and it increases with increase in impact parameter [169]. The ALADIN/MINIBALL Collaboration has also observed the out-of-plane emission and its transition to rotational emission pattern as a function of collision geometry [170]. The balance energy and transition energy has also been emphasised at GSI, Darmstadt by using FOPI detector system for charged particles having Z $\geq$ 2 for the reaction of $^{197}_{79}$Au+$^{197}_{79}$Au [171].

The FOPI Collaboration [148, 172] has extensively studied the directed and elliptical flow along with their balance and transition energies for nuclear reactions (at incident energies) of $^{40}_{20}$Ca+$^{40}_{20}$Ca (at 0.4, 0.6, 0.8, 1.0, 1.5, 1.93 GeV/nucleon), $^{58}_{28}$Ni+$^{58}_{28}$Ni (at 0.09, 0.15, 0.25, 0.4 GeV/nucleon), $^{96}_{40}$Zr+$^{96}_{40}$Zr and $^{96}_{44}$Ru+$^{96}_{44}$Ru (at 0.4, 1.5 GeV/nucelon), $^{129}_{54}$Xe+$^{133}_{55}$Cs$^{127}_{53}$I (at 0.15, 0.25, 0.4 GeV/nucleon) and $^{197}_{79}$Au+$^{197}_{79}$Au (at 0.09, 0.12, 0.15, 0.25, 0.4, 0.6, 0.8, 1.0, 1.2, 1.5 GeV/nucleon). The collaborated work of INDRA and ALADIN groups [173–175] has studied collective flow for the reaction of $^{197}_{79}$Au+$^{197}_{79}$Au at incident energies between 40 and 150 MeV/nucleon. The transition energy from in-plane to out-of-plane emission has been obtained around 100 MeV/nucleon at semi-central collisions for particle having Z $\leq$ 2. This collaboration has also brought attention to the centrality and transverse momentum dependence of directed and elliptical flow for the reactions with $^{124,129}_{54}$Xe as projectile and $^{112,124}_{50}$Sn as target at beam energies of 100 and 150 MeV/nucleon. The FOPI and INDRA groups have made an systematic study upon excitation function of flow and stopping correlations for the entire regime of the intermediate energy [176]. It has been discussed in a study made by Ollitrault and co-workers [177] regarding the elliptical flow in the intermediate energy regime that the elliptical flow is rigorously influenced by non-flow effects as well as flow fluctuations. In the recent com-

munication [178], the nuclear (in)compressibility has been studied through elliptical flow of free protons and deuterons at incident energies of between 400 MeV/nucleon and 1.0 GeV/nucleon. The experimental results after comparing with the theoretical calculations of UrQMD model proclaims that the parameter v_{2n} is easily influenced by the in-medium nucleonnucleon cross section compared to the nuclear symmetry energy. Moreover, an average value of (in)compressibility K = 220 40 MeV is obtained through the FU3FP4 parametrization of in-medium nucleonnucleon cross section.

1.6.3 Nuclear Stopping

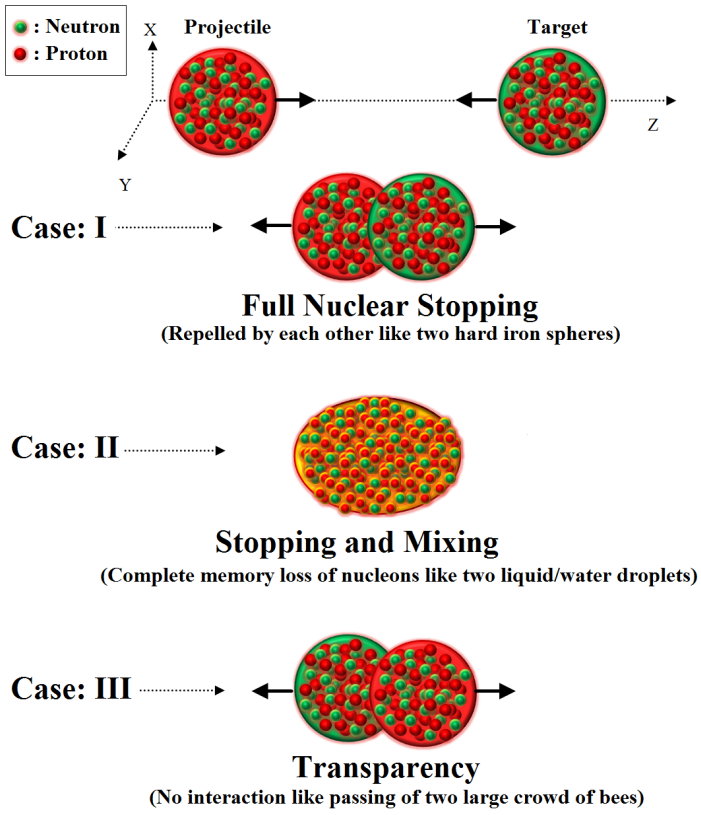

Figure 1.8: Pictorial view of the various possibilities in nuclear stopping.

The nuclear stopping is another crucial phenomenon of HICs as it gives estimation of energy lost during the collisions and nucleonic density of compressed nuclear matter. It describes the degree of thermalization or equilibrium achieved in particular type of reaction while converting the motion of the colliding system from one degree of freedom (i.e.

longitudinal direction) into other degree of freedom (i.e. transverse directions). During the collision process in overlapping region, each nucleon transfer its longitudinal energy (or momentum) into transverse energy (or momentum). The part of energy lost during this energy (or momentum) conversion in the fire ball defines the nuclear stopping. The Fig. 1.8 shows the various possibilities that may arise in the nuclear reaction depending upon various entrance channel conditions. These possibilities are discussed as below:

1. In the first case, the projectile and target nuclei (initially moving towards each other) get repelled by each other like two hard iron spheres assigned as "full stopping".

2. In the second case called "stopping and mixing", both the nuclei collide like two liquid/water droplets. This represents the complete memory loss of nucleons and breakage of correlations among them.

3. The third case shows transparency of both nuclei like passing of two large crowd of bees.

The amount of stopping depends upon incident energy, mass of colliding nuclei [179], geometry of collision [180], mass-asymmetry [181] as well as orientation [182]. The nuclear stopping observables has been studied experimentally and theoretically through various entrance channel conditions and models ingredients [183, 184]. All of these prospectives are described as follows:

Theoretical attempts

In the literature, the nuclear stopping has been studied theoretically to quantify the importance and effects of various model ingredients. The spherical momentum flow pattern of emitted nucleon for the reaction of $^{40}_{18}$Ar+ $^{207}_{82}$Pb gave a very first correspondence to the full nuclear stopping determined for near-zero impact parameter [185]. In an analysis performed by Bauer [186], the multipole moments of the momentum distribution of nucleons has been studied for a wide range of incident energy, impact parameter and the composite system mass using BUU model. In a study made by Peilert *et al.* [187], nuclear stopping has been studied through the rapidity distribution of fragments for the reactions of $^{197}_{79}$Au+ $^{197}_{79}$Au and $^{93}_{41}$Nb+ $^{93}_{41}$Nb at incident energy between 100 to 800 MeV/nucleon

using QMD model. Their study pointed out that at the early stage of expansion, the compressed nuclear matter flows out of the mid-rapidity zone. As a consequence of that the longitudinal momentum gets converted into transverse momentum. Therefore, the participant matter in the central zone is responsible for achieving the better thermalization. Afterward, Bass *et al.* [188] gave the idea of 'isospin mixing' to study the isospin degree of freedom through nuclear stopping. The nuclear stopping has been found to be sensitive towards nucleon-nucleon cross-section and insensitive to symmetry potential as well as initial N/Z ratio of colliding systems for the reactions of $^{20}_{10}$Ne+$^{20}_{10}$Ne, $^{40}_{18}$Ar+$^{40}_{18}$Ar, $^{80}_{30}$Zn+$^{80}_{30}$Zn, $^{112}_{50}$Sn+$^{112}_{50}$Sn, and $^{124}_{50}$Sn+$^{124}_{50}$Sn at beam energy range from 15 to 150 MeV/nucleon [189].

The quantization of participant and spectator matter has been proved as a good signature of degree of thermalization as it shows similar behavior to anisotropy ratio [190]. The study of participant-spectator matter, the anisotropy ratio, the relative momentum, average and maximum density as well as temperature achieved in a reaction for the isotopic series of $^{x_1}_{20}$Ca+$^{x_1}_{20}$Ca and $^{x_2}_{54}$Xe+$^{x_2}_{54}$Xe (varying N/Z between 1.0 and 2.0 for different values of x_1 and x_2 as mass number) represents no isospin effects on nuclear stopping through the initial neutron-to-proton ratio [191]. The memory loss ratio has also been studied using IQMD model by Su *et al.* [192, 193] to probe the equilibrium. The isospin effects in terms of Coulomb interaction reduces the nuclear stopping [194, 195]. It has been shown by Liu *et al.* in Ref. [196] and by Kumar *et al.* in Ref. [197] that the inclusion of momentum dependent interactions weaken the finite size effects in nuclear stopping and enhances the role of isospin dependent quantities of hydrodynamical models. The nuclear stopping has also been examined by using Antisymmetrized Molecular Dynamics (AMD) model in terms of different equation of state (stiff and soft NEOS) as well as nucleon-nucleon cross-sections for the reaction of $^{129}_{54}$Xe+$^{120}_{50}$Sn at incident energies between 10 and 100 MeV/nucleon [198]. The recent articles represent the role of different potentials as well as density dependent symmetry energy on the local and global nuclear stopping by varying the mass-asymmetry as well as composite mass of the reaction [199–202].

Experimental attempts

Experimentally, the observables of nuclear stopping have been measured by FOPI, INDRA and ALADIN collaborations at GANIL and GSI, Germany. The rapidity distribution is the first indicator of nuclear stopping studied by Hong *et al.* [203] for the

reaction of $^{58}_{28}$Ni+$^{58}_{28}$Ni at incident beam energies of 1.06, 1.45 and 1.93 GeV/nucleon. The experiment was performed in SIS using FOPI detector system. The studied rapidity spectra of pions, proton and deuteron reveals that even for central collisions, only a fraction of nucleons at mid-rapidity corresponds to the thermally equilibrated fireball. Therefore, no signature of fully equilibrated fireball has been seen. The isospin effects on particle spectra have been studied experimentally for the isospin-asymmetric nuclear reactions of $^{96}_{44}$Ru+$^{96}_{44}$Ru and $^{96}_{40}$Zr+$^{96}_{40}$Zr at beam energies of 400 MeV/nucleon and shows the partial transparency or incomplete mixing of the projectile and target nuclei [204, 205]. The FOPI Collaboration also studied the nuclear stopping parameter, $< varxz >$ for the reactions of $^{40}_{20}$Ca+$^{40}_{20}$Ca, $^{58}_{28}$Ni+$^{58}_{28}$Ni, $^{96}_{44}$Ru+$^{96}_{44}$Ru, $^{129}_{54}$Xe+CsI and $^{197}_{79}$Au+$^{197}_{79}$Au at a wide range of incident energy from 90 MeV/nucleon to 1.93 GeV/nucleon [206]. The dependency of nuclear stopping on incident energy shows a broad plateau from 200 to 800 MeV/nucleon and shows its maximum value at 400 MeV/nucleon [206, 207]. The INDRA and ALADIN collaborations uses 4π multi-detector to observe the nuclear stopping parameter, the momentum based anisotropy ratio at lower tail of incident energy from 10 MeV/nucleon to 100 MeV/nucleon for the mass-symmetric and mass-asymmetric reactions such as $^{197}_{79}$Au+$^{197}_{79}$Au, $^{129}_{54}$Xe+ $^{118}_{50}$Sn and $^{58}_{28}$Ni+$^{58}_{28}$Ni [208]. The study shows that irrespective to the system size, the nuclear stopping is least around 35-40 MeV/nucleon and again rises with increase in incident energy. The recent experimental article [209] provides the largest body of experimental data of the energy based anisotropy ratio of protons for the 42 (quasi) symmetric nuclear reactions with total mass ranging from 72 to 476 a.m.u. and N/Z from 1.0 to 1.6 in the Fermi energy domain. In addition to this, the in medium effects are also found to affect the nucleon-nucleon cross-section significantly.

1.7 Organisation of thesis

The thesis is organized as follow:

- As the present study is fully theoretical, therefore in **chapter 2**, various theoretical tools to understand the reaction dynamics of heavy ion collisions at intermediate energies have been discussed. A detailed description of the Isospin dependent Quantum Molecular Dynamics (IQMD) model has been demonstrated, which is used to fulfill the aim of present work. A brief survey of secondary models: the Minimum Spanning Tree (MST) and the Minimum Spanning Tree method with momentum cut (MSTM), used to identify various fragments is also presented.

- In **Chapter 3**, the influence of isospin dependent nuclear charge radii parameterizations on the time evolution of nucleonic density and the binary nucleon-nucleon collisions have been studied. The role of radii parameterizations on the system size effects of the multiplicity of various fragments and its power law behaviour have been optimized at incident energy E = 50 MeV/nucleon. The isospin degree of freedom has been studied through the dependence of multiplicity of various fragments on the initial neutron-to-proton ratio of colliding nuclei via isospin independent as well as dependent nuclear charge radii parameterizations for two isobaric series of reactions. The theoretical calculations for the mean multiplicity of IMFs has been compared with the experimental findings of ALADIN Collaboration.

- In **Chapter 4**, the structural and isospin effects on the excitation function of reduced flow as well as elliptical flow via nuclear charge radii parameterizations for a wide range of composite mass and neutron-to-proton ratio has been studied. The incident energy is varied from 30 MeV/nucleon to 600 MeV/nucleon for the semi-central nuclear collision. A radius dependence of balance energy E_{bal} and transition energy E_{trans} is determined with a power law fit. Moreover, the theoretical results on impact parameter dependence of E_{bal} and E_{trans} is also compared with experimental data provided by INDRA, FOPI and ALADIN collaborations. Work has been embellished to calculate the balance geometry and transition geometry from the scaled impact parameter dependence of reduced flow and elliptical flow respectively. In addition to this, the isospin dependence of clusterization technique has

also been studied as per the radii parametrization used for azimuthal distribution of $dN/d(Cos2\phi)$.

- In **Chapter 5**, the different aspects of nuclear stopping with different nuclear charge radii parameterizations have been discussed. The isospin effects has been quantified for isospin-asymmetric nuclear reactions. The excitation function of nuclear stopping is studied for the beam energies from 30 MeV/nucleon to 1.5 GeV/nucleon and thus the calculations are compared with experimental data of INDRA and ALADIN collaborations. The study is also extended to examine the role of momentum dependent interactions along with nuclear charge radii parameterizations.

- In previous chapters, the focus is on the initialization effects on the isospin-asymmetric nuclear reaction with different N/Z. **Chapter 6** presents a comparative observation on the initialization effects in mass-symmetric and mass-asymmetric nuclear reactions at E = 100 MeV/nucleon. For this purpose, first the time evolution of average density and temperature is examined. After that, the maximal average temperature achieved in the compression stage (around time 10-20 fm/c) and multiplicity of fragments (at time 200 fm/c) is correlated with the momentum-based anisotropy ratio.

- **Chapter 7**, summarizes the result of the work presented in this thesis along with possible extension for future prospective.

Chapter 2

Methodology

2.1 Introduction

In previous chapter, the complex dynamics of nuclear reaction involving nuclear forces and non-equilibrium physics along with various experimental as well as theoretical aspects in the heavy ion collisions (HICs) at intermediate energies has been interpreted. The astrophysical objects like neutron stars and occurrence of nova and supernova explosions are remote in space and are natural. Furthermore, in the laboratory experiments, the studies depend only on the end products which cannot quantify the hot and dense phase of the nuclear matter because particles detected are cold in nature. Moreover, the condensed phase of the nuclear matter appears for a very short interval of time ($\approx$ few fm/c) which is not possible to record experimentally. Since, the astrophysical phenomena and experimental facilities have limitations, a theoretical treatment to this complicated nuclear reaction dynamics is need to study the NEOS and to trace the time evolution of nuclear collisions. Therefore, in this chapter a brief review on the various theoretical approaches and dynamical models is given.

2.2 Review of various theoretical approaches in HICs at intermediate energies

The theoretical approaches in the HICs at intermediate energies are broadly classified into statistical models and dynamical models. The statistical models include calculation only at starting point by presuming partial or complete equilibrate system and at end point of the reaction by looking into the fragment phase-space as well as its properties at freeze-out, similar to experimental studies. These models are mainly based on precolation and

droplet description theory of nucleus. Instead of detailed dynamics, different decay mode probabilities are involved by considering large number of degree of freedom at high excitation energies. Some of these models, Statistical Multi-fragmentation Model (SMM) [108], Berlin Multi-fragmentation Model (BMM) [210], Participant-Spectator Model [211], Lattice Gas Approach [212,213] and Expanding Emitting Source (EES) model [214] are good to describe the experimental data of multi-fragmentation at final stage of reaction. However, matching the experimental results are not sufficient for the complete understanding of dynamics involved during the compression stage. Therefore, the dynamical approach is included in the theory of statistical models called hybrid approach [215–217] which describe the different stages of equilibrium and non-equilibrium during the complete evolution of HICs at intermediate energies in a better way.

The interaction mechanism between the nucleons under extreme conditions is mainly intended by nucleon-nucleon collision/binary collision, mean field and Pauli blocking. The first fully microscopic model which handled two body nucleon-nucleon collisions is Intra Nuclear Cascade (INC) model [95, 218]. The nucleon follows straight trajectory until it collides with another nucleon elastically or inelastically. However, absence of mean field and quantum effects (such as Pauli blocking and Fermi momentum) reduces the use of this model [219]. Therefore its application is restricted at high incident energies only. The correct information on the entire dynamics of HICs at intermediate energies appeals equal participation of nucleon-nucleon binary collisions, Pauli blocking and mean field. Therefore, keeping the demand of nuclear reaction dynamics at intermediate energies in mind, a theoretical model should be capable of dealing with various non-equilibrium conditions of the reactions. For this purpose, transport dynamical models are introduced which are further classified into two groups. The first group includes models like Time Dependent Hartee-Fock (TDHF) [17], Vlasov Uehling Uhlenbeck (VUU) [220] or Boltzmann Uehling Uhlenbeck (BUU) model [221], Landau-Vlasov (LV) [222], Boltzmann Nordheim Vlasov (BNV) model [223], Stochastic Mean Field (SMF) model [224] and Isospin dependent Boltzmann Uehling Uhlenbeck (IBUU) model [38, 39] in which the time evolution is described as one body phase-space distribution. The essential quantum characteristics such as stochastic nucleon-nucleon scattering, Fermi momentum and Pauli blocking are significantly entrenched in these models.

The TDHF [225,226] theory which includes the time dependent Schrödinger equation along with mean field approximation calculations, is useful theoretical tool to describe the shock wave propagation, formation of compound nucleus and its various decay channels up to incident energy, E <10 MeV/nucleon [227]. In the TDHF theory, the time dependent density equation involving many body hamiltonian is reduced into one body equation. However, the binary collisions which are responsible for two body interactions are neglected, which results in the failure of this model at intermediate energies. The dynamics of HICs at the intermediate energies evolves both real as well as imaginary part of potential i.e. mean field and nucleon-nucleon binary collisions respectively. For this purpose, the extended version of TDHF called Extended Time Dependent Hartee-Fock (ETDHF) theory was developed by including Vlasov equation accompanied by nucleon-nucleon collisions, formerly known as *"Vlasov -Uehling - Uhlenbeck equation" (VUU equation) or "Boltzmann -Uehling - Uhlenbeck equation" (BUU equation)* [228]. Here, the one body equation of TDHF is described NA times (here, A is mass number of nucleus and N is event number), which finally originate lack of correlation between N parallel runs. Therefore, the large scale complicated investigation of HICs at intermediate energies can not be analyzed through event by event with this theory [229]. In early 80's, The BUU/VUU model was the best replacement of TDHF/ETDHF and cascade models. The BUU model describes the one body phase-space distribution of nucleons by test particle method. Till late 80's, this model was fully developed and able to portray one body observables of HICs and also the photon induced reactions. Furthermore, the mean free path conception has been applied by Bonasara *et al.* [230] to analyze the collision integral in the Boltzmann-Nordheim-Vlasov equation. This approach also perform large number of parallel events and calculate average value of observables to quantify various phenomena in the HICs over all events such as nuclear stopping, particle spectra and collective flow. However, in this approach, the event by event correlations are conserved [231]. The main drawback of one body approach models is its inability to depict the N-body or many body phenomena such as two particle correlation and formation of fragments. This led to the development of many body molecular dynamics models with the capability to incorporate the correlations and fluctuations among nucleons. The N-body molecular dynamics is the second group of transport models. The N-body molecular dynamics is the successful approach

and is being used till date to describe the complete evolution of HICs at intermediate energies. Therefore, in the following section, a brief review on the various N-body molecular dynamical models and the recent updates is given.

2.2.1 Many body molecular dynamics approach and its recent updates

In the list of many body molecular dynamics transport models, the Classical Molecular Dynamics (CMD) model comes at the forefront position. This model gave a very intersecting description for the motion of nucleons with classical equation of motion in place of quantum mechanical time evolution [232, 233]. The classical many body dynamics i.e. Hamilton's equations of motion and finite range nucleon-nucleon potential are capable of explaining the production of fragments and compression stage of the nuclear matter [234]. Due to improper description of the essential quantum features (like Pauli corrected stochastic scattering and nuclear potentials) the nucleonic collisions and particle production can not be quantified in this model. Later on, these feature were included into the classical N-body approach of CMD by Aichelin and Stöcker to design a new, well systemized and undeniable approach till today named as Quantum Molecular Dynamics (QMD) model [18, 235]. Till present date, many realizations of QMD approach are available and the interaction among the nucleons as a relativistic quantum mechanical wave packets inside a high dense medium is being studied. However, the foremost idea initiating the simulation procedure of all the updated version of QMD approach is same. The process of many body molecular dynamics incorporates three steps:

1. *Initialization*: In the first step, one has to generate two stable and cold projectile and target nuclei.

2. *Propagation*: In the second step, the appropriately initialized projectile nucleus is boosted upon the target nucleus with some incident energy under the Hamiltonian equation of motion.

3. *Nucleon-nucleon collision*: In the third and last step, the nucleons experience scattering or collision via elastic or inelastic manner depending upon their momenta if they come too closer and satisfies Pauli's exclusion principle.

The detailed illustration of this series of steps is given in Sec. 2.3. The QMD model incorporates N-body Liouville equation, stochastic scattering as well as the time evolution of all nucleons through classical orbits. After one collision process if the nucleon moves to occupy the phase-space which is already occupied by another nucleon, then the collision process is said to be blocked. The solution of N-body equation can be obtained without reducing it into one body level. Therefore the solution is time reversible and all the time correlations are possibly described in the QMD approach. To describe the fragmentation process at low incident energies, the stability of nuclei is improved and rewritten in original QMD code by Bohnet *et al.* [236]. It was designed for the proper description of binding energies of nuclei hence, named as BQMD. Here, Skyrme-type two body interaction are also modified and binding energies are kept as its experimental values. The another modified version of QMD dubbed as HQMD includes higher resonances concerning the meson production and developed by Huber *et al.* [237]. This model incorporated proper isospin coupling in addition to the nucleons and deltas. The PQMD model developed by Peilert *et al.* [238, 239], includes Gaussian Pauli potential [240, 241] in addition to QMD modelling. Frankfurt theoretical physics group in Germany, wrote another realization named Modified Quantum Molecular Dynamics (MQMD) [242]. This model was designed by coupling QMD with RAM (Reconstructed Aggregation Model) [243] for the much better description on clusterization of nucleons. The Temperature dependent Quantum Molecular Dynamics (TQMD) model [244], G-matrix QMD [245], Constrained Molecular Dynamics (CoMD) [246] and DQMD [247] are another realizations of QMD featuring local temperature particle at each time step, strong momentum dependence of the Brueckner G-matrix, shortening the computation time to study heaviest nuclear systems and dynamical formation of highly-excited fragments respectively.

The incident energy range of various versions of QMD models was expanded to AGS, CERN/SPS as well as up to RHIC domain by developing the Relativistic and Ultra-relativistic Quantum Molecular Dynamics (RQMD and UrQMD) models respectively. In comparison to QMD, the RQMD model (build by Faessler and Co-workers [248]) includes the covariant dynamics, string-excitation for high energy hadron-hadron interactions as well as an improved and extended collision term containing heavy baryon-resonances and strange particles. Beside this, the UrQMD build by the Frankfurt group [249, 250]

includes the features like interaction potential and cross section (for meson-baryon, meson-meson and baryon-baryon), the formation time of fragments and string fragmentation. Both the models have been used extensively to investigate symmetry energy at very high densities [251, 252]. The initialized nuclei of original QMD model are not really in their ground state with respect to the Hamiltonian equation of motion under which they propagate. Thus, Feldmeier [97, 253] developed an approach named as Fermionic Molecular Dynamics (FMD). This model couples the Fermi-Dirac statistics with a semi-quantal trajectory picture by adjusting the Hamiltonian parameters according to EOS of infinite nuclear matter, binding energy and root mean square radii of nuclei. The Ono *et al.* [98, 254] succeeded in developing the antisymmetrized version of QMD named as Antisymmetrized Molecular Dynamics (AMD) by including two nucleon collision process. However, the calculated values of spins of fragments quantified by AMD model are not reliable as the two-nucleon collisions violates the conservation of total angular momentum. Moreover, because of complicated numerical problems, the use of both AMD and FMD models are restricted to lighter nuclear systems only.

As discussed in chapter 1, the isospin degree of freedom is an important aspect to study the NEOS of isospin-asymmetric nuclear matter. Also the interaction between the nucleonic pair: neutron-neutron, proton-proton as well as proton-neutron is different; therefore, one should undertake the isospin degree of freedom in the nucleon-nucleon cross-section and interaction potentials. The symmetry energy (in Bethe-Weizsäcker mass formula) and the isospin dependent nucleon-nucleon cross-section has been incorporated in the QMD model to develop the Isospin dependent Quantum Molecular Dynamics (IQMD) Model. The BUU model has also been advanced with isospin dependent model ingredient, named Isospin dependent Boltzmann -Uehling - Uhlenbeck (IBUU) model [38, 39]. Both the models, IBUU and IQMD have been used extensively to study the isospin dependence to account for the asymmetry between the interaction among neutrons and protons. The main objective of present work is to study the initialization effects as well as isospin effects in the isospin-asymmetric nuclear matter via different nuclear charge radii parameterizations. Therefore, the entire calculations to achieve the objectives of present thesis are done with in the framework of IQMD model which is based on many body molecular dynamics approach. The detailed description of various processes, potentials, dynamical

equations, quantum features and isospin degree of freedom of IQMD model in contrast to QMD model is demonstrated in the next section.

2.3 Isospin dependent Quantum Molecular Dynamics (IQMD) model

The Isospin dependent Quantum Molecular Dynamics (IQMD) model established by Hartnack *et al.* [94, 255–258] is an extended version of QMD approach, however, its technical computer programming is based on VUU model. Since it is based on N-body molecular dynamics so it manifest both the compression as well as expansion stages of HICs in the entire range of intermediate energies. The speciality of IQMD model is its ability to rationalize different hadrons like neutrons, protons, deltas, pions on the basis of their charge and isospin state explicitly. The isospin degree of freedom is included in this models via symmetry potential (in Bethe-Weizsäcker mass formula similar to IBUU model), Coulomb potential (by constituting the real charge, i.e., $Z_{proton} = 1$ and $Z_{neutron} = 0$) and isospin dependent nucleon-nucleon scattering cross section to achieve the corrected information on distribution as well as interaction among the neutrons and protons. Likewise other dynamical transport models, the IQMD model also consists of three broad steps: initialization, propagation and nucleon-nucleon collisions. Beside this, the Pauli blocking is also an essential aspect in this model. These aspects of IQMD model are discussed in the following subsections.

2.3.1 Initialization

The nucleons of projectile and target nuclei are initialized in rest frame, assigned as the time, t = 0 fm/c. The position and momentum of nucleons are uniformly distributed inside a phase-space Fermi sphere (with radius, $r \leq R$ and momentum, $p \leq P_F$) having the ground state density of nucleus i.e. $\rho_o = 0.17 fm^{-3}$. Here $R = 1.12A^{1/3}$ (also regarded as R_{LDM} in Section 1.4 of chapter 1) is defined as nuclear radius and P_F = 268.4 MeV/c is defined as Fermi momentum. The IQMD model differ to QMD model in the initialization. The QMD model adopts the radii parametrization, R = 1.142 $A^{1/3}$ and the Fermi momentum of nucleons is governed by the local potential as per relation $P_F(\mathbf{r}_i) = \sqrt{-2mU(\mathbf{r}_i)}$. Where $U(\mathbf{r}_i)$ is the local potential and $\mathbf{r}_i$ is position of i^{th}

nucleon. However in the IQMD model, the uniform distribution of nucleonic momentum in the ground state makes the surface nucleons initially unbound which leads to lesser binding energy per nucleon of nucleus in comparison to Weizsäcker mass formula (i.e. E_{bind} = 4 to 5 MeV/nucleon for heavy nuclei rather than 8 MeV/nucleon). Therefore, the radius profile of nuclei initialized in the IQMD is not as stable as in the QMD. But due to availability of full Fermi energy calculated from the Skyrme ansatz, a strong density profile is achieved against vibration modes in the IQMD. In both QMD and IQMD, the nucleons are defined as a Gaussian wave packets and the wave function of i^{th} nucleon is given by:

$$\psi_i(\mathbf{r},\ \mathbf{p}_i(t),\ \mathbf{r}_i(t)) \ = \ \frac{1}{(2\pi L)^{3/4}}\ exp\left[\frac{i}{\hbar}\ \mathbf{p}_i(t)\cdot\mathbf{r}\ -\ \frac{(\mathbf{r}\ -\ \mathbf{r}_i(t))^2}{4L}\right]. \tag{2.1}$$

Here, $\mathbf{r}_i(t)$ and $\mathbf{p}_i(t)$ are mean position and mean momentum of i^{th} nucleon respectively. The another difference between QMD and IQMD lies in the value of Gaussian width of the wave packets 'L' which defines the interaction range of the nucleon. In the QMD model, L is system size independent and has constant value of 1.08 fm^2. Whereas in the IQMD model, L has been kept system size dependent to achieve maximum stability in the nucleonic density. For heavier systems, e.g. $^{197}_{79}Au + ^{197}_{79}Au$, $L = 2.16 fm^2$ and for $^{40}_{20}Ca + ^{40}_{20}Ca$ and lighter nuclei, $L = 1.08 fm^2$. For the middle case, L value lies in between two values. The product of all coherent states of Eqn. 2.1 determines the total N-body wave function of system and represented by Φ as:

$$\Phi \ = \ \prod\nolimits_i \psi_i(\mathbf{r},\ \mathbf{r}_i, \mathbf{p}_i, t). \tag{2.2}$$

Wigner density formalism is used to describe the density distribution which correspond to the phase-space densities in the classical mechanics. Wigner densities formulates the quantum mechanics in a very easy way such that quite inherent interpretation of the reaction dynamics can be obtained. Wigner density yields phase-space coordinate (i.e. r, p and t) dependent observables. Which is not possible through the solution of N-body Schrödinger equation. Using Wigner density as a substitute of wave function keeps the formulation of model on the verge of classical transport theory and fabricate the model as semi-classical model. The Wigner transformation of all coherent states (a composite nucleon system of projectile and target nuclei i.e. $A_{tot} = A_P + A_T$) yields Gaussian-shaped

density distribution function as:

$$f_i(\mathbf{r},\ \mathbf{p}, t) \ = \ \frac{1}{(2\pi\hbar)^3} \int exp\ \left[-\frac{i}{\hbar}\mathbf{p}\cdot\mathbf{r}_{12}\right] \psi_i\left(\mathbf{r}+\frac{\mathbf{r}_{12}}{2},\ t\right)\ \psi_i^*\left(\mathbf{r}-\frac{\mathbf{r}_{12}}{2},\ t\right) d^3\mathbf{r}_{12},$$

by solving the integration using Eqn. 2.1, density distribution function read as:

$$f_i(\mathbf{r},\ \mathbf{p}, \mathbf{r}_i(t),\ \mathbf{p}_i(t)) \ = \ \frac{1}{(\pi\hbar)^3}\ exp\ \left[\frac{-(\mathbf{r}\ -\mathbf{r}_i(t))^2}{2L}\right]\ exp\ \left[\frac{-(\mathbf{p}\ -\mathbf{p}_i(t))^2\ 2L}{\hbar^2}\right] \quad (2.3)$$

Here, $\mathbf{r}_i(t)$ and $\mathbf{p}_i(t)$ characterize the classical orbit or the centeriod of the Gaussian wave packet in the phase-space which is time-dependent. Whereas, L is time-independent. Therefore, the density of i^{th} particle in the coordinate space reads as:

$$\begin{aligned}\rho_i(\mathbf{r}, \mathbf{r_i(t)}) \ &= \ \int\ f_i(\mathbf{r}, \mathbf{p}, \mathbf{r}_i(t), \mathbf{p}_i(t))\ d^3p, \\ &= \ \frac{1}{(2\pi L)^{3/2}}\ exp\ \left[\frac{-\left[\mathbf{r}\ -\ \mathbf{r}_i(t)\right]^2}{2L}\right], \end{aligned} \quad (2.4)$$

and in the momentum space is:

$$\begin{aligned} g_i(\mathbf{p}, \mathbf{p_i(t)}) \ &= \ \int\ f_i(\mathbf{r}, \mathbf{p}, \mathbf{r}_i(t), \mathbf{p}_i(t))\ d^3r, \\ &= \ \left(\frac{2L}{\pi\hbar}\right)^{3/2}\ \ exp\ \left[\frac{-\left[\mathbf{p}\ -\ \mathbf{p}_i(t)\right]^2\ 2L}{\hbar^2}\right]. \end{aligned} \quad (2.5)$$

In polar co-ordinates, the three dimensional center of Gaussian wave packets is uniformly distributed as:

$$\begin{aligned} r \ &= \ R\ c_1^{1/3}, \\ cos\theta \ &= \ 1\ -\ 2c_2, \\ \phi \ &= \ 2\pi\ c_3, \end{aligned}$$

where $c_1,\ c_2,\ c_3$ are the random numbers. Those events are rejected if the distance between the centroids of Gaussian wave packets of i^{th} and j^{th} particle do not fulfil the requirement:

$$|r_i\ -\ r_j| \ > \ r_{min} \ = \ 1.5\ fm. \quad (2.6)$$

The nucleons are initialized as per the liquid drop model and $R = R_{LDM}$ as per Eqn. 1.9 with $r_o = 1.12\ fm$. Every nucleon takes h^3 as its volume. The phase-space in the IQMD model is evenly replete. The initial momentum of each nucleon is arbitrary selected

between zero and P_F, without any other local constraint. The center of each Gaussian wave packet in the momentum space is evenly disseminated in the polar coordinate by:

$$\begin{aligned} p_i &= P_F(\mathbf{r}_i)c_4^{1/3}, \\ cos\theta &= 1 - 2c_5, \\ \phi &= 2\pi c_6. \end{aligned}$$

Where $c_4,\ c_5,\ c_6$ are again random numbers. The stability of the nucleus can not be maintained for a sufficiently long time through randomly chosen centers (r_i, p_i) of the Gaussian phase-space. The nucleus generated in this way is in meta-stable excited state which can decay nucleons due to fluctuations. Therefore, to create a stable nucleus and smoother distribution of nucleons, only those phase-space distribution of nucleons are taken into account which fulfils the condition:

$$|r_i - r_j|^2\ |p_i - p_j^2|\ \geq\ d_{min}. \tag{2.7}$$

Under this criteria, out of fifty thousand initializations, only one is well accepted. The another important characteristics of IQMD model is that, the relativistic effects have been included in this model by involving Lorentz contraction in the coordinate distribution of nucleus. However, the significance of relativistic effects below E = 1 GeV/nucleon is negligible. A sample of nuclei with the required stability are chosen to prevent the unstable nuclei initialization. Moreover, the coordinates of a nucleon is rotated around its center of mass by choosing two Euler angels randomly. This procedure is repeated for different sets of Euler angles. Thus, absolutely different reaction is produced by each different set of Euler angels without changing the stability of initialized nuclei.

Numerical test

For a successful reaction evolution and its proper understanding, it is important to check the stability of perfectly initialized nucleus from a hydrodynamical transport model, as the unstable nucleus may emit few nucleons after time few hundreds of fm/c. The cold nucleus thus generated must be in its ground state as per the quantum mechanical system. *"Heidelberg-Nantes-Frankfurt-Tübingen-Chandigarh"* groups have performed various comprehensive studies to test the ground state properties of nucleus generated

using IQMD model. Before subjecting the nucleus with some incident energy, its nucleons are interacting with neighboring nucleons and moving under mean field only. In a stable nucleus, the mean field experienced by a nucleon is different in the core and surface of the nucleus. When the nucleon, during its motion between core and surface, comes close to the surface, it will be deflected back to the core to maintain the confined state of nucleus within the Fermi sphere of radius *'R'*. Majority of the nucleons remains inside the nucleus up to time 60-80 fm/c. After this time interval, the nucleus gets unstable and few nucleons start defusing out.

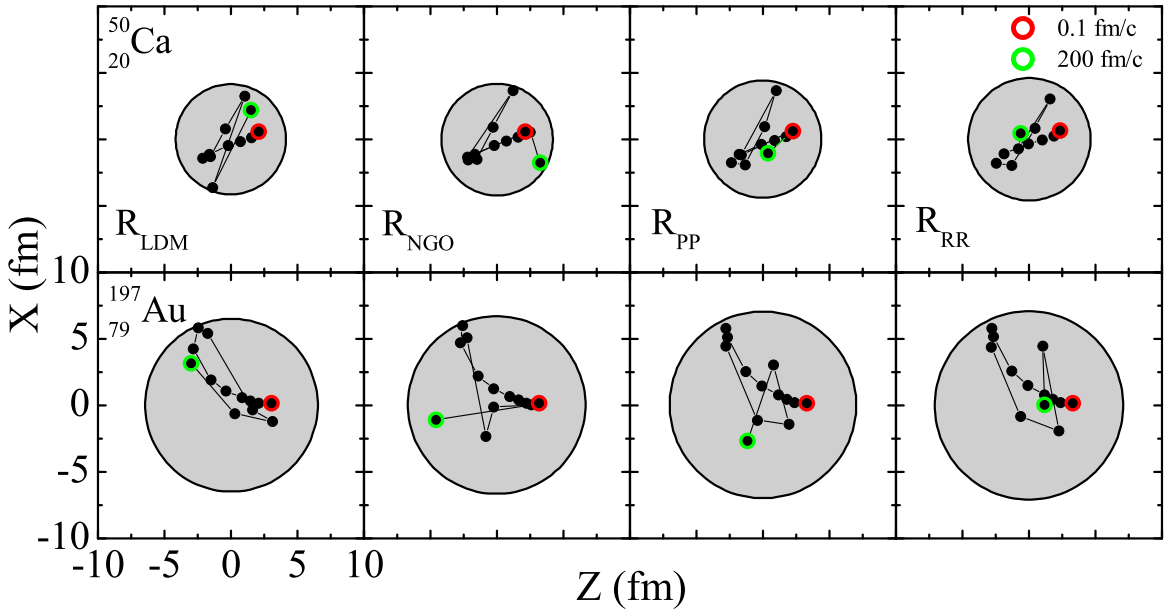

Figure 2.1: Single nucleonic trajectory from time 0.1 fm/c to 200 fm/c moving under mean field inside the nucleus of $^{50}_{20}$Ca (upper panels) and $^{197}_{79}$Au (lower panels) initialized with four different nuclear charge radii parameterizations: R_{LDM}, R_{NGO}, R_{PP} and R_{RR} (left to right panels respectively).

In Fig. 2.1, the stability of single nucleus simulated by using initialization of IQMD model has been tested through four different nuclear charge radii parameterizations: R_{LDM}, R_{NGO}, R_{PP} and R_{RR} (left to right panels respectively) by plotting single nucleonic trajectory from time, t = 0.1 fm/c to the 200 fm/c for the nuclei of $^{50}_{20}$Ca (upper panels) and $^{197}_{79}$Au (lower panels). The solid black circles indicate the positions of the nucleon at different time interval inside the radius of nucleus (shown by solid grey circle in the X-Z plane). In figure, the positions of nucleon at initial time (0.1 fm/c) and final

time (200 fm/c) are highlighted with open red and green circles respectively. The figure reveals that the nucleon remains inside the nucleus for all the radii parameterizations. It is worth to mention that the initial point of the nucleon is same for all the radii parameterizations (since same nucleon is selected). However, after getting reflected back from surface towards core, the trajectory followed by the nucleon is different for all radii parameterizations for both $^{50}_{20}$Ca and $^{197}_{79}$Au nuclei, which alters its final position. The calculated radius of nuclei increases as one switches from R_{LDM} to other parametrization, thus the density in its core will reduces. Therefore, the number of nucleons on surface of larger radius is more compared to smaller radius which thus affects the motion of the nucleon. The trajectory of those nucleon which has not reached to the surface and remain in the core through out the time span has also been checked (results not shown here). The positions of nucleon is same for all the radii parameterizations at all the time steps. Hence, the change in radii parametrization in the initialization of IQMD model affects the surface only, not the core.

2.3.2 Propagation

The projectile and target nuclei with well accepted distribution of nucleons, are subjected to move towards each other with some incident energy in the center of mass frame along Z-axis called longitudinal direction or beam axis in a co-ordinate space. The motion of both nuclei till they collide with each other is under Coulomb trajectories. The further time evolution of the combined nuclear system is accounted as equation of motion of many body system which is calculated by Ritz variational principle. The action between time t_1 and t_2 is defined as:

$$S = \int_{t_1}^{t_2} \mathcal{L}[\Phi, \Phi^*] d\tau \tag{2.8}$$

Therefore, a generalized Lagrange function is defined as:

$$\mathcal{L} = \langle \Phi | i\hbar \frac{d}{dt} - H | \Phi \rangle. \tag{2.9}$$

Here, Φ is the product of all coherent state wave function as defined in Eqn. 2.2 and H is total Hamiltonian of N-body system. The time evolution is accomplished by the condition that the action is stationary under the allowed variation of the wave function. Which implies,

$$\delta S = \delta \int_{t_1}^{t_2} \mathcal{L}[\Phi, \Phi^*] dt = 0. \tag{2.10}$$

The Lagrange function depends upon all parameters and their time derivatives. This give rise to an Euler-Lagrange equation for each parameter (say λ) as:

$$\frac{d}{dt}\frac{\partial \mathcal{L}}{\partial \dot{\lambda}} - \frac{\partial \mathcal{L}}{\partial \lambda} = 0. \tag{2.11}$$

For wave function $\psi_i(\mathbf{r},\ \mathbf{p}_i(t),\ \mathbf{r}_i(t))$, the variation of the action defined in Eqn. 2.10 leads to the exact solution of the Schrödinger equation. If the parameter space is very much restricted then the wave function obtained in the restricted parameter space will be closest to the solution of the Schrödinger equation. The superposition principle does not hold here because the set of wave functions is not necessarily a subspace of Hilbert-space.

The Hamiltonian is described as:

$$H = \sum_i T_i \ + \ \frac{1}{2}\sum_{ij} V_{ij} \tag{2.12}$$

Here T_i is the kinetic energy of i^{th} particle and V_{ij} is the potential energy between i^{th} and j^{th} particles (with i$\neq$ j). For the direct product of all coherent states and Hamiltonian (H), the generalized Lagrange function reads as:

$$\mathcal{L} = \sum_i \dot{\mathbf{r}}_i \mathbf{p}_i - \sum_{j\neq i} < V_{ij} > -\frac{3}{2Lm}. \tag{2.13}$$

Thus, the Euler-Lagrange equation defined in Eqn. 2.11 for centroids p_i and $r_i = r_i^{'} + p_i t/m$ can be represented as:

$$\frac{d}{dt}\frac{\partial \mathcal{L}}{\partial \dot{p_i}} - \frac{\partial \mathcal{L}}{\partial p_i} = 0 \Rightarrow \dot{\mathbf{r}}_i = \frac{\mathbf{p}_i}{m} + \nabla_{\mathbf{p}_i}\sum_j < V_{ij} >= \nabla_{\mathbf{p}_i} < H >, \tag{2.14}$$

and

$$\frac{d}{dt}\frac{\partial \mathcal{L}}{\partial \dot{r_i}} - \frac{\partial \mathcal{L}}{\partial r_i} = 0 \Rightarrow \dot{\mathbf{p}}_i = -\nabla_{\mathbf{r}_i}\sum_{j\neq i} < V_{ij} >= -\nabla_{\mathbf{r}_i} < H >, \tag{2.15}$$

with $\langle V_{ij}\rangle$ is defined by the integral: $\int d^3\mathbf{r}_1 d^3\mathbf{p}_2 \langle \psi_i^* \psi_j^* | V(\mathbf{r}_1, \mathbf{r}_2) | \psi_i \psi_j \rangle$. The above two equations represents time evolution of co-ordinate as well as momentum space. Therefore, the Ritz variational principle converts the time evolution of the N-body Schrödinger equation into the time evolution of the parameters as per the classical Hamilton equations of motion. Hence the time derivatives of momentum and co-ordinate space reads as,

$$\dot{\mathbf{p}}_i \ = \ -\frac{\partial \langle H \rangle}{\partial \mathbf{r}_i} \ ; \ \dot{\mathbf{r}}_i \ = \ \frac{\partial \langle H \rangle}{\partial \mathbf{p}_i}. \tag{2.16}$$

The numerical solution can be achieved as per the classical molecular dynamics [232, 259, 260]. The total energy or Hamilton equation of i^{th} particle is the sum of kinetic and potential energies and represented by H_i as:

$$H_i \;=\; T_i + V_i \;= T_i \;+ \frac{1}{2!}\sum_{j;i\neq j} V_{ij}^{(2)} \;+ \frac{1}{3!}\sum_{j,k;i\neq j\neq k} V_{ijk}^{(3)}, \tag{2.17}$$

where T_i is defined as the total kinetic energy of the system:

$$T_i \;=\; \;= \sum_i \frac{\mathbf{p}_i^2(t)}{2m} \tag{2.18}$$

$V_{ij}^{(2)}$ and $V_{ijk}^{(3)}$ in Eqn. 2.17 are the two and three body interactions respectively, experienced by i^{th} particle in the presence of other particles (say j^{th} and k^{th}). Therefore the two body interactions $V_{ij}^{(2)}$ can be written as:

$$V_{ij}^{(2)} \;=\; V(\mathbf{r}_i(t) - \mathbf{r}_j(t)).$$

Where, $V(\mathbf{r}_i(t) - \mathbf{r}_j(t))$ is defined as:

$$V(\mathbf{r}_i(t) - \mathbf{r}_j(t)) \;=\; \int f_i(\mathbf{r}_i, \mathbf{p}_i, t)\; f_j(\mathbf{r}_j, \mathbf{p}_j, t)\; V(\mathbf{r}_i, \mathbf{r}_j)\; d^3\mathbf{r}_i\; d^3\mathbf{r}_j\; d^3\mathbf{p}_i\; d^3\mathbf{p}_j.$$

Now, the second part of Eqn. 2.17 can be written as:

$$\begin{aligned}
\frac{1}{2\,!}\sum_{j;i\neq j} V_{ij}^{(2)} \;&=\; \frac{1}{2\,!}\sum_{j;i\neq j}\; \int f_i(\mathbf{r}_i, \mathbf{p}_i, t)\; f_j(\mathbf{r}_j, \mathbf{p}_j, t)\; V(\mathbf{r}_i, \mathbf{r}_j) \\
&\quad \times\; d^3\mathbf{r}_i\; d^3\mathbf{r}_j\; d^3\mathbf{p}_i\; d^3\mathbf{p}_j, \\
&=\; \frac{1}{2\,!}\sum_{j;i\neq j} \int f_i(\mathbf{r}_i, \mathbf{p}_i, t)\; f_j(\mathbf{r}_j, \mathbf{p}_j, t)\; t_1 \\
&\quad \times \delta(\mathbf{r}_i - \mathbf{r}_j) d^3\mathbf{r}_i\; d^3\mathbf{r}_j\; d^3\mathbf{p}_i\; d^3\mathbf{p}_j, \\
&=\; \frac{1}{2\,!}\sum_{j;i\neq j}\; t_1 \int f_i(\mathbf{r}_i, \mathbf{p}_i, t)\; f_j(\mathbf{r}_j, \mathbf{p}_j, t) \\
&\quad \times\; d^3\mathbf{r}_i\; d^3\mathbf{p}_i\; d^3\mathbf{p}_j, \\
&=\; \frac{1}{2\,!}\sum_{j;i\neq j}\; t_1 \int \frac{1}{(\pi\hbar)^3}\; exp\;\left[\frac{-(\mathbf{r} - \mathbf{r}_i(t))^2}{2L}\right]\; exp\;\left[\frac{-(\mathbf{p} - \mathbf{p}_i(t))^2\; 2L}{\hbar^2}\right] \\
&\quad \times \frac{1}{(\pi\hbar)^3}\; exp\;\left[\frac{-(\mathbf{r} - \mathbf{r}_j(t))^2}{2L}\right]\; exp\;\left[\frac{-(\mathbf{p} - \mathbf{p}_j(t))^2\; 2L}{\hbar^2}\right]\; d^3\mathbf{r}_i\; d^3\mathbf{p}_i\; d^3\mathbf{p}_j, \\
&=\; \frac{1}{2\,!}\sum_{j}\; t_1 \frac{1}{(4\pi L)^{3/2}}\; exp\;\left[\frac{-(\mathbf{r}_i - \mathbf{r}_j)^2}{4L}\right], \\
&=\; \frac{t_1}{2}\sum_{j;i\neq j} \rho_{ij}.
\end{aligned} \tag{2.19}$$

Where, ρ_{ij} is the interaction density between ith and jth particle, given by:

$$\rho_{ij} = \int d^3\mathbf{r}\ \rho_i(\mathbf{r})\ \rho_j(\mathbf{r}) = \frac{1}{(4\pi L)^{3/2}}\ exp\ \left[\frac{-(\mathbf{r}_i - \mathbf{r}_j)^2}{4L}\right]. \tag{2.20}$$

Similarly, the three body interaction potential defined as follows:

$$V^{(3)}_{ijk} = \int f_i(\mathbf{r}_i, \mathbf{p}_i, t)\ f_j(\mathbf{r}_j, \mathbf{p}_j, t)\ f_k(\mathbf{r}_k, \mathbf{p}_k, t)\ V(\mathbf{r}_i, \mathbf{r}_j, \mathbf{r}_k)\ d^3\mathbf{r}_i\ d^3\mathbf{r}_j\ d^3\mathbf{r}_k\ d^3\mathbf{p}_i\ d^3\mathbf{p}_j\ d^3\mathbf{p}_k.$$

Therefore, the third part of Eqn. 2.17 become as:

$$\begin{aligned}
\frac{1}{3\,!}\sum_{j,k;i\neq j\neq k} V^{(3)}_{ijk} &= \frac{1}{3\,!}\sum_{j,k;i\neq j\neq k}\int f_i(\mathbf{r}_i, \mathbf{p}_i, t)\ f_j(\mathbf{r}_j, \mathbf{p}_j, t)\ f_k(\mathbf{r}_k, \mathbf{p}_k, t)\ V(\mathbf{r}_i, \mathbf{r}_j, \mathbf{r}_k) \\
&\quad \times d^3r_i\ d^3r_j\ d^3r_k\ d^3p_i\ d^3p_j\ d^3p_k, \\
&= \frac{1}{3\,!}\sum_{j,k;i\neq j\neq k}\int f_i(\mathbf{r}_i, \mathbf{p}_i, t)\ f_j(\mathbf{r}_j, \mathbf{p}_j, t)\ f_k(\mathbf{r}_k, \mathbf{p}_k, t)\ t_2 \\
&\quad \times\delta(\mathbf{r}_i - \mathbf{r_j})\ \delta(\mathbf{r}_i - \mathbf{r}_k) d^3r_i\ d^3r_j\ d^3r_k\ d^3p_i\ d^3p_j\ d^3p_k, \\
&= \frac{t_2}{3\,!\ (2\pi L)^3\cdot 3^{3/2}}\sum_{j,k;i\neq j\neq k} exp\ \left[\frac{-\left[(\mathbf{r}_i - \mathbf{r}_j)^2 + (\mathbf{r}_i - \mathbf{r}_k)^2 + (\mathbf{r}_k - \mathbf{r}_j)^2\right]}{6L}\right], \\
&= \frac{t_2}{3\,!\ (2\pi L)^3 3^{3/2}}\sum_{j,k;i\neq j\neq k} exp\ \left[\frac{-\left[(\mathbf{r}_i - \mathbf{r}_j)^2 + (\mathbf{r}_i - \mathbf{r}_k)^2\right]}{6L}\times\frac{3}{2}\right], \\
&= \frac{t_2\ (4\pi L)^{3/2\times 2}}{3\,!\ (2\pi L)^3\cdot 3^{3/2}}\left[\sum_{j\neq i}\frac{1}{(4\pi L)^{3/2}}\ exp\ \left[\frac{-(\mathbf{r}_i - \mathbf{r}_j)^2}{4L}\right]\right]^2
\end{aligned} \tag{2.21}$$

Using Eqn. 2.20, the above equation becomes:

$$\frac{1}{3\,!}\sum_{j,k;i\neq j\neq k} V^{(3)}_{ijk} = \frac{1}{3\,!}\frac{t_2\ 2^3}{3^{3/2}}\left[\sum_{j\neq i}\rho_{ij}\right]^2. \tag{2.22}$$

Therefore, the above derivation shows that for three body interaction potential, the mean field can be represented as $[\sum_{j\neq i}\rho_{ij}]^2$. With this, one can show that for $(\zeta + 1)$ body interaction (considering ζ as an integer) the mean field can be represented as $[\sum_{j\neq i}\rho_{ij}]^\zeta$. Hence, for two body and $(\zeta + 1)$ interaction, by using Eqs.2.18, 2.19 & 2.22, the Hamiltonian in Eqn. 2.17 can be written as:

$$\begin{aligned}
H_i &= \sum_i \frac{\mathbf{p}_i^2(t)}{2m} + \frac{1}{2}\sum_{i,j;i\neq j} V_{ij} + \frac{1}{\zeta+1)\ !}\sum_{i_1,i_2....i_{\zeta+1};i_1\neq i_2....\neq i_{\zeta+1}} V_{i_2,i_3....i_{\zeta+1}} \\
&= \sum_i \frac{\mathbf{p}_i^2(t)}{2m} + \frac{1}{2\,!}\sum_i\left[\sum_{j\neq i}\ t_1\frac{1}{(4\pi L)^{3/2}}\ exp\ \left[\frac{-(\mathbf{r}_i - \mathbf{r}_j)^2}{4L}\right]\right] \\
&\quad + \frac{t_2\ 2^3}{(\zeta+1)\ !\ (\zeta+1)^{3/2}}\sum_{i_1}\left[\sum_{i_2\neq i_1}\frac{1}{(4\pi L)^{3/2}}\ exp\ \left[\frac{-(\mathbf{r}_i - \mathbf{r}_j)^2}{4L}\right]\right]^\zeta
\end{aligned} \tag{2.23}$$

As the Hamiltonian is defined for the composite nucleon system i.e. for both projectile and target nuclei, therefore the average momentum in the IQMD model is conserved. The HICs should be followed with the help of G-matrix (a solution of Bethe-Goldstone equation [261]). The real part of G-matrix is responsible for the propagation of nucleons whereas, the imaginary part corresponds to the nucleon-nucleon collisions. The numerical solution of Bethe-Goldstone equation at every point in the phase-space and time is very much difficult. Therefore it can only be done by converting the momentum as well as density dependent G-matrix components into parameterized form in terms of two and three body interactions. The required condition to determine the parameters t_1 and t_2 in Eqn. 2.23 is that the Hamiltonian must reproduce the equation of state of finite nuclear matter. In this context, the propagation of nucleons in the HICs treated under Hamiltonian equation of motion are able to probe the nuclear equation of state (NEOS). Thus, for finite nuclear matter, the Skyrme parametrization of the NEOS from Eqn. 2.23 is:

$$\frac{E}{N}\ \left(or\ \frac{E}{A}\right) = \frac{1}{\rho}\frac{E}{V} = \frac{3}{5}\frac{\hbar^2 k_F^2}{2m} + \frac{\alpha}{2}\frac{\rho}{\rho_o} + \frac{\beta}{\zeta+1}\frac{\rho^\zeta}{\rho_o^\zeta} \tag{2.24}$$

Here, k_F is the Fermi vector in the nuclear matter defined as,

$$k_F = \left(\frac{3}{2}\pi^2\rho\right)^{1/3} \tag{2.25}$$

For infinite nuclear matter limits, the potential energy of Eqn. 2.23 can be written as:

$$V_N \Rightarrow^{nuclear\ matter} \frac{1}{2}Nt_1\rho + \frac{t_2 2^{3\zeta/2}}{(\zeta+1)!\ (\zeta+1)^{3/2}}N\rho^\zeta \tag{2.26}$$

On comparing Eqn. 2.24 and 2.26, the following expressions are obtained:

$$\frac{t_1}{2} \Rightarrow \frac{\alpha}{2\rho} \quad and \quad \frac{t_2 2^{3\zeta/2}}{(\zeta+1)!\ (\zeta+1)^{3/2}} \Rightarrow \frac{\beta}{\zeta+1}\frac{1}{\rho_o^\zeta} \tag{2.27}$$

With constant nuclear matter density, the interaction density coincides with single particle density. The two body part of interaction potential (i.e. $V_{loc}^{(2)}$ and $V_{Yukawa}^{(2)}$) is directly proportional to (ρ/ρ_o) and the three body part of interaction potential (i.e. $V_{loc}^{(3)}$) is directly proportional to $(\rho/\rho_o)^2$. Therefore, the local potential energy in the nuclear matter has the form:

$$V^{loc} = \frac{\alpha}{2}(\frac{\rho}{\rho_o}) + \frac{\beta}{\gamma+1}(\frac{\rho}{\rho_o})^2. \tag{2.28}$$

Table 2.1: The values of $\alpha(MeV)$, $\beta(MeV)$ and γ for different NEOS [18].

K(MeV)	$\alpha(MeV)$	$\beta(MeV)$	γ	NEOS
200	-356	303	1.17	Soft
380	-124	70.5	2	Hard

The free parameters α and β in the above potential can be determined by the condition that at normal nuclear matter density (ρ_o), the average binding energy (B.E) of nucleus should be -15.75 MeV and total energy should have a minima at ρ_o. The generalized form of above potential energy for different (in)compressibility factors can be written as:

$$V^{loc} = \frac{\alpha}{2}(\frac{\rho}{\rho_o}) + \frac{\beta}{\gamma+1}(\frac{\rho}{\rho_o})^{\gamma}. \tag{2.29}$$

The above equation of local interaction potential of the nuclear matter leads to various NEOS depending upon the different values of α, β and γ. The Skyrme potential of the NEOS contains two sets of parameter which yields same B. E. and saturation density but with two different (in)compressibility factors (K). The set of parameters for K = 200 MeV/nucleon (the one corresponds to soft NEOS) and for K = 380 MeV/nucleon (the hard NEOS) has been listed in Table 2.1. Therefore, the total Skyrme potential has the form:

$$V^{Skyrme} = \sum_{j;i\neq j} t_1\delta(\mathbf{r_i}-\mathbf{r_j}) + t_2\delta(\mathbf{r_i}-\mathbf{r_j})\rho^{\zeta-1}((\mathbf{r_i}+\mathbf{r_j})/2). \tag{2.30}$$

In addition to soft and hard NEOS, the other type of the NEOS e.g. super-stiff and super-soft NEOS with different values of parameters are also available in the literature. Despite this, as already discussed in Sec. 1.3 of chapter 1, the theoretical study established that hadronic matter is soft in nature [262, 263]. Therefore, in the present work, the simulations have been carried with soft NEOS.

The parameterized form of finite range Yukawa potential reads as [264]:

$$V_{ij}^{Yuk} = t_3\frac{exp\{-|\mathbf{r}_i-\mathbf{r}_j|\}/\mu}{|\mathbf{r}_i-\mathbf{r}_j|/\mu}. \tag{2.31}$$

Here, the value of t_3 is -6.66 MeV. This potential is short range in the IQMD model (with $\mu = 0.4$ fm) compared to QMD model (with $\mu = 1.5$ fm) where the Yukawa potential is long range. Yukawa potential reduces the fluctuation produced as a consequence of scarcity of pressure build up by the Fermi momentum and improves the surface properties.

Table 2.2: The values of $\alpha(MeV)$, $\beta(MeV)$ and γ for different momentum dependent NEOS [18].

K(MeV)	$\alpha(MeV)$	$\beta(MeV)$	γ	δ	ϵ	NEOS
200	-390	320	1.14	1.57	21.54	SMD
380	-130	59	2.09	1.57	21.54	HMD

The momentum dependent interaction potential (which is optional), includes additional repulsions among the projectile and target nucleons. The following equation describes the parameterized form of momentum dependence of real part of optical potential:

$$V_{ij}^{mdi} \;=\; t_4 ln^2[t_5(\vec{p_i}' - \vec{p_j})^2 + 1]\delta(\vec{r_i} - \vec{r_j}). \tag{2.32}$$

Here $t_4 = 1.57$ MeV and $t_5 = 5 \times 10^{-4}\ MeV^{-2}$ [265, 266]. The MDI readjusted the parameters of Skyrme potential to have some correction in the saturation nuclear matter density. However, the (in)compressibility factor (K) remains same. Hence, including MDI into calculations obtain new NEOS i.e. Soft Momentum Dependent (SMD) and Hard Momentum Dependent (HMD) NEOS. The parameters of SMD and HMD NEOS are listed in Table 2.2. The static NEOS in addition to MDI has the form:

$$U \;=\; \alpha\left(\frac{\rho}{\rho_0}\right) \;+\; \beta\left(\frac{\rho}{\rho_0}\right)^{\gamma} \;+\; \delta\cdot\ln^2\left(\epsilon\cdot(\Delta\vec{p})^2+1\right)\cdot\left(\frac{\rho}{\rho_0}\right). \tag{2.33}$$

The parameterized form of Coulomb potential is given by:

$$V_{ij}^{Coul} \;=\; \frac{Z_{eff}^2\ e^2}{|\mathbf{r}_i - \mathbf{r}_j|}. \tag{2.34}$$

Here Z_i and Z_j are the charge of i^{th} and j^{th} particle respectively. The Coulomb potential incorporates isospin degree of freedom by differentiating the neutrons and protons from their charge state i.e. 1 for proton and 0 for neutron. In contrast to IQMD, the QMD model only has effective charge (Z_{eff}) for all the hadrons without distinguishing between them.

Symmetry potential plays a vital role in the interaction of nuclear system with N $\neq$ Z i.e. isospin-asymmetric nuclear matter. The difference in energy per nucleon (E/A) between the isospin-symmetric nuclear matter (N = Z) and pure neutron matter is described as symmetry energy which is shown in Fig. 1.4 and discussed in Sec. 1.3 of chapter 1.

The density dependence of symmetry energy is given by the relation [267]:

$$E_{sym}(\rho) \;=\; E_{sym}(\rho_0)\left(\frac{\rho}{\rho_0}\right)^{\gamma}, \tag{2.35}$$

The value of symmetry energy at normal nuclear matter density (i.e. $E_{sym}(\rho_0)$) is 32 MeV. The stiffness (or strength) of symmetry energy at densities away from the normal nuclear matter density is described by the value of γ. The parameterized from of symmetry potential between protons and neutrons can be written as [268]:

$$V_{ij}^{sym} \;=\; t_6\frac{1}{\varrho_0}T_3^iT_3^j\delta(\vec{r_i}' - \vec{r_j}). \tag{2.36}$$

Here, the value of component t_6 is 100 MeV. T_{3i} and T_{3j} are defined as the isospin projection of particles i^{th} and j^{th}. The values of T_3 is +1/2 and -1/2 for protons and neutrons, respectively. As discussed in previous chapter, the IQMD model incorporate isospin degree of freedom through Coulomb interaction and symmetry potential. However, the remaining Skyrme, Yukawa and MDI potentials are isospin independent. The expectation value of the total Hamiltonian correspond to total binding energy of nucleus in its ground state. The comparison of the Bethe-Weizsäcker mass formula with total Hamiltonian represents that the MDI, kinetic energy as well as the Skyrme interactions contributes to the volume energy part. The Yukawa interaction corresponds to the surface as well as the volume energy. Whereas, the symmetry interactions corresponds to the volume symmetry energy. In the IQMD model, there is no term which corresponds to the pairing energy. Since the pairing energy represents the global property of the nucleus, hence it would be difficult to incorporate the pairing energy by microscopic local forces. Hence in the IQMD model, the total baryon-baryon potential described as:

$$\begin{aligned}
V_{ij} \;&=\; V_{ij}^{Skyrme} + V_{ij}^{Yukawa} + V_{ij}^{MDI} + V_{ij}^{Coul} + V_{ij}^{Sym} \\
&=\; \left(t_1\delta(\mathbf{r_i}-\mathbf{r_j}) + t_2\delta(\mathbf{r_i}-\mathbf{r_j})\rho^{\zeta-1}\left(\frac{\mathbf{r_i}+\mathbf{r_j}}{2}\right)\right) \\
&\quad + \; t_3\frac{exp(|\mathbf{r_i}-\mathbf{r_j}|/\mu)}{(|\mathbf{r_i}-\mathbf{r_j}|/\mu)} \\
&\quad + t_4\ln^2[t_5(\mathbf{p_i}-\mathbf{p_j})^2+1]\delta(\mathbf{r_i}-\mathbf{r_j}) \\
&\quad + \; \frac{Z_iZ_je^2}{|\mathbf{r_i}-\mathbf{r_j}|} \\
&\quad + t_6\frac{1}{\varrho_0}T_{3i}T_{3j}\delta(\mathbf{r_i}-\mathbf{r_j}).
\end{aligned} \tag{2.37}$$

The total baryon-baryon potential in the IQMD model is described as a sum of terms: A contact interaction of Skyrme-type (V_{ij}^{Skyrme}), a finite-range Yukawa term (V_{ij}^{Yukawa}), a momentum-dependent interaction (MDI) (V_{ij}^{MDI}), Coulomb interaction between the charged particles (V_{ij}^{Coul}) and a symmetry contact interaction that distinguishes between protons and neutrons (V_{ij}^{sym}).

2.3.3 Nucleon-nucleon collisions

The IQMD model incorporates, the collision term from the well-established *VUU-BUU* equations [269–271]. Similar to other cascade models, the nucleon-nucleon collisions are accomplished in a stochastic manner [218, 272]. The collision process in the QMD and IQMD model is different. The QMD model uses the Cugnon parametrization which do not take isospin into consideration. On the other hand, the IQMD model uses the VerWest and Arndt parameterizations [271]. However, the collisions are appraised in a similar manner as done in the QMD. The two nucleons are said to suffer binary collision with each other if the distance between the centroid of their Gaussian wave packets is fulfilled by the following requirement:

$$|\mathbf{r_i} - \mathbf{r_j}| \leq \sqrt{\frac{\sigma_{tot}}{\pi}}, \quad \sigma_{tot} = \sigma(\sqrt{s}, type). \tag{2.38}$$

The word "type" in the above equation denotes the incoming collision partners such as N-N, N-Δ, N-π. Here, $\sqrt{s}$ is the nucleon-nucleon center of mass energy given by:

$$\sqrt{s} = \sqrt{(E_i + E_j)^2 + (P_i + P_j)^2} \tag{2.39}$$

Here E_i (P_i) and E_j (P_j) are the energies (momenta) of i^{th} and j^{th} nucleon respectively. The term σ_{tot} in Eqn. 2.38 is the total cross-section which is the sum of elastic and inelastic cross-section is defined as,

$$\sigma^{tot} = \sigma^{el} + \sigma^{inel} = \sigma_{NN}^{el} + \sum_{channels} \sigma_i^{inel}. \tag{2.40}$$

In QMD model, the average nucleon-nucleon cross-section is used. Whereas, the IQMD model assimilate the parameterized free nn, np and pp cross-section. In inelastic reaction channels, in additions to nucleons and deltas, the pions are also formed through decay of delta resonances. The IQMD model take all inelastic channels explicitly in

account. The following inelastic channels constitute the imaginary part of the pion optical potential:

$$\begin{aligned} \text{(hard-delta production)} &\Rightarrow N\ N \rightarrow\ \Delta\ N \qquad (a), \\ \text{(delta decay)} &\Rightarrow \Delta \rightarrow\ N\ \pi \qquad (b), \\ \text{(delta absorption)} &\Rightarrow \Delta\ N \rightarrow\ N\ N \qquad (c), \\ \text{(soft-delta production)} &\Rightarrow N\ \pi \rightarrow\ \Delta \qquad (d). \end{aligned}$$

Elastic scattering between $\pi - \pi$, $\pi - N$, $\pi - \Delta$, $\Delta - \Delta$, $\Delta - N$ are not taken into account. For elastic nucleon-nucleon cross-section and the processes (a) and (d), experimental cross-sections are used [271]. The elastic cross-section is defined as:

$$\sigma_{NN}^{el} = \begin{cases} 55 \text{ (mb)}, & \text{if } \sqrt{s} < 1.8993 \\ \frac{35}{1+100(\sqrt{s}-1.8993)} + 20; & \text{if } \sqrt{s} \geq 1.8993 \end{cases} \tag{2.41}$$

The angular distribution for the elastically scattered nucleons is given by:

$$\frac{d\sigma_{NN}^{el}}{d\Omega} \sim exp[A(s) \cdot t] \tag{2.42}$$

where,

$$t = -2p^2(1 - cos\theta) \quad and \quad A(s) = 6\frac{[3.65(\sqrt{s} - 1.8766)]^6}{1 + [3.65(\sqrt{s} - 1.8766)]^6}, \tag{2.43}$$

with $\sqrt{s}$ in GeV and A(s) is given in $(GeV/c)^{-2}$. The inelastic channels are treated in an analogous fashion. The elastic nucleon-nucleon scattering angular distribution is same in both IQMD and QMD model. However, in the particle production (for inelastic scattering) the isospin degree of freedom through cross-section play an important role. The inelastic channels like ΔN $\rightarrow$ NN are not accessible experimentally. Therefore, these are calculated using modified detailed balance formula from their reverse reactions (here NN $\rightarrow$ Δ N) [273]. The inelastic scattering cross-section is parameterized as:

$$\sigma_{NN \rightarrow N\Delta}^{inel} = \begin{cases} 0, & \text{if } \sqrt{s} < 2.015 \\ \frac{20(\sqrt{s}-2.015)^2}{0.015+(\sqrt{s}-2.015)^2}; & \text{if } \sqrt{s} \geq 2.015 \end{cases} \tag{2.44}$$

The cross section for Δ absorption, i.e. channel (d) can be obtained from Eqn. 2.44 using detailed balance principle.

$$\sigma_{N\Delta \rightarrow NN} = \frac{1}{8}\left(\frac{p_f^2}{p_i^2}\right)\sigma_{NN \rightarrow N\Delta} \tag{2.45}$$

The angular distribution for inelastic channels is assumed to be isotropic. The parametrization suggested by Huber and Aichelin [237] is used where the fitted differential cross sections are extracted from One-Boson-Exchange (OBE) calculations:

$$\frac{d\sigma_{in}}{d\Omega} \approx a(s)exp\left[b(s)cos\theta\right]. \tag{2.46}$$

The $a(s)$ and $b(s)$ are defined as a functions of square-root of center of mass energy i.e. $\sqrt{s}$ and described in Table 2.3 for different intervals of $\sqrt{s}$. θ is the polar angle.

Table 2.3: Values of a(s) and b(s) for different intervals of $\sqrt{s}$.

$\acute{x} = \sqrt{s}\ (GeV)$	$a\ (fm)$	b
2.104 - 2.12	$294.6(\acute{x} - 2.014)^{2.578}$	$19.71(\acute{x} - 2.014)^{1.551}$
2.12 - 2.43	$\frac{0.01224}{(\acute{x}-2.225)^2 + 0.004112}$	$19.71(\acute{x} - 2.014)^{1.551}$
2.43 - 4.50	$\left(\frac{2.343}{\acute{x}}\right)^{43.17}$	$33.14\ arctan(0.5404(\acute{x} - 2.146)^{0.9784})$

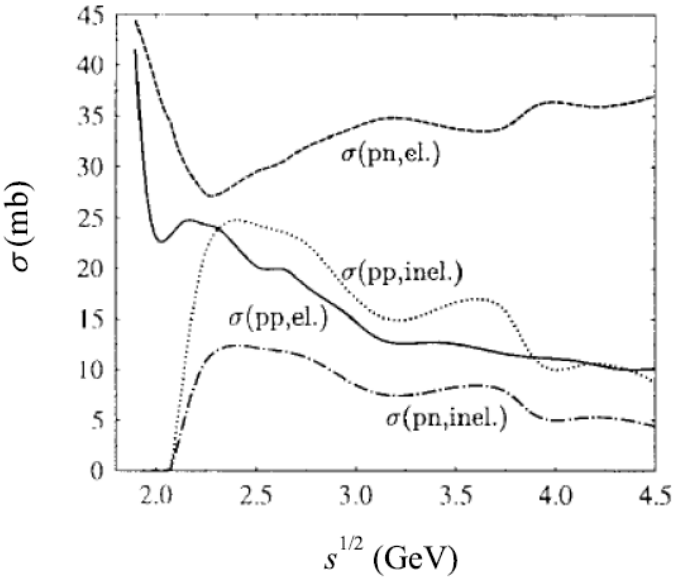

Figure 2.2: The elastic and inelastic cross sections for proton-proton (pp) and proton-neutron (pn) collisions in the IQMD model. The neutron-neutron cross section is assumed to be equal to proton-proton cross section. The total cross section is equal to the sum of the elastic and inelastic cross sections. The figure is taken from Ref. [94, 256, 257].

The limit on $\sqrt{s}$ in Eqn. 2.41 refers to the context that the total mass of two colliding nucleons (elastic scattering channels) is approximately equals to 1.876 GeV.

Accordingly, for two nucleons colliding with very small velocity, a constant cross-section of 55 mb is used. In Eqn. 2.44, the limit on $\sqrt{s}$ is 2.22 GeV corresponds to the formation of Δ in an inelastic scattering channel. Mass of Δ (= N + π) is 1.076 (= 0.938 + 0.138) GeV. Therefore, for NN→NΔ channel, the outgoing mass (N + Δ) will be equal to 2.22 (1.076 + 0.938)GeV.

The cross-section becomes isospin dependent due to the difference between the neutron-proton (np) and pp/nn interactions. Generally, the interaction cross-section of pp assumes to be equal to that of nn. In Fig. 2.2, the respective strength of free-space cross sections for np and pp/nn scattering is presented as a function of bombarding energy for elastic as well as inelastic channels. Due to transition matrices difference for the isospin T = 1 and T = 0, the cross-section of neutron-proton is always higher than the cross-section of the proton-proton or neutron-neutron. Moreover, both isospin-singlet as well as isospin-triplet channels contribute to np scattering. However, in the case of pp and nn, only isospin-singlet channel is involved. Therefore, in the IQMD model, neutron-proton cross-section is about a factor of two to three times larger that the proton-proton or neutron-neutron cross-section.

2.3.4 Pauli blocking

The Pauli blocking is an essential quantum feature to be included in the theory of nuclear reaction dynamics since the approch deal with the nucleons which are Fermion. Analogous to the propagation part of IQMD model, there exist no classical equivalent to the Pauli blocking. This can only be treated quantum mechanically but the proper inclusions of a quantum feature in a semi-classical approach is rather a difficult task. In the literature, two approaches are mentioned for this purpose. In first method, the Pauli potential has been introduced according to the short range repulsion between the near by nucleons in the phase-space. In the second method, the Pauli blocking has been included in transport model in a phenomenological manner [274, 275]. The basic idea of this approach is to prevent the overlapping of final phase-space of nucleons occupied after the collision. The first mentioned approach involves the origin of big and highly excited fragments which needs additional statistical calculations to get the exact fragmentation pattern. Therefore, the second approach is most favourable and used in the present study.

In this method, after each binary collision, the phase-space around the scattered partner is checked. If the phase-space of scattered partner is already occupied (fully or partialy) then the collision is said to be blocked. In a simple way, each nucleon is supposed to occupy a sphere in the spatial as well as momentum space and the overlapping of two phase-space spheres is prohibited in accordance to Pauli exclusion principle. This method obtain same Pauli blocking ratio as yields in the exact calculation of the overlapping of Gaussian wave packets of nucleons. The probability of blocked collision is written as:

$$P_{block} \; = \; 1 \; - \; \left[1 \; - min(P_1, 1)\right] \left[1 - \; min(P_2, 1)\right]. \tag{2.47}$$

Here, P_1 and P_2 are the fractions of final phase-spaces for each of the two scattering partners which is already occupied by other particles. In context to above equation, the probability of allowed collision is:

$$P_{allow} \; = \; 1 \; - \; \left[1 \; - min(P_1, 1)\right] \left[1 - \; min(P_2, 1)\right] = 1 \; - P_{block} \tag{2.48}$$

From Eqn. 2.47, the averaged blocking probability of collisions in a ground state nucleus (where all the collisions are blocked) is obtained to be $< P_{block} >= 0.96$ i.e. 96% collisions are blocked. However, for a complete blocking this factor should be one. Therefore, the Pauli blocking factor will be zero or one depending upon the occupancy of final phase-space. This sharp occupancy is valid only for the cold nuclear matter. Faessler *et al.* [244] have included the temperature by smearing the Fermi spheres for Pauli-operator. However, the effect of this exercise is very feeble on the dynamics and the temperature dependence of the Pauli-operator can be neglected.

Using all the above discussed formalisms of IQMD, the evolution of HICs can be followed. The IQMD model generates the phase-space of each nucleon from initial time to the freeze-out (saturation) time along with isospin, energy, number of collisions suffered by each nucleon, as well as the total and blocked collision in the reaction at each time steps as output. To identify the fragments in the final stage of reaction from the stored phase-space, one need clusterization algorithms. These algorithms are called secondary models or secondary algorithms.

2.4 Secondary algorithms

Among all the clusterization techniques available in the literature, the **Minimum Spanning Tree (MST) method** has been used most extensively to identify the clusters from the final phase-space of nucleons [18,276]. In this method, two nucleons are assumed to be part of same fragment if the distance between their centroids fulfil the requirement:

$$| \vec{r_i} - \vec{r_j} | \leq R_{clus}. \tag{2.49}$$

Here, $\vec{r_i}$ and $\vec{r_j}$ are the co-ordinates of i^{th} and j^{th} nucleon. The R_{clus} is the spatial constraint and its value can vary between 2 and 4 fm. In the present work the value spacial constraint is taken to be 4 fm. It has been reported that the different values of R_{clus} do not affect the fragmentation pattern at saturation time drastically. However, this algorithm optimize big fragment during the early stage of the reaction which decays into several types of fragments. This method is best to analyze asymptotic configurations where the fragmenting system can be viewed as a very dilute mixture of free particles.

The improved version of the **MST** algorithm includes additional momentum constraint and dubbed as **MSTM** (**Minimum Spanning Tree with Momentum constraint method**) [277]. It neglects those fragments which are close in the position (or co-ordinate space) and satisfies the Eqn. 2.49, but far in the momentum space. In this algorithm, for a nucleon to be the part of same fragment, firstly their co-ordinate position has to satisfy Eqn. 2.49 and then relative momentum should be less than P_{clus} i.e.

$$| \vec{p_i} - \vec{p_j} | \leq P_{clus}. \tag{2.50}$$

Here, $\vec{p_i}$ and $\vec{p_j}$ are the average momentum of i^{th} and j^{th} nucleon. The value of P_{clus} has been considered around the average Fermi momentum of nucleons as reported in [94, 256]. For QMD model, P_{clus} = 150 MeV/c and for IQMD it is 268.4 MeV/c.

These clusterization techniques identifies the phase-space of all fragments from the IQMD output and store them as another output in a sorted manner. Thus the properties of these fragments can be studied individually. Therefore, one can calculate various observable parameters of phenomenon such as multi-fragmentation, collective (or nuclear) flow and nuclear stopping arising in the HICs at intermediate energies.

Chapter 3

Influence of isospin dependent nuclear charge radii on fragmentation

3.1 Introduction

In the typical reaction dynamics of heavy-ion collision (HICs), the projectile and target nuclei collide with each other to form a compressed form of the nuclear matter. The condensed nuclear matter thus start expanding and the matter finally burst into multiple nucleonic fragments. The fragments are categorised as per their mass number and distinguished as FN's (free nucleons) [$A = 1$], LMF's (light mass fragments) [$2 \leq A \leq 4$], MMF's (medium mass fragments) [$5 \leq A \leq 9$], IMF's (intermediate mass fragments) [$5 \leq A \leq A_{tot}/6$] and HMF's (heavy mass fragments). The process of forming multiple fragments is called multi-fragmentation [278]. The purpose of studying the multi-fragmentation is to examine the susceptibility of condensed fermionic nuclear matter into clusters, to optimize the explosive properties of reaction, nuclear equation of state (NEOS) as well as the compressibility of the nuclear matter. The size and number of fragments formed in a particular reaction depends upon the density of compression zone which further depends upon various reaction conditions. Density of fragmenting system is one of the observable linked with the compression and expansion of the nuclear matter. The average nucleonic density is calculated as [18]:

$$< \rho/\rho_o >= \Big\langle \frac{1}{A_T + A_P} \sum_{i=1}^{A_T+A_P} \sum_{j=1}^{A_T+A_P} \frac{1}{(2\pi L)^{3/2}} exp[-(\vec{r_i} - \vec{r_j})^2/2L] \Big\rangle, \qquad (3.1)$$

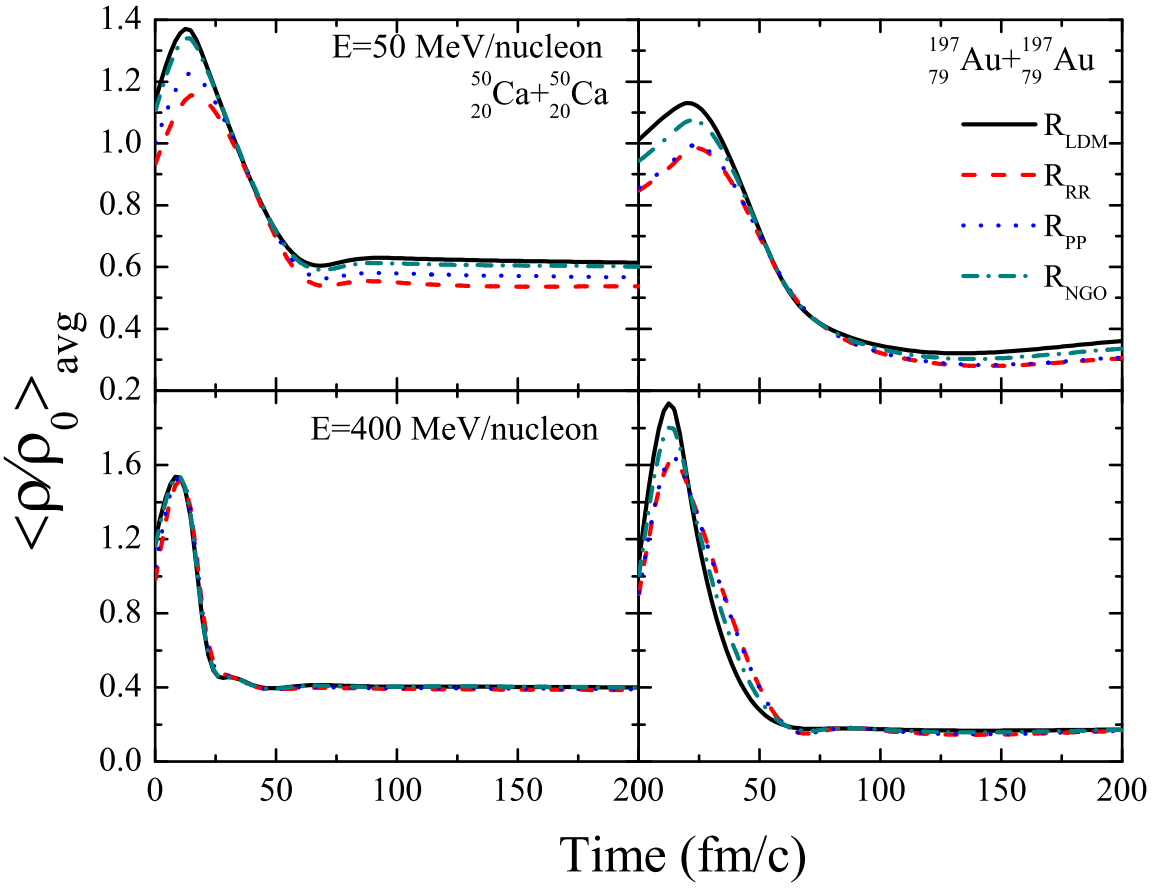

Figure 3.1: Time evolution of average nucleonic density for the reactions of $^{50}_{20}Ca+^{50}_{20}Ca$ (left panels) and $^{197}_{79}Au+^{197}_{79}Au$ (right panels) for central collisions at E = 50 MeV/nucleon (upper panels) and E = 400 MeV/nucleon (lower panels).

where $\vec{r_i}$ and $\vec{r_j}$ are the position coordinates of i^{th} and j^{th} nucleons respectively and L is the Gaussian width of the wave packets. A_T and A_P are mass of target and projectile nuclei respectively. The simulations have been performed for the reactions of $^{50}_{20}$Ca+$^{50}_{20}$Ca and $^{197}_{79}$Au+$^{197}_{79}$Au having $N/Z = 1.5$ at incident energies of 50 and 400 MeV/nucleon for central collisions. In this chapter, all the reactions are simulated within the framework of Isospin dependent Quantum Molecular Dynamics (IQMD) model. A soft equation of state along with isospin dependent nucleon-nucleon cross-section reduced by 10% i.e. $\sigma = 0.9\sigma_{NN}^{free}$ has been implemented. Calculations are performed for three different isospin dependent nuclear charge radii parameterizations as well as for liquid drop model (LDM) radius. Simulations have been carried out by keeping the Fermi momentum of the nucleons same for each parameterizations of nuclear charge radius.

Fig.3.1 displays the time evolution of average nucleonic density at incident energies of 50 (upper panels) and 400 MeV/nucleon (lower panels) for the reactions of $^{50}_{20}$Ca+$^{50}_{20}$Ca (left panels) and $^{197}_{79}$Au+$^{197}_{79}$Au (right panels) for different parameterizations of nuclear charge radii (i.e. R_{LDM}, R_{NGO}, R_{PP} and R_{RR}). It can be noted that, due to different formalization, the calculated charge radii (of particular nuclei) is more with isospin dependent parameterized form (because of difference in the density distribution of neutrons and protons in the nuclear charge radius) compared to isospin independent parameterized form. The change in the nuclear charge radii is observed to be 1.7% (R_{NGO}), 7.6% (R_{PP}) and 12% (R_{RR}) for $^{50}_{20}$Ca nucleus and 3.2% (R_{NGO}), 7.6% (R_{PP}) and 8% (R_{RR}) for $^{197}_{79}$Au nucleus with respect to R_{LDM}. One can see that maximal average nucleonic density tends to reduce with isospin dependent nuclear charge radii. This is due to the reduction in the density of nucleons inside the nucleus during initialization. However, the initialization effects on density, decreases at 400 MeV/nucleon for lighter colliding nuclei only. This happen because for head-on collisions and with increase in incident energy, correlation between nucleons get destroyed.

Due to 12% change in the radius of $^{50}_{20}$Ca nucleus, 15% change in the maximal average nucleonic density has been observed for the reaction of $^{50}_{20}$Ca+$^{50}_{20}$Ca whereas, 14% change has been observed for the reaction of $^{197}_{79}$Au+$^{197}_{79}$Au, due to 8% change in the radius of $^{197}_{79}$Au nucleus at an incident energy of 50 MeV/nucleon. However, this change in the maximal average nucleonic density become 4% for $^{50}_{20}$Ca+$^{50}_{20}$Ca system and 14% for $^{197}_{79}$Au+$^{197}_{79}$Au system at an incident energy of 400 MeV/nucleon. The ratio of change in the maximal nucleonic density to the change in radius is more for heavier colliding nuclei (i.e. $^{197}_{79}$Au+$^{197}_{79}$Au) compared to lighter one (i.e. $^{50}_{20}$Ca+$^{50}_{20}$Ca). It is evident that the heavier system is more sensitive to the initialization effects (via nucleus charge radii) compared to lighter system (having same $N/Z = 1.5$). Moreover, the percentage change in the maximal average nucleonic density diminishes with increase in incident energy for lighter colliding pairs only and remains nearly constant for heavier colliding pairs. The percentage change of results are calculated for R_{RR} radius parameterization only, with respect to R_{LDM}, because of the maximum change in the calculated nuclear charge radii.

3.2 Results and discussion

As, the nuclear density is being affected by different nuclear charge radii parameterizations, so the compression in the condensed nuclear matter and nucleon-nucleon collision will also be affected. Therefore, in this section, the initialization effects via nuclear charge radii on fragmentation for a wide range of system mass and initial N/Z ratio has been studied taking isospin-asymmetric nuclear reactions [279]. All the reactions in this section has been studied at E = 50 MeV/nucleon as the influence of radius is more at this incident energy on maximal average nucleonic density (concluded from Fig. 3.1)

3.2.1 Collision rate of nuclear reaction

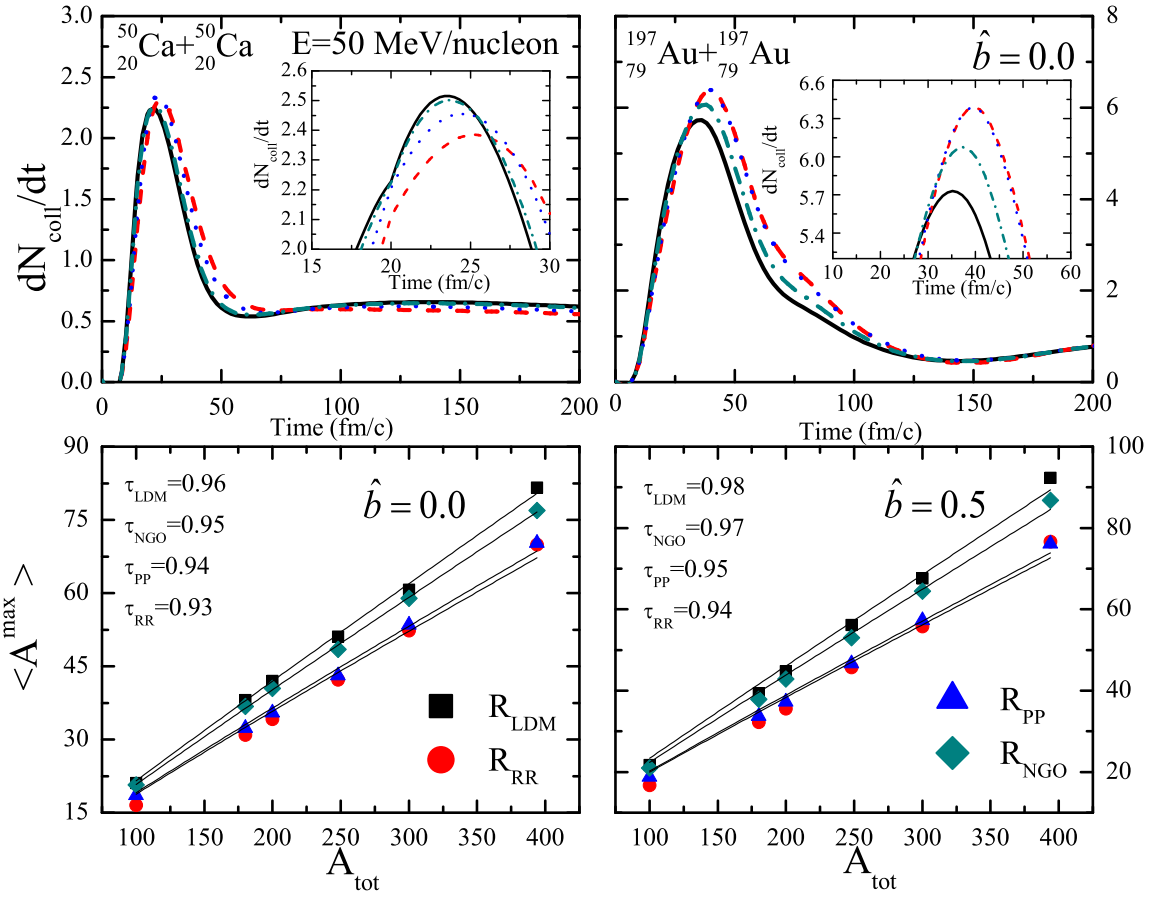

Figure 3.2: Upper panels displays the rate of nucleon-nucleon binary collisions for the reactions of $^{50}_{20}$Ca+$^{50}_{20}$Ca (upper left panel) and $^{197}_{79}$Au+$^{197}_{79}$Au (upper right panel) at $\hat{b} = 0$. Lower panels displays the average mass of the largest fragment (A^{max}) as a function of composite mass (A_{tot}) at 200 fm/c for central (lower left panel) and semi-central (lower right panel) collisions.

Rate of binary collisions is the another important quantity related with initial compression of the nuclear matter. In the upper panels of Fig.3.2, the rate of binary collisions for the reactions of $^{50}_{20}$Ca+$^{50}_{20}$Ca (upper left panel) and $^{197}_{79}$Au+$^{197}_{79}$Au (upper right panel) at an incident energy of 50 MeV/nucleon have been displayed. Different lines in the figure corresponds to the different parameterizations of nuclear charge radii as in Fig.3.1 and the calculations for the comparison of results due to different radii forms has been done for R_{RR} with respect to R_{LDM}. It has been observed that due to 12% change in the radius there is a 5% change in the peak value of nucleon-nucleon binary collisions for the reaction of $^{50}_{20}$Ca+$^{50}_{20}$Ca, whereas this change is 12% for $^{197}_{79}$Au+$^{197}_{79}$Au due to 8% change in the radius. This is because, the same number of nucleons of a particular nuclei are simulated in a sphere of larger radii compared to R_{LDM} and the initialized particles are far apart from each other. Also, it is worth to notice that there is a reduction in the peak value of dN_{coll}/dt for $^{50}_{20}$Ca+$^{50}_{20}$Ca and on the contrary for $^{197}_{79}$Au+$^{197}_{79}$Au, increment has been observed. This may be because of different density distribution of nucleons in lighter and heavier colliding nuclei. Also the peak of dN_{coll}/dt has been shifted towards right (i.e. higher time values), that means for isospin dependent radii parameterizations (or as the radius increases), the system will take more time to saturate. Therefore due to change in the geometry of nucleus, the correlation between nn, pp and np collisions has been affected. Hence, it has been concluded that the effect of initialization via nuclear charge radius on collision dynamics is more for $^{197}_{79}$Au+$^{197}_{79}$Au system compared to $^{50}_{20}$Ca+$^{50}_{20}$Ca system.

3.2.2 System size effects on final state fragment multiplicities

To study the role of structural effects more precisely for the wide mass range of periodic table, the simulations have been carried out for the reactions of $^{50}_{20}$Ca+$^{50}_{20}$Ca, $^{90}_{36}$Kr+$^{90}_{36}$Kr, $^{100}_{40}$Zr+$^{100}_{40}$Zr, $^{124}_{50}$Sn+$^{124}_{50}$Sn, $^{150}_{60}$Nd+$^{150}_{60}$Nd and $^{197}_{79}$Au+$^{197}_{79}$Au at an incident energy of 50 MeV/nucleon. The system size effects are studied by keeping the neutron to proton ratio same for all reactions (i.e. $N/Z = 1.5$). The reactions are followed till 200 fm/c and clusters are identified with the minimum spanning tree (MST) [18, 276] method using clustering radius of 4.0 fm. The lower panels of Fig. 3.2 displays the variation of A^{max} (mass of largest fragment formed at 200 fm/c) as a function of composite mass of

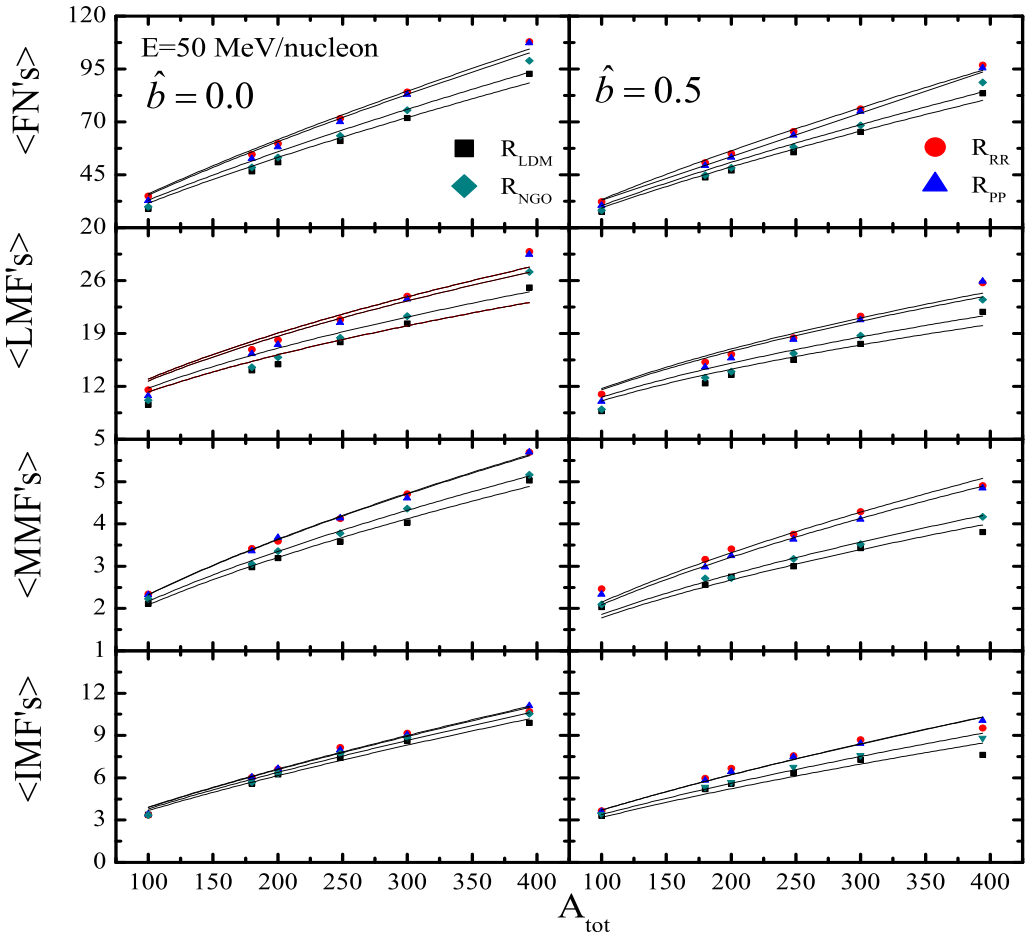

Figure 3.3: The mean multiplicity of FN's, LMF's, MMF's and IMF's as a function of total mass of the system (A_{tot}) at 200 fm/c for central collisions (left panels) and semi-central collision (right panels).

the system i.e. A_{tot} (where, $A_{tot} = A_T + A_P$) at scaled impact parameter, $\hat{b} = b/b_{max} = 0$ (lower left panel) and 0.5 (lower right panel) (where $b_{max} = (R_P + R_T)fm$, R_P and R_T are radii of target and projectile nuclei) at an incident energy of 50 MeV/nucleon. One can see that, A^{max} tends to increase with increase in A_{tot} for R_{LDM} and same trend is followed by isospin dependent radii parameterizations. It has been observed that, due to increase in number of collisions for isospin dependent radii parameterizations (as concluded from upper panels of Fig. 3.2), the mass of the largest fragment is less. It is clear from the figure that the role of isospin dependent nuclear charge radii parameterizations on the production of largest fragment increases as the composite mass of the system increases.

Table 3.1: The value of exponent τ for different fragments and for different radii parameterizations at $\hat{b} = 0.0$ and $\hat{b} = 0.5$

	$\hat{b} = 0.0$				$\hat{b} = 0.5$			
	τ_{LDM}	τ_{NGO}	τ_{PP}	τ_{RR}	τ_{LDM}	τ_{NGO}	τ_{PP}	τ_{RR}
FN's	0.74	0.75	0.77	0.78	0.73	0.74	0.75	0.76
LMF's	0.52	0.53	0.55	0.56	0.50	0.51	0.53	0.53
MMF's	0.62	0.63	0.64	0.64	0.58	0.59	0.62	0.63
IMF's	0.74	0.75	0.76	0.76	0.71	0.72	0.74	0.75

The system mass dependence of A^{max} has been fitted by a power law behaviour for all parameterized forms of nuclear charge radii as:

$$A^{max} = C(A_{tot}^{\tau}) \tag{3.2}$$

In figure, the different solid symbols represent the theoretical calculations with different nuclear charge radii parameterizations and lines represent the power law fit as per Eqn. 3.2. The values of exponent τ tends to decrease with increase in radii and is least for R_{RR}. It is to notify that, the difference between τ values (presented in Fig. 3.2) of R_{RR} and R_{LDM} is more at $\hat{b} = 0.5$ compared to $\hat{b} = 0$. These observations suggested that, the role of isospin dependent nuclear charge radii parameterizations is dominating at higher colliding geometries.

Further to study the influence of isospin dependent nuclear charge radii on various fragment's mean multiplicity for the wide mass range of periodic table, the simulations have been carried out for the similar set of reactions as in the lower panels of Fig.3.2. Fig.3.3 displays the mean multiplicity of FN's, LMF's , MMF's and IMF's as a function of A_{tot} at an incident energy of 50 MeV/nucleon for central (left panels) and semi-central collisions (right panels). The symbols have the same meaning as in lower panels of Fig.3.2. It has been observed that the isospin dependent parameterizations enhance the mean multiplicity of FN's and other fragments. This is due to increase in nucleon-nucleon binary collisions for the isospin dependent nuclear charge radii parameterizations. The solid lines represent the power law fit of kind: $\propto (A_{tot}^{\tau})$ to the mean multiplicity of FN's and fragments.

The values of exponent τ obtained from Fig. 3.3 are listed in Table 3.1. One can see that τ increases for isospin dependent nuclear charge radii parameterizations and is highest for R_{RR}. This observation is true for all fragments and FN's , but the change in proportion from τ_{LDM} to τ_{RR} vary for different fragments. Moreover, the change in the values of τ_{LDM} and τ_{RR} is more at $\hat{b} = 0.5$ compared to $\hat{b} = 0.0$ for the case of MMF's and IMF's. Whereas, this difference remains almost same for the case of FN's and LMF's. This is because, the production of MMF's and IMF's is affected more by the geometry of collision compared to FN's and LMF's.

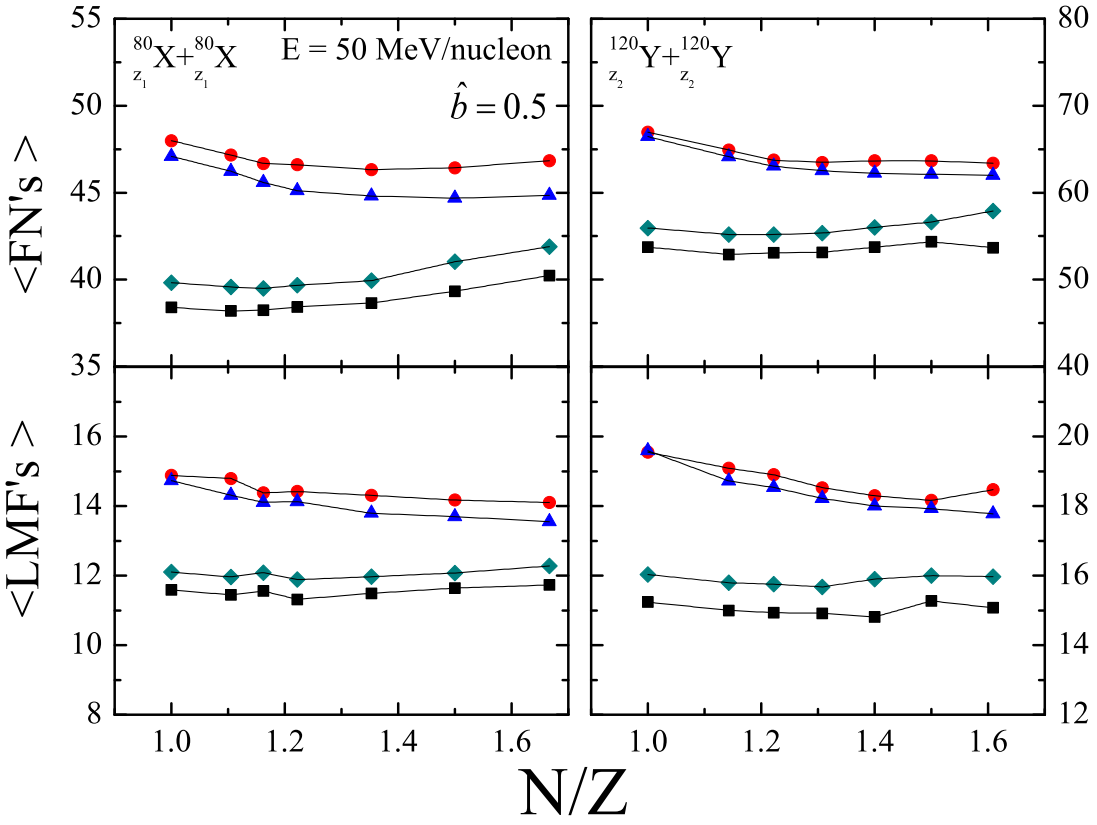

Figure 3.4: N/Z dependence of multiplicity of FN's (upper panels) and LMF's (lower panels) at incident energy of 50 MeV/nucleon for semi-central collisions for two isobaric series with mass 80 (left panels) and 120 (right panels) units.

3.2.3 Isospin effects on multiplicity of fragments

Till now, the initialization effects via nuclear charge radii has been studied for a fixed value of neutron to proton ratio (i.e. $N/Z = 1.5$). Therefore in the next step, to elucidate

the role of isospin dependent nuclear charge radii parameterizations the mean multiplicity of FN's and LMF's has been examined for isospin-asymmetric reactions by keeping the mass of colliding nuclei same. Fig. 3.4 displays the effect of initialization on the N/Z dependence of multiplicity of FN's (upper panels) and LMF's (lower panels). For this, the two set of isobaric series of reactions have been simulated at scaled impact parameter of $\hat{b} = 0.5$ and incident energy of 50 MeV/nucleon. It has been observed from Ref. [280] that the isospin effect has a significant role at semi-peripheral collisions for the reaction. The left panels of this figure presents the calculations for the reaction series of $^{80}_{z_1}\mathrm{X}+^{80}_{z_1}\mathrm{X}$ (having total mass number = 160 a.m.u. with charge, z_1 = 30, 32, 34, 36, 37, 38 and 40) whereas the right panels presents calculations for the reaction series of $^{120}_{z_2}\mathrm{Y}+^{120}_{z_2}\mathrm{Y}$ (having total mass number = 240 a.m.u. with charge, z_2 = 46, 48, 50, 52, 54, 56 and 60). Symbols in Fig. 3.4 have the same meaning as in Fig.3.2 and points are connected with the solid lines to guide the eye. It is worth to notice that, the radius of isobaric nuclei is same according to isospin independent nuclear charge radii parametrization but varies for isospin dependent parameterizations because of change in neutron to proton ratio (N/Z) which affects the dependence of multiplicity on N/Z. For R_{LDM}, very weak dependence of multiplicity on N/Z has been observed and the minimum value of multiplicity has been observed at $N = Z$ in the case of FN's. But it is nearly constant for LMF's. These observations are in agreement with the observations in Ref. [120]. The similar trend has been observed for R_{NGO} with minor enhancement in the multiplicity because change in the values of radius calculated via R_{NGO} and R_{LDM} is very less and are comparable. But the scenario is different for the case of R_{PP} and R_{RR}, the multiplicity of FN's, firstly decreases with increase in N/Z and then becomes constant as N/Z increases beyond 1.5. Moreover, the multiplicity of LMF's is not independent to isospin-asymmetry of colliding nuclei, it decreases with increase in N/Z due to isospin dependent nuclear charge radii. The N/Z dependence of the multiplicity of MMF's and IMF's has also been checked (results not shown here). It has been observed that their behavior is found to be independent to initial neutron-to-proton ratio of the system for isospin dependent and independent nuclear charge radii parameterizations at incident energy of 50 MeV/nucleon. This is because at lower incident energies, the nuclear matter does not break into smaller pieces, only heavy mass fragments are produced [281]. Here, the emission of free nucleons is due

to thermal emission of excited fragments. The production of LMF's show small variation because at low energies the participant zone is not much excited. Therefore it results in small variation in the production of these fragments with increase in N/Z for isospin dependent nuclear charge radii parameterizations.

3.3 Comparison with ALADIN experimental data on IMF's multiplicity

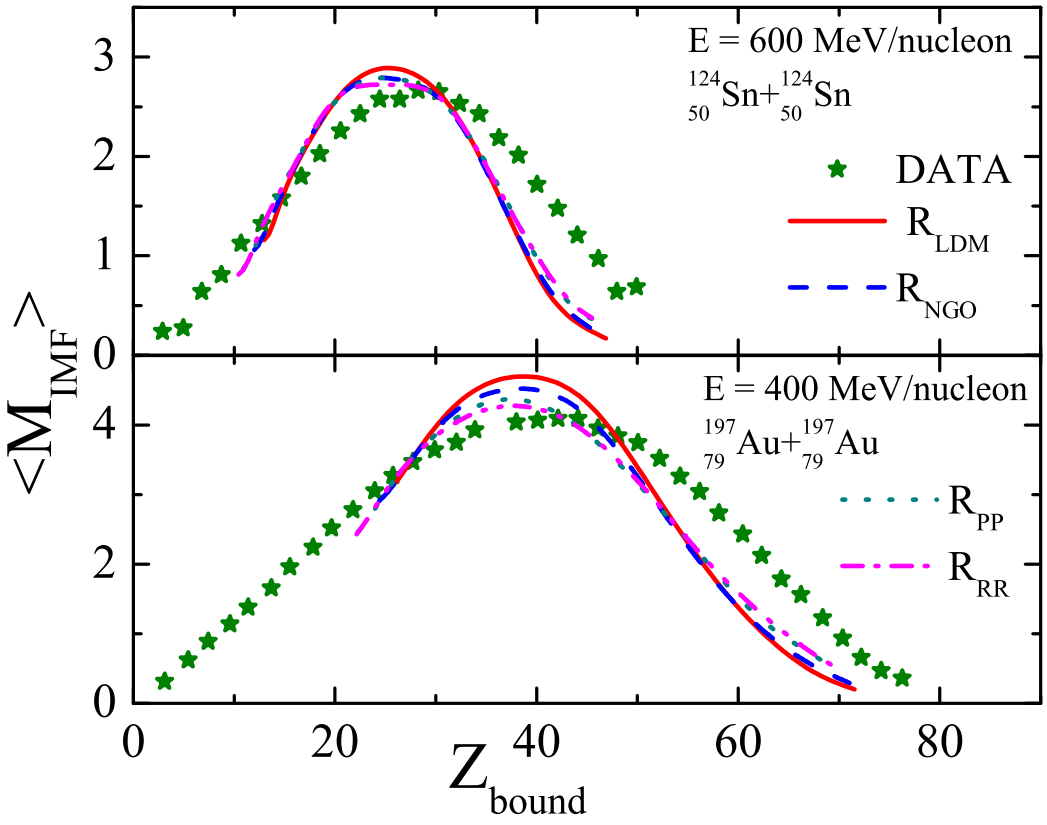

Figure 3.5: The average multiplicity of IMF (M_{IMF}) as a function of Z_{bound} for the reactions of $^{124}_{50}Sn+^{124}_{50}Sn$ at 600 MeV/nucleon (top panels) and $^{197}_{79}Au+^{197}_{79}Au$ at 400 MeV/nucleon (bottom panels) at 200 fm/c Comparison has been made with experimental data of ALADIN Collaboration [128, 282].

To further strengthen our interpretation of results, the multiplicity of IMF's as a function of Z_{bound} for the reaction of $^{124}_{50}$Sn+$^{124}_{50}$Sn at 600 MeV/nucleon and $^{197}_{79}Au+^{197}_{79}$Au at 400 MeV/nucleon is presented in Fig. 3.5. Here, Z_{bound} is defined as the sum of the atomic numbers Z_i of all fragments with $Z_i > 2$. The symbol (star) represents the experimental

data [128, 282] and different colored lines corresponds to different parameterizations of nuclear charge radii (as in Fig. 3.1). The rise and fall in the multi-fragmentation emission has been observed. The small value of Z_{bound} corresponds to central collisions and due to violent phase of collisions most of the nuclear matter emitted as FN's and LMF's (fall of multi-fragmentation). At large value of Z_{bound} i.e. at semi central collisions, the multiplicity of IMF's shows a peak because most of the spectator part does not participate in the collision and large number of IMFs are produced. At peripheral collisions i.e. very large Z_{bound}, there is again fall in the formation of number of IMF's. Peripheral collisions may lead to spallation process in which only a single heavy fragment is produced. It has been observed from this figure that with increase in nuclear charge radius (i.e. for isospin dependent nuclear charge radii parameterizations), the multiplicity of IMF's decreases (at E = 400 and 600 MeV/nucleon); however, it is observed to be increase at E = 50 MeV/nucleon (in Fig. 3.3). This is because, as the incident energy increases, for larger radii, the IMF's (in addition to heaviest fragment) also splits and undergo secondary decay to produced more smaller fragments (like FN's and LMF's). One can see that the isospin dependent nuclear charge radii further reduce the gap between the theoretical calculations and the experimental findings and this effect is more in semi-central collisions.

3.4 Summary

In summary, the influence of isospin dependent nuclear charge radii parameterizations on the fragmentation using IQMD model has been studied. Due to inclusion of isospin parameter (I) in the nuclear charge radii parameterizations, a significant role on fragmentation has been observed. The calculations conclude that with increase in radius, the density of compressed nuclear matter decreases. With larger nuclear radius, the colliding system takes more time to saturate. The increase in radius leads to production of more fragments and decreases the mass of largest fragment. The multiplicity of FNs and LMFs is observed to be dependent upon the initial N/Z ratio of colliding nuclei only for R_{PP} and R_{RR}. Moreover, our calculations with the R_{RR} radii parametrization are able to reproduce the experimental data of ALADIN Collaboration better than R_{LDM}.

Chapter 4

Structural and isospin effects on collective flow

4.1 Introduction

The pressure gradient developed during collisions, pushes the nuclear matter away from the interacting region and towards the transverse direction which is basically the azimuthal distribution of particles [283]. If two nuclei are approaching towards each other parallel to the Z-axis and impact parameter is parallel to the X-axis, then the X-Z plane is the reaction plane and X-Y plane is the azimuthal plane, which describes the azimuthal distribution of particles. Let ϕ be the azimuthal angle between the trajectory of outgoing particles and the reaction plane such that the distribution of particles in the azimuthal plane can be represented by Fourier expansion [284], reads as:

$$\frac{dN}{d\phi} \propto 1 + 2\sum_{n=1}^{\infty} v_n Cos(n\phi). \tag{4.1}$$

The flow parameter v_n is called n^{th} harmonic function or Fourier coefficient of Fourier expansion where, n = 1, 2, 3..... and so on. The first two harmonics, v_1 and v_2 are the directed flow and elliptical flow respectively. The parameter of directed flow is further expressed as the ratio of transverse momentum gained by the emitted particle, i.e. p_x (along the impact parameter direction) to the mean transverse momentum (p_t) given by, $p_t = \sqrt{p_x^2 + p_y^2}$ where, p_x and p_y are the x and y components of momentum. The directed flow is defined as:

$$v_1 \;=\; < Cos\phi > \;=\; \langle \frac{p_x}{p_t} \rangle. \tag{4.2}$$

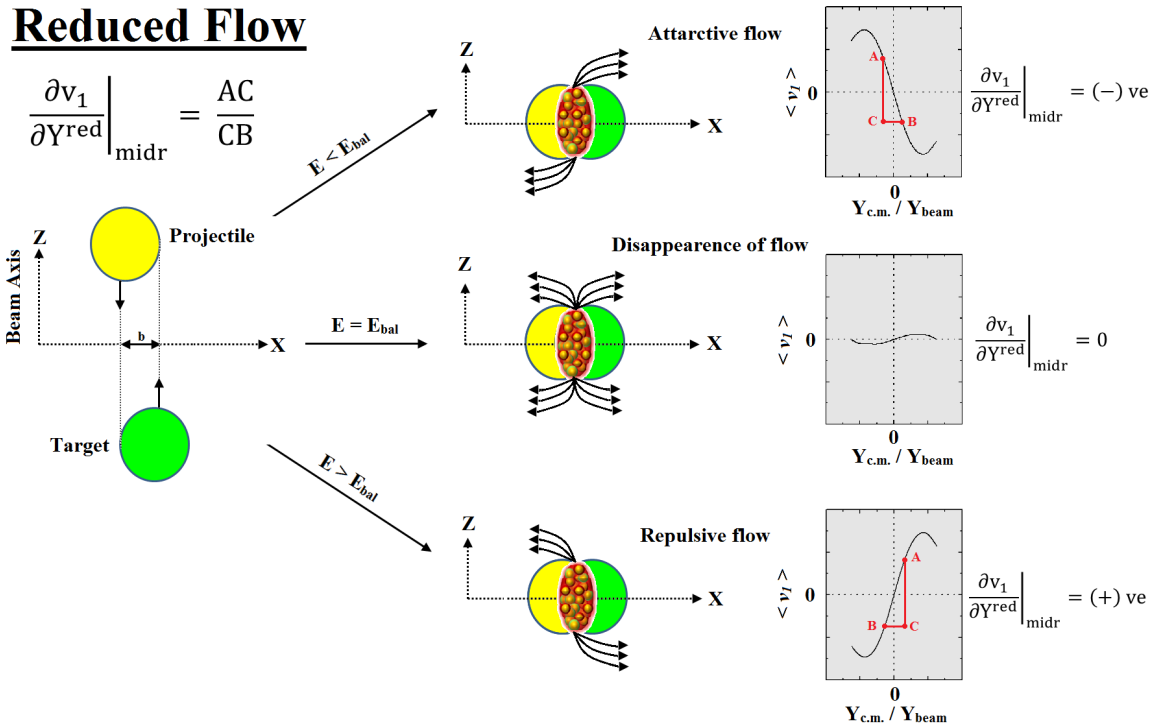

Figure 4.1: Pictorial view of reduced flow below, at and above balance energy. Figure is modified from Ref. [147]

The nucleonic flow basically arises from the most compressed zone of the system, i.e. participant zone, which measure the total momentum transfer in the collision process. This compressed nuclear matter lies in the mid-rapidity region. The rapidity is defined as $Y^{red} = Y_{c.m.}/Y_{beam}$, and $Y_{c.m.}$ is further defined as:

$$Y_{c.m.} = \frac{1}{2} ln \frac{E(i) + p_z(i)c}{E(i) - p_z(i)c}. \tag{4.3}$$

Here, $E(i)$ and $p_z(i)$ are the total energy and longitudinal momentum of i^{th} particle. The region (-0.1$\leq Y_{c.m.}/Y_{beam} \leq$0.1) is stated as mid-rapidity region and the region beyond the mid-rapidity corresponds to spectator matter regions. The study of rapidity distribution of azimuthal anisotropy of particles reveals important information about collective flow. The slope parameter around mid-rapidity obtained by plotting v_1 as a function of rapidity, measures the strength of directed flow called *reduced flow* and represented as: $\frac{\partial v_1}{\partial Y^{red}}$ [285]. The magnitude of reduced flow is negative at low incident energies and positive at relatively high incident energies [286]. The balance energy (E_{bal}) is the incident energy where attractive mean field and repulsive nucleon-nucleon collisions counterbalance each other and $\frac{\partial v_1}{\partial Y^{red}}$=0. The demonstration of reduced flow is presented in Fig. 4.1 below, at and above balance energy.

The second harmonic, v_2 can be written as [148, 287]:

$$v_2 \;=\; < Cos2\phi > \;=\; \langle \frac{p_x^2 - p_y^2}{p_t^2} \rangle. \tag{4.4}$$

The elliptical flow represents the ellipse like distribution of emitted particles in the reaction plane [288–290]. The change in the sign of elliptical flow from positive to negative value with increase in incident energy, represents the transition from in-plane to out-of-plane emission of particles. The energy at which this transition occurs is dubbed as transition energy (E_{trans}) signifying isotropic distribution of particles with zero values of v_2 [176, 291]. At E_{trans}, strength of expanding nuclear matter equalizes the impact of rotational behaviour of spectator matter. The Fig. 4.2 represents the schematic view of elliptical flow below, at and above transition energy.

So far, the studies have been made to give a comparative description of the dependence of elliptical flow on the transverse momentum, reduced rapidity, incident energy, mass of fragments as well as colliding geometry for different types of colliding systems, experimentally as well as through various theoretical models in the intermediate energy

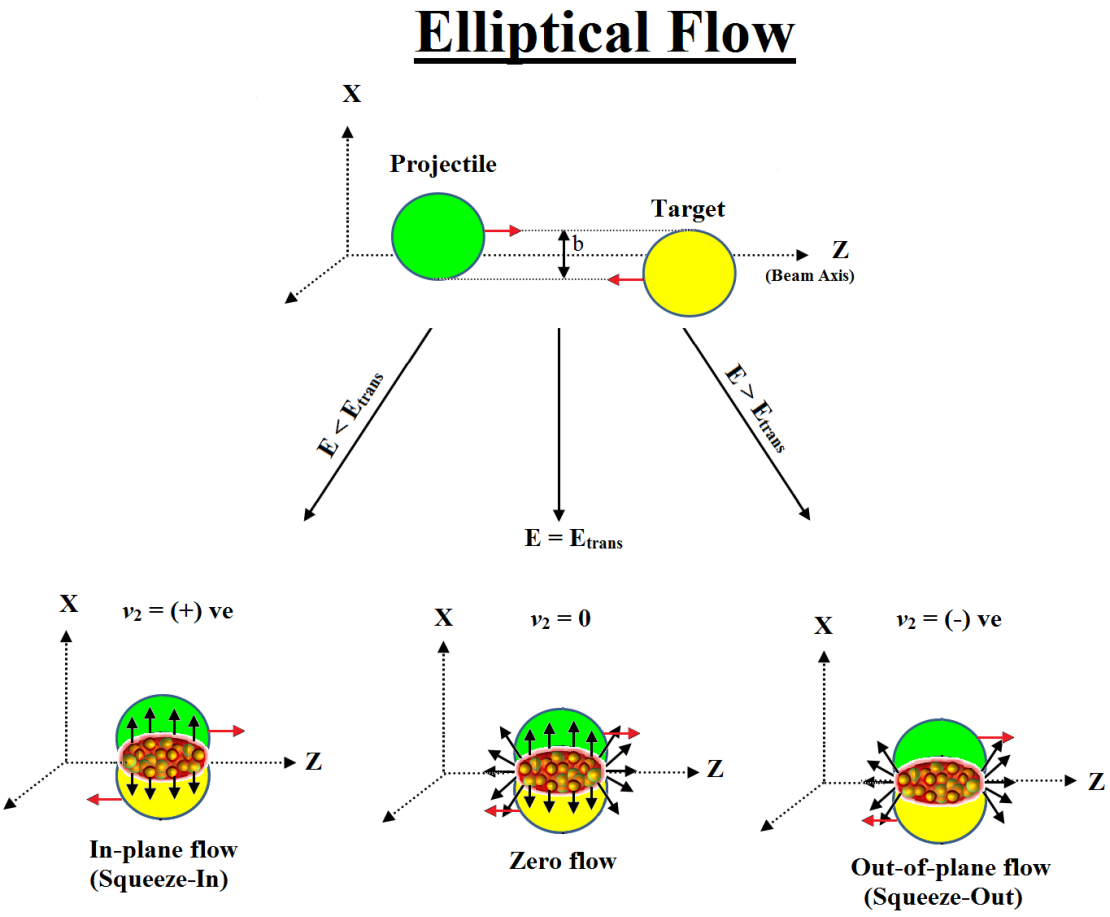

Figure 4.2: Pictorial view of elliptical flow below, at and above transition energy. Figure is reproduced from Ref. [147].

regime [174,292–294]. The study of E_{bal} and E_{trans} has attained a special interest because of its dependence upon various physical observables like composite mass of colliding system, impact parameter, mass-asymmetry and charge asymmetry of the reactions. Both the energies are also sensitive towards various isospin dependent model ingredients e.g. in-medium and isospin-dependent nucleon-nucleon cross-section, nuclear equation of state (NEOS), symmetry energy and its various density dependent forms as well as Coulomb potential [295–301]. Therefore, both reduced flow and elliptical flow are proven to be good probes to investigate the isospin physics in the HICs.

Therefore structural and isospin effects have been studied through isospin dependent and independent nuclear charge radii parameterizations on the collective flow within the framework of Isospin-dependent Quantum Molecular Dynamics (IQMD) model [304]. The calculations have been carried out by using two different approaches: (i) for the reaction series having fixed N/Z ratio and (ii) for the isobaric reaction series with different N/Z ratio.

4.2 Neutron and proton density profile

To check the stability of nucleus with different radii parameterizations (R_{LDM}, R_{NGO}, R_{PP} and R_{RR}), Fig. 4.3 display, the neutron density $\rho_n(r)$ (left panels) and proton density $\rho_p(r)$ (right panels) profile of isospin symmetric (or neutron-deficient) $^{80}_{40}$Zr ($N/Z = 1.0$) (upper panels) and isospin asymmetric (or neutron-rich) $^{80}_{29}$Cu ($N/Z = 1.8$) (lower panels) nuclei initialized with four different nuclear charge radii parameterizations. The sampling of neutrons and protons is different for different nuclear charge radii parameterizations. The figure reveals that, for $^{80}_{40}$Zr nucleus, the neutron as well as the proton density profile are identical, which reveals that, both the neutrons and protons are symmetrically distributed in the phase-space sphere. This observation holds true for all radii parameterizations. Moreover, the increase in radii affects the $\rho_n(r)$ and $\rho_p(r)$ equally. However, for $^{80}_{29}$Cu nucleus, $\rho_n(r)$ is greater than $\rho_p(r)$ by a factor of 1.8 (for all radii forms). This is because the number of neutrons is more than the number of protons by same factor i.e. $N/Z = 1.8$. The influence of increase in radius on $\rho_n(r)$ is more as compared to $\rho_p(r)$. The distribution of neutrons and protons inside the Fermi sphere of isospin independent as well as dependent radii parameterizations is uniform. The total density ($\rho(r) = \rho_n(r) + \rho_p(r)$)

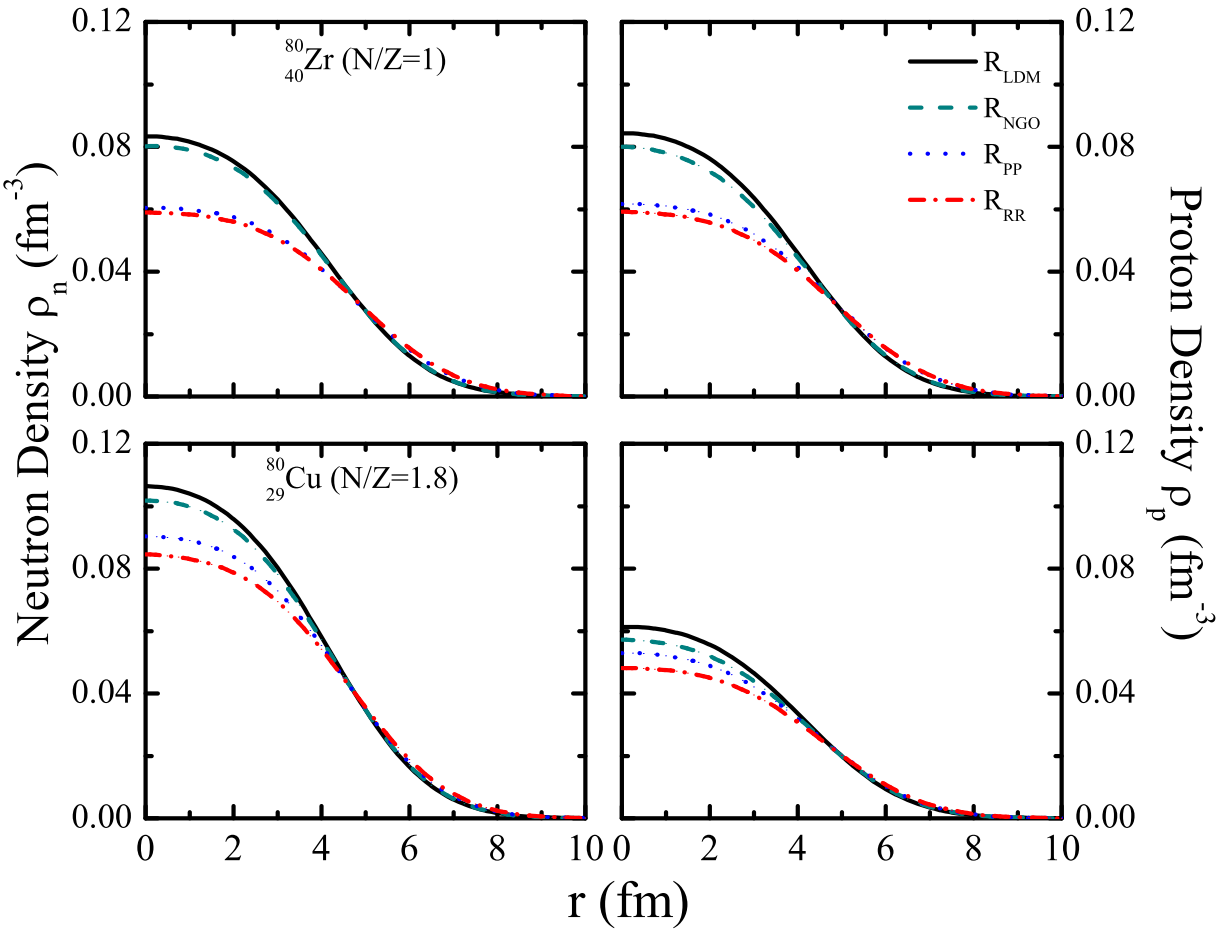

Figure 4.3: The neutron density profile $\rho_n(r)$ (left panels) and proton density profile $\rho_p(r)$ (right panels) for $^{80}_{40}$Zr (upper panels) and $^{80}_{29}$Cu (lower panels) nucleus initialized in the IQMD with four different radii parameterizations at time t = 0 fm/c.

of $^{80}_{40}$Zr and $^{80}_{29}$Cu nuclei are same for R_{LDM} and different for isospin dependent nuclear charge radii parameterizations. Therefore, for isospin dependent radii parameterizations, neutron-rich nucleus is more dense as compared to neutron-deficient nucleus [106]. One can see that with increase in radii, both the $\rho_n(r)$ and $\rho_p(r)$ reduces in the core of nucleus and the number of nucleons in surface of nucleus increases. Therefore, the surface of the nuclei become more diffused for larger radii. This influence of nuclear charge radii parameterizations on the population of nucleon in surface of nucleus will affect the flow of particles originating from the participant zone.

4.3 Results and discussion

Simulations have been carried out for the isospin-asymmetric nuclear reactions in the incident energy range between 30 MeV/nucleon and 600 MeV/nucleon at scaled impact parameter of $\hat{b}$=b/b$_{max}$=0.3 (i.e. semi-central collisions) where, b$_{max}$ = $(R_P + R_T)fm$, (R_P and R_T are radii of projectile and target nuclei respectively) using soft equation of state and isospin dependent nucleon-nucleon cross-section reduced by 10% i.e. $\sigma = 0.9\sigma_{NN}^{free}$. For systematic study, two approaches have been adopted. In the first approach, the structural effects have been studied by simulating a series of five different reactions of $^{50}_{20}$Ca+$^{50}_{20}$Ca, $^{90}_{36}$Kr+$^{90}_{36}$Kr, $^{124}_{50}$Sn+$^{124}_{50}$Sn, $^{150}_{60}$Nd+$^{150}_{60}$Nd and $^{197}_{79}$Au+$^{197}_{79}$Au covering a wide range of composite mass number (A_{tot}) and having same N/Z=1.5, specified as *structural series*. In the second approach, isospin effects have been studied by simulating a series of five isobaric reactions (having different N/Z) of $^{80}_{40}$Zr+$^{80}_{40}$Zr (N/Z=1), $^{80}_{36}$Kr+$^{80}_{36}$Kr (N/Z=1.2), $^{80}_{32}$Ge+$^{80}_{32}$Ge (N/Z=1.5), $^{80}_{30}$Zn+$^{80}_{30}$Zn (N/Z=1.7) and $^{80}_{29}$Cu+$^{80}_{29}$Cu (N/Z=1.8) having A_{tot} = 160 units a.m.u., specified as *isospin series*. The outcome of reactions is analyzed at saturation time of 200 fm/c by using minimum spanning tree (MST) method [18, 276].

4.3.1 Incident energy dependence of reduced flow and elliptical flow

The reduced flow and elliptical flow decomposes in the mid-rapidity region where the compressibility of the nuclear matter is more than the spectator matter region. To study how the change in the nuclear radius affects the compressibility of the nuclear matter,

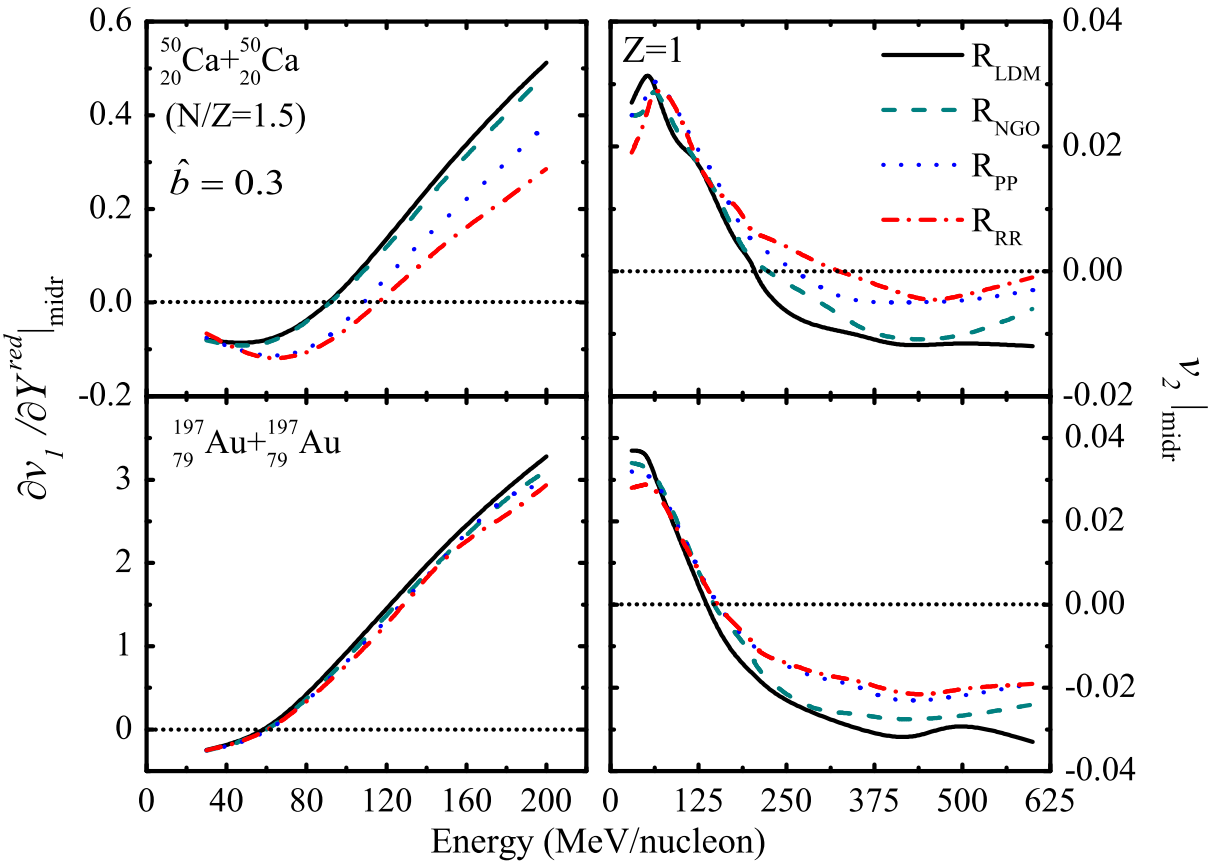

Figure 4.4: Energy dependence of reduced flow (left panels) and elliptical flow (right panels) of particles having Z=1 for the reaction of $^{50}_{20}$Ca+$^{50}_{20}$Ca (upper panels) and $^{197}_{79}$Au+$^{197}_{79}$Au (lower panels) representing the structural effects at $\hat{b} = 0.3$. The different lines corresponds to results obtained by using different radii parameterizations as explained in the text.

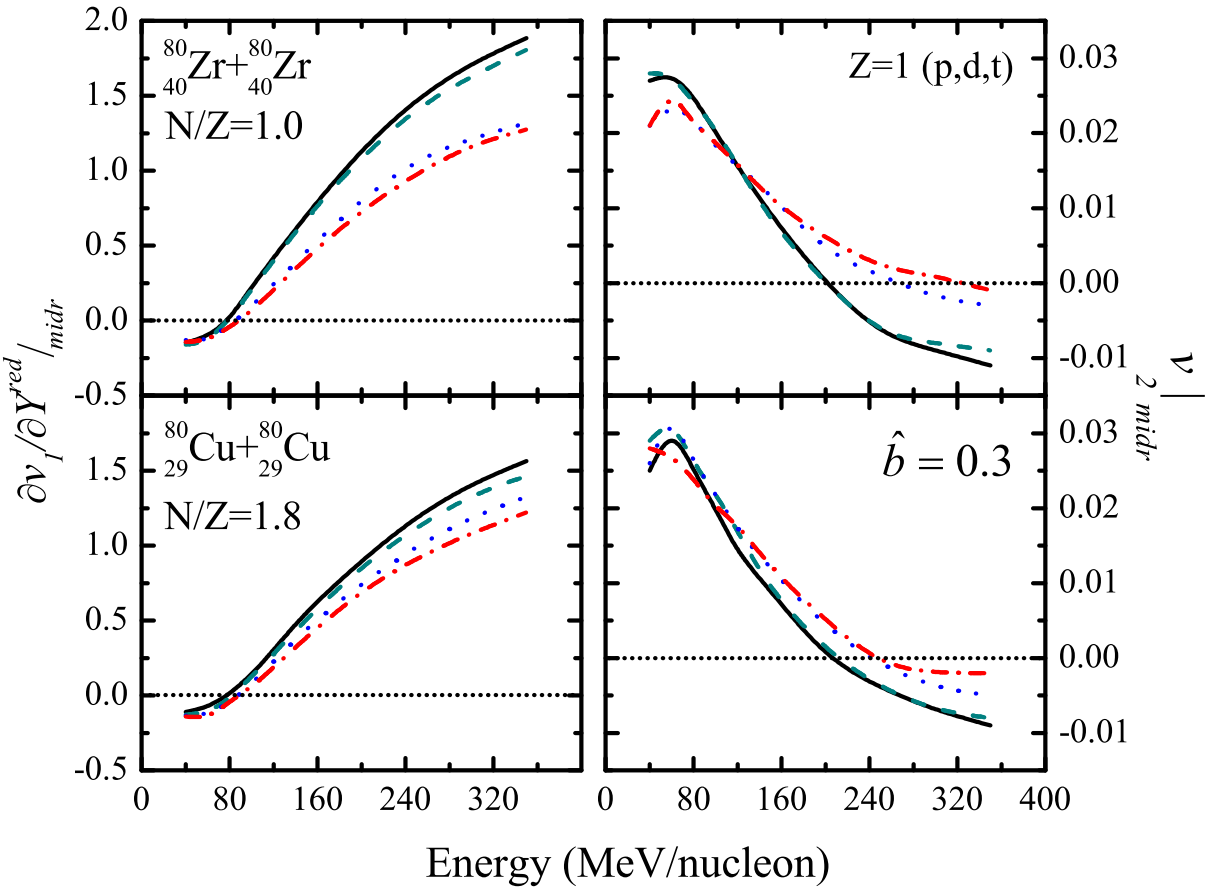

Figure 4.5: Energy dependence of reduced flow (left panles) and elliptical flow (right panels) of particles having Z=1 for the reaction of $^{80}_{40}$Zr+$^{80}_{40}$Zr (upper panels) and $^{80}_{29}$Cu+$^{80}_{29}$Cu (lower panels) representing isospin effects at $\hat{b} = 0.3$. Lines have the same meaning as in Fig.4.4.

Fig.4.4 presents the energy dependence of reduced flow (left panels) and elliptical flow (right panels) of particles having Z=1 in the mid-rapidity region for only two reactions of $^{50}_{20}$Ca+$^{50}_{20}$Ca (upper panels) and $^{197}_{79}$Au+$^{197}_{79}$Au (lower panels) from structural series. The influence of nuclear charge radius on the excitation function of reduced flow and elliptical flow is also studied for the other reactions of structural series (results not shown here). The observation reveals same conclusion as for the reactions of $^{50}_{20}$Ca+$^{50}_{20}$Ca and $^{197}_{79}$Au+$^{197}_{79}$Au. For all radii parameterizations used, the excitation function of reduced flow and elliptical flow shows its usual behavior. It is visible from the figure that structural effects through nuclear charge radii parameterizations influences the magnitude of both types of flow drastically. With increase in the incident energy, reduced flow sharply goes to its positive value (repulsive flow) and elliptical flow to its negative value (squeeze-out flow) with R_{LDM} as compared to R_{NGO}, R_{PP} and R_{RR}. This is because, the increase in radius means increase in the available phase space, i.e. same number of nucleons are now initialized in the relatively larger Fermi sphere. In larger radii (i.e. R_{RR}), the nucleons will get more space to accommodate themselves and therefore there will be less Coulomb interaction among the protons from the initial level. This reduction in the strength of Coulomb repulsions affects the flow of ejected particles. With larger radius, the mean field gets more importance and nucleon-nucleon collisions gets suppressed. Hence, one can say that, larger is the radii, lesser will be the Coulomb repulsion and more negative will be the reduced flow as well as more positive will be the elliptical flow. Therefore, more energy is needed to strengthen the repulsive nucleon-nucleon collisions which will compensate the effect of attractive mean field and shadowing of the rotating spectator. The flow physics in the HICs at intermediate energies is dominated entirely by the surface effects; however, the bulk properties of the nuclear matter dominates for the heavier colliding nuclei. Since, the surface of light nuclei is more diffused as compared to heavier nuclei and this surface diffuseness further increases with increase in radius. Consequently, the sensitivity of magnitude of both types of flow on the different radii parameterizations is more pronounced for the reaction of $^{50}_{20}$Ca+$^{50}_{20}$Ca (lighter system) as compared to $^{197}_{79}$Au+$^{197}_{79}$Au (heavier systems).

The above stated results obtained for same neutron-to-proton content (i.e. N/Z=1.5), reveals the structural effects. The next study has been carried out for the

isospin series. Fig.4.5 displays the isospin effects through nuclear charge radii parameterizations on the excitation function of reduced flow (left panels) and elliptical flow (right panels) for only two isobaric nuclear reaction of $^{80}_{40}$Zr+$^{80}_{40}$Zr (upper panels) and $^{80}_{29}$Cu+$^{80}_{29}$Cu (lower panels). For detailed study, The influence of radii on the excitation function of both types of flow is examined for the other reactions of isospin series (results not shown here) and the conclusion obtained from the calculations is same as for the nuclear reaction of $^{80}_{40}$Zr+$^{80}_{40}$Zr and $^{80}_{29}$Cu+$^{80}_{29}$Cu. The radius of $^{80}_{40}$Zr and $^{80}_{29}$Cu are equal with R_{LDM} as the mass number is same. For R_{NGO}, the radius of $^{80}_{40}$Zr is smaller than the radius of $^{80}_{29}$Cu with difference of 0.0145 fm. However, the number of protons is more in $^{80}_{40}$Zr nucleus as compared to $^{80}_{29}$Cu nucleus and the nucleus with greater number of protons must have larger radii as compared to nucleus having less number of protons, because of the Coulomb repulsions, which is being observed in the case of R_{PP} and R_{RR} radii parameterizations. Moreover, one can observe from the figure that the influence of nuclear charge radii on the nuclear flow is more for neutron-deficient reaction (i.e. $^{80}_{40}$Zn+$^{80}_{40}$Zr) as compared to neutron-rich nuclear reactions (i.e. $^{80}_{29}$Cu+$^{80}_{29}$Cu). Moreover, the comparative role of nuclear charge radii on the reduced flow and elliptical flow increases with increase in incident energy.

4.3.2 Radius dependence of balance energy and transition energy

The sensitivity of reduced flow and elliptical flow towards the different nuclear charge radii parameterizations is different at different incident energies. It can not be concluded that which type of flow is more influenced by which type of nuclear charge radii. Therefore, the study has been extended to observe the influence of radii parameterizations on particular type of energy. This particular type of energy is called balance energy (E_{bal}) in the case of reduced flow and transition energy (E_{trans}) in the case of elliptical flow.

Fig. 4.6 display the radius dependence of E_{bal} (upper panel) and E_{trans} (lower panel) for the reactions of structural series revealing structural effects. The different symbols in the figure are the results obtained by initializing the nuclei with four different nuclear charge radii parameterizations as demonstrated in Sec. 1.4 of chapter 1. One can see that, the balance energy and the transition energy reduces with increase in system mass because of increase in Coulomb repulsions, as justified in Ref. [296, 302]. It has been also observed from the figure that E_{bal} and E_{trans} are enhanced with increase in

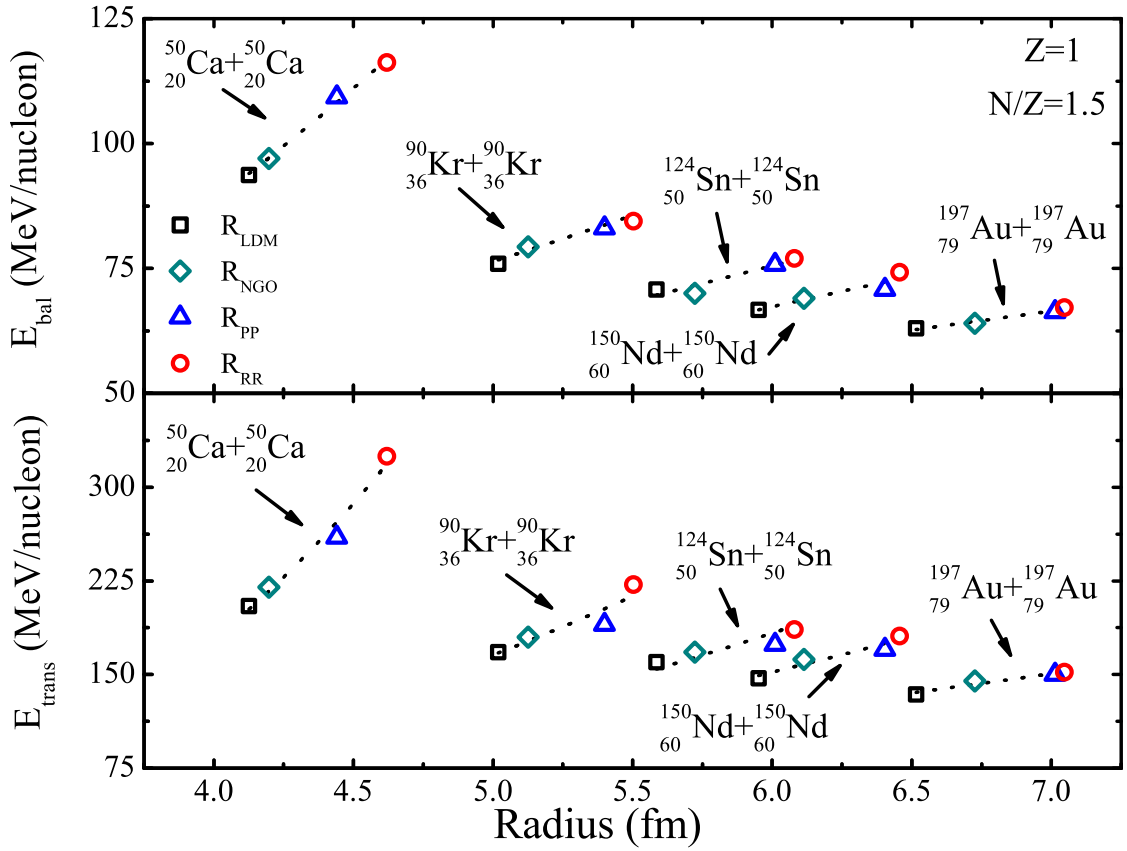

Figure 4.6: Radius dependence of E_{bal} (upper panel) and E_{trans} (lower panel) for all the reactions of structural series. The different symbols corresponds to results obtained by using different radii parameterizations as explained in the text. The dotted lines represents the power law fit.

radius. As the radius increases, the nucleonic density reduces (as discussed in chapter 3), which consequently reduces the pressure gradient in the mid-rapidity region. Due to less pressure gradient, there is less transformation of longitudinal momentum into transverse momentum. Therefore, with larger radii, the initial longitudinal momentum gets stored in the system and thermal energy gets more important which do not allow the particles to move towards transverse direction. Moreover, with larger radius, more strength of nucleon-nucleon repulsions in the compressed nuclear matter is required to compensate the effect of larger spectator movement. Hence, more energy to pump is needed in order to obtain zero flow. The sensitivity of balance energy and transition energy on the radius is more pronounced for the reactions with relatively small composite mass number and further reduces with increase in system mass. This observation is in agreement with Ref. [104]. From both types of energies, the transition energy is more influenced by the different nuclear charge radii parameterizations as compared to balance energy. The percentage change in the transition (or balance) energy due to change in the radius of nucleus from R_{LDM} to R_{RR} parametrization is calculated by using the following formula:

$$\Delta E(\%) = \frac{E_{R_{RR}} - E_{R_{LDM}}}{E_{R_{LDM}}} \times 100. \tag{4.5}$$

Here, ΔE (%) is percentage change in E_{trans} (or E_{bal}) and E could be E_{trans} or E_{bal}. For example, the percentage increment in radius is 9.64% for $^{90}_{36}$Kr nucleus, corresponding to this increase in radius, the value of transition energy (or balance energy) is enhanced by 32.14% (or 11.33%) for the reaction of $^{90}_{36}$Kr+$^{90}_{36}$Kr when switching from R_{LDM} to R_{RR}. This observation holds true for other reactions as well.

Fig.4.7 represents the radius dependence of balance energy and transition energy for the reactions of isospin series revealing the isospin effects. Various symbols have same meaning as used in Fig.4.6. Here also, E_{bal} and E_{trans} are enhanced with increase in radius. Owing to 13.34% change in radius of $^{80}_{40}$Zr, 47.5% (or 13.92%) enhancement in E_{trans} (or E_{bal}) is observed for the nuclear reaction of $^{80}_{40}$Zr+$^{80}_{40}$Zr whereas, 25% (or 16.88%) enhancement in E_{trans} (or E_{bal}) has been observed for the nuclear reaction of $^{80}_{29}$Cu+$^{80}_{29}$Cu, caused by 8.8% change in the radius of $^{80}_{29}$Cu. These calculations have been also done between R_{LDM} and R_{RR} results. For R_{LDM}, E_{bal} and E_{trans} lies around 80 MeV/nucleon and 200 MeV/nucleon respectively for all isobaric reactions. The E_{bal} and E_{trans} do not depends upon the initial neutron-to-proton content of the colliding nuclei pair because all

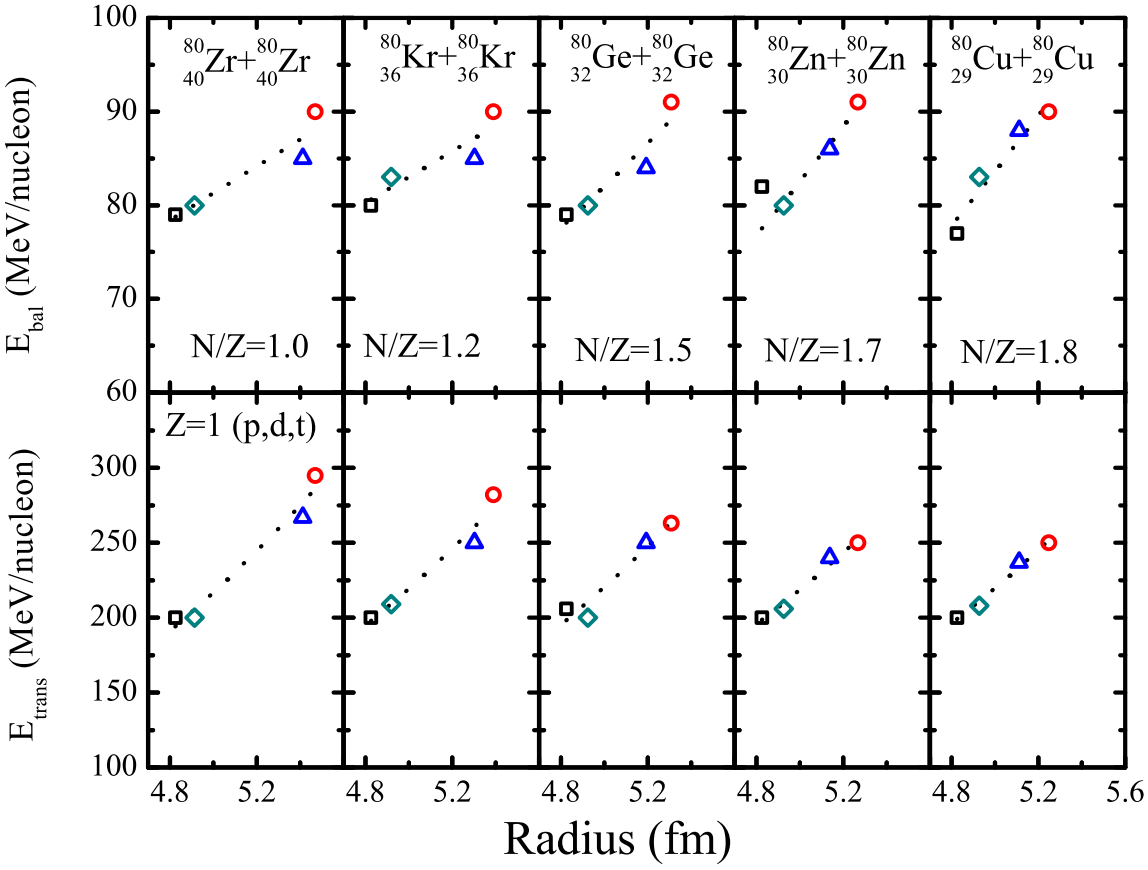

Figure 4.7: Radius dependence of E_{bal} (upper panel) and E_{trans} (lower panel) for all the reactions of isospin series. Symbols and lines have same meaning as in Fig.4.6.

Table 4.1: The values of exponent τ obtained from power law fit with radius in Fig. 4.6 and Fig. 4.7 for all the reactions of structural and isospin series.

Structural effects $N/Z = 1.5$				Isospin effects $A_{tot} = 160$			
Reaction	A_{tot}	$\tau_{E_{bal}}$	$\tau_{E_{trans}}$	Reaction	N/Z	$\tau_{E_{bal}}$	$\tau_{E_{trans}}$
$^{50}_{20}$Ca+$^{50}_{20}$Ca	100	1.93	4.03	$^{80}_{40}$Zr+$^{80}_{40}$Zr	1.0	0.83	3.09
$^{90}_{36}$Kr+$^{90}_{36}$Kr	180	1.20	2.62	$^{80}_{36}$Kr+$^{80}_{36}$Kr	1.2	0.87	2.92
$^{124}_{50}$Sn+$^{124}_{50}$Sn	248	1.13	2.39	$^{80}_{32}$Ge+$^{80}_{32}$Ge	1.5	1.38	2.99
$^{150}_{60}$Nd+$^{150}_{60}$Nd	300	1.09	2.16	$^{80}_{30}$Zn+$^{80}_{30}$Zn	1.7	1.76	2.73
$^{197}_{79}$Au+$^{197}_{79}$Au	394	0.79	1.46	$^{80}_{29}$Cu+$^{80}_{29}$Cu	1.8	1.76	2.79

the reactions are initialized with isospin-independent radii parameterizations and the radii are equal. Therefore, the N/Z dependence of E_{bal} and E_{trans} do not exhibit isospin effects. This observation is in agreement with the observations of Ref. [303]. For R_{NGO}, the radius of isobaric nuclei increases with very small value while going from neutron-deficient nuclei to neutron-rich nuclei (i.e. N/Z=1 to N/Z=1.8). Therefore, the dependence of E_{bal} and E_{trans} on the N/Z is very feeble with this radii parametrization. It has been observed that for R_{PP} and R_{RR}, the magnitude of balance energy remains almost unchanged with increase in N/Z; however, the radii of nuclei decreases with increase in initial neutron-to-proton ratio. For example, $E_{bal} \approx 90$ MeV/nucleon for the nuclear reaction of $^{80}_{40}$Zr+$^{80}_{40}$Zr with R_{RR}= 5.47 fm and same value of balance energy is observed for the nuclear reaction of $^{80}_{29}$Cu+$^{80}_{29}$Cu with R_{RR}= 5.25 fm. Beside this, one can notice that the transition energy reduces with increase in N/Z for R_{PP} and R_{RR}. Therefore the influence of change in the nuclear charge radii on E_{bal} (E_{trans}) increases (decreases) with increase in initial N/Z ratio of colliding nuclei pair. Hence, the isospin-dependent parameterizations of nuclear charge radii alters the isospin effects in the N/Z dependence of E_{bal} and E_{trans}. The another observation made from Fig. 4.6 and 4.7 is that, both balance energy and transition energy are found to follow a power law with nuclear charge radii. The dotted lines in both figures represents a power law fit of kind:

$$E \propto R^{\tau} \tag{4.6}$$

Here, E has same meaning as in Eqn. 4.5 and R is the radius of the nucleus (in fm) calculated by using four different nuclear charge radii parameterizations. The exponent τ

values for the reactions of structural series and the isospin series are presented in Table. 4.1. The purpose of obtaining τ values is that, one can estimate the balance and transition energy from the Eqn. 4.6 by knowing the calculated radii of the nuclei using any nuclear charge radii parameterization (in addition to four parameterizations that have been opted for present work) by referring to respective τ value. One can see that the τ values of E_{bal} and E_{trans} reduces with increase in system mass of the colliding nuclei pair. Also, the τ values of E_{bal} are enhanced and of E_{trans} are reduced with increase in initial neutron-to-proton ratio. This examination of exponent τ further strengthen our interpretation of results made from Fig.4.6 and Fig.4.7. Moreover, the τ values for balance energy are smaller than the τ values of transition energy. This is another signature which proves the elliptical flow to be more sensitive towards the different nuclear charge radii as compared to reduced flow. The gap between the τ values of E_{trans} and E_{bal} decreases with increase in A_{tot} and N/Z. Therefore, Table. 4.1 also exhibits the correlation between the E_{trans} and E_{bal} for different nuclear charge radii parameterizations.

4.3.3 Impact parameter dependence of balance energy and transition energy

As per the definitions, the reduced and elliptical flow arises due to the interplay between the impact of the spectator matter and the strength of compression in the participant zone. The spectator (participant) matter increases (decreases) with increase in collision geometry. Therefore, Fig. 4.8 display the influence of nuclear charge radii parameterizations on the scaled impact parameter dependence of balance energy (upper panel) as well as transition energy (lower panel). The open symbols represents the theoretical calculations for different radii parameterizations (as per the Fig. 4.6) whereas, the closed symbols star, sphere and pentagon represents the experimental data provided by INDRA [173], FOPI [149, 207] and INDRA & ALADIN [174] collaborations respectively. The figure reveals that the role of different radii parameterizations on the E_{trans} and E_{bal} increases with increase in collision geometry. This is because, the size of spectator matter initialized with large radii is also large. Therefore at higher collision geometry, the strength of highly compressed zone need more energy to overcome the effects of rotating spectator matter. The magnitude of theoretical E_{bal} and E_{trans} with different nuclear charge radii parameterizations are in agreement with experimental data.

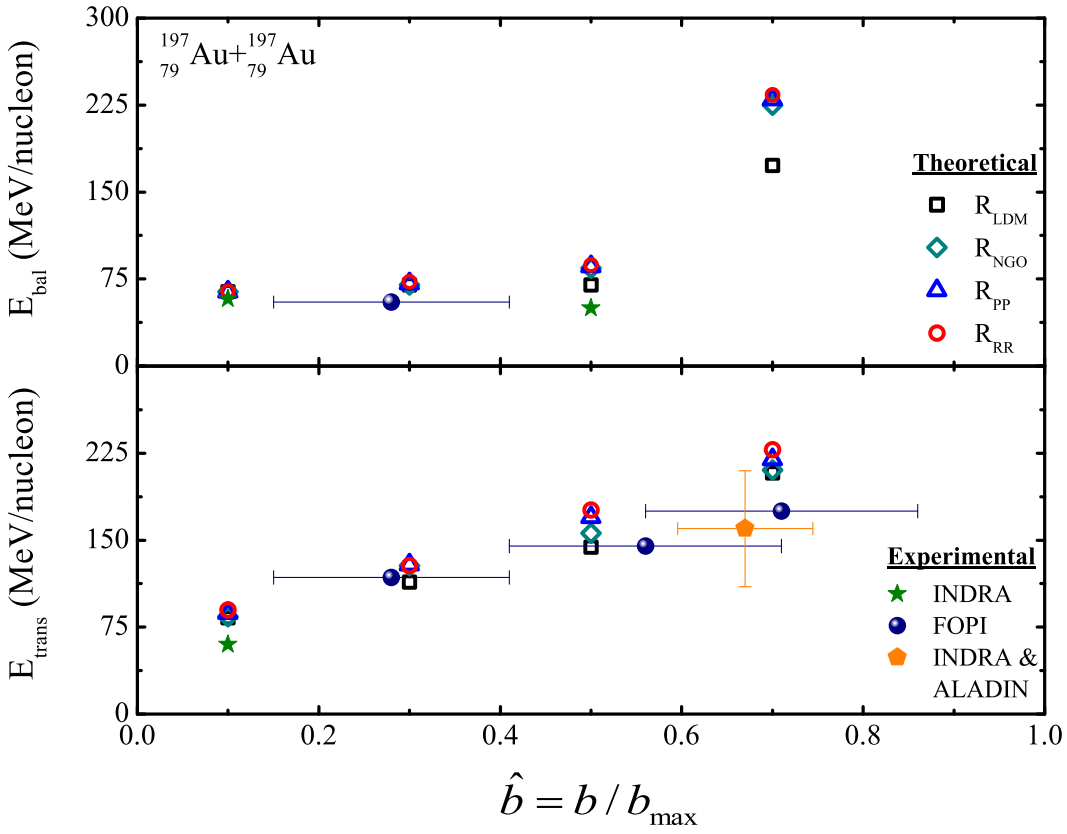

Figure 4.8: Scaled impact parameter dependence of E_{bal} (upper panel) and E_{trans} (lower panel) for the reaction of $^{197}_{79}$Au+$^{197}_{79}$Au.

4.4 Balance geometry and transition geometry

As discussed in previous sections that the magnitude of both reduced flow and elliptical flow changes its sign with increase in beam energy at balance energy and transition energy respectively. In Ref. [305], a new observable is proposed to quantify the effects of spectator matter in the reaction dynamics. The study shows that, at a fixed incident energy of 150 MeV/nucleon, the impact parameter dependence of transverse in-plane flow ($< p_x >_{dir}$) crosses zero value at specific collision geometry termed as geometry of vanishing flow (GVF). Since then, study has been embellished to explore the role of different NEOS and mass-asymmetry of the reaction by keeping the total mass fixed [306] as well as with fixed target nuclei [307]. The previous study in the literature on GVF has been made at incident energy of 100, 150, 200 and 400 MeV/nucleon only. In addition to that, very less literature exist on the impact parameter dependence of collective flow at mid-rapidity region. In this section of study, the collision geometry dependence of reduced flow and elliptical flow has been calculated as a function of scaled impact parameter for a wide range of incident energy to explore, whether there exists any collision geometry at which the reduced flow as well as the elliptical flow passes through zero or not. If yes, then what range of incident energy contribute in this scenario. In addition to this, the structural effects through nuclear charge radii parameterizations have also been studied by taking only two radii parameterizations i.e. R_{LDM} and R_{RR}. The simulations have been carried out for the reactions of $^{50}_{20}$Ca+$^{50}_{20}$Ca and $^{197}_{79}$Au+$^{197}_{79}$Au at incident energy between 50 MeV/nucleon and 450 MeV/nucleon. The reactions are simulated at seven scaled impact parameter ($\hat{b}$) bins of [a] 0-0.28, [b] 0.28-0.39, [c] 0.39-0.48, [d] 0.48-0.56, [e] 0.56-0.62, [f] 0.62-0.76, [g] 0.76-0.88 covering the wide range of collision geometry. However, while obtaining the required figures, the magnitude of reduced flow and elliptical flow are plotted in the center of each impact parameter bin.

4.4.1 Collision geometry dependence of reduced flow and elliptical flow

Fig. 4.9 display the scaled impact parameter dependence of reduced flow for the reactions of $^{50}_{20}$Ca+$^{50}_{20}$Ca (upper panels) and $^{197}_{79}$Au+$^{197}_{79}$Au (lower panels) at different incident energies (represented by different line in the figure) for particles having Z=1 with R_{LDM}

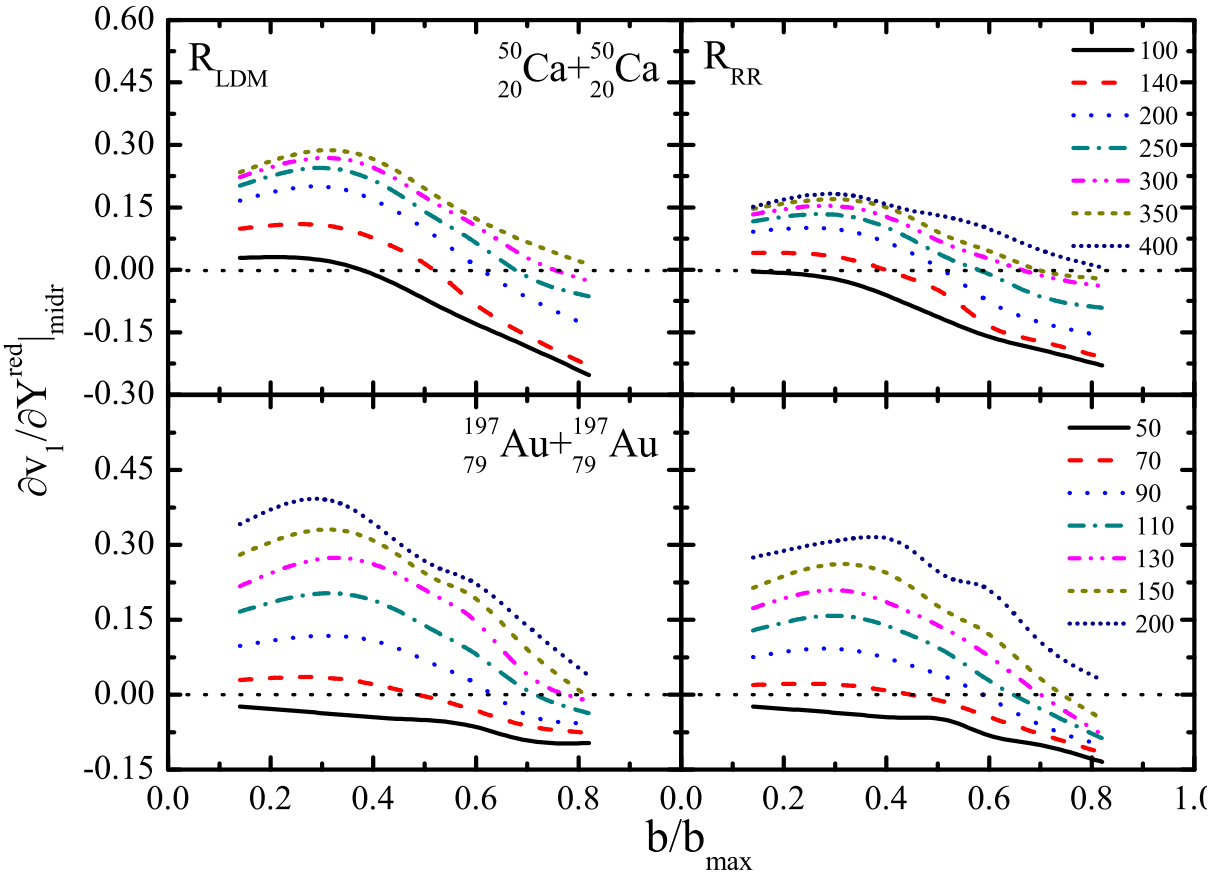

Figure 4.9: Scaled impact parameter dependence of reduced flow for the reactions of $^{50}_{20}$Ca+$^{50}_{20}$Ca (upper panel) and $^{197}_{79}$Au+$^{197}_{79}$Au (lower panel) at different incident energies for two nuclear charge radii parameterizations: R_{LDM} (left panels) and R_{RR} (right panels). Different lines in figure represents different incident energies in upper and lower panels.

(left panels) and R_{RR} (right panels) nuclear charge radii parameterizations. One can observe that, for both the reactions, the magnitude of reduced flow decreases with increase in collision geometry and at some point it passes through a zero value. This is because, as the spectator matter increases, the inward flow of particles decreases and the flow of particles shift to outward flow. Moreover, with increase in impact parameter, the strength of repulsive nucleon-nucleon collision reduces as the participant matter decreases. Therefore, the attractive mean filed dominates the reaction dynamics resulting in negative values of reduced flow. The collision geometry at which the flow is zero or one can say that both the attractive mean field and repulsive nucleon-nucleon collision counter balance each other and the reduced flow vanishes, is labelled as *"balance geometry"* and represented by $\hat{b}_{bal}$. One can observe that the reduced flow passes through zero value at particular incident energy range only. At low energy (for example below 100 MeV/nucleon in the case of $^{50}_{20}$Ca+$^{50}_{20}$Ca and below 70 MeV/nucleon in the case of $^{197}_{79}$Au+$^{197}_{79}$Au reaction), the value of reduced flow remains negative through out the collision geometry. This is because the attractive mean field increases with increase in the spectator matter. Therefore, the strength of the attractive force further increase and positive value of reduced flow can not be achieved. On the other hand, at high incident energies (for example, beyond 350 MeV/nucleon and 200 MeV/nucleon for the case of $^{50}_{20}$Ca+$^{50}_{20}$Ca and $^{197}_{79}$Au+$^{197}_{79}$Au respectively), the strength of repulsive nucleon-nucleon collision is much higher that it can not be overcome by decreasing the participant matter.

Similar observation has been made in Fig. 4.10 for the collision geometry dependence of elliptical flow in the mid-rapidity region for the reaction of $^{50}_{20}$Ca+$^{50}_{20}$Ca (upper panels) and $^{197}_{79}$Au+$^{197}_{79}$Au (lower panels) at different incident energies (represented by different line in the figure) with R_{LDM} (left panels) and R_{RR} (right panels) nuclear charge radii parameterizations. One can observe that, the elliptical flow increases with increase in impact parameter. The negative value of v_2 corresponds to the strength of compressed nuclear matter and positive value is due to shadowing of the spectator matter. For fixed incident energy, the negative value of elliptical flow passes the zero value to become positive with as the collision geometry increases. The scaled impact parameter at which the transition of elliptical flow from out-of-plane to in-plane emission occurs is labelled as "*transition geometry*" and represented by $\hat{b}_{trans}$. This occurs because the impression of

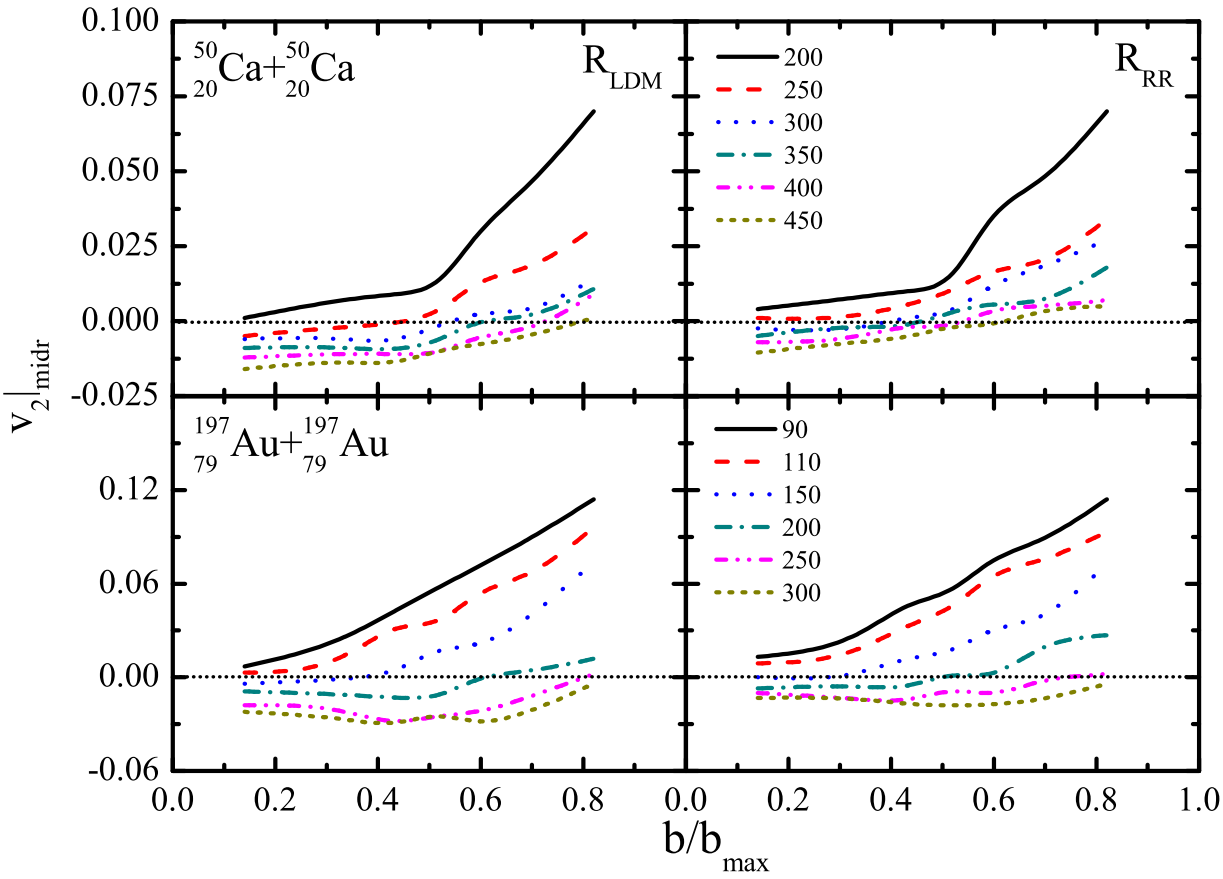

Figure 4.10: Scaled impact parameter dependence of elliptical flow for the reactions of $^{50}_{20}$Ca+$^{50}_{20}$Ca (upper panel) and $^{197}_{79}$Au+$^{197}_{79}$Au (lower panel) at different incident energies for two nuclear charge radii parameterizations: R_{LDM} (left panels) and R_{RR} (right panels). Different lines in figure represents different incident energies in upper and lower panels.

spectator matter movement increases with increase in collision geometry. At relatively lower incident energies (i.e. below 200 MeV/nucleon and 110 MeV/nucleon for $^{50}_{20}$Ca+$^{50}_{20}$Ca and $^{197}_{79}$Au+$^{197}_{79}$Au respectively) the value of elliptical flow is already positive and can not show transition effect with increase in $\hat{b}$. Moreover, at higher incident energies (like beyond 450 and 300 MeV/nucleon in the case of $^{50}_{20}$Ca+$^{50}_{20}$Ca and $^{197}_{79}$Au+$^{197}_{79}$Au respectively), the strength of compressed nuclear matter can not be overcome by increasing the spectator matter. The above stated observation is true for both the nuclear charge radii parameterizations. However, the change in the magnitude of reduced flow (and elliptical flow) from R_{LDM} to R_{RR} is already discussed in Fig. 4.4 and 4.5.

4.4.2 Incident energy dependence of $\hat{b}_{bal}$ and $\hat{b}_{trans}$

The values of $\hat{b}_{bal}$ and $\hat{b}_{trans}$ obtained from Fig. 4.9 and 4.10 are displayed in upper and lower panels of Fig. 4.11 respectively for the reactions of $^{50}_{20}$Ca+$^{50}_{20}$Ca and $^{197}_{79}$Au+$^{197}_{79}$Au. The open squares and circles in this figure represents the calculations with R_{LDM} and R_{RR} respectively. One can see that the values of $\hat{b}_{bal}$ and $\hat{b}_{trans}$ increases with increase in incident energy for both reactions and radii parameterizations. The magnitudes of both balance geometry and transition geometry are lower for larger radius. This is because, with increase in radius the size of spectator matter also increases (since scaled impact parameter is taken here which corresponds to percentage of interacting matter), which consequently increase the role of mean field. The range of incident energy which contributes to the observation of balance and transition geometries is comparatively lower for heavier colliding nuclei and higher for lighter colliding nuclei. Because at fixed incident energy, the impression of spectator matter is larger in the heavier colliding nuclei compared to lighter systems. The figure also reveals that the role of nuclear charge radii parametrization is more for lighter colliding systems which is in agreement of Fig. 4.6. Also, the influence of increase in nuclear radius is more in $\hat{b}_{trans}$ as compared to $\hat{b}_{bal}$, which again proves elliptical flow to be more sensitive towards the choice of nuclear charge radii parametrization than directed or reduced flow.

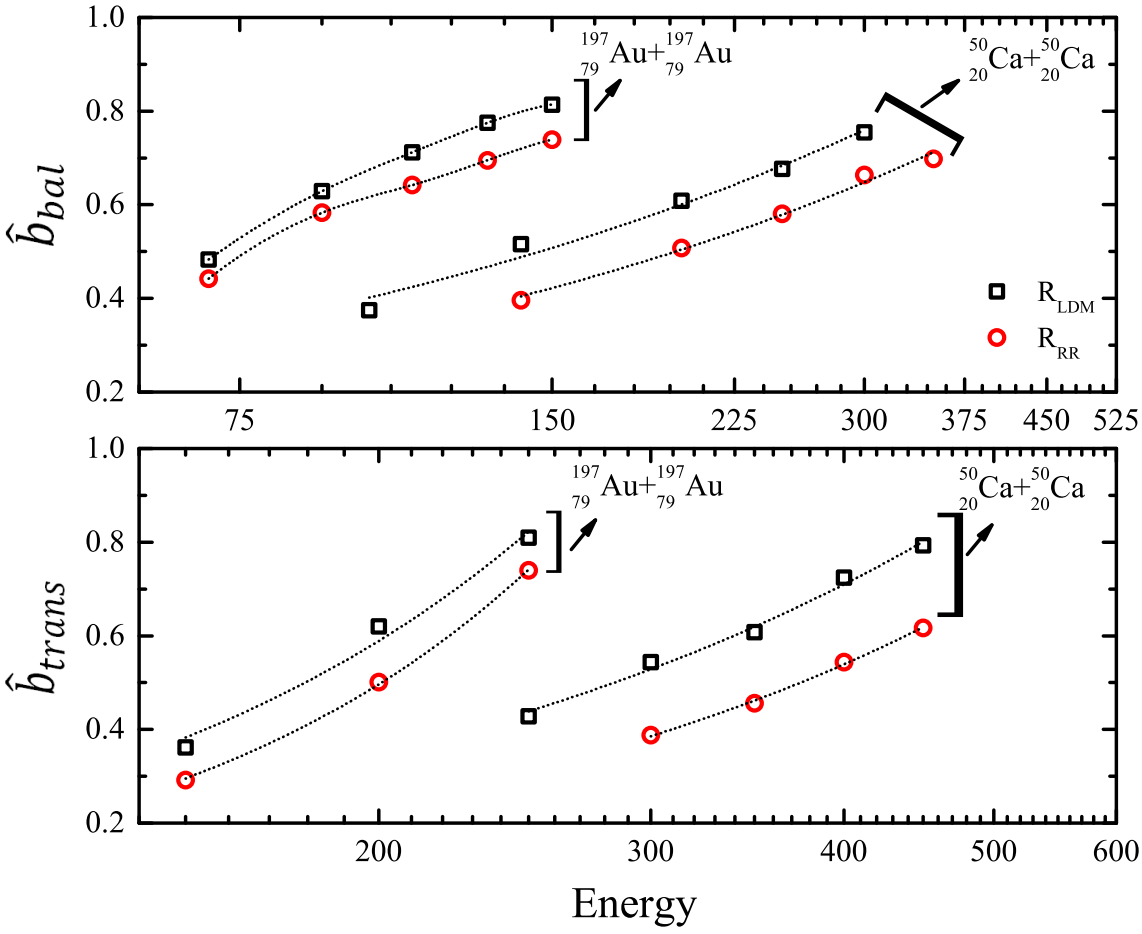

Figure 4.11: Incident energy dependence of $\hat{b}_{bal}$ (upper panel) and $\hat{b}_{trans}$ (lower panel) for the reactions of $^{50}_{20}$Ca+$^{50}_{20}$Ca and $^{197}_{79}$Au+$^{197}_{79}$Au.

4.5 Clusterization technique as per isospin dependent nuclear charge radius

All the dynamical models simulate the time-evolution of the single particles, its excitation in the compressed zone and de-excitation during the expansion. No model can simulate the phase-space of the fragments. It is briefly discussed in Sec. 2.4 that the phase-space generated by the dynamical models (IQMD in the present study) is analyzed by some clusterization techniques to identify the different types of fragments so that their properties can be studied in virtue of understanding the physics involved in the HICs at intermediate energies. Therefore, the clusterization techniques are also referred as cluster identifiers. Many clusterization techniques have been proposed in the literature to obtain the best fragmentation array. These techniques can also be used to probe the stability of the fragments generated by the models. From the list of cluster identifiers, the Minimum Spanning Tree **MST** method and its various version like **MST-M** (with additional momentum cut) and **MSTB** (with additional binding energy cut). have been used widely regardless its some limitations. This method is based on the spatial, momentum and cold B.E. constraints upon the nucleons. The fragments identified through this technique may have the excited fragments which may have undergo secondary decay in the momentum space. However, when the nuclear matter is dilute, these limitations do not matter. The recent work of Puri and collaborators [308], reveals the importance of thermal binding energy cuts in the MST (MST-BT) method over the binding energy cut of cold nuclear matter (MSTB) as well as the MST method in the formation process of fragments. However, at saturation time of the reaction, the multiplicity and binding energy per nucleon of various types fragments obtained via MST-BT is same as that of MST. From this, one can conclude that the fragment formation process of MST method is not adequate nonetheless the final stage fragmentation array does a fair job.

The different spatial constraints in the MST method have been deployed to observe its influence on the observables arising in the HICs at intermediate energies. In a study by *Zhang et al.* [45], isospin dependent MST (iso-MST) method has been developed to observe the influence of isospin degree of freedom associated with the nucleons in the fragment production and nuclear stopping. However, the momentum constraint has not been modified in the MST. Therefore, in this section, the momentum constraint has been

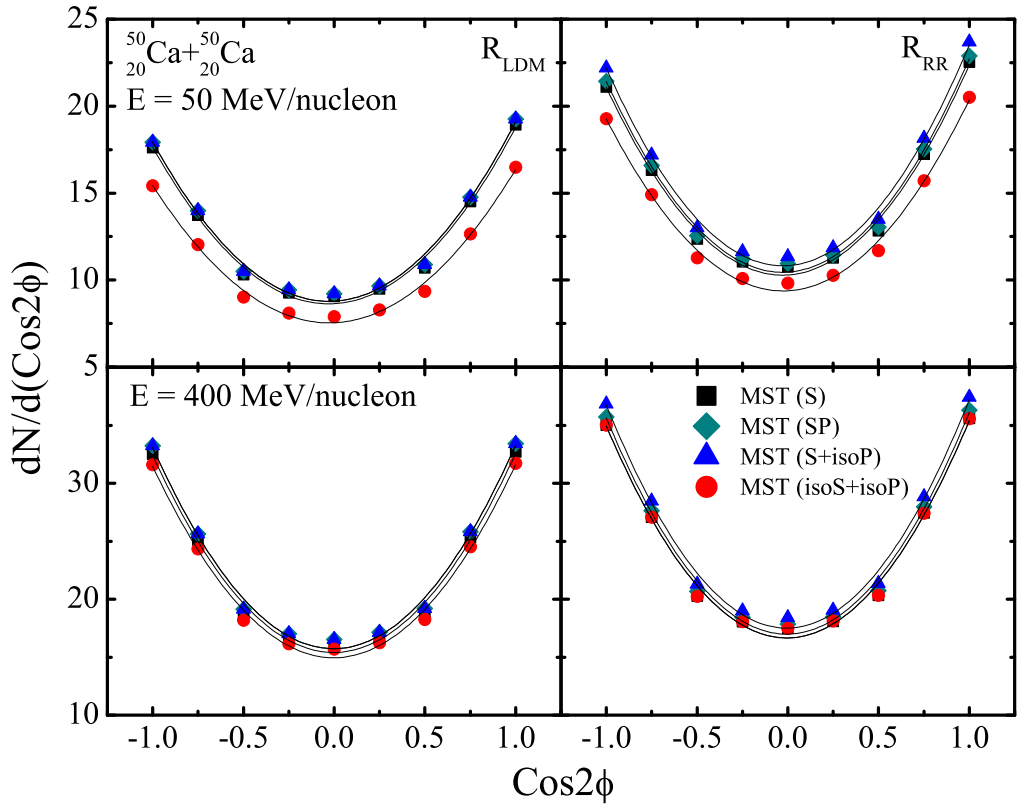

Figure 4.12: The azimuthal angle dependence of $dN/d(Cos2\phi)$ of FNs for the reactions of $^{50}_{20}$Ca+$^{50}_{20}$Ca at incident energy of 50 MeV/nucleon (upper panel) and 400 MeV/nucleon (lower panel) for two nuclear charge radii parameterizations: R_{LDM} (left panels) and R_{RR} (right panels). Different lines in figure represents different clusterization techniques mentioned in Table. 4.2.

Table 4.2: List of different clusterization techniques.

Sr. No.	Notation	Spatial (S) constraint	Momentum (P) constraint
1.	MST(S)	$R_{clus}^{NN} = 4$ fm	-
2.	MST(S+P)	$R_{clus}^{NN} = 4$ fm	$P_{clus}^{NN} = P_F^{LDM}$
3.	MST(S+isoP)	$R_{clus}^{NN} = 4$ fm	$P_{clus}^{NN} = P_F^{LDM}$ and P_F^{RR}
4.	MST(isoS+isoP)	$R_{clus}^{pp} = 3$ fm and $R_{clus}^{nn/np} = 6$ fm	$P_{clus}^{NN} = P_F^{LDM}$ and P_F^{RR}

modified as per the isospin dependent and independent nuclear charge radii parameterizations (i.e. R_{LDM} and R_{RR} only) to study the isospin degree of freedom thorough the clusterization technique. The simulations have been carried out using IQMD model for the reaction of $^{50}_{20}$Ca+$^{50}_{20}$Ca and $^{197}_{79}$Au+$^{197}_{79}$Au at incident energy of 50 and 400 MeV/nucleon and scaled impact parameter of $\hat{b} = 0.3$ (i.e. semi-central collisions). The reactions are followed till 200 fm/c and clusters are formed with four different algorithms MST(S), MST(S+P), MST(S+isoP) and MST(isoS+isoP) as listed in Table. 4.2. Here 'S' corresponds to spatial constraint as in Eqn. 2.49 of MST and 'P' corresponds to momentum constraint as in Eqn. 2.50 also referred as MSTM in chapter 2. The isospin dependent spatial constraints have been kept as per the optimization of Ref. [45]. The small value of spatial constraints for pp is because of long range Coulomb forces and large value for nn & np is due to properties of neutron-rich nuclei and they do not exert repulsive forces. The calculation of Fermi momentum P_F has been done through the following formula:

$$P_F \ = \ \eta k_F \tag{4.7}$$

Where, k_F is defined in Eqn. 2.25 and ρ is the normal nuclear matter density defined as:

$$\rho \ = \ \frac{A}{\frac{4}{3}\pi R_{para}^3} \tag{4.8}$$

Here, R_{para} could be any nuclear charge radii parametrization. It is worth to mention that the Fermi momentum for R_{LDM} labelled as $P_F^{LDM} = 268.4$ MeV/c (the

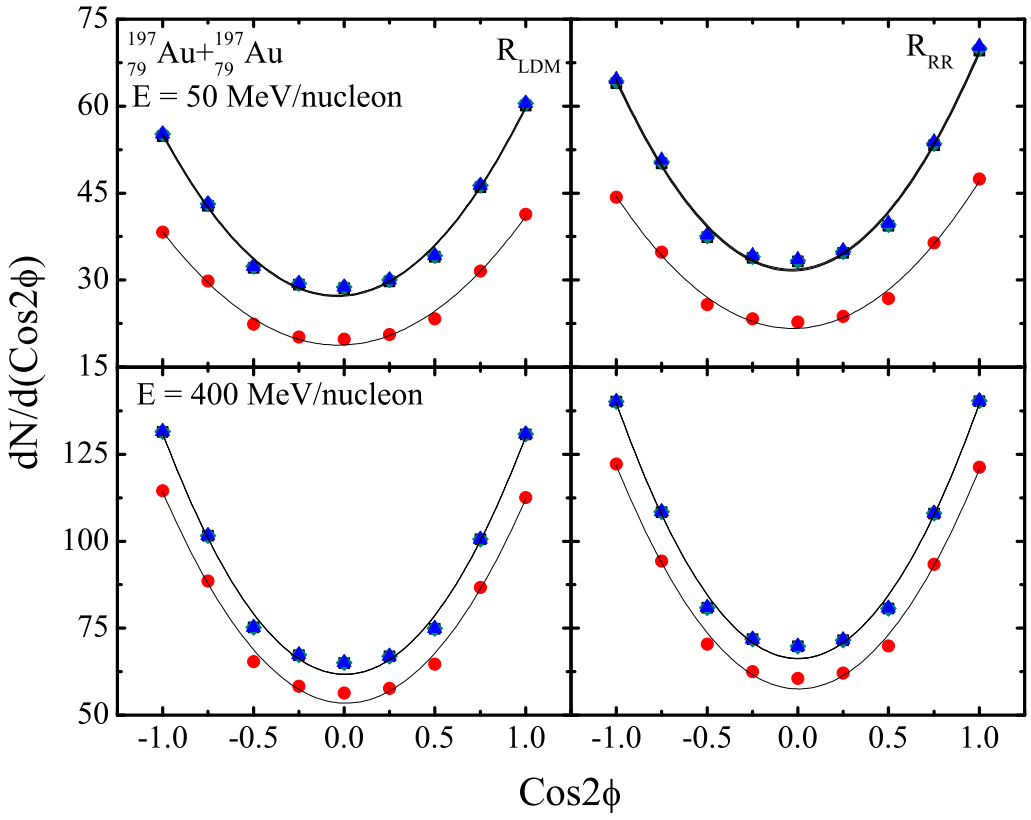

Figure 4.13: The azimuthal angle dependence of $dN/d(Cos2\phi)$ of FNs for the reactions of $^{197}_{79}$Au+$^{197}_{79}$Au at incident energy of 50 MeV/nucleon (upper panel) and 400 MeV/nucleon (lower panel) for two nuclear charge radii parameterizations: R_{LDM} (left panels) and R_{RR} (right panels). Different lines in figure represents different clusterization techniques mentioned in Table. 4.2.

Table 4.3: The values of Radius of Curvature (ROC) obtained from Fig. 4.12 and 4.13 for all the reactions of $^{50}_{20}$Ca+$^{50}_{20}$Ca and $^{197}_{79}$Au+$^{197}_{79}$Au.

	$^{50}_{20}$Ca+$^{50}_{20}$Ca			
Clusterization	E = 50 MeV/nucleon		E = 400 MeV/nucleon	
technique	ROC_{LDM}	ROC_{RR}	ROC_{LDM}	ROC_{RR}
MST(S)	0.08	0.074	0.03	0.262
MST(S+P)	0.116	0.074	0.029	0.264
MST(S+isoP)	0.116	0.0725	0.029	0.265
MST(isoS+isoP)	0.0798	0.0719	0.0304	0.094
	$^{197}_{79}$Au+$^{197}_{79}$Au			
Clusterization	E = 50 MeV/nucleon		E = 400 MeV/nucleon	
technique	ROC_{LDM}	ROC_{RR}	ROC_{LDM}	ROC_{RR}
MST(S)	0.2741	0.0294	0.0098	0.0069
MST(S+P)	0.2724	0.0288	0.00969	0.0069
MST(S+isoP)	0.2724	0.0279	0.00969	0.00685
MST(isoS+isoP)	0.109	0.02937	0.0244	0.0079

default value used in the IQMD), is system size independent. However, the P_F^{RR} is system size dependent. For the mass-symmetric nuclear reactions involving $^{50}_{20}$Ca nuclei, the value of P_F^{RR} is 239.7 MeV/c and for the nuclear reaction involving $^{197}_{79}$Au nuclei, P_F^{RR} is 248.2 MeV/c. The comparison between MST(S) and MST(S+P) reveals the importance of momentum constraint in addition to spatial constraint; MST(S+P) and MST(S+isoP) reveals significance of using momentum constraint as per isospin nuclear charge radii parametrization. Finally, the calculations done by MST(isoS+isoP) gives the significance of using isospin dependent clusterization technique.

To observe the influence of different clusterization techniques, the azimuthal angle dependence of $dN/d(Cos2\phi)$ of FNs has been presented at incident energies of 50 MeV/nucleon (upper panels) and 400 MeV/nucleon (lower panels) for the reactions

$^{50}_{20}$Ca+$^{50}_{20}$Ca in Fig. 4.12 and $^{197}_{79}$Au+$^{197}_{79}$Au in Fig. 4.13 simulated by using R_{LDM} (left panels) and R_{RR} (right panels) radii parameterizations. Since the elliptical flow is more influenced by the choice of radii parametrization, the azimuthal angle dependence of $dN/d(Cos2\phi)$ has been analyzed which is an indicator of elliptical flow. It is worth notifying that, the calculations performed with MST(S+P) and MST(S+isoP) for R_{LDM} radii parametrization is exactly same in both figures. It has been observed that $dN/d(Cos2\phi)$ behaves in similar fashion for all cases [309]. Both the figures reveals that the influence of momentum constraint as per radii parameterizations in the cluserization technique is visible for lighter colliding nuclei ($^{50}_{20}$Ca+$^{50}_{20}$Ca) at low incident energies (around 50 MeV/nucleon) only. For heavier colliding nuclei and at relatively higher incident energies, effect of different momentum cuts is very feeble. Hence, role of MST(S+isoP) decreases with increase in system mass and incident energy. However, the spatial constraint plays an important role. The magnitude of $dN/d(Cos2\phi)$ decrease equally from $Cos2\phi = +1$ to -1 as one uses the MST(isoS+isoP) cluster identifier. The influence of MST(isoS+isoP) is more for lighter colliding nuclei at low energies since it considers the momentum constraint effect also.

To further strengthen the interpretation of results, the azimuthal angle distribution of $dN/d(Cos2\phi)$ has been fitted to parabola equation of type: $y = a + bx + cx^2$. Here, y represents $dN/d(Cos2\phi)$ and x represents $Cos2\phi$. The Radius of Curvature (ROC) at $Cos2\phi = 0$, has been calculated and displayed in Table. 4.3. It has been observed that, with increase in nuclear charge radius (as one switches from R_{LDM} to R_{RR}, the magnitude of $dN/d(Cos2\phi)$ increases in all cases. Moreover, the value of ROC decrease with increase in incident energy for R_{LDM} while increase for R_{RR} nuclear charge radii parameterizations.

4.6 Summary

Summarizing the above work, it can be stated that a systematic study of the influence of nuclear charge radii parameterizations on the excitation function of reduced flow and elliptical flow as well as on the radius dependence of balance and transition energies has been presented over a wide composite mass number range and initial neutron-to-proton ratio range. It has been concluded that with increase in radius (while going from R_{LDM} to

R_{RR}) the repulsive nucleon-nucleon collisions gets suppressed which consequently reduces the pressure gradient at mid-rapidity region. The neutron-deficient nuclear reactions are more affected by change in the radii parameterizations than the neutron-rich nuclear reactions. The increase in E_{bal} and E_{trans} with increase in nuclear radius follows a power law fit. The elliptical flow has been found to be more sensitive towards different nuclear charge radii parameterizations as compared to reduced flow. Moreover, the isospin dependent nuclear charge radii parameterizations (R_{PP} and R_{RR}) are important to account for the isospin degree of freedom in the nuclear reaction dynamics. In addition to that, for collective flow, the theoretical calculations are appropriate with experimental data of FOPI, INDRA and ALADIN collaborations. The impression of mean field and spectator matter has been studied through the collision geometry dependence of reduced flow and elliptical flow. Thus the $\hat{b}_{bal}$ and $\hat{b}_{trans}$ are obtained for wide incident energy range. The importance of momentum constraint as per the nuclear charge radii parametrization has been presented through clusterization technique.

Chapter 5

Structural effects via different nuclear charge radii parameterizations on nuclear stopping with momentum dependent interactions

5.1 Introduction

Physics of nuclear reactions can be explained by knowing the relative motion of the fragments and the nuclear stopping. The degree of thermalization or nuclear stopping of colliding nuclear matter is an essential characteristics of heavy ion collisions (HICs) at intermediate energies, which determines that how much part of incident energy has been utilized in the production of fire ball (central compressed zone) and in raising its temperature leading towards the production of multiple fragments of different sizes. The estimation of this deposited energy (or utilized energy) describes the nature of compressed nuclear matter and in consequence of that its subsequent time evolution. Therefore, the study of nuclear stoping is of great interest to scrutinize the dynamics of HICs [185, 186, 310].

In 1984, Renfordt *et al.* [185] gave very first description of nuclear stopping for the reaction of $^{40}_{18}$Ar+$^{207}_{82}$Pb at incident energy of 772 MeV/nucleon and summarizes that a spherical shaped distribution is achieved in nearly central collisions which defines nuclear stopping power. The study of nuclear stopping provides the information about the fragmentation phase transition and thermalisation as well as expansion of the system [186].

The extensive study of nuclear reactions with different neutron-to-proton ratios is contributive to essence the nuclear equation of state (NEOS) and the isospin degree of freedom for isospin-asymmetric nuclear matter. In view of this, Yang and co-workers [311] observed that at low energy regime, nuclear stopping is sensitive to both isospin dependent nucleon-nucleon cross-section and symmetry potential. However, as the incident energy increases above Fermi energy, the impact of isospin dependent nucleon-nucleon cross-section is more pronounced compared to symmetry potential. In another study by Li and Li [312], the excitation function of nuclear stopping (the momentum quadrupole i.e. $< Q_{zz}/nucleon >$ and transverse-longitudinal ratio of momentum i.e. $< R >$) is found to be sensitive towards the isospin dependence of in-medium correction of two-body cross-section. However, a weaker dependence of global nuclear stopping on initial N/Z ratio of colliding nuclei as well as on symmetry potential has been reported.

Puri and collaborators [179, 313] investigated the nuclear stopping and its relation to the origin of light charged fragments with Isospin dependent Quantum Molecular Dynamics (IQMD) model. Their study reported that the magnitude of nuclear stopping depends strongly on isospin dependent nucleon-nucleon cross-section and weakly on symmetry energy. Efforts have been made to improve the sensitivity of symmetry energy on nuclear stopping by considering its various density-dependent parameterizations. This enlightened that the small sensitivity of nuclear stopping to different forms of density-dependent symmetry energy is due to the small variation in the instantaneous density of the nuclear matter [314]. The global stopping observable $< varxz >$, introduced in Ref. [315], defined as the ratio of the variances of the transverse to the longitudinal rapidity distributions, can be used in best way to correlate stopping and flow, demonstrating the common origin of two observable in the HICs at intermediate energies [176]. The $< varxz >$ observable is strongly dependent on isospin content of nucleon-nucleon cross-section [316]. FOPI Collaboration [206], widely examined the $< varxz >$, as a measure of degree of nuclear stopping in the central HICs at incident energies between 90 and 1500 MeV/nucleon for isospin-symmetric as well as isospin asymmetric nuclear reactions. In Ref. [317], authors widely studied the excitation functions of nuclear stopping observable (anisotropy ratio $< R >$) at the incident energies between 10 and 1200 MeV/nucleon. Their study reveals that the mean value of nuclear stopping reaches a minima near Fermi energy and maxima

around 400 MeV/nucleon. The experimental data provided by INDRA and ALADIN collaborations [208, 209] on the energy-based isotropy ratio $< R_E >$ and momentum-based isotropy ratio $< R_P >$ for a wide range of system mass reveals negligible effect of isospin content of colliding nuclei.

The isospin effects has been investigated through various entrance channel conditions like initial neutron-to-proton ratio and charge asymmetry as well as through various isospin dependent model ingredients like Coulomb potential, isospin dependent nucleon-nucleon cross-section and density dependent symmetry energy. One of the most fascinating topic of heavy ion collisions (HICs) is the structural effects on the nuclear reaction dynamics and its by-products. The another quantity which has been used to account for the isospin degree of freedom is the isospin dependent nuclear charge radii. In previous chapters, these different parameterizations have been proved to be a good probe to embellish the isospin effects on collective flow and multi-fragmentation. In this chapter, our aim is to study the initialization effects as well as isospin degree of freedom via different nuclear charge radii parameterizations (i.e. isospin independent [65] and isospin dependent [71, 77, 78, 80, 81] with additional isospin parameter term in $A^{1/3}$ dependence of nuclear charge radii) on the nuclear stopping of isospin-asymmetric reactions [318, 319]. Before discussing the calculations and results, various parameters for describing the nuclear stopping are explained in the following section.

5.2 Parameters for describing nuclear stopping

The degree of thermalization or equilibrium in the HICs can be studied through various observables. The global nuclear stopping/equilibrium can be measured by two quantities: (i) anisotropy ratio $< R >$ [185] and (ii) Quadrupole Moment $< Q_{zz} >$ [186]. The **"momentum-based anisotropy ratio"** $< R_P >$, defined as:

$$< R_P >= \frac{2}{\pi} \frac{[\sum_i^{A_{tot}} |p_\perp(i)|]}{[\sum_i^{A_{tot}} |p_\parallel(i)|]}, \tag{5.1}$$

and **"energy-based anisotropy ratio"** $< R_E >$ is defined as

$$< R_E >= \frac{2}{\pi} \frac{[\sum_i^{A_{tot}} |E_\perp(i)|]}{[\sum_i^{A_{tot}} |E_\parallel(i)|]}, \tag{5.2}$$

Here, the composite mass number of the system (A_{tot}) is the sum of the mass number of the projectile A_P and target A_T nuclei i.e. $A_{tot} = A_P + A_T$. The transverse energy

$E_{\perp}(i)$ and longitudinal energy $E_{\parallel}(i)$ of i^{th} particle defined as:

$$E_{\perp}(i) = \sqrt{E_x^2(i) + E_y^2(i)} \;\; and \;\; E_{\parallel}(i) = E_z(i), \tag{5.3}$$

Similarly, the transverse momentum $p_{\perp}(i)$ and longitudinal momentum $p_{\parallel}(i)$ of i^{th} particle defined as:

$$p_{\perp}(i) = \sqrt{p_x^2(i) + p_y^2(i)} \;\; and \;\; p_{\parallel}(i) = p_z(i), \tag{5.4}$$

The physical significance of R_P (or R_E) is the probability of transformation of longitudinal momentum (or energy) into the transverse momentum (or energy) [208,209]. The value of R_P (or R_E) between zero and unity, equals to zero, equals to unity and greater than unity conveys partial transparency, full transparency, complete stopping and super stopping respectively. The value of nuclear stopping greater than unity can be explained by the preponderance of transverse momentum [185]. The word *global* represents that this observable do not depend on the local density and thus indicate the equilibrium of the whole system. The quadrupole of single particle momentum distribution $< Q_{ZZ} >$ called **quadrupole moment**, defined as:

$$< Q_{ZZ} >= \sum_{i}^{A_{tot}} (2p_z^2(i) - p_x^2(i) - p_y^2(i)), \tag{5.5}$$

For present analysis, "inverse of $< Q_{ZZ} >$" has been studied because $< R >$ and $< Q_{ZZ} >$ behave in opposite fashion. For complete nuclear stopping, one can expect the values of $< Q_{ZZ} >$ equals to 0. The **"rapidity distribution"** of particles is also an indicator of nuclear stopping. The rapidity distribution is defined in Eqn. 4.3 in chapter 4. A sharp narrow Gaussian shape of rapidity distribution of particles indicates better thermalization compared to broad one. The rapidity distribution of entire nuclear matter expresses the global thermalization of the hot and dens matter. However, the rapidity distribution of particular fragment type define the nature of fragment emitting source and expresses the local thermalization. The another local observable to describe nuclear stopping is **"variances of the rapidity distributions"** denoted by "$< varxz >$", which is the ratio of the longitudinal variance of rapidity distribution of particles $varx$ to the transverse variance of rapidity distribution of particles $varz$. Mathematically, it is represented as [176]:

$$< varxz >= \frac{< varx >}{< varz >} = \frac{\sigma_x^2}{\sigma_z^2}. \tag{5.6}$$

Here $varx$ and $varz$ are calculated from the $FWHM$ (full width at half maxima) of the rapidity distribution along transverse and longitudinal directions respectively using the relation:

$$FWHM = 2.36\sqrt{variance}. \tag{5.7}$$

5.3 Results and discussion

In this section, our aim is at least four fold: (i) to observe the initialization effects via nuclear charge radii parameterizations on the nuclear stopping and its relations to distribution and production of light mass fragments for a wide range of system mass; (ii) to study how the isospin dependent nuclear charge radii parameterizations alters the isospin degree of freedom in the nuclear stopping for isobaric series of reactions; (iii) to pin down the influence of nuclear radius in the vicinity of momentum dependent interactions; and (iv) to compare the theoretical calculations of excitation function of nuclear stopping with the existing experimental data. This study is carried out by using IQMD model with isospin dependent nucleon-nucleon cross-section reduced by 10% i.e. $\sigma = 0.9\sigma_{nn}^{free}$ along with linear density dependent symmetry energy and soft equation of state [262]. Here, the nucleons are primarily initialized in a sphere of radius in accordance with the liquid drop model (R_{LDM}). The isospin effects are added in terms of three different isospin dependent parameterized forms of nuclear charge radii, i.e. R_{NGO}, R_{PP} and R_{RR} as discussed in Sec. 1.4 of chapter 1.

5.3.1 System size dependence on nuclear stopping

Simulations are carried out for central and semi-central isospin-asymmetric nuclear reactions of $^{50}_{20}$Ca+$^{50}_{20}$Ca, $^{90}_{36}$Kr+$^{90}_{36}$Kr, $^{100}_{40}$Zr+$^{100}_{40}$Zr, $^{124}_{50}$Sn+$^{124}_{50}$Sn, $^{150}_{60}$Nd+$^{150}_{60}$Nd and $^{197}_{79}$Au+$^{197}_{79}$Au ($N/Z = 1.5$) at E = 50 MeV/nucleon. Left panels of Fig. 5.1, shows the influence of nuclear charge radii on the rapidity distribution of light mass fragments (LMFs) [$2 \leq A \leq 4$] for central collisions of $^{50}_{20}$Ca+$^{50}_{20}$Ca (lighter) and $^{197}_{79}$Au+$^{197}_{79}$Au (heavier) respectively. The central panels [(b) and (c)] and right panels [(e) and (f)] represents, the influence of nuclear charge radii on the system size dependence of $< R_P >$ and $< \frac{1}{Qzz/nucleon} >$ respectively at scaled impact parameter of $\hat{b}$=b/b_{max}=0 (upper panel) and 0.5 (lower panel). Here, $b_{max} = (R_P + R_T)fm$, R_P and R_T are radii of target and pro-

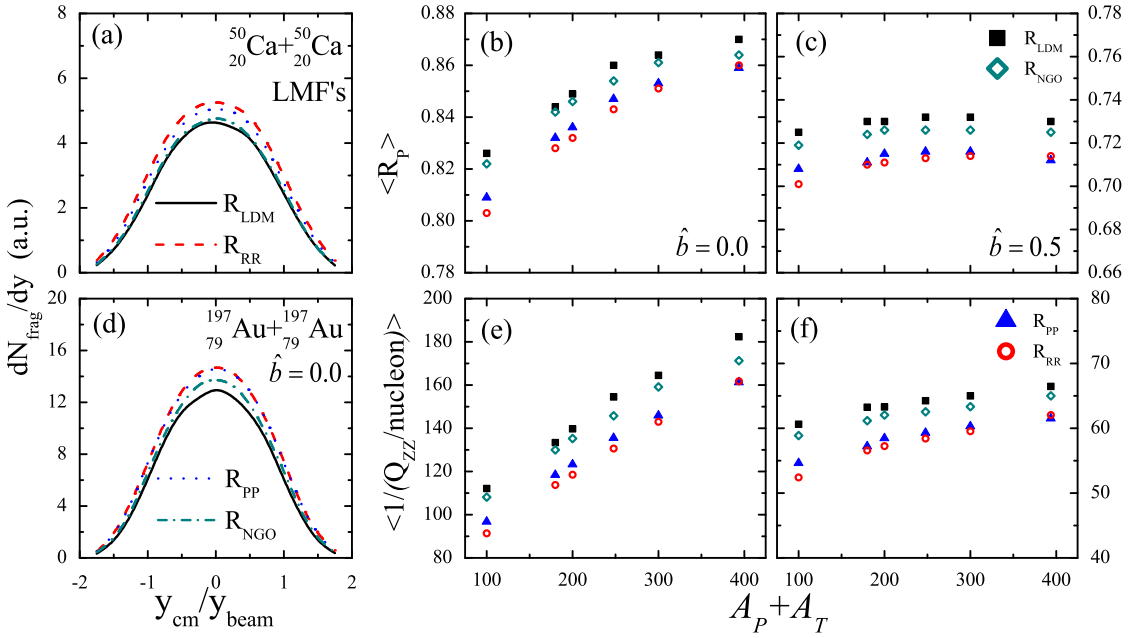

Figure 5.1: Panels (a) and (d) displays the rapidity distribution of LMF's for central $^{50}_{20}$Ca+$^{50}_{20}$Ca and $^{197}_{79}$Au+$^{197}_{79}$Au collisions respectively at E = 50 MeV/nucleon. Panels (b) and (c) represents $< R_P >$ whereas (e) and (f) represents $< 1/(Q_{ZZ}/nucleon) >$ as a function of system mass in central (upper panels) and semi-central (lower panels) collisions at E = 50 MeV/nucleon.

jectile nuclei. From Fig. 5.1, it has been observed that, for lighter system more particles are distributed near target rapidity and projectile rapidity which results in the broader Gaussian shape compared to heavier system. Moreover, a narrow Gaussian shape of distribution of particles indicates a better thermalization compared to broader Gaussian shape. Therefore, with increase in system mass, due to increase in density and temperature, more thermalisation is achieved and accordingly nuclear stopping increases. This observation is in supportive nature with the observation of Ref. [311].

Since the calculated radii of a particular nuclei increases as $R_{LDM} < R_{NGO} < R_{PP} < R_{RR}$. Therefore, Fig. 5.1 also reveals that the larger nuclear radii results in the enhancement of production of LMF's which is because of increase in the number of binary collisions. It has been noted that system mass dependence of nuclear stopping observable in Fig. 5.1 and multiplicity of LMF's in Fig. 3.3 follows the same trend which is in agreement with the findings of Refs. [179, 313]; however, due to increase in radius,

the multiplicity of fragments increases but in the present scenario, reduction in the nuclear stopping has been observed. This is because, the increment in radius intensifies the transverse and longitudinal momentum of nucleons, which enhances the multiplicity of fragments. Whereas, the probability of transformation of initial longitudinal momentum into transverse momentum is less with the larger radii. The increase in radius due to different isospin dependent nuclear charge radii parameterizations causes the transformation of longitudinal motion into transverse direction which consequently affect the degree of thermalization of the system. In other words, one can say that the percentage increment in the longitudinal momentum is more compared to transverse momentum, due to which nuclear stopping decreases. The percentage increment in radius is 12% for ${}^{50}_{20}Ca$ and 8% for ${}^{197}_{79}Au$ nuclei, corresponding to this change in radius, for central collisions the value of $< R >$ (or $< \frac{1}{Qzz/nucleon} >$) changes by 3% (or 18%) for ${}^{50}_{20}$Ca+${}^{50}_{20}$Ca and 1.1% (or 11%) for ${}^{197}_{79}$Au+${}^{197}_{79}$Au when switching from R_{LDM} to R_{RR}. Also, the dependence of nuclear stopping on system mass diminishes as the participant matter goes on reducing with increase in colliding geometry while the initialization effects via nuclear charge radii on nuclear stopping remains the same for central and semi-central collisions.

5.3.2 Initial $< N/Z >$ dependence of global nuclear stopping observables

Further, to observe the isospin effects on the N/Z dependence of nuclear stopping, the isobaric series of reactions of ${}^{80}_{z_1}$X+${}^{80}_{z_1}$X (having total mass number = 160 a.m.u. with charge, z_1 = 30, 32, 34, 36, 37, 38 and 40) and ${}^{120}_{z_2}Y$ +${}^{120}_{z_2}$ Y (having total mass number = 240 a.m.u. with charge, z_2 = 46, 48, 50, 52, 54, 56 and 60) have been simulated for semi-central collisions at E = 50 MeV/nucleon. Fig. 5.2 display the initial N/Z ratio of colliding nuclei dependence of $< R_P >$ (upper panels) and $< 1/(Q_{ZZ}/nucleon) >$ (lower panels) for the isobaric series of reaction with A_{tot} = 160 a.m.u. (left panels) and A_{tot} = 240 a.m.u. (right panels). This figure reveals that the magnitude of nuclear stopping parameters is same for both the reaction series, since at semi-central collisions, system size effects on nuclear stopping is very feeble. With increase in calculated radii, the magnitude of nuclear stopping reduces which is already discussed in the previous section. Referring to Fig. 3.4, it has been concluded that the N/Z dependence of multiplicity of fragments is slightly affected by including isospin dependent nuclear charge radii. Whereas from

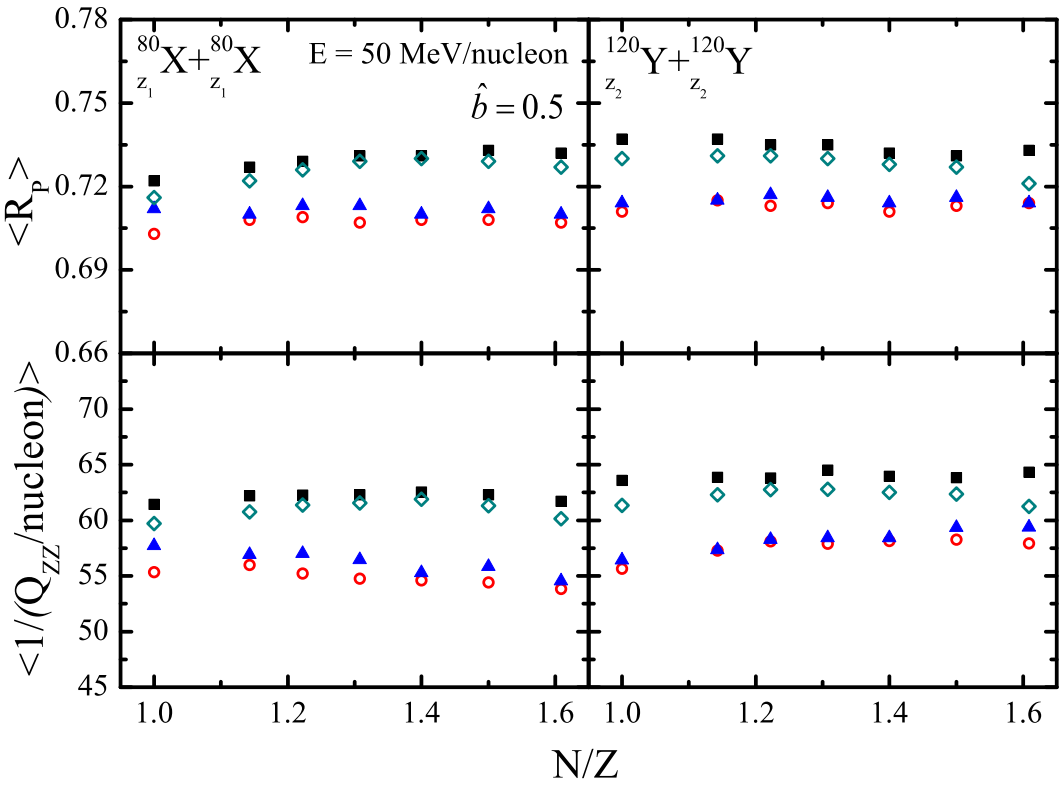

Figure 5.2: Nuclear stopping observable $< R >$ (left panels) and $< 1/(Q_{ZZ}/nucleon) >$ (right panels) as a function of neutron-to-proton ratio in semi-central collisions of two isobaric series with mass 80 (lower panels) and 120 (upper panels) units at E = 50 MeV/nucleon. Symbols have the same meaning as in Fig. 5.1.

Fig. 5.2, one can see that the behaviour of nuclear stopping is independent towards N/Z content of colliding partners even if one consider isospin dependent nuclear charge radii parameterizations for both the reaction series. Hence, isospin effects on the N/Z dependence of nuclear stopping through isospin dependent nuclear charge radii parametrization is very feeble. The percentage reduction in the parameter of nuclear stopping is same through out the N/Z ratio range which signifies the system mass effects only.

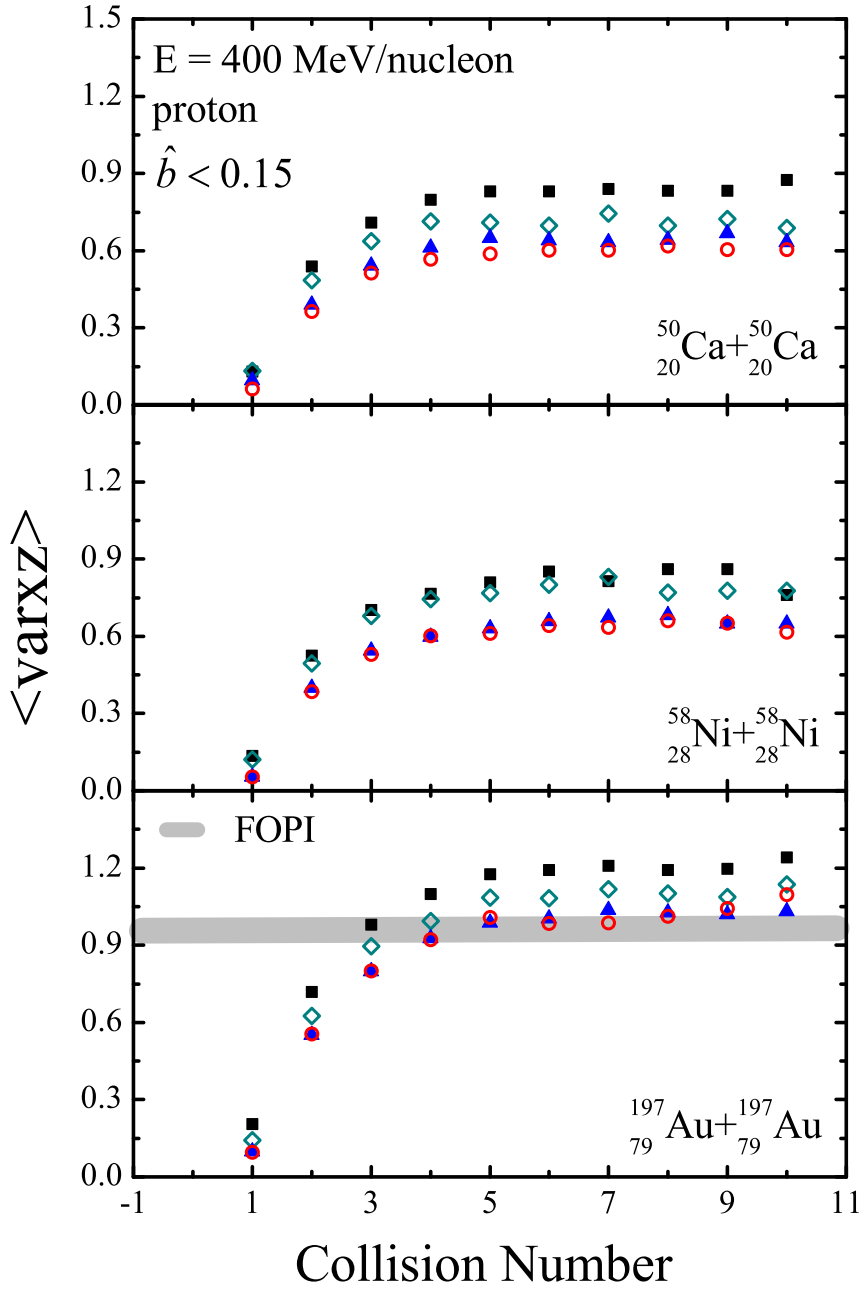

Figure 5.3: The collision number dependence of $< varxz >$ for the reactions of $^{50}_{20}$Ca+$^{50}_{20}$Ca (upper panel), $^{58}_{28}$Ni+$^{58}_{28}$Ni (middle panels) and $^{197}_{79}$Au+$^{197}_{79}$Au (lower panel) at E = 400 MeV/nucleon for different radii parameterizations.

5.3.3 Effect of nuclear radii parameterizations on the equilibrium using collision dynamics

The study of nuclear stopping provides the information about the thermalisation as well as expansion of the system [186, 320]. The preservation of the initial memory of nucleons is directly related with the number of collisions it suffers. In the HICs, a nucleon of one nucleus can collide with many nucleons of other nucleus and after each collision it loses some part of its energy. The amount of energy lost describes the nuclear stopping. Now, it would be of great interest to ruminate that how many collisions are sufficient to stop the nucleon completely. Therefore, this section intend to study the effect of different nuclear charge radii parameterizations on the equilibrium using collision dynamics. To study the nuclear stopping through the collision dynamics, simulations have been carried out for the reactions of $^{50}_{20}$Ca+$^{50}_{20}$Ca, $^{58}_{28}$Ni+$^{58}_{28}$Ni and $^{197}_{79}$Au+$^{197}_{79}$Au at E = 400 MeV/nucleon and scaled impact parameter, $\hat{b} < 0.15$. The collision geometry has been selected as per the experimental data of FOPI Collaboration [206].

Fig. 5.3 displays the dependence of $< varxz >$ on collision number of protons at an incident energy of 400 MeV/nucleon and $\hat{b} < 0.15$ for the reactions of $^{50}_{20}$Ca+$^{50}_{20}$Ca (upper panel), $^{58}_{28}$Ni+$^{58}_{28}$Ni (middle panel) and $^{197}_{79}$Au+$^{197}_{79}$Au (lower panel). The figure reveals that, more is the particle collides, more equilibrium is achieved and hence the nuclear stopping increases. The study carried out by using QMD model in Ref. [321], suggested that the nucleon suffering at least 10 collisions is the most thermalize and hence close to complete equilibrium. However from present calculations by using IQMD model, one can interestingly notice that the nuclear stopping variable $< varxz >$ becomes almost independent of collision number as the collision number exceeds from five which means that on average, those nucleons which have experienced at least five collisions are close to complete equilibrium. This observation is appropriate for all the reactions as well as for all the radii parameterizations studied here. It has been observed that the change in radius has sizeable effect on the $< varxz >$. The value of $< varxz >$ decreases with increase in radii. The percentage reduction in the magnitude of $< varxz >$ (above five collisions) is $\sim$ 30%, $\sim$ 24% and $\sim$ 14% for the reaction of $^{50}_{20}$Ca+$^{50}_{20}$Ca, $^{58}_{28}$Ni+$^{58}_{28}$Ni and $^{197}_{79}$Au+$^{197}_{79}$Au respectively, as one switches from R_{LDM} to R_{RR}. Therefore, the lighter systems are good probe to study the role of nuclear charge radius on the nuclear stopping observable as

compared to heavier colliding nuclei pair. This observation strengthen the conclusion of Fig. 5.1. The solid line (grey) in the figure presents the experimental data for the reaction of $^{197}_{79}$Au+$^{197}_{79}$Au $\hat{b} < 0.15$ for protons [206]. The thickness of line corresponds to the experimental value including the error bar (i.e. $< varxz > = 0.95 \pm 0.05$).

5.4 Effect of nuclear radius along with momentum dependent interactions (MDI)

The compressibility achieved in the nuclear reaction is dependent upon the density of central overlapping zone as well as on the momentum plane. In the reaction dynamics, during the early stage of collision phase, the interaction between the nucleons also depends upon the momentum they acquire. This exchange of momentum during the interaction leads to momentum dependence of mean field. In the initial stage when both target and projectile nuclei are approaching towards each other and have not overlapped yet, the momentum gained by the nucleons is less and the momentum dependent interactions (MDI) are not remarkable. But as both the nuclei overlap each other and the projectile nucleons with high momentum comes closer to target nucleons, they feel a repulsive force. However, the potential in the spectator region is comparatively attractive. This potential gradient affects the various observables of HICs at intermediate energies significantly.

The momentum dependent nuclear equation of state is capable of breaking the spectators into further small fragments which reduces the multiplicity of heavier fragments like IMFs and HMFs [322]. As, the fragmentation pattern generated with NEOS by including and excluding MDI is different, hence, the properties of these fragments like collective flow, rapidity distribution and stopping power of nuclei will also be different. In a tremendous work by Kumar *et al.* [197, 323], the isospin effects have been investigated with and without MDI using IQMD model for the system size dependence of multi-fragmentation and nuclear stopping for a wide range of composite system mass. Their study draws the conclusion that the NEOS with MDI are able to break the initial bonding of nucleon in the smaller colliding nuclei giving opportunity to study their properties which is however, not possible in the NEOS without MDI case. MDI suppresses the magnitude of nuclear stopping and enhances the isospin effects through symmetry energy on nuclear stopping. In the recent article on the role of different potentials on excitation function

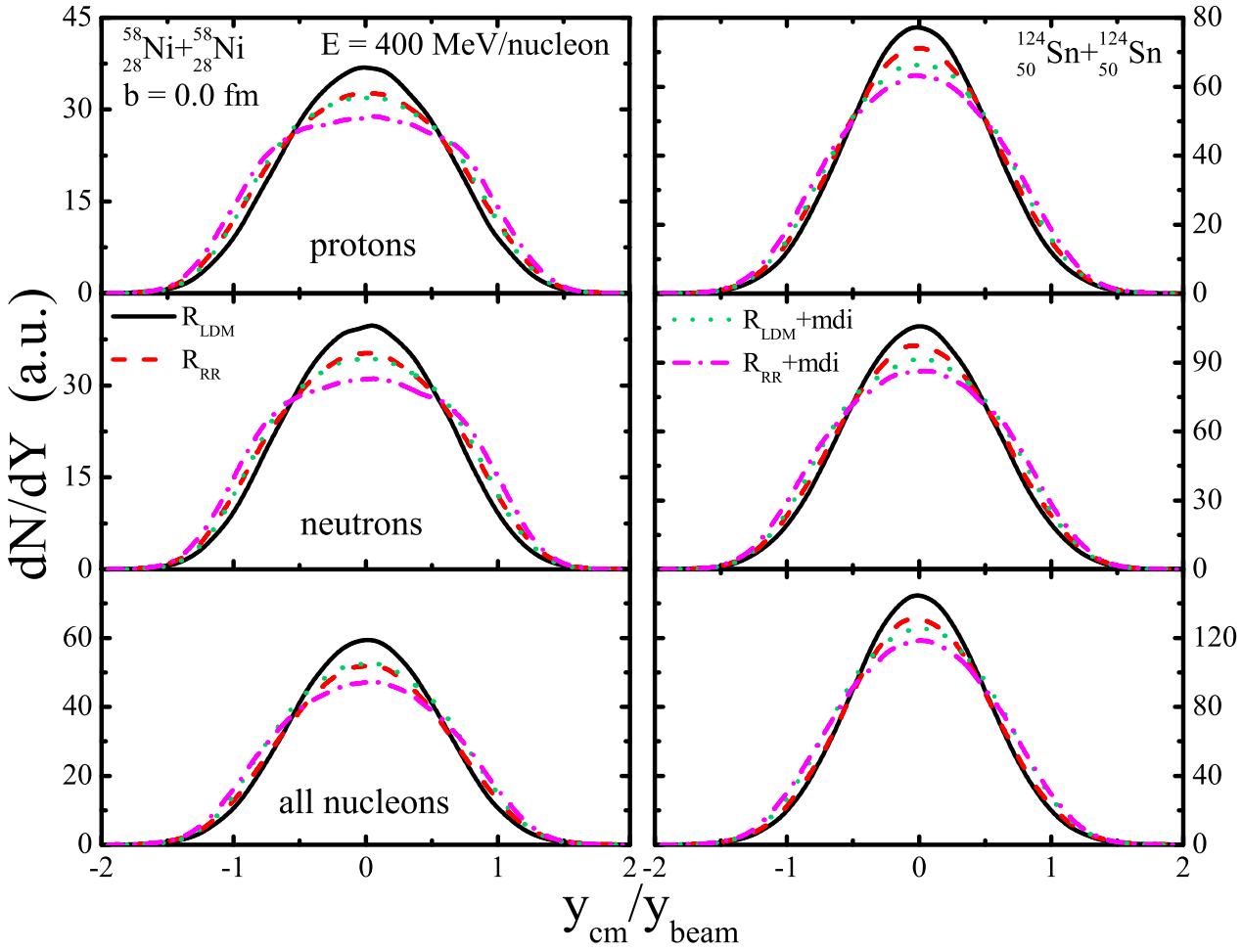

Figure 5.4: The rapidity distribution dN/dY for the reaction of $^{58}_{28}$Ni+$^{58}_{28}$Ni (left panels) and $^{124}_{50}$Sn+$^{124}_{50}$Sn (right panels) at incident energy of 400 MeV/nucleon. The top, middle and bottom panels are for protons, neutron and all nucleons respectively.

of nuclear stopping, the MDI affects the stopping power in large extent at low beam energies [201]. It has been shown in Refs. [324, 325] that the soft nuclear equation of state with momentum dependent interactions (SMD) are better to explain the evolution of nuclear reaction and its density-temperature relation than the hard nuclear equation of state without MDI.

Since, the increase in radii of colliding nuclei affects the momentum of the nucleons [279, 304] and the momentum dependent interactions (MDI) (as explained in chapter 2) also play crucial role to understand the relative interaction of the nuclear matter [197], hence the present exercise is carried out to focus on the influence of different nuclear charge radii parameterizations in the vicinity of MDI. Also, it is worth mentioning that, the study

made in the previous sections for structural effects via nuclear radii parametrization on nuclear stopping has been carried out at a particular energy i.e. E = 50 MeV/nucleon. Now, it is crucial to know that how the dominance of longitudinal momentum due to increase in radius changes with the entire range of the intermediate energy regime. Therefore, in the vicinity of above discussion, it would be interesting to explore the influence of nuclear charge radii parameterizations on the nuclear stopping along with MDI and see if it would help in better agreement of theoretical calculation with the experimental data.

5.4.1 Rapidity dependence of nucleons in final state

To study the rapidity dependence of nucleons in the final state, the reactions of $^{58}_{28}$Ni+$^{58}_{28}$Ni and $^{124}_{50}$Sn+$^{124}_{50}$Sn at an incident energy E = 400 MeV/nucleon for b = 0 fm (i.e. central collisions) have been simulated. Since, isospin dependent nuclear charge radii parameterizations does not quantify the isospin effects, therefore, the reactions are studied only for two parameterizations R_{LDM} and R_{RR} to investigate only structural effects on nuclear stopping along with MDI. Fig. 5.4 displays the influence of nuclear charge radii parameterizations on the rapidity distribution (as an indicator for nuclear stopping) of all protons (p) (upper panels), all neutrons (n) (middle panels) and all nucleons (N) (lower panels) for the reactions of $^{58}_{28}$Ni+$^{58}_{28}$Ni (left panels) and $^{124}_{50}$Sn+$^{124}_{50}$Sn (right panels) initialized with R_{LDM} (solid lines) and R_{RR} (dash lines). The doted and dash-dotted lines represent the calculation with R_{LDM} and R_{RR}, respectively, which includes the momentum dependence in the nuclear mean field i.e. R_{LDM}+MDI and R_{RR}+MDI respectively. From Fig. 5.4, it is observed that the Gaussian shape distribution becomes broader as the radii parametrization switched from R_{LDM} to R_{RR}. This is because the calculated radii of $^{58}_{28}$Ni and $^{124}_{50}$Sn with R_{LDM} parametrization are lesser than the calculated radii with R_{RR} parametrization. Therefore, the increase in radius shifts some of the nuclear matter from mid-rapidity zone to the projectile as well as target like rapidity zone in equal amount. This concludes that the compression in the participant zone is lesser in the case of R_{RR} compared to R_{LDM} which signalizes the less number of binary collisions.

The inclusion of MDI reduces the stability of nuclei [326, 327], which further reduces the peak value of dN/dY. The percentage increment in radius of $^{58}_{28}$Ni and $^{124}_{50}$Sn nuclei are 13.98% and 8.85% respectively, while switching from R_{LDM} to R_{RR}. Corre-

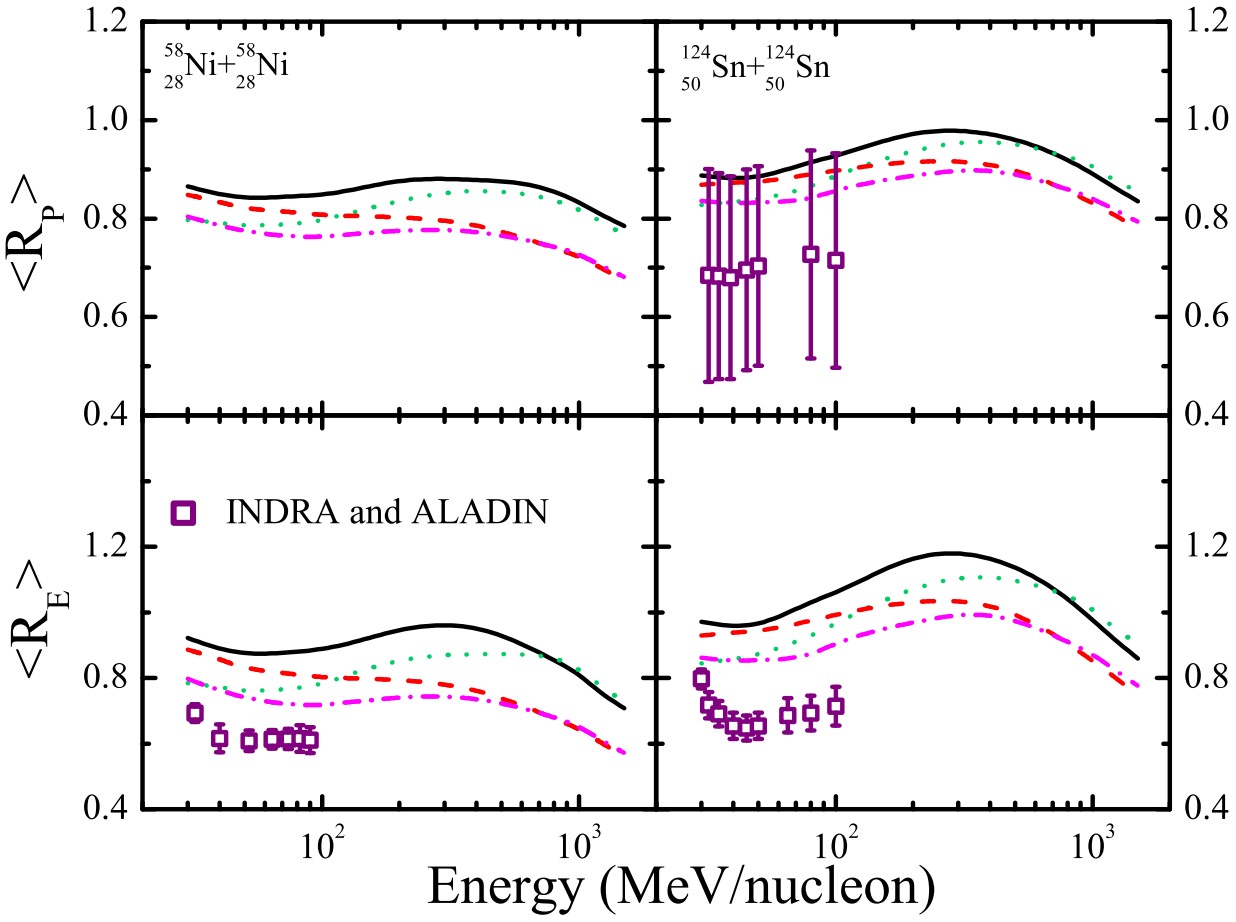

Figure 5.5: Incident energy dependence of R_P (upper panels) and R_E (lower panels) for the reactions of $^{58}_{28}$Ni+$^{58}_{28}$Ni (left panels) and $^{124}_{50}$Sn+$^{124}_{50}$Sn (right panels). The different lines have same meaning as in Fig. 5.4.

sponding to this increase in radius, the peak value of dN/dY reduces 11.1% (p), 12.5% (n) and 13.6% (N) for $^{58}_{28}$Ni+$^{58}_{28}$Ni and 7 % (p), 7.6 % (n) and 9.65 % (N) for $^{124}_{50}$Sn+$^{124}_{50}$Sn without MDI. On the other hand these percentages are 6.45 % (p), 8.8 % (n) and 9.6 % (N) for $^{58}_{28}$Ni+$^{58}_{28}$Ni and 4.5% (p), 6.6% (n) and 5.6% (N) for $^{124}_{50}$Sn+$^{124}_{50}$Sn with MDI. This information clearly indicates that the inclusion of MDI reduces the influence of nuclear charge radii parameterizations on the rapidity distribution. However, the peak value of rapidity distribution is more broader for R_{RR} radius parametrization which includes MDI (i.e. R_{RR}+MDI). This quantifies both radius as well as MDI effect.

5.4.2 Excitation function of nuclear stopping

To see how the radii parameterizations as well as the MDI affect the reaction dynamics throughout the energy range, the excitation function of nuclear stopping has been studied at incident energies between 30 MeV/nucleon to 1.5 GeV/nucleon. Fig. 5.5 display the influence of nuclear charge radii parameterizations by including as well as excluding MDI for the reactions of $^{58}_{28}$Ni+$^{58}_{28}$Ni (left panels) and $^{124}_{50}$Sn+$^{124}_{50}$Sn (right panels) on the nuclear stopping of protons (as per the available experimental data). To estimate the stopping power momentum-based (R_P) and energy-based (R_E) anisotropy ratio has been used. From Fig. 5.5, one can see that the value of stopping is relatively small at low incident energies and the rising part is due to decreasing effect of Pauli-blocking. The maximum value of stopping has been obtained around 400 MeV/nucleon. Also, when energy exceeds 400 MeV/nucleon, the value of nuclear stopping falls gradually because of the ineffective role of Pauli-blocking. The influence of isospin dependent nuclear charge radius on nuclear stopping is more around 400 MeV/nucleon. The nuclear charge radii parametrization starts affecting the magnitude of nuclear stopping observable above 50 MeV/nucleon. This effect increases with increase in energy up to 800 MeV/nucleon and becomes constant above 800 MeV/nucleon. This reveals that, at relatively low incident energies (i.e. below 50 MeV/nucleon), the predominance of longitudinal momentum (or energy) over transverse momentum (or energy) is very feeble. With increase in incident energy the longitudinal momentum (or energy) starts dominating the reaction dynamics.

The inclusion of MDI further reduces the values of R_P and R_E. The influence of MDI is more effective at lower energies and vanishes as the energy increases. Hence, it is clear from the figure that the isospin dependent radii parametrization along with MDI reduces the gaps between the theoretical calculations and experimental findings of INDRA and ALADIN [208, 209] collaborations. Moreover, Fig. 5.4 and 5.5 also verifies the previous conclusion that the lighter nuclei are good probe to study the role of nuclear charge radii parameterizations on the nuclear stopping.

5.5 Summary

In summary, the structural effects through different nuclear charge radii parameterizations have been studied on the various observables of nuclear stopping for a wide range

of composite system mass and initial neutron-to-proton ratio. In addition to that the study has also been made on the role of nuclear charge radii in the vicinity of momentum dependent interactions. The results concludes that the increment in radii increases the momenta of particles which consequently enhances the fragments multiplicity. However, the increase in the longitudinal momentum is more compared to transverse momentum which results in the reduction of nuclear stopping. The nuclear stopping is found to be independent to the initial neutron-to-proton ratio of colliding nuclei for isospin independent as well as dependent nuclear charge radii parameterizations. Moreover, the study also reveals that in the IQMD model at least five collisions (on average) are sufficient for a nucleon to completely loose its energy. In addition to that, the R_{RR} radii parameterizations along with MDI is able to describe the experimental data of energy as well as momentum based anisotropy ratio provided by INDRA and ALADIN collaborations.

Chapter 6

Initialization effects on thermalization with mass-asymmetry

6.1 Introduction

In the heavy ion collisions (HICs), the multifragmentation and nuclear stopping essentially depends on incident energy (E), collision geometry (b), mass of the colliding nuclei (A_P, A_T) and mass-asymmetry $\eta = |A_T - A_P/A_T + A_P|$ [328]. Here A_T and A_P are mass-number of target and projectile nuclei respectively. Apparently η=0 corresponds to completely mass-symmetric collisions and the distribution of fragments is spherical whereas, mass-asymmetric collisions having non-zero η leads to non-spherical distribution at central collision geometry. The reaction dynamics and the by-products are entirely different for reactions with different values of η.

The different reaction outcomes in the mass-symmetric and mass-asymmetric nuclear reactions provide qualitative understanding of the different processes and nuclear dynamics involved [329]. A phenomenological study of these reactions can provide an information about the energy dissipation and nuclear equation of state (NEOS) of mass-asymmetric nuclear matter [330]. The study of these reactions (by keeping the total mass of the system same), actually conveys the structural effects where the total number of nucleons are equal with different combinations of the size of projectile and target nuclei [331]. The nuclear charge radii is the another entrance channel parameter which is essential to initialize the nuclear matter in the HICs and it affects the reaction dynamics very drastically [104,106]. From the literature, it has been concluded that the nuclear reaction dynamics is very much sensitive towards the structural effects. These declared facts form the basis to study the role of nuclear charge radii parameterizations on the thermal equilibrium in the nuclear

reactions (mass-symmetric and mass-asymmetric) at all geometry conditions. Although in the previous chapters, the dynamics of symmetrically heavy nuclei is prominently studied with different parameterizations of nuclear charge radii. Now it is intended to study the comparable role of different nuclear charge radii parameterizations on the fragmentation and nuclear stopping in the mass-symmetric and mass-asymmetric collisions [332, 333].

6.2 Theoretical interpretation of density and temperature

Apart from discussed parameters of nuclear stopping in the previous chapter, the thermalisation is also related to the temperature and density of the nuclear matter during early stage of compression. The increment in the radius affects the transverse as well as longitudinal momentum of nucleons from the initial state to the final fragment production stage of the reaction. The thermalization of the nuclear matter is completely related to the momentum of the nucleons. The normal nuclear matter density is defined as [244,334]:

$$\rho(r,t) = \sum_{i=1}^{A_T+A_P} \frac{1}{(2\pi L)} exp[-(\vec{r} - \vec{r_i})^2/2L]. \tag{6.1}$$

Here, $\vec{r_i}$ is the position co-ordinate of i^{th} particle. The density of the nuclear matter has been calculated in a central sphere of radius r = 2 fm. In this process the calculations of density yields two possibilities. In the first possibility, $< \rho^{max} >$ is calculated by looking at the maximum density reached in that sphere. On the other hand, the second possibility calculates the average value of density $< \rho^{avg} >$ over the whole sphere. If the nuclear matter is uniformly distributed in the sphere, then the values of $< \rho^{max} >$ and $< \rho^{avg} >$ are almost same.

The temperature of the system is also associated with the compression achieved during the reaction. Only a complete thermalized and equilibrated nuclear matter can have a true temperature. However, in the HICs at intermediate energies, the nuclear matter is in the non-equilibrium stage. Therefore, direct consideration of temperature is not possible and one has to opt for local environment. The temperature (T) is extracted from the volume element surrounding the position of each nucleon in the co-ordinate space at every time step. This method is based on the local density approximation which is associated with the well established hot Thomas-Fermi approach [335]. This formalism

determine the value of temperature from the local density, kinetic energy and entropy with the help of momentum distributions. The momentum distribution of nucleons in a hot nuclear matter at a temperature T is given by the Fermi dirac distribution as:

$$n(k,t) = \frac{1}{1 + exp\{[\epsilon(k) - \mu]/T\}} \tag{6.2}$$

Here $\epsilon(k)$ is the energy of the nucleon with momentum k. The chemical potential μ is determined by the normalization to a given density of the nuclear matter ρ as:

$$\rho = \frac{g}{(2\pi)^3} \int n(k)dk, \tag{6.3}$$

where g (=4) is the spin-isospin degeneracy of a nucleon with momentum k. The effective mass approximation for the single particle energies ϵ (k) is defined as:

$$\epsilon(k) = \frac{\hbar^2 k^2}{2m} \; + \; U(k) \simeq \frac{\hbar^2 k^2}{2m^*} \; + \; U(0), \tag{6.4}$$

Therefore using above equation, the Eqn. 6.2 can be written as:

$$n(k,t) = \{1 + exp[\frac{\hbar^2 k^2}{2m^* T} - \eta]\}^{-1} \tag{6.5}$$

Here, η = (μ - U(0))/T. With this the nuclear matter can be used to tabulate the entropy densities and kinetic energy for different temperatures and densities. The kinetic energy density ($\hbar^2\tau$/2m) and the entropy σ can be defined as:

$$\tau = \frac{g}{(2\pi)^3} \int k^2 n(k)dk, \tag{6.6}$$

$$\sigma = -\frac{g}{(2\pi)^3} \int \{n(k) \; ln \; n(k) + [1 - n(k)] \; ln[1 - n(k)]\}. \tag{6.7}$$

For single nuclear matter limit, the integration in Eqs. 6.3, 6.6 and 6.7 can be accomplished in a standard manner [336]. However, for the limits T $\longrightarrow$ 0 and $\sigma \longrightarrow 0$; the density ρ and τ corresponds to the results of the Thomas-Fermi formalism at temperature T = 0. At the decomposition stage of the reaction, the relative momentum (k_R) becomes very less and differs significantly from zero. Thereupon, one has to consider the momentum distribution consisting of two interpenetrating Fermi spheres to be deformed. The nuclear matter densities in the two Fermi spheres is given by:

$$\rho_i = \frac{g}{(2\pi)^3} \int_{V_i} n(k)dk, \tag{6.8}$$

where indices i = 1, 2 represent the nucleons in the first (F_1) and second (F_2) fermi spheres, respectively. V_1 and V_2 are the volumes in the momentum space. Considering the normalization to the nuclear matter densities in the two Fermi spheres F_1 & F_2 the kinetic energy density ($\hbar^2\tau/2$m) and the entropy density σ are defined as:

$$\tau_i = \frac{g}{(2\pi)^3}\int_{V_i} k^2 n(k) dk, \tag{6.9}$$

and

$$\sigma_i = -\frac{g}{(2\pi)^3}\int_{V_i} \{n(k)\ ln\ n(k) + [1-n(k)] \\ ln[1-n(k)]\} \tag{6.10}$$

The integrations of above two equations must be performed over the cylindrical coordinates k_r and k_z with the center chosen as that of the big sphere (F_1). To calculate the local temperature at each point in a sphere of radius 'r' at each time step, the matter density and kinetic energy densities of target and projectile are required. These are given as [244, 334, 337]:

$$\rho_T(r,t) = \sum_{i=1}^{A_T} \rho_i(r,t), \qquad \rho_P(r,t) = \sum_{i=1}^{A_P} \rho_i(r,t) \tag{6.11}$$

and

$$\tau_T(r,t) = \sum_{i=1}^{A_T} \frac{p_i^2}{2m}\rho_i(r,t), \qquad \tau_P(r,t) = \sum_{i=1}^{A_P} \frac{p_i^2}{2m}\rho_i(r,t) \tag{6.12}$$

where $\rho_i(r,t)$ has been stated above in equation 6.1.

The nuclear matter densities and kinetic-energy densities are calculated with respect to the position of each particle in each time step. Using these four values, one can determine the Fermi energies, the local temperature T and the relative momentum k_R. This methodology made the extraction of local temperature in the heavy-ion collisions as simple as the density calculation. Using this formulation, the average temperature and density have been extracted within a central sphere of two fermi radius.

6.3 Result and discussion

The present work has been done by using Isospin-dependent Quantum Molecular Dynamics (IQMD) model and the temperature of the nuclear system is calculated by

using the formalism: the Hot Thomas-Fermi approach [244, 334]. The simulations have been carried out for the reactions of $^{50}_{20}$Ca+$^{50}_{20}$Ca (η=0.0) and $^{14}_{7}$N+$^{86}_{36}$Kr (η=0.7) with fixed composite system mass number A_{tot} = 100 a.m.u. and for the reactions of $^{124}_{50}$Sn+$^{124}_{50}$Sn (η=0.0) and $^{38}_{18}$Ar+$^{210}_{82}$Pb (η=0.7) with A_{tot} = 248 a.m.u. over the entire range of collision geometry at incident energy of 100 MeV/nucleon.

6.3.1 Time evolution of average density and temperature

To observe the role of radius on thermalization, the time evolution of the average scaled density ($< \rho^{avg}/\rho_o >$) and average temperature ($< T^{avg} >$) of the nuclear system has been examined as shown in upper and lower panels of Fig. 6.1 respectively, for the central mass-symmetric reaction ($^{50}_{20}$Ca+$^{50}_{20}$Ca) (left panels) and mass-asymmetric reaction ($^{14}_{7}$N+$^{86}_{36}$Kr) (right panels). The different lines in the figure corresponds to different nuclear charge radii parameterizations i.e. R_{LDM}, R_{NGO}, R_{PP} and R_{RR}. Here, ρ^{avg} is the instantaneous density of all nucleons and ρ_o is ground state density which is 0.17 fm^{-3} in the IQMD model. The same observation has been made for the reactions of $^{124}_{50}$Sn+$^{124}_{50}$Sn and $^{38}_{18}$Ar+$^{210}_{82}$Pb (results not shown here). The conclusion is same as for the reactions of $^{50}_{20}$Ca+$^{50}_{20}$Ca and $^{14}_{7}$N+$^{86}_{36}$Kr. For both types of reactions (mass-symmetric and mass-asymmetric), with increase in nuclear radius, the average scaled density of the nuclear system decreases apparently from initial level up to the time, t $\approx$ 20 fm/c. The role of radius on $< \rho^{avg}/\rho_o >$ is maximum during the highly dense phase of the reaction when both the target and projectile nuclei completely overlap each other and diminishes as the system starts expanding. The increment in radius consequently enhance the momentum of all nucleons and the average temperature of the system increases. This influence of radius on average temperature is maximum at t $\approx$ 10-20 fm/c and reduces slowly as the system cools down. One can observe that the time at which the average scaled density and temperature attains its maximum value also increase with increase in radius which reveals that the nuclear system will take more time to saturate and cool down with large radius. This observation is also in agreement with study made in Fig. 3.2 of chapter 3.

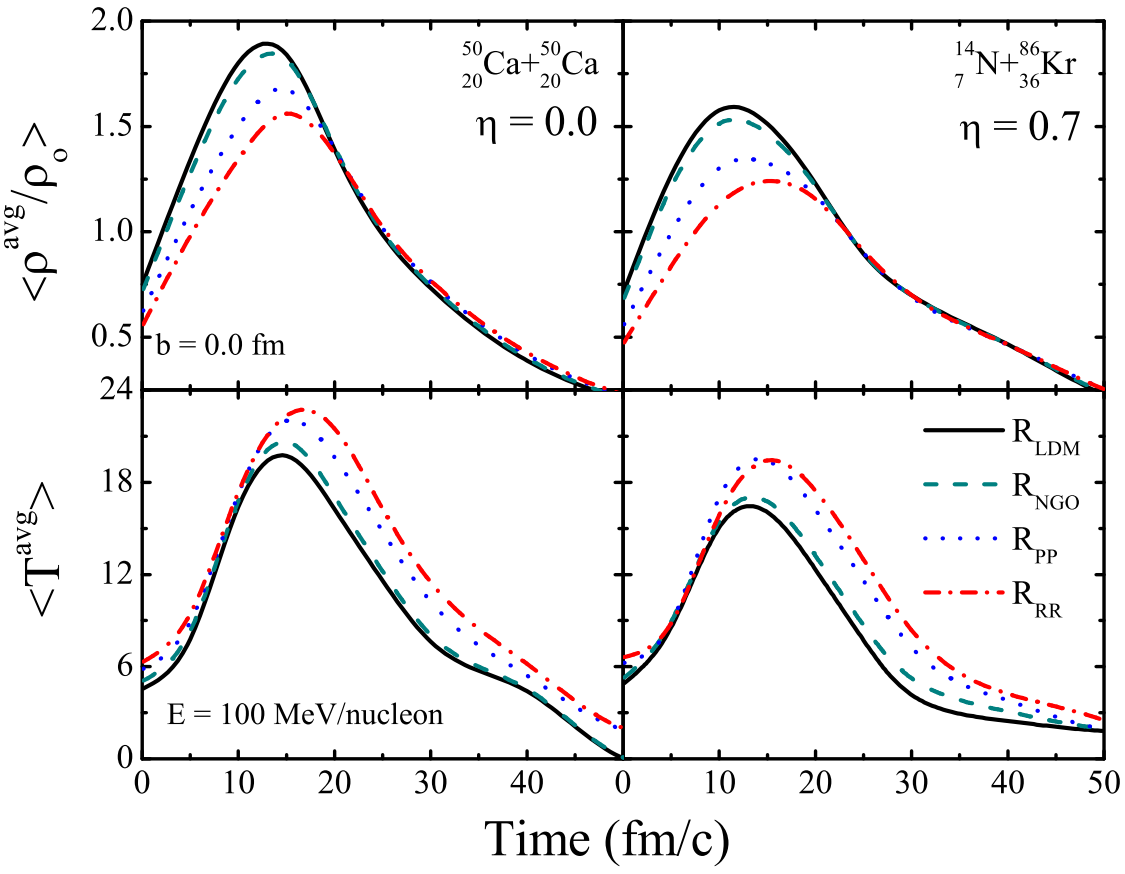

Figure 6.1: The time evolution of average scaled density (upper panels) and average temperature (lower panels) for central mass-symmetric (left panels) and mass-asymmetric (right panels) collisions with A_{tot} = 100 a.m.u. at E = 100 MeV/nucleon for four different nuclear charge radii parameterizations (described by various lines).

6.3.2 Correlation between maximal value of average temperature and nuclear stopping

The comparable role of radius on the average scaled density and temperature is different at different time for mass-symmetric as well as mass-asymmetric reactions. Therefore as a next step, the role of radius on thermalization has been studied by analyzing the maximal value of average temperature ($< T^{avg} >_{max}$) of the highly complex nucleonic matter achieved during the time span of the nuclear reaction and momentum based anisotropy ratio i.e. $< R_P >$. It is clear from the literature [180, 338–340], that the maximal average temperature and nuclear stopping decreases with increase in scaled impact parameter i.e. $\hat{b}$ = b/b$_{max}$ where, b$_{max}$ = $(R_P + R_T)fm$, (R_P and R_T are radii of target and projectile nuclei respectively). Therefore, the present study is also focused on the direct correlation between the temperature and the nuclear stopping of mass-symmetric and mass-asymmetric nuclear reaction. Fig. 6.2 displays the maximal value of average temperature (achieved at t $\approx$ 10-20 fm/c) as a function of nuclear stopping at t = 200 fm/c for mass-symmetric (left panels) and mass-asymmetric (right panels) nuclear reactions having A_{tot} = 100 a.m.u. (upper panels) and 248 a.m.u. (lower panels) at E = 100 MeV/nucleon. The calculations have been done at six different collision geometries described by various symbols and for four different nuclear charge radii parameterizations described by various lines (i.e. R_{LDM}, R_{NGO}, R_{PP} and R_{RR}) in the figure.

For mass-symmetric reactions, the curves presenting the correlation, first increases with decrease in $\hat{b}$ and then shows saturation effect. This happen because, while going from semi-central to central collisions, the nuclear stopping still increases but the temperature of the system is not interestingly modified. Whereas, in the mass-asymmetric reactions, the curve shows straight line behavior, which means $< T^{avg} >_{max}$ and $< R_P >$ increases monotonically with decrease in collision geometries. This is because, in the mass-symmetric reaction, the percentage participant matter (the nuclear matter which takes part in the collision process) is almost the same in central and nearly central collisions, whereas, the participant matter increases with decrease in $\hat{b}$ in the mass-asymmetric reactions.

It has been already observed from chapter 5 that the nuclear stopping of mass-symmetric reactions decreases with increase in radius. This observation also holds true for

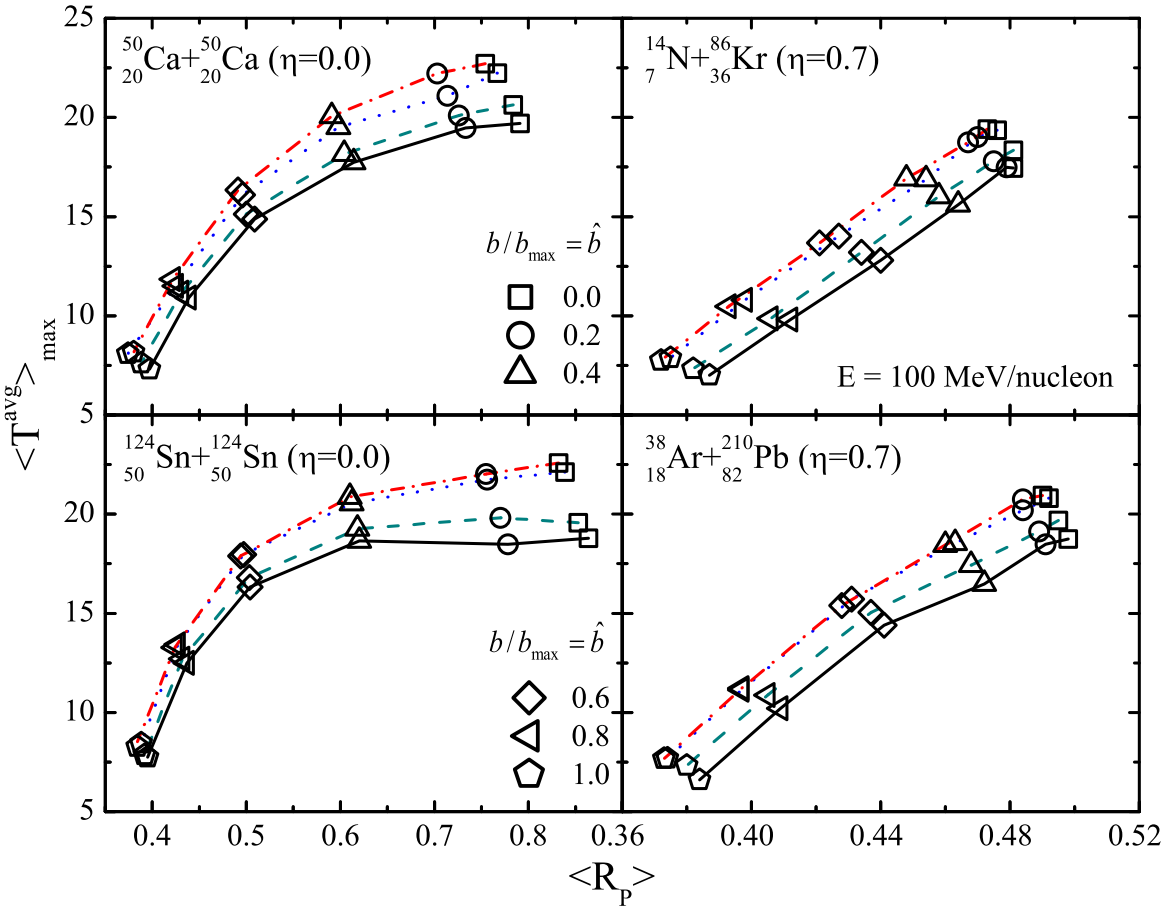

Figure 6.2: Correlation between maximal value of average temperature and nuclear stopping for mass-symmetric (left panels) and mass-asymmetric (right panels) nuclear reactions with A_{tot} = 100 a.m.u. (upper panels) and 248 a.m.u. (lower panels) at E = 100 MeV/nucleon for six different collisions geometries (described by various symbols) and lines have same meaning as in Fig. 6.1.

the case of mass-asymmetric reactions. The reason of reduction in the nuclear stopping is that, with increase in radius the increment in longitudinal momentum is more compared to transverse momentum. Hence, there is less momentum transfer in the transverse direction. Therefore enhanced longitudinal momentum (due to increase in radius) of the particles contributes more in raising the temperature of the system compared to transverse momentum. Because of these effects, the curves of correlation are lifted upward as the radii parametrization is switched from R_{LDM} to other three radii parameterizations. Obviously, the mass-symmetric systems and the heavier colliding nuclei pair are more thermalized compared to mass-asymmetric systems and lighter colliding nuclei pair respectively. It is observed that the influence of radius is more pronounced in the mass-symmetric reactions and lighter reactions. The ratio of change in $< R_P >$ as well as $< T^{avg} >_{max}$ to the change in radius (while switching from R_{LDM} to R_{RR}) is more for mass-symmetric reactions (and also for lighter reactions i.e. with $A_{tot} = 100$ a.m.u. in present study) compared to mass-asymmetric reactions (and also for heavier reactions i.e. $A_{tot} = 248$ a.m.u.).

One can also see that for mass-symmetric reactions, the role of nuclear charge radii parameterizations on the correlation of temperature and nuclear stopping decreases with increase in impact parameter; however, it remains almost the same for mass-asymmetric reactions through out the entire range of $\hat{b}$. This is because the lighter projectile and heavier target nucleus contributes differently in the thermal equilibrium of mass-asymmetric reactions at different collision geometries. These results also motivate to explore the role of nuclear charge radii parameterizations on the thermalization of mass-asymmetric nuclear reaction explicitly for projectile and target nucleus for further studies.

6.3.3 Correlation between fragment multiplicity and nuclear stopping

Fig.6.3 displays the multiplicity of free nucleons (FN's, $A = 1$) (left panels) and light mass fragments (LMF's, $2 \leq A \leq 4$) (right panels) as a function of $< R_P >|_{FNs}$ and $< R_P >|_{LMFs}$ respectively (momentum-based anisotropy ratio) for mass-symmetric (upper panels) and mass-asymmetric (lower panels) collisions at six collision geometries described by various symbols and for four different nuclear charge radii parameterizations described by various lines. One can observe that the multiplicity and the nuclear stopping decreases

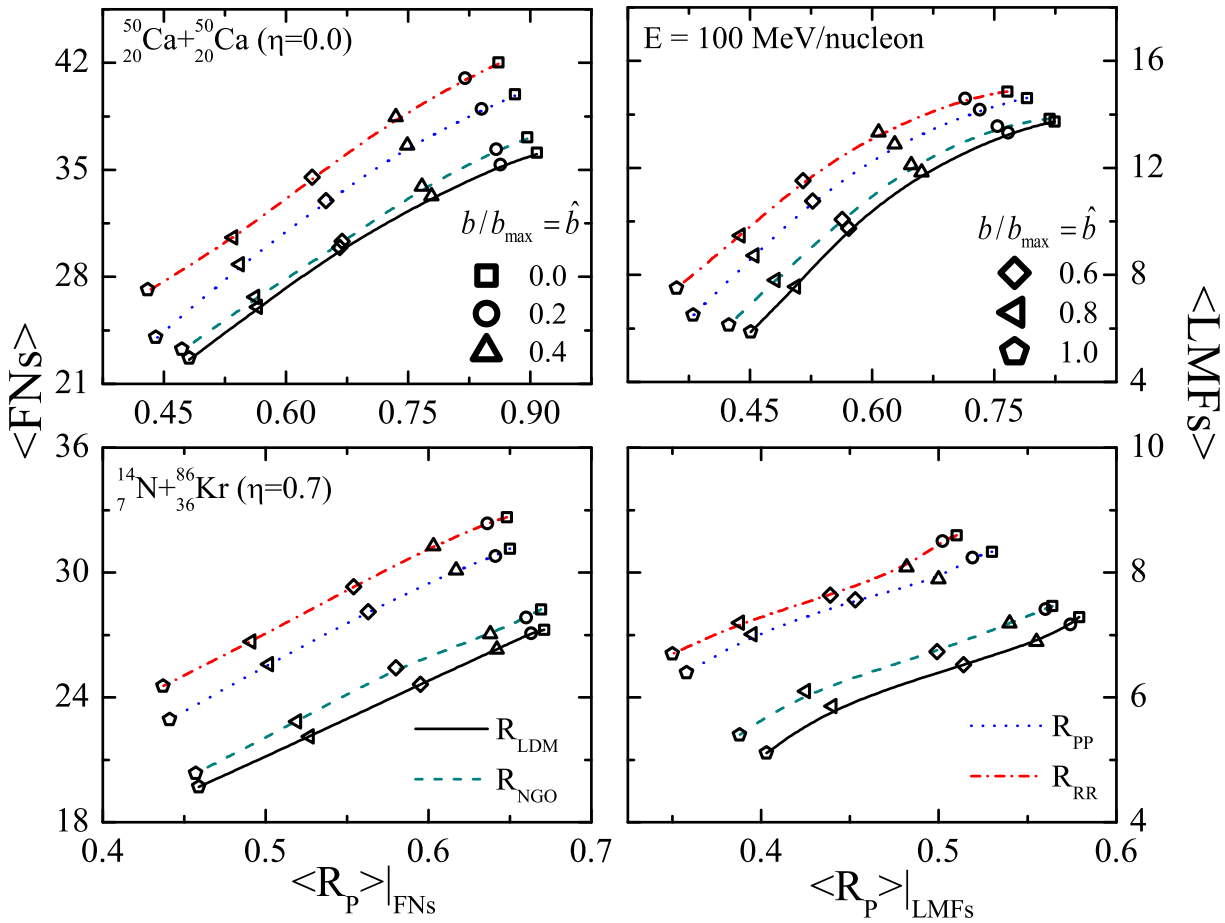

Figure 6.3: Multiplicity of FNs (left panels) and LMFs (right panels) as a function of nuclear stopping for mass-symmetric (upper panels) and mass-asymmetric (lower panels) nuclear reactions with A_{tot} = 100 a.m.u. at E = 100 MeV/nucleon.

with increase in scaled impact parameter i.e. $\hat{b}$ = b/b$_{max}$ where, b$_{max}$ = $(R_P + R_T)fm$, (R_P and R_T are radii of target and projectile nuclei respectively). The correlation curve of multi-fragmentation and nuclear stopping reveals that, more is the nuclear stopping more will be the fragmentation and therefore the curve increases monotonically with decrease in $\hat{b}$ for all radii parameterizations. As concluded in chapter 3 and 5, for mass-symmetric collisions, if the nucleus is initialized with relatively larger radii (i.e. R_{LDM} to other three parameterizations) then the multiplicity of fragments increases and the nuclear stopping decreases. This is because with increase in radius, $p_\perp(i)$ and $p_\parallel(i)$ increase and moreover,

the increment in longitudinal momentum is higher than transverse momentum. This observation also holds true for mass-asymmetric collisions.

The ratio of change in the multiplicity of fragments as well as the nuclear stopping to the change in the nuclear radii of the colliding nuclei (switching from R_{LDM} to R_{RR}) is more for mass-symmetric collisions compared to mass-asymmetric collisions while, the total mass number is same in both types of collisions. This is because of the involvement of smaller projectile nucleus in the mass-asymmetric collisions.

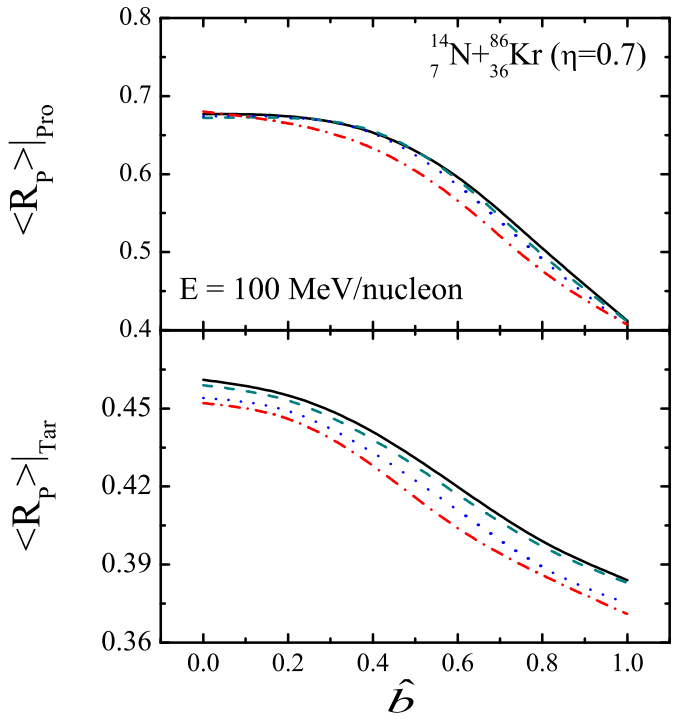

Figure 6.4: Collision geometry dependence of nuclear stopping due to projectile (upper panel) and target (lower panel) nuclei for the reaction of $^{14}_{7}$N+$^{86}_{36}$Kr (η=0.7) at E = 100 MeV/nucleon. Lines have the same meaning as in Fig. 6.3.

6.3.4 Nuclear stopping due to projectile and target nuclei

The percentage increment in the nuclear radius from R_{LDM} to R_{RR} is 28.5% for $^{14}_{7}$N and 10% for $^{86}_{36}$Kr nucleus. It shows that the effect of radius on smaller projectile and heavier target will be different. Therefore, as a next step, Fig.6.4 display the structural effects on nuclear stopping due to projectile (upper panel) and target (lower panel) nucleus

explicitly for mass-asymmetric collisions of $^{14}_{7}$N+$^{86}_{36}$Kr. Figure reveals that, the contribution of projectile nucleus ($^{14}_{7}$N) is more compared to target nucleus ($^{86}_{36}$Kr) in the nuclear stopping. Furthermore, it is observed that the structural effects via nuclear charge radius are more pronounced in the nuclear stopping due to relatively smaller nucleus compared to larger nucleus. This is because, in the mass-asymmetric collisions, most of the nuclear matter of heavier target nucleus do not participate in the collision process. At $\hat{b}$=0 the projectile nucleus completely emerges into target nucleus and at $\hat{b}$=1.0, projectile and target nuclei barely touch each other. So, there is very less role of radius on nuclear stopping due to projectile nuclei at these collision geometries.

6.4 Summary

In summary, the influence of nuclear charge radii on the correlation of the temperature and multi-fragmentation with the nuclear stopping has been examined. The study reveals that the change in the nuclear radius at initial state (t = 0 fm/c) due to different nuclear charge radii parameterizations affects the maximal average temperature of the nuclear matter at 10-20 fm/c and the global nuclear stopping at 200 fm/c. Change in the phase-space available to the nucleons at the initial level influences the reaction dynamics for the whole time span of highly interacting nuclear matter. Moreover, the role of nuclear charge radii on thermal equilibrium decreases with increase in impact parameter for mass-symmetric reactions; however, remain almost equal for mass-asymmetric reactions. The influence of nuclear charge radii parameterizations on the correlation between multi-fragmentation and nuclear stopping is more pronounced in the mass-symmetric collisions compared to mass-asymmetric collisions. Moreover, the structural effects via nuclear charge radii parameterizations are more prominent for nuclear stopping due to smaller projectile nucleus compared to heavier target nucleus.

Chapter 7

Summary and outlook

" The three great essentials to achieve anything worthwhile are: Hard work, Stick-to itiveness, and Common sense".....Thomas A. Edison

7.1 Summary

With the availability of highly accelerated radioactive-ion beams, it becomes possible to study the different nuclear reactions and to extract the knowledge about isospin dependence of nuclear equation of state (NEOS). Since quite some time, the isospin degree of freedom in the NEOS has been scrutinized through many components like symmetry energy, initial N/Z ratio of colliding nuclei, isospin momentum dependent interactions and Coulomb interactions. Theoretically, the observables of heavy-ion collisions (HICs) at intermediate energies such as multi-fragmentation, nuclear stopping and collective flow, do not show any dependency upon the initial N/Z of colliding nuclear matter. However, it is evidenced in the experimental studies that these observables yield different values in the isospin-symmetric and -asymmetric nuclear reaction. Moreover, the reaction dynamics is strongly influenced by the interaction range as well as by the the initial conditions. In the theoretical studies, the nuclear charge radii parametrization is the first and essential model ingredient. This radii parametrization has been considered isospin-independent in the hydrodynamical models of this field. However, till present day numerous radii parameterizations have been proposed in the literature which took isospin into account. Therefore, the present work addressed the isospin as well as initialization effects through the isospin-dependent nuclear charge radius on the reaction dynamics of isospin-asymmetric

colliding nuclei.

The study has been carried out by using Isospin-dependent Quantum Molecular Dynamics (IQMD) model. To observe the initialization effects through isospin dependent nuclear charge radius, three isospin dependent nuclear charge radii parameterizations: R_{NGO}, R_{PP} and R_{RR}, which are upgraded versions of basic $A^{1/3}$ form and includes isospin degree of freedom through isospin parameter: I = (N-Z)/A, have been incorporate in the IQMD model in addition to one isospin independent nuclear charge radii parametrization: R_{LDM}, which has been used extensively in the theoretical research. The numerical test has been performed with all the radii parameterizations to check the stability of initialized nucleus and the propagation of nucleons. The secondary algorithms: Minimum Spanning Tree (MST) method and its updated versions MSTM (with momentum constraint) method has also been discussed, which has been further used to identify fragments from the final stage phase-space of the reaction. The simulations have been carried out for different sets of reactions: (i) by varying N/Z and keeping the composite system mass same for two isobaric series of reactions and (ii) by keeping the initial N/Z same and varying the composite system mass to quantify the initialization effects.

In **chapter 3**, the influence of isospin dependent nuclear charge radii on fragmentation in the HICs has been studied for a wide range of atomic mass and neutron-to-proton ratio. It has been observed that with increase in radius the peak value of $< \rho/\rho_o >_{avg}$ reduces. This effect further decreases with increase in incident energy for lighter colliding pairs and remain nearly the same for heavier colliding pairs. The influence of isospin dependent radii parameterizations on average nucleonic density and dN_{coll}/dt, is more for heavier colliding nuclei compared to lighter colliding nuclei. Moreover, the colliding system takes more time to saturate for isospin dependent nuclear charge radii. Due to increase in phase-space for isospin dependent nuclear charge radii, the role of Pauli blocking is less. Hence the mass of largest fragment is less and the mean multiplicity of other fragments is higher. Also, the role of isospin dependent nuclear charge radii is more in the semi-central collisions compared to central collisions. The N/Z dependence of the multiplicity of FN's and LMF's shows different behavior for isospin dependent nuclear charge radii parameterizations as for isospin independent radii parametrization. Moreover, isospin dependent radii reduces the gap between the theoretical calculations and the experimental findings of ALADIN

collaboration. It has been concluded that, heavier colliding nuclei are good probe to study the influence of isospin dependent nuclear charge radii on multi-fragmentation in the heavy ion collisions at E = 50 MeV/nucleon.

In **chapter 4**, a systematic study of the influence of nuclear charge radii parameterizations on the excitation function of reduced flow and elliptical flow as well as on the balance and transition energies for the whole mass range and initial neutron-to-proton ratio has been presented. Two view points have been applied; structural effects and isospin effects. The study concludes that the pressure gradient developed in the mid-rapidity region reduces with increase in nuclear charge radius of colliding nuclei and repulsive nucleon-nucleon collisions gets suppressed. With increase in nuclear charge radius (due to use of different nuclear charge radii parameterizations) the magnitude of reduced flow decreases and of elliptical flow increases. This influence of change in the radius on flow magnitude further decreases with increase in system mass.

Moreover, the role of change in the radius on collective flow is more for the neutron-deficient reactions compared to neutron-rich reactions. Both transition energy of elliptical flow (E_{trans}) and balance energy of reduced flow (E_{bal}) increases with increase in nuclear radius and follows a power law behavior. The influence of nuclear radius on E_{trans} and E_{bal} decreases with increase in system mass and increases with increase in N/Z of the reaction. From both types of collective flow, the elliptical flow has been found to be more sensitive towards different nuclear charge radii parameterizations compared to reduced flow. From the impact parameter dependence of reduced flow and elliptical flow, the balance geometry of reduced flow and transition geometry of elliptical flow have been analyzed. This signifies the increasing role of attractive mean field and shadowing of the spectator matter with increase in collision geometry.

Chapter 5 describes the influence of nuclear charge radius on the observables of nuclear stopping along with momentum dependent interactions (MDI). The study concludes that the increase in available phase space at initial state enhances the longitudinal as well as transverse momentum which increases the production of fragments. However, the increment in longitudinal momentum is more than in the transverse momentum which in turn reduces the nuclear stopping. A ratio of change in the values of nuclear stopping to the change in radius is more for lighter colliding nuclei pair compared to heavier one.

The isospin-dependent nuclear charge radii is unable to alter the dependence of nuclear stopping on the initial neutron-to-proton content of the colliding nuclei for semi-central collisions at E = 50 MeV/nucleon. The study also shows that an average of those nucleons which have experienced at least five collisions are close to complete equilibrium. This observation is appropriate for both lighter and heavier reactions as well as for all the radii parameterizations. The rapidity distribution of the nuclear matter becomes broad for larger radii as well as by the inclusion of MDI. This clearly results in reducing the stopping values. The radii parametrization affects the nuclear stopping at relatively high energies and influence of MDI is at lower energies. Hence, the nuclear stopping calculations via isospin-dependent radius parametrization along with MDI are more closer to the experimental findings of INDRA and ALADIN collaborations.

In **chapter 6**, as a last step, a comparative study upon the correlation of temperature and multi-fragmentation with nuclear stopping for mass-symmetric as well asymmetric nuclear reactions has been performed. Our results reveal that the role of nuclear charge radii on thermal equilibrium decreases with increase in impact parameter for mass-symmetric reactions; however, remain almost the same for asymmetric reactions. In addition to that, the nuclear charge radii parameterizations affect the correlation curve of multi-fragmentation and temperature with nuclear stopping more for mass-symmetric reaction as compared to mass-asymmetric reaction (having the same total mass). In an asymmetric reaction, the smaller projectile experiences more influence through nuclear charge radii compared to heavier target. For mass-asymmetric nuclear reactions, the contribution of smaller projectile in the nuclear stopping is more but the collective contribution of projectile and target nuclei becomes less than as that of mass-symmetric reaction.

7.2 Outlook

The study of this thesis is limited to the colliding nuclei with mass number A = 197 a.m.u.. However, the study of different nuclear radius can be extended in the heavier side of periodic table (super-heavy nuclei) by using the nuclear charge radii parameterizations available for super heavy nuclei. In the present studies, the nuclear charge radii which is obtained from the charge density distribution in the nucleus has been opted because the information about the neutron distribution is inadequate in the literature. With

the progress in the neutron distribution, one can further quantify the comparative role of different nuclear charge as well as neutron matter radii parameterizations on the sensitivity of hydrodynamical models and on the dynamics of HICs.

Moreover, the density of nucleus is related to both its radius and Fermi momentum. A constant value of Fermi momentum indicates constant nucleonic density. In present calculations, the influence of change in the radii on the fragmentation, nuclear flow and nuclear stopping has been studied with constant ground state Fermi momentum associated with nucleons in the IQMD model (i.e. as per the LDM radii, 268.4 MeV/c). However, the Fermi momentum can be varied according to the radii parameterizations used to simulate the nuclear reactions. The variation in the ground state Fermi momentum may affect the surface properties of the nuclear sphere and its binding energy. The present study can be extended to examine the role of different nuclear radii parameterizations on the observables of HICs by keeping the Fermi momentum according to respective radius parametrization used.

Bibliography

[1] P. Möller, A.J. Sierka, T. Ichikawa and H. Sagawa, Atom. Data Nucl. Data tab. **109-110** , 1-204 (2016).

[2] Meng Wang, G. Audi, F.G. Kondev, W.J. Huang, S. Naimi and Xing Xu, Chin. Phys. C **41**, 030003 (No. 3) (2017).

[3] E. Rutherford and H. Geiger, Proc. R. Soc. London A **81**, 162 (1908).

[4] J. Dilling *et. al.*, Hyperfine Interactions **225**, 253 (2014).

[5] M. J. G. Borge and B. Jonson, J. Phys. G: Nucl. Part. Phys. **44**, 079501 (2012).

[6] S. K. Patra, C. L. Wu, C. R. Praharaj and R. K. Gupta, Nucl. Phys. A **651**, 117 (1999) .

[7] Sunita Gupta *et al.* (B.P. Singh), Jour. Phys. Soc. Japan **71**, 2334 (2002).

[8] B. P. Singh, M. G. V. Sankaracharyulu, H. D. Bhardwaj and R. Prasad, Phys. Rev. C **47**, 2055 (1993).

[9] S. Kailas, Physics Reports **284**, 381 (1997).

[10] C. Bhattacharya *et al.*, Phys. Rev. C **65**, 014611(2001).

[11] S. K. Patra, C. L. Wu, C. R. Praharaj and G. K. Khamari, J. Phys. G **25**, 501 (1999).

[12] Mohd. Shuaib *et al.* (B. P. Singh), Phys. Rev. C **94**, 014613 (2016).

[13] K. Wei and H. F. Zhang, Phys. Rev. C **96**, 021601(R) (2017).

[14] S. Mukherjee *et al.*, Phys. Rev. C **80**, 014607 (2009).

[15] R. Baiera,Y. L. Dokshitzerb, A. H. Muellercd S.Peignée and D.Schiff, Nucl. Phys. B **483**, 291 (1997).

[16] J. R. Smith and G. A. Miller, Phys. Rev. C **72** , 022203(R) (2005).

[17] H. Stöcker and W. Greiner, Phys. Rep. **137**, 277 (1986).

[18] J. Aichelin, Phys. Rep. **202**, 233 (1991).

[19] C. Bhattacharya *et al.*, Phys. Rev. C **54**, 3099(1996).

[20] P. J. Siemens, Nature London **305**, 410 (1983).

[21] A Guide to the Nuclear Science Wall Chart @ 2004, Contemporary Physics Education Project (CPEP).

[22] C. Y. Wong, Introdution to high-energy heavy-ion collisions, World Scientific, Singapore (1994).

[23] N. K. Glendenning, Phys. Rev. D **46**, 1274 (1992).

[24] J. Ritman [FOPI Collaboration], Nucl. Phys. B **44** (Proc. Suppl.), 708 (1995).

[25] Yu.B. Ivanov, Phys. Lett. B **690**, 358362 (2010).

[26] T. Ablyazimov *et al.* [CBM Collaboration], Eur. Phys. J. A **53**, 60 (2017).

[27] V. D. Kekelidze [NICA Collaboration], J. of Instrum. **12**, C06012 (2017).

[28] P. Coles and F. Lucchin, Cosmology (First Edition), Wiley & Sons, LTD, Chichester (1995).

[29] G. Peilert, H. Stöcker and W. Greiner, Rep. Prog. Phys. **57**, 533 (1994).

[30] B. H. Sun *et al.*, Science Bulletin **63**, 78 (2018).

[31] S. Chebotaryov *et al.*, Prog. Theor. Exp. Phys. **2018**, 053D01 (2018).

[32] P. Russotto *et al.*, J. of Phys: Conf. Ser. **863**, (2018).

[33] E. Petit [SPIRAL2 collaboration]; North American Particle Accelerator Conference (NAPAC2016), 9^{th}-14^{th} Oct. 2016, Chicago, IL U.S.A.; P. Bertrand and R. Ferdinand; XXVI Linear Accelerator Conference - LINAC12 Sep. 2012, Proc. of LINAC2012, pp.773- 777, 2013.

[34] Whitepapers of the 2007 NSAC Long Range Plan Town Meeting, Jan., 2007, Chicago, http://dnp.aps.org.

[35] A. Bandyopadhyay, V. Naik, S. Dechoudhury, M. Mondal And A. Chakrabarti, Pramana J. Phys. **85**, 505-515 (No. 3) (2015).

[36] C. F. Weizsäcker, Z. Physik **96**, 431 (1935).

[37] H. A. Bethe and R. F. Bacher, Rev. Mod. Phys. **8**, 82 (1936).

[38] B. A. Li and S. J. Yennello, Phys. Rev. C **52**, R1746 (1995).

[39] B. A. Li, Z. Ren, C. M. Ko and S. J. Yennello, Phys. Rev. Lett. **76**, 4492 (1996).

[40] B. A. Li, C. M. Ko and W. Bauer, Int. J. of Mod. Phys. E **7**, 147 (1998).

[41] W. Cassing and U. Mosel, Prog. Part. Nucl. Phys. **25**, 235 (1990).

[42] A. Faessler, W. H. Dickhoff, M. Trefz and M. R. Brown, Nucl. Phys. A **428**, 271 (1981).

[43] M. Trefz, A. Faessler and W. H. Dickhoff, Nucl. Phys. A **443**, 499 (1985).

[44] J. Y. Liu, W. J. Guo, Z. Y. Xing, and X. G. Lee, Chin. Phys. Lett. **22**, 65 (2005).

[45] Y. Zhang, Z. Li, C. Zhou and M. B. Tsang, Phys. Rev. C **85**, 051602(R) (2012).

[46] G. Gamow, Z. Phys. **51**, 204 (1928).

[47] R. W. Gurney and E. U. Condon, Nature **122**, 439 (1928).

[48] I. Tanihata *et al.*, Phys. Lett. B **160**, 380 (1985).

[49] I. Tanihata *et al.* , Phys. Rev. Lett. **55**, 2676 (1985).

[50] A. Ozawa *et al.*, Nucl. Phys. A **608**, 63 (1996).

[51] Nuclear Physics, 8th edition, D. C. Tayal, Himalaya Publishing House (2011).

[52] A.E. Barzakh and V.P. Denisov, Z. Phys. A **346**, 265 (1993).

[53] G. Fricke *et al.*, Atom. Data Nucl. Data tab. **60**, 177 (1995).

[54] A. Bohr and B. R. Mottelson, Nuclear Structure, Vol. **1** (World Scientific, Singapore, 1998).

[55] G.F. Lima *et al.*, Nucl. Phys. A **735**, 303 (2004).

[56] A. Kohama, K. Iida and K. Oyamatsu, Phys. Rev. C **69**, 064316 (2004).

[57] D. Ni, Z. Ren, T. Dong and Y. Qian, Phys. Rev. C **87**, 024310 (2013).

[58] Y. Qian, Z. Ren and D. Ni, Phys. Rev. C **87**, 054323 (2013).

[59] I. Angeli, Atom. Data Nucl. Data Tab. **87**, 185 (2004).

[60] I. Angeli and K.P. Marinova, Atom. Data Nucl. Data Tab. **99**, 69 (2013).

[61] I. Angeli *et al.*, J. Phys. G: Nucl. Part. Phys. **36**, 085102 (26pp) (2009).

[62] M. Warda, B. N. Pomorska and K. Pomorski, Nucl. Phys. A **635**, 484 (1998).

[63] C. A. Bertulani, H. Liu, and H. Sagawa, Phys. Rev. C **85**, 014321 (2012).

[64] E. Ryberg, Ch. Forssén, H. W. Hammer and L. Platter, Phys. Rev. C **89**, 014325 (2014).

[65] A. Bohr and B. Mottelson, Nuclear Structure (W. A. Benjamin Inc., New York, Amsterdam) Vol. **1**, p.268 (1969).

[66] P. G. Reinhard, M. Bender, W. Nazarewicz and T. Vertse, Phys. Rev. C **73**, 014309 (2006)

[67] J. Blocki, J. Randrup, W. J. Świątecki and C. F. Tsang, Ann. Phys. (N.Y.) **105**, 427 (1977).

[68] R. Bass, Nucl. Phys. A **231**, 45 (1974).

[69] P. R. Christensen and A. Winther, Phys. Lett. B **65**, 19 (1976).

[70] A. Winther, Nucl. Phys. A **594**, 203 (1995).

[71] H. Ngô and Ch. Ngô, Nucl. Phys. A **348**,140 (1980) .

[72] M. Beiner, R.J. Lombard and D. Mas, Nucl. Phys. A **249**, 1 (1975).

[73] J. Dechargé and D. Gogny, Phys. Rev. C **21**, 1568 (1980)

[74] T. Suzuki, J. Phys. G: Nucl Part. Phys. **19**, 1319 (1994).

[75] B.A. Nikolaus, T. Hoch and D.G. Madland, Phys. Rev. C **46**, 1757 (1992).

[76] M.M. Sharma and P. Ring, Phys. Rev. C **45**, 2514 (1992).

[77] B. N. Pomorska and K. Pomorski, Z. Phys. A **344**, 359 (1993).

[78] B. N. Pomorska and K. Pomorski, Z. Phys. A **348**, 169 (1994).

[79] V. Y. Denisov, Phys. lett. B **526**, 315 (2002).

[80] G. Royer, Nucl. Phys. A **807**, 105 (2008).

[81] G. Royer and R. Rousseau, Eur. Phys. J. A **42**, 541 (2009).

[82] W. D. Myers and W. J. Świątecki, Phys. Rev. C **62**, 044610 (2000).

[83] S. Q. Zhan, J. Meng, S. G. Zhou and J.Y. Zeng, Eur. Phys. J. **13**, 285-289 (2002).

[84] R. K. Puri, P. Chattopadhyay and R. K. Gupta, Phys. Rev. C **43**, 315 (1991).

[85] N. K. Dhiman and R. K. Puri, Acta Phys. Pol. B **37**, 1855 (2006).

[86] I. Dutt and R. K. Puri, Phys. Rev. C **81**, 064609 (2010).

[87] Y. K. Vermani, J. K. Dhawan, S. Goyal, R. K. Puri and J. Aichelin, J. Phys. G: Nucl Part. Phys. **37**, 015105 (2010).

[88] Y. K. Vermani and R. K. Puri, Eur. Phys. Lett. **85**, 62001 (2009).

[89] J. Dobaczewki, W. Nazarewicz and T. R.Werner, Z Phys. A **354**, 27 (1996).

[90] A. E. L. Dieperink, Y. Dewulf, D. Van Neck, M. Waroquier, and V. Rodin, Phys. Rev. C **68**, 064307 (2003).

[91] L. W. Chen, C. M. Ko and B. A. Li, Phys. Rev. C **72**, 064309 (2005).

[92] M. B. Tsang *et al.*, Phys. Rev. C **86**, 015803 (2012).

[93] B. A. Brown, Phys. Rev. Lett. **85**, 5296 (2000).

[94] C. Hartnack et al., Eur. Phys. J. A **1**, 151 (1998).

[95] Y. Kitazoe, M. Sano, Y. Yamamura, H. Furutani and K. Yamamoto, Phys. Rev. C **29**, 828 (1984).

[96] J. Cugnon, Phys. Rev. C **22**, 1885 (1980).

[97] H. Feldmeier and J. Schnack, Prog. Part. Nucl. Phys. **39**, 393 (1997).

[98] A. Ono, H. Horiuchi, T. Maruyama, and A. Ohnishi, Phys. Rev. Lett. **68**, 2898 (1992).

[99] N. Ohtsuka, R. Linden, and A. Faessler, Nucl. Phys. A **465**, 550 (1987).

[100] G. C. Yong, Y. Gao, W. Zuo, and X. C. Zhang, Phys. Rev. C **84**, 034609 (2011).

[101] Rajni and S. Kumar, Eur. Phys. J. A **48**, 19 (2012).

[102] F. D. Qing M. Y. Gang, C. X. Zhou, T. W. Dong and W. H. Wei, Chin. Phys. Lett. **28**, 102102 (2011).

[103] Z. T. Dai *et al.*, Phys. Rev. C **91**, 034618 (2015).

[104] R. Bansal, S. Gautam, R. K. Puri and J. Aichelin, Phys. Rev. C **87**, 061602 (R) (2013).

[105] R. Bansal and S. Gautam, EPJ Web of Conf. **69**, 00025 (2014).

[106] S. Gautum, Phys. Rev. C **88**, 057603 (2013).

[107] J.P. Bondorf, J. de Physique **37**, (C5) 195 (1976).

[108] J. P. Bondorf, A. S. Botvina, A. S. Iljinov, I. N. Mishustin and K. Sneppen, Phys. Rep. **257**, 133 (1995).

[109] W. Trautmann, Nucl. Phys. A **752**, 407c (2005).

[110] L. Phair *et al.*, Phys. Lett. B **285**, 10 (1992).

[111] C. A. Ogilvie *et al.*, Phys. Rev. Lett. **67**, 1214 (1991).

[112] N. Marie *et al.*, Phys. Rev. C **58**, 256 (1998).

[113] J. Colin *et al.* [INDRA Collaboration], Phys. Rev. C **67**, 064603 (2003).

[114] F.S. Zhang, L.W. Chen, Z.Y. Ming and Z.Y. Zhu, Phys. Rev. C **60**, 064604 (1999).

[115] J.Y. Liu *et al.*, Phys. Rev. C **63**, 054612 (2001).

[116] J.Y. Liu, Y.Z. Xing and W.J. Guo, Chin. Phys. Lett. **20**, 832 (2003).

[117] Q. Wu *et al.*, Phys. Rev. C **91**, 014617 (2015).

[118] M. Colonna, J. Rizzo, P. Comaz, and M.D. Toro, Nucl. Phys. A **805**, 454c (2008).

[119] H. Imal *et al.*,Phys. Rev. C **91** 034605 (2015).

[120] A. Jain and S. Kumar, Pramana J. Phys. **78**, 749 (2012).

[121] I. I. Gurevich *et al.*, Dokl. Akad. Nauk SSSR **18**, 169 (1938).

[122] O.V. Lozkin and N.A. Perfilov, J. Exp. Theor. Phys. **31**, 913 (1956).

[123] L. Phair *et al.*, Phys. Rev. Lett. **77**, 822 (1996).

[124] R. Planeta *et al.* [ISOSPIN Collaboration], Phys. Rev. C **77**, 014610 (2008).

[125] W. Reisdorf, Nucl. Phys. A **630**, 15c (1998).

[126] A. Andronic *et al.*, GSI Rep. **98-1**, p. 55 (1997).

[127] A.S. Botvina *et al.*, Nucl. Phys. A **584**, 737 (1995).

[128] A. Schüttauf *et al.*, Nucl. Phys. A **607**, 457 (1996).

[129] W. Trautmann *et al.*, Nucl. Phys. A **538**, C473 (2007).

[130] W. Trautmann *et al.*, Int. J. Mod. Phys. E **17**, 1838 (2008).

[131] W. Trautmann *et al.*, Nucl. Phys. A **787**, 575 (2007).

[132] C. Sfienti *et al.*, Phys. Rev. Lett. **102**, 152701 (2009).

[133] Y.G. Ma *et al.*, Phys. Rev. C **69**, 031604 (2004).

[134] J. Wang *et al.*, Phys. Rev. C **71**, 054608 (2005).

[135] D.V. Shetty *et al.*, J. Phys. G: Nucl Part. Phys. **36** , 075103 (2009).

[136] S. Hudan *et al.*, Phys. Rev. C **67**, 064613 (2003).

[137] E. Bohnet *et al.*, Phys. Rev. Lett. **103**, 072701 (2009).

[138] O. V. Lozhkin and W. Trautmann, Phys. Rev. C **46**, 1996 (1992).

[139] W. Trautmann, Nucl. Phys. A 834, 548C (2010).

[140] W. Trautmann, U. Milkau, U. Lynen and J. Pochodzalla, Z Phys. A **344**, 447 (1993).

[141] W. Reisdorf and M. G. Ritter, Ann. Rev. Nucl. Sci. **47**, 663 (1997).

[142] M. B. Tsang *et al.*, Phys. Rev. Lett. **57**, 559 (1986).

[143] J. W. Harrisa, Nucl. Phys. A **471**, 241 (1987).

[144] D. Krofcheck *et al.*, Phys. Rev. Lett. **63**, 2028 (1989).

[145] B. Zhang, M. Gyulassy and C. M. Ko, Phys. Lett. B **455**, 45 (1999).

[146] J. Y. Ollitrault, Phys. Rev. D **48**, 1132 (1993).

[147] J. Y. Ollitrault, Nucl. Phys. A **638**, 195c (1998).

[148] A. Andronic *et al.*, Nucl. Phys. A **679**, 765 (2001).

[149] A. Andronic *et al.*, Phys. Lett. B **612**, 173 (2005).

[150] B. A. Li and C. M. Ko, Nucl. Phys. A **654**, 797 (1999).

[151] H.Y. Zhang *et al.*, Eur. Phys. J. A **15**, 399 (2002).

[152] Y. Wang *et al.*, Phys. Rev. C **89**, 034606 (2014).

[153] H. M. Xu, Phys. Rev. C **46**, 389 (R) (1992).

[154] G. D. Westfall *et al.*, Phys. Rev. Lett. **71**, 1986 (1993).

[155] J. Y. Chen, W. Zuo, L. Ma, F. Zhang and B. A. Li, Chin. Phys. Lett. **24**, 76 (2007).

[156] S. Gautum and A. D. Sood, Phys. Rev. C **82**, 014604 (2010).

[157] X. Liu *et al.*, Phys. Rev. C **90**, 014604 (2014).

[158] J. Steinheimer, J. Auvinen, H. Petersen, M. Bleicher and H. Stöcker, Phys. Rev. C **89**, 054913 (2014).

[159] H. Stöcker *et al.*, Phys. Rev. C **25**, 1873 (1982).

[160] M. D. Toro *et al.*, Nucl. Phys. A **787**, 585 (2007).

[161] M. D. Toro, V Baran, M Colonna and V Greco, J. Phys. G: Nucl. Part. Phys. **37**, 083101 (2010).

[162] K. S. Vinayak and S. Kumar, Eur. Phys. J. A **47**, 144 (2011).

[163] A. Jain, S. Arora and S. Kumar, Eur. Phys. J. Web of Conf. **66**, 03039 (2014).

[164] A. Jain, S. Kumar and R. K. Puri, Phys. Rev. C **85**, 064608 (2012).

[165] A. Jain and S. Kumar, Nucl. Phys. A **876**, 109 (2012).

[166] H. A. Gustafsson *et al.*, Phys. Rev. Lett. **52**, 1590 (1984).

[167] H. H. Gutbrod *et al.*, Phys. Lett. B **216**, 267 (1989).

[168] M. Demoulins *et al.*, Phys. Lett. B **241**, 476 (1990).

[169] R. Popescu *et al.*, Phys. Lett. B **331**, 285 (1994).

[170] M. B. Tsang *et al.*, Phys. Rev. C **53**, 1959 (1996).

[171] P. Crochet *et al.*, Nucl. Phys. A **624**, 755 (1997).

[172] W. Reisdorf *et al.*, Phys. Lett. B **595**, 118 (2004).

[173] J. Lukasik *et al.* [INDRA Collaborations], Int. Workshop on Multifragmentation and related topics (IWM 2003) Caen, France (2003).

[174] J. Lukasik, G. Auger, and M. L. Begemann-Blaich, Phys. Lett. B **608**, 223 (2005).

[175] J. Lukasik *et al.*, Proc. of INPC **2**, 513 (2007).

[176] A. Andronic, J. Lukasik, W. Reisdorf, and W. Trautmann, Eur. Phys. J. A **30**, 31 (2006).

[177] J. Y. Ollitrault, A. M. Poskanzer, and S. A. Voloshin, Phys. Rev. C **80**, 014904 (2009).

[178] Y. Wang et al., Phys. Rev. Lett. **778**, 207 (2018).

[179] S. Kumar, S. Kumar, and R. K. Puri, Phys. Rev. C **81**, 014601 (2010).

[180] A. Jain, S. Kumar, and R. K. Puri, Phys. Rev. C **84**, 057602 (2011).

[181] Z. Li *et al.*, Nucl. Phys. A **559**, 603 (1993).

[182] X.G. Cao *et al.*, Phys. Rev. C **81**, 061603(R) (2010).

[183] B. Hong *et al.*, Phys. Rev. C **71**, 034902 (2005).

[184] T. Gaitanos, C. Fuchs and H.H. Wolter, Phys. Lett. B **609**, 241 (2005).

[185] R. E. Renfordt *et al.*, Phys. Rev. Lett. **53**, 763 (1984).

[186] W. Bauer, Phys. Rev. Lett. **61**, 2534 (1988).

[187] G. Peilert, H. Stöcker, W. Greiner, A. Rosenhauer, A. Bohnet and J. Aichelin, Phys. Rev. C **39**, 1402 (1989).

[188] S. A. Bass *et al.*, GSI Rep. **94**, 66 (1995).

[189] J.Y. Liu, W.J. Guo, S.J. Wang, W. Zuo, Q. Zhao, and Y.F. Yang, Phys. Rev. Lett. **86**, 975 (2001).

[190] A. D. Sood and R. K. Puri, Phys. Rev. C **79**, 064618 (2009).

[191] S. Gautam, Eur. Phys. J. A **48**, 3 (2012).

[192] J. Su and F.S. Zhang, Phys. Rev. C **87**, 017602 (2013).

[193] J. Su, K. Cherevko, W.J. Xie, and F.S. Zhang, Phys. Rev. C **89**, 014619 (2014).

[194] J.Y. Liu, W.J. Guo, Y.Z. Xing, X. G. Li, and Y. Gao, Phys. Rev. C **70**, 034610 (2004).

[195] J.Y. Liu, W.J. Guo, Y.Z. Xing, X. G. Li, and Y. Gao, Chin. Phys. Lett. **21**, 1914 (2004).

[196] J.Y. Liu, W.J. Guo, Y.Z. Xing, W. Zou and X.G. Lee, Phys. Rev. C **67**, 024608 (2003).

[197] S. Kumar and S. Kumar, Chin. Phys. Lett. **27**, 062504 (2010).

[198] M.H. Zhao *et al.*, Phys. Rev. C **89**, 037001 (2014).

[199] R. Bansal, A. Jain and S. Kumar, Indian J. Phys. **89**, 1077 (2015).

[200] M. Kaur and S. Kumar, Pramana J. Phys. **84**, 101 (2015).

[201] M. Kaur and S. Kumar, Indian J. Phys. **89**, 967 (2015).

[202] A. Kaur and S. Kumar, Indian J. Phys. **91**, 1095 (2017).

[203] B. Hong *et al.*, Phys. Rev. C **57**, 244 (1998).

[204] B. Hong *et al.*, Phys. Rev. C **66**, 034901 (2002).

[205] B. Hong and FOPI Collaboration, Nucl. Phys. A **721**, 317c (2003).

[206] W. Reisdorf *et al.*, Nucl. Phys. A **848**, 366 (2010).

[207] A. Andronic *et al.*, Phys. Rev. C **64**, 041604 (R) (2001).

[208] G. Lehaut *et al.* [INDRA and ALADIN collaborations], Phys. Rev. Lett. **104**, 232701 (2010).

[209] O. Lopez *et al.* (INDRA collaboration), Phys. Rev. C **90**, 064602 (2014).

[210] D. H. E. Gross, Rep. Prog. Phys. **53**, 605 (1990).

[211] D. V. Fedorov, A. S. Jensen and E. Garrido, Acta. Phys. Hungarica **18**, 203 (2003).

[212] J. Pan, S. D. Gupta, Phys. Rev. C **51**, 1384 (1995).

[213] S. D. Gupta and J. Pan, Phys. Rev. C **53**, 1319 (1996).

[214] W. A. Friedman, Phys. Rev. C **42**, 667 (1990).

[215] A. S. Botvina, A. S. Iljinov and I. N. Mishustin, Nucl. Phys. A **507**, 649 (1990).

[216] S. D. Gupta, C. Gale and J. Gallego, Phys. Rev. C **33**, 1634 (1986).

[217] K. Sneppen and L. Vinet, Nucl. Phys. A **480**, 342 (1988).

[218] Y. Yariv and Z. Fraenkal, Phys. Rev. C **20**, 2227 (1979);

[219] I. A. Pshenichnov, A. S. Iljinov, Y. S. Golubeva and D. Polster, Phys. Rev. C **52**, 947 (1995).

[220] H. Kruse, B. V. Jacak, and H. Stöcker, Phys. Rev. Lett. **54**, 289 (1985).

[221] G. F. Bertsch, H. Kruse and S. Das Gupta. Phys. Rev. C **29**, 673 (R) (1984).

[222] C. Gregorie, B. Rëmaud, F. Sëbille, L. Vinet and Y. Raffray, Nucl. Phys. A **465**, 317 (1987).

[223] A. Bonasera, F. Gulminelli and P. Schuck, Phys. Rev. C **46**, 1431 (1992).

[224] M. Colonna, M. D. Toro, G. Fabbri, and S. Maccarone, Phys. Rev. C **57**, 1410 (1998).

[225] F. Sakata, T. Kubo, T. Marumori, K. Iwasawa, and Y. Hashimoto, Phys. Rev. C **50**, 138 (1994).

[226] D. Lacroix and Ph. Chomaz, Phys. Rev. C **58**, 1604 (1998).

[227] J. P. Bondorf, H. T. Feldmeier, S. Garpman and E. C. Halbert, Phys. Lett. B **65**, 217 (1976).

[228] E. A. Uehling and G. E. Uhlenbeck, Phys. Rev. **43**, 552 (1933).

[229] E. Surad, Ch, Gregoire and B. Tamian, Prog. Part. Nucl. Phys. **23**, 357 (1989).

[230] A. Bonasera, G. F. Burgio, and M. D. Toro, Phys. Lett. B **221**, 233 (1989).

[231] A. Bonasera, G. Russo, and H. H. Wolter, Phys. Lett. B **246**, 337 (1990).

[232] L.Wilets, Y. Yariv, and R. Chestnut, Nucl. Phys. A **301**, 359 (1978).

[233] A. R. Bodmer, C. N. Panos, and A. D. MacKellar, Phys. Rev. C **22**, 1025 (1980).

[234] A. Vicentini, G. Jacucci and V. R. Pandharipande, Phys. Rev. C **31**, 1783 (1985).

[235] J. Aichelin and H. Stöcker, Phys. Lett. B **176**, 14 (1986).

[236] A. Bohnet et al., Phys. Rev. C **44**, 2111 (1991).

[237] S. Huber and J. Aichelin, Nucl. Phys. A **573**, 587 (1994).

[238] G. Peilert, J. Konopka, M. Blann, M. G. Mustafa, H. Stöcker and W. Greiner, Phys. Rev. C **46**, 1457 (1992)

[239] G. Peilert, J. Randrup, H. Stc̈ker and W. Greiner, Phys. Lett. B **260**, 271 (1991).

[240] C. Dorso, S. Duarte and J. Randrup, Phys. Lett. B **188**, 287 (1987).

[241] C. Dorso and J. Randrup, Phys. Lett. B **215**, 611 (1988).

[242] L. Jianye and Z. S. Guang, Z. Phys. A **348**, 31 (1994).

[243] C. Ngo, H. Ngo, S. Leray, M. E. Spina, Nucl. Phys. A **499**, 148 (1989).

[244] R. K. Puri, N. Ohtsuka, E. Lehmann, A. Faessler, M.A. Matin, D.T. Khoa, G. Batko, and S.W. Huang, Nucl. Phys. A **575** , 733 (1994).

[245] J. Jaenicke, J. Aichelin, N. Ohtsuka, R. Linden and A. Faessler, Nucl. Phys. A **536**, 201 (1992).

[246] M. Papa, G. Giuliani and A. Bonasera, J. Comp. Phys. **208**, 403 (2005).

[247] K. A. Waged, Phys. Rev. C **63**, 024618 (2001).

[248] H. Sorge, H. Stöcker, and W. Greiner, Ann. Phys. **192**, 266 (1989).

[249] M. Belkacem *et al.*, Phys. Rev. C **58**, 1727 (1998).

[250] S. A. Bass *et al.*, Prog. Part. Nucl. Phys. **41**, 255 (1998).

[251] Q. Li *et al.*, J. Phys. G: Nucl. Part. Phys. **31**, 1359 (2005).

[252] Q. Li, Z. Li and H. Stöcker, Phys. Rev. C **73**, 051601 (2006).

[253] H. Feldmeier, Nucl. Phys. A **515**, 147 (1990).

[254] A. Ono, H. Horiuchi, T. Maruyama, and A. Ohnishi, Prog. Theor. Phys. **87**, 1185 (1992).

[255] C. Hartnack *et al.*, Nucl. Phys. A **495**, 303 (1989).

[256] C. Hartnack, J. Aichelin, H. Stöcker, and W. Greiner, Mod. Phys. Lett. A **9**, 1151 (1994); *ibid*, Phys. Lett. B **336**, 131 (1994).

[257] S. Soff *et al.*, Phys. Rev. C **51**, 3320 (1995).

[258] C. Hartnack *et al.*, Phys. Rep. **510**, 119 (2012).

[259] J. Molitoris, J.B. Hoffer, H. Kruse and H. Stöcker, Phys. Rev. Lett. **53**, 899 (1984).

[260] S.M. Kiselew and Y.E. Polrowskil, Sov. J., Nucl. Phys. **38**, 46 (1983).

[261] Z. X. Li , C. Hartnack, H. Stöcker and W. Greiner, Phys. Rev. C **44**, 824 (1991).

[262] C. Hartnack, H. Oeschler, J. Aichelin, Phys. Rev. Lett. **96**, 012302 (2006).

[263] C. Fuchs, A. Faessler, E. Zabrodin, Y.M. Zheng, Phys. Rev. Lett. **86**, 1974 (2001).

[264] H. Yukawa, Phys. Rev. **76**, 300 (1949); H. Yukawa, Nobel Lecture, Dec. **12** (1949).

[265] L.G. Arnold *et al.*, Phys. Rev. C **25**, 936 (1982).

[266] G. Passatore, Nucl. Phys. A **95**, 694 (1967).

[267] B.A. Li, L.W. Chen and C.M. Ko, Phys. Rep. **464**, 113 (2008).

[268] B. A. Li, Phys. Rev. C **69**, 034614 (2004).

[269] P. Bonche, S. Koonin, and J.W. Negele, Phys. Rev. C **13**, 1226 (1976).

[270] R. Cusson and J. Maruhn, Phys. Rev. Lett. **36**, 1166 (1976).

[271] S.A. Bass, C. Hartnack, H. Stöcker, and W. Greiner, Phys. Rev. C **51**, 3343 (1995).

[272] J. Cugnon, Phys. Rev. C **22**, 1885 (1980).

[273] P. Danielewicz and G.F. Bertsch, Nucl. Phys. A **533**, 712 (1991).

[274] J. Aichelin, G. Peilert, A. Bohnet, A. Rosenhauer, H. Stöcker and W. Greiner, Phys. Rev. C **37**, 2451 (1998).

[275] Z. X. Li , C. Hartnack, H. Stöcker and W. Greiner, Phys. Rev. C **44**, 824 (1991).

[276] Y. K. Vermani and R. K. Puri, Eur. Phys. Lett. **85**, 62001 (2009).

[277] S. Kumar and R.K. Puri, Phys. Rev. C **58**, 320 (1998).

[278] L. Manduci *et al.*, Nucl. Phys. A **811**, 93 (2008).

[279] Sangeeta, A. Jain and S. Kumar, Nucl. Phys. A **927** 220 (2014).

[280] E. Galichet, M. Colonna, B. Borderie and M.F. Rivet, Phys. Rev. C **79**, 064615 (2009).

[281] M. B. Tsang *et al.*, Phys. Rev. Lett. **71**, 1502-1505 (No. 10) (1993).

[282] C. Sfienti *et al.*, Nucl. Phys. A **749**, 83c-92c (2005).

[283] S. A. Voloshin, Nucl. Phys. A **715**, 379c-388c (2003).

[284] S. A. Voloshin, Phys. Rev. C **55**, R1630 (1997).

[285] P. Russoto *et al.*, Eur. Phys. J. A **50**, 38 (2014).

[286] A. Butta *et al.*, Nucl. Phys. A **584**, 397-412 (1995).

[287] H. Sorge, Phys. Rev Lett., **78**, 2309-2312 (1997).

[288] A. Bonasera and L. P. Csernai, Phys. Rev. Lett. **59**, 630 (1987).

[289] C. A. Ogilvie *et al.*, Phys. Rev. C **40**, 2592 (1989).

[290] J. Y. Ollitrault, Phys. Rev. D **46**, 229 (1992).

[291] C. Pinkenburg *et al.*, Phys. Rev. Lett. **83**, 1295 (1999).

[292] Y. Zhang and Z. Li, Phys. Rev. C **74**, 014602 (2006) .

[293] A. Andronic, et al., Phys. Rev. C **67**,034907 (2003) .

[294] S. Kumar, V. Kaur and S. Kumar, Cent. Eur. J. Phys. **9**, 986 (2011).

[295] A. D. Sood and R. K. Puri, Phys. Rev. C **69**, 054612 (2004).

[296] S. Kumar, S. Kumar and R. K. Puri, Phys. Rev. C **81**, 014611 (2010).

[297] G. D. Westfall, Nucl. Phys. A **681**, 343c-350c (2001).

[298] A. D. Sood and R. K. Puri, Phys. Rev. C **73**, 067602 (2006).

[299] P. Russotto *et al.*, Phys. Lett. B **697**, 471 (2011).

[300] V. Kaur, S. Kumar and R. K. Puri, Phys. Lett. B **697**, 512 (2011).

[301] A. Jain and S. Kumar, Phys. Scr. **88**, 025201 (2013); *ibid.* **89**, 035301 (2014) .

[302] R. Bansal, S. Gautam and R. K. Puri, J. Phys. G: Nucl. Part. Phys. **41**, 035103 (2014).

[303] A. Jain and S. Kumar, Phys. Scr. **88**, 025201 (2013); *ibid.* **89**, 035301 (2014).

[304] Sangeeta and V. Kaur, Nucl. Phys. A **966** 20-33 (2017).

[305] R. Chugh and A. D. Sood, Pram. J Phys. **77**, 289 (2011).

[306] S. Goyal, Nucl. Phys. A **856**, 154 (2011).

[307] Lovejot and S. Gautam, Phys. of Part. and Nucl. Lett. **11**, 232 (2014).

[308] R. Kumar, S. Gautam and R. K. Puri, Phys. Rev. C **89**, 064608 (2014).

[309] A. Jain and S. Kumar, Nucl. Phys. A **876**, 109 (2012).

[310] Yu.B. Ivanov, Phys. Lett. B **690**, 358-362 (2010).

[311] Y. F. Yang, J. Y. Liu and W. Zuo, Chin. Phys. Lett. **18**, 1040 (2001).

[312] Q.F. Li and Z.X. Li, Chin. Phys. Lett. **19**, 321 (2002).

[313] J. K. Dhawan *et al.*, Phys. Rev. C **74**, 057901 (2006).

[314] K. S. Vinayak and S. Kumar, J. Phys. G: Nucl. Part. Phys. **39**, 095105 (2012).

[315] W. Reisdorf *et al.*, Phys. Rev. Lett. **92**, 232301 (2004).

[316] Y. Zhang et al., Phys. Rev. C **75**, 034615 (2007).

[317] G. Q. Zhang et al., Phys. Rev. C **84**, 034612 (2011).

[318] Sangeeta, Acta Phys. Pol. B **47**, 991-996 (2016).

[319] Sangeeta and V. Kaur, Ind. J. Sci. and Tech. **10**, 31 (2017).

[320] F. Fu *et al.*, Phys. Lett. B **666**, 359 (2008).

[321] R. K. Puri and A. D. Sood, Heavy Ion Phys. **16**, 429 (2002).

[322] S. Kumar and R.K. Puri, Phys. Rev. C **60**, 054607 (1999).

[323] S. Kumar, S. Kumar and R. K. Puri, Phys. Rev. C **78**, 064603 (2008).

[324] Q. Pan and P. Danielewicz, Phys. Rev. Lett. **70**, 2062 (1993).

[325] J. Zhang, S. D. Gupta and C. Gale, Phys. Rev. C **50**, 1617 (1994).

[326] J. Singh, S. Kumar and R. K. Puri, Phys. Rev. C 63, 054603 (2001).

[327] Y. K. Vermani et al., Phys. Rev. C **79**, 064613 (2009).

[328] J. Singh and R. K. Puri, J. Phys. G: Nucl. Part. Phys. **27**, 2091 (2001).

[329] J. Singh, S. Kumar, R.K. Puri, Phys. Rev. C **62**, 044617 (2000).

[330] V. Kaur and S. Kumar, J. Phys. G: Nucl. Part. Phys. **39** 085114 (2012).

[331] V. Kaur and S. Kumar, Phys. Rev. C **81**, 064610 (2010).

[332] Sangeeta and V. Kaur, Acta Phys. Pol. B **48**, 623-627 (2017).

[333] Sangeeta and V. Kaur, EPJ web of conferences 146, 12017 (2017).

[334] D.T. Khoa, N. Ohtsuka, M. Matin, A. Faessler, S. Huang, E. Lehmann and R.K. Puri, Nucl. Phys. A **548**, 102 (1992).

[335] D. T. Khoa *et al.*, Nucl. Phys. A **542**, 671 (1992).

[336] M. Barronco and J. Treiner, Nucl. Phys. A **351**, 269 (1987).

[337] R. K. Puri, E. Lehmann, A. Faessler and S.W. Huang, J. Phys. G: Nucl. Part. Phys. **20**, 1817 (1994).

[338] V. Kaur, S. Kumar and R.K. Puri, Nucl. Phys. A **861**, 37 (2011).

[339] K. Singh Vinayak and S. Kumar, Eur. Phys. J. A: Hadrons and Nuclei **48**, 1 (2012).

[340] K.S. Vinayak and A.K. Chaudhuri, J. Phys. G: Nucl. Part. Phys. **42**, 025108 (2015).